



Advanced Ultrasonic Ambient
Ionisation Sources for Mass
Spectrometry and Microdroplet
Accelerated Reactions

Harry James Taylor

A thesis submitted in partial fulfilment of the
requirements of Nottingham Trent University
for the degree of Doctor of Philosophy

September 2022

Declaration

I confirm that this is my own work and the use of all materials from other sources has been properly and fully acknowledged. No part of this thesis has already been, or is being currently submitted for any such degree, diploma or other qualification.

The copyright in this work is held by the author. You may copy up to 5% of this work for private study, or personal, non-commercial research. Any re-use of the information contained within this document should be fully referenced, quoting the author, title, university, degree level and pagination. Queries or requests for any other use, or if a more substantial copy is required, should be directed to the author

Signed:.....

Date:.....

Harry James Taylor

Acknowledgements:

Any mistakes that lie within this thesis are the direct result of regular contributions made by two cats, Rocky and Pepper, walking across my keyboard, and are certainly not a reflection on the author's work.

The journey of this PhD has been a strange one, and I am not entirely sure how I have come to the end of it. One thing I do know, is that the journey would have been impossible without the support of the following:

Firstly, to my supervisor, Dr. David Kilgour. Thank you for your patience, knowledge, mentorship, time, guidance, and jokes. The imposter syndrome monster, or "inner-Harry" as you refer to it, has been a tough beast for you to slay, but you managed it.

Thank you to Prof. John Wallis, Dr. Lee Martin, Dr. Muriel Funck, and Dr. Quentin Hanley, all of whom moulded me into the researcher I am today. I'd like to make a special thank you to Dr. Muriel Funck, who was there to pick up the pieces of an occasionally very tired and overly emotional PhD student.

My thanks also go out to - Dr. Patrick Sears, Dr. Logan Mackay, Prof. Ron Heeren, Dr. Graham Hickman, and Dr. David Boocock for letting me play around with various pieces of very expensive kit. I'm glad I didn't break anything.

Thank you to Charlotte, Mark, Hannah, Nigel, Kelly, and all the technical team for keeping the lab a well-oiled machine. A particular thanks to Charlotte for being my partner in crime whilst teaching, and clearing up the mess as I went along.

To the surviving members of the Kilgour Lab gang who helped me along the way - Tania, Andrej, Dan K, Can and Bruna - thank you for making the journey a fun one. Andrej - sorry for those very long days in the lab on my visit to Maastricht, it was all worth it in the end!

To my friends - Jack, Matt, Alex, Amy, Ed, Holly, Lauren, and Charlotte. Thank you for listening to me moan about everything in the pub for four years, even though some of you still think I've made a machine that makes Smarties.

Mum, Dad, we did it. Thank you for everything, you have always been the light guiding me along my path. Without your support this would not have been possible. I love you both so much.

To my fiancé, Beth. Thank you for your endless love and support. Your radiant positivity that I could finish this project has so often been the only reason I kept going. You have carried me through this process, and I would not have crossed this finish line without you. I promise I won't make you read this thesis. I love you, always.

Finally, thank you Nottingham Trent University. I'll miss you

This thesis is dedicated to those we lost along the way.

John Richard Lattimore

Simon John Farrow

John Philip Gray

Abstract

This PhD thesis presents two related projects, linked because both benefit from the use of a specific kind of ultrasonic nebulizer.

The first project describes the development and subsequent application of a novel droplet-on-demand ionisation source which provides a solution to some of the limitations currently associated with performing mass calibration for mass spectrometry. After an initial development phase using a commercially available piezoelectric droplet-on-demand device, the system chosen for use was a Porous Ultrasonic Piezoelectric Plate (PUPP) device coupled to a conventional micro/nano-electrospray system.

The PUPP system was used in the analysis of a highly complex organic matter sample, Suwannee River Fulvic Acid, and used encoded internal recalibration to generate high confidence automated peak assignment. Due to the droplet-on-demand nature of the PUPP device, calibrant could be introduced whenever needed during analysis, and the intensity of the calibrant peak relative to sample peaks could be adjusted through the system's ability to modulate the volume of calibrant sprayed, in real time.

Although the analysis of the samples using encoded internal recalibration showed no improvement in the peak assignment as expected, the workflow to get to the same stage is significantly simplified. The system is entirely automated, meaning that large batches of samples could be analysed, calibrated, and processed without the need for manual input by a user for each individual spectrum.

Further beneficial applications of the PUPP ionisation source are also presented, including the capability to perform rapid analysis of samples, component confirmation analysis and real-time adduct modification.

Additional tasks which were undertaken to support the development process of each project are presented, including the development of a 3D printed fused silica capillary grinding system to make custom electrospray needles and the software written to process the complex data generated for the ionisation source. Finally, recommendations for further development and other potential applications of the ionisation source are presented, which were beyond the scope of this project.

The second project, aimed to use the PUPP system to perform chemical synthesis in microdroplets, by taking advantage of the significantly enhanced chemical

reaction rates observed inside microdroplets reported in the literature. The Hydrazone reaction is shown to proceed offline using the PUPP system. However, the reaction is shown to preferentially form the E isomer when performed inside a microdroplet, whilst during bulk synthesis the Z isomer is preferentially formed. Evidence for this is given, including the subsequent photorelaxation of the E isomer to form the more stable Z isomer.

Results indicated that the Pechmann condensation would be a new and suitable reaction which undergoes this reaction rate enhancement. However, this same success could not be achieved away from the mass spectrometer, and this was later discovered to be because of the difference in ionisation efficiencies of the reactants and products, which masked the true picture of the acceleration effect. Therefore, the decision was taken to shift the focus of the project towards establishing a robust screening method for microdroplet accelerated reactions which could be suitable for scale-up investigations, which is presented within this thesis.

Table of Contents

Section A: Ionisation Source Development1

Chapter 1: Introduction, Aims & Experimental2

1.0	Mass Spectrometry Principles	2
1.1	Mass Recalibration.....	4
1.1.1	Mass Recalibration Calculations	6
1.2	Instrumentation	9
1.2.1	Quadrupole Time-of-Flight Mass Spectrometry	9
1.2.2	Orbitrap Mass Spectrometry	12
1.2.3	Fourier Transform Ion Cyclotron Resonance Mass Spectrometry ..	14
1.3	Ionisation Sources.....	17
1.3.1	Electrospray Ionisation (ESI)	18
1.3.2	Direct Analysis in Real Time (DART).....	20
1.3.3	Desorption Electrospray Ionisation (DESI)	21
1.4	Droplet-on-Demand Ionisation Sources	22
1.4.1	Acoustic Mist Ionisation (AMI).....	23
1.4.2	Surface Acoustic Wave Nebulisation (SAWN).....	24
1.4.3	Array of Micromachined Ultrasonic Electrosprays (AMUSE).....	25
1.4.4	Ultrasonic Assisted Spray Ionisation (UASI)	25
1.5	Ion Sources for Improved Mass Accuracy	26
1.6	Summary	28
1.7	Aims	29
1.7.1	Internal Encoded Recalibration and Duty Cycle.....	29
1.8	Experimental	30
1.8.1	Equipment.....	30
1.8.2	Chemicals.....	31
1.8.3	Instrumentation	32
1.8.4	Software	32

Chapter 2: Microdrop System Development34

2.0	Ion Source - Microdrop.....	34
2.1	Microdrop System Structure.....	35
2.2	Microdrop Ion Source Development	38
2.2.1	Ion Source 1.0 - Single Microdrop into MS Inlet (MDD)	39
2.2.2	Ion Source 2.0 - Double Microdrop into MS Inlet (MDD ²)	41
2.2.3	Ion Source 3.0 - Single Microdrop into ESI Stream (MDD-ESI)	42

2.2.4	Ion Source 4.0 - Single Microdrop onto Needle (MDD-PESI)	45
2.2.5	Ion Source 5.0 - Double Microdrop onto Needle – MDD ² -PESI	47
2.3	Microdrop System: Limitations	49
Chapter 3: PUPP System Development		50
3.0	Ion Source - PUPP	50
3.1	PUPP System	50
3.1.1	Duty Cycle Control of PUPP	54
3.1.2	Scanning Electron Microscope Analysis of PUPP	54
3.1.3	Elemental Analysis of Plates via SEM-EDS.....	55
3.2	PUPP Ion Source Development	56
3.2.1	Ion Source 6.0 - Single PUPP into MS Inlet (PUPP).....	57
3.2.2	Ion Source 7.0 - Single PUPP onto Needle (PUPP-PESI)	59
3.2.3	Ion Source 8.0 – Single PUPP into ESI Spray (PUPP-ESI).....	60
3.3	Application onto different Mass Spectrometers	63
3.3.1	Waters Xevo G2-XS Q-TOF	64
3.3.2	ABSciex Triple TOF 6600	64
3.3.3	Bruker solariX 12T FT-ICR	66
3.3.4	Thermo Fisher Q-Exactive Orbitrap	71
3.4	Instrument Synchronization	73
3.4.1	Q-TOF Trigger	74
3.4.2	Orbitrap Trigger	75
3.4.3	FT-ICR Trigger	76
3.5	Summary	77
Chapter 4: Ion Source Applications		79
4.0	Ion Source Applications	79
4.1	Encoded Internal Mass Recalibration	79
4.1.1	Complex Organic Matter Analysis - Suwanee River Fulvic Acid.....	84
4.2	Rapid Sample Analysis	86
4.2.1	Rapid Sample Analysis - Beer	86
4.2.2	Rapid Sample Analysis – Juice	89
4.2.3	Rapid Sample Analysis – Human Plasma	91
4.2.4	PUPP-PESI - Sequential Ionisation Effect	94
4.2.5	Carryover Effect	95
4.2.6	PUPP-PESI Polysiloxane Background Signal.....	96
4.2.7	Rapid Analysis - BMSS Ambient Ionisation Study.....	98
4.3	Adduct Modification	103
4.4	Component Confirmation.....	107

4.4.1	Confirmation using Direct Infusion.....	109
4.4.2	Confirmation using LC-MS Dead Volume.....	110
4.4.3	Confirmation during LC-MS peak elution.....	112
4.5	Summary	113
Chapter 5: Tools Developed		115
5.0	Software	116
5.1	LabVIEW Introduction	116
5.2	Data Processing Tools	117
5.2.1	“Mezzo” – Reading mz5 format files.....	117
5.2.2	“Transcend” – Viewing and process transient data	119
5.2.3	“THRASHer” - Baseline Calculation (THRASH Algorithm)	120
5.3	Hardware Control	122
5.3.1	“MISSI” – Microdrop Ion Source System Interface	122
5.3.2	“Ion-Sync” - Q-TOF Trigger	123
5.4	Custom Fused Silica Grinder	124
5.4.1	Fused Silica Grinder – Version 1	126
5.4.2	Fused Silica Grinder – Version 2	127
5.4.3	Fused Silica Grinder – Version 3	128
5.4.4	Fused Silica Grinder – Version 4	128
5.4.5	Further Development	130
5.5	Summary	130
Chapter 6: Future Suggested Work.....		131
6.0	Future Suggested Work	132
6.1	Tandem MS Internal Encoded Calibration.....	132
6.2	“In-source” Enzymatic Digestion.....	133
6.3	Rapid Analysis - Liquid Handling Robot Capability	134
6.4	PUPP-DART-MS	135
6.5	Summary	136
Conclusion		137
Section B: Microdroplet Accelerated Reactions		139
Chapter 7: Introduction, Aims & Experimental		140
7.0	Introduction.....	140
7.1	History	141
7.2	Mechanism	141
7.2.1	Rapid Desolvation.....	142

7.2.2	pH Effects.....	143
7.2.3	Enthalpy.....	143
7.2.4	Entropy	144
7.2.5	Rapid Diffusion/Mixing of Reactants	144
7.3	Microdroplet Generating Methods	145
7.4	Current Reactions.....	146
7.5	Large Scale Microdroplet Synthesis.....	146
7.6	Summary	147
7.7	Aims	148
7.8	Experimental	148
7.8.1	Equipment/Instrumentation	148
7.8.2	Reagents.....	148
7.8.3	Instrument Methods	149
7.8.4	Hydrazone Reaction.....	149
7.8.5	Pechmann Condensation	150
Chapter 8: Microdroplet Accelerated Synthesis.....		151
8.0	Microdroplet Accelerated Synthesis	152
8.1	Hydrazone Synthesis	152
8.1.1	Online Synthesis:	153
8.1.2	Offline Synthesis:	154
8.2	Pechmann Synthesis.....	159
8.2.1	Online Synthesis	160
8.2.2	Offline Synthesis	161
8.2.3	Online Investigation.....	162
8.3	Recommended Screening Methods.....	163
8.3.1	Test 1: Identification of Products.....	164
8.3.2	Test 2: Confirmation of True Microdroplet Effect.....	165
8.3.3	Test 3: Determine the Yield for Online Microdroplet Synthesis...	166
8.3.4	Test 4: Determine the Yield for Offline Microdroplet Synthesis...	168
8.4	Summary	169
Conclusion		171
References.....		173
Courses and Oral/Poster Presentations:.....		197
Appendix		198

Figures

Figure 1 - Peak Resolution (FWHM)	2
Figure 2 - Effect of increasing peak resolution	3
Figure 3 – Mass Error vs m/z for a Spectrum of Triton QS-15	6
Figure 4 – Mass Error for Beer Sugars (Before Recalibration)	7
Figure 5 – Mass Error for Beer Sugars (After Correction)	9
Figure 6 – Quadrupole Time-of-Flight Mass Spectrometer	10
Figure 7 – Quadrupole Rod Positions & Voltages	11
Figure 8 – Quadrupole Mathieu Stability Diagram.....	11
Figure 9 – Q-Exactive Orbitrap Mass Spectrometer (reprinted with permission from Thermo Fisher)	13
Figure 10 – Ion Motion in Orbitrap Mass Analyser Cell (reprinted with permission from Thermo Fisher)	13
Figure 11 – Bruker solariX FT-ICR Schematic (reprinted with permission from Bruker)	14
Figure 12 – FT-ICR Cell Structure	15
Figure 13 – Ion Motion inside an FT-ICR Cell	16
Figure 14 - Electrospray Ionisation (ESI)	19
Figure 15 - Direct Analysis in Real Time (DART)	20
Figure 16 - Desorption Electrospray Ionisation (DESI)	21
Figure 17 - Acoustic Mist Ionisation (AMI).....	23
Figure 18 - Surface Acoustic Wave Nebulisation (SAWN).....	24
Figure 19 - Array of Micromachines Ultrasonic Electrospray (AMUSE)	25
Figure 20 - Ultrasonic Assisted Spray Ionisation (UASI)	25
Figure 21 - Examples of Mechanically and Electrically Switched Dual Electrospray Systems	26
Figure 22 - Theoretical PUPP Duty Cycle Control & Calibration Curve	30
Figure 23 – Overall Microdrop system (Left) and Internal Components of Microdrop Unit (Right).....	35

Figure 24 - Difference in quality of droplet formation when Microdrop system is tuned and untuned	36
Figure 25 - Microdrop Single Pulse Emission Sequence	36
Figure 26 - Microdrop Triple Pulse Emission Sequence	37
Figure 27 - Microdroplet formation process	38
Figure 28 - Ion Source 1.0 - Single Microdrop directly into MS Inlet	39
Figure 29 - Microdrop Ion Source - Ion Intensity vs Applied Voltage.....	39
Figure 30 - Effect of Charging Droplets on Microdrop Signal	40
Figure 31 - Microdrop Frequency vs Intensity Relationship	41
Figure 32 - Ion Source 2.0 - Double Microdroplet directly into MS Inlet	41
Figure 33 - Interference observed between highly charged Microdrop streams	42
Figure 34 - Single Microdrop directed into ESI Plume	42
Figure 35 - Single Microdrop directed onto ESI Needle Tip	42
Figure 36 - Spectra obtained from ESI Microdrop Dataset	44
Figure 37 - ESI Analysis of Beer with Microdrop Triton Calibration Peaks.....	44
Figure 38 - Single Microdrop onto Needle.....	45
Figure 39 - Single Microdrop onto Needle EIC.....	46
Figure 40 - Single Microdrop onto Needle Triton Spectra	46
Figure 41 - Double Microdrop onto Needle	47
Figure 42 - Ion Source 5.0 Design Images	48
Figure 43 - Two Microdrop Heads onto Needle - Beer & Triton Signal.....	48
Figure 44 - PUPPs with Scale.....	51
Figure 45 - PUPP Schematic	51
Figure 46 - PUPP Mechanism of Droplet Ejection	52
Figure 47 - PUPP in Operate Mode.....	52
Figure 48 - Extractive Electrospray Ionisation coupled to Ultrasonic Nebulisers for Analysis of Inorganics.....	53
Figure 49 - Scanning Electron Microscope Images of PUPPs.....	55
Figure 50 - Elemental Mapping of 1-Hole PUPP by Energy-Dispersive X-Ray Spectroscopy	56

Figure 51 - Single PUPP Directly into Inlet.....	57
Figure 52 - PUPP Analysis of Beer - Positive & Negative Spectra	57
Figure 53 - PUPP coupled to Thermo Q-Exactive Orbitrap.....	58
Figure 54 - Inconsistent PUPP Total Ion Chromatogram	58
Figure 55 - Single PUPP onto Needle	59
Figure 56 - Single PUPP into ESI Spray	60
Figure 57 - Ion Source Prototype Design	61
Figure 58 - PUPP-ESI Ion Source - Triton Intensity	61
Figure 59 - PUPP-ESI Ion Source - Beer Intensity	62
Figure 60 - PUPP-ESI Ion Source - Triton Intensity vs Duty Cycle	62
Figure 61 - PUPP-ESI Ion Source - Triton Intensity vs Duty Cycle (Linear Region)	63
Figure 62 - Ion Source Version 7.0 coupled to Waters Xevo G2-XS Q-TOF	64
Figure 63 - PUPP Setup with Sciex TripleTOF 6600	64
Figure 64 - Sciex TripleTOF 6600 Ion Source Testing.....	65
Figure 65 - PUPP-ESI Set Up Schematic on Bruker solariX FT-ICR.....	66
Figure 66 - Photograph of PUPP-ESI Set Up on Bruker solariX FT-ICR	66
Figure 67 - Effect of PUPP Plume Impacting on Different Needle Types	68
Figure 68 - Pivot System generated for Bruker FT-ICR Inlet Shape	68
Figure 69 - Variance in mass and intensity of the PUPP signal	69
Figure 70 - Reduced variance in both mass and intensity after introduction of trigger system.....	70
Figure 71 - Updated PUPP-ESI Set Up on Bruker solariX FT-ICR	70
Figure 72 - PUPP coupled to Thermo Fisher Q-Exactive Orbitrap	71
Figure 73 - Custom Base Plate for Thermo Q-Exactive Ion Source.....	72
Figure 74 - Ion Source coupled to Thermo Fisher Q-Exactive HF Orbitrap.....	72
Figure 75 - PUPP Synchronization with FT-MS Instruments.....	74
Figure 76 - PUPP Synchronisation with TOF Instruments	74
Figure 77 - Waters LC-MS PUPP Trigger Flowchart	75

Figure 78 - Q-Exactive HF Orbitrap Triggers Flowchart	76
Figure 79 - solariX FT-ICR Trigger User Event	77
Figure 80 - Calibration peak with a complex mass spectrum region	80
Figure 81 - "Beacon" Software User Interface (Vibrat-Ion, UK)	81
Figure 82 - Internal Recalibration Programmatic Workflow	82
Figure 83 - Peak Detection of Internal Calibrant using Beacon software	82
Figure 84 - Automatic Peak Detection of Calibrant (Triton) from Analysis of Beer Samples using Beacon software.....	83
Figure 85 - Internal Calibrant Peak Intensity - "Beacon Effect"	84
Figure 86 - SRFA spectra (Top) and SRFA spectra with Triton calibrant (Bottom)	85
Figure 87 - Mass Error vs m/z plot for Triton QS-15 calibrant	85
Figure 88 - SRFA - Mass error with and without encoded internal mass recalibration.....	86
Figure 89 - TIC for Rapid Analysis of Beers	87
Figure 90 - Extracted Spectrum for "Old Crafty Hen" Sample taken during Rapid Analysis testing	88
Figure 91 - PCA Analysis of Beer via ESI.....	89
Figure 92 - PCA Analysis of Beer via PUPP.....	89
Figure 93 - TIC for the Rapid Analysis of Juices	90
Figure 94 - Extracted Spectrum for Orange Juice Sample taken during Rapid Analysis.....	91
Figure 95 - Human Plasma Spectra - Lipid Peaks Identified	93
Figure 96 - Extracted Ion Chromatograms showing the sequential ionisation of analytes	94
Figure 97 - Sequential Ionisation Effect	95
Figure 98 - Carryover effect observed during rapid analysis of juices.....	96
Figure 99 - Polysiloxane Contaminant Spectra	96
Figure 100 - Using Polysiloxane Contamination as a Calibration Tool	98
Figure 101 - BMSS Solution Analysis - Pharmaceutical Mixture in Acetonitrile ..	99

Figure 102 - BMSS Solution Analysis - Pharmaceutical Mixture in Surine.....	100
Figure 103 - Paracetamol in Acetonitrile - Intra-Day repeatability	101
Figure 104 - Paracetamol/Paracetamol-d ₄ Ratio - Intra-Day Repeatability	102
Figure 105 - Paracetamol/Paracetamol-d ₄ Ratio - Inter-Day Repeatability	103
Figure 106 - PUPP-ESI Ion Source - Sodium/Potassium Adduct Ratio	104
Figure 107 - Shift in Sodium/Potassium Adduct Ratio caused by Triton Burst	105
Figure 108 - Relative Intensity of Lithium Adducts of Beer Sugars.....	106
Figure 109 - Effect of introducing Lithium Chloride into Beer via PUPP	106
Figure 110 - Relative Intensity of Silver Adducts of Beer Sugars	107
Figure 111 - Effect of introducing Silver Nitrate into Beer via PUPP	107
Figure 112 - Structure of Paracetamol, Ethyl 2-Picolinate and D-(-)- α -phenylglycine	108
Figure 113 - Compound Fragmentation Patterns	108
Figure 114 - Intensity Heatmap for different component fragments.....	109
Figure 115 - Paracetamol delivered via PUPP during the LC-MS/MS Dead Time	111
Figure 116 - Paracetamol delivered via PUPP during the LC-MS/MS Dead Time with flow splitter.....	111
Figure 117 - Simulated chromatogram showing how the PUPP signal could interact with the LC-MS peak signal	112
Figure 118 - Simulated Chromatograms to show the effect of increasing the signal obtained for the PUPP on the LC-MS peak obtained	113
Figure 119 - Simulated Chromatograms to show the effect of increasing the frequency of the PUPP peaks on the LC-MS peak	113
Figure 120 - LabVIEW Block Diagram (Left) and the Front Panel User Interface (Right)	116
Figure 121 - Identical Basic Functions in MATLAB (Left) and LabVIEW (Right)	117
Figure 122 - User Interface for Waters File Reading Software	118
Figure 123 - Processing Raw Transients in LabVIEW Workflow	119
Figure 124 - Transcend - User Interface	120

Figure 125 - Calculating Baseline Workflow and Spectrum Intensity Histogram	120
Figure 126 – THRASHer - User Interface.....	121
Figure 127 – THRASHer - Peaks Detected over a 0.25 m/z Window.....	121
Figure 128 –	121
Figure 129 - Microdrop Control User Interface	122
Figure 130 - PUPP Trigger System for Waters LC-MS System	123
Figure 131 – Ion-Sync User Interface.....	123
Figure 132 - Fused Silica Electrospray Needle Methods	124
Figure 133 - Fused Silica Etching with Hydrofluoric Acid.....	124
Figure 134 - Fused Silica Pulling with Glass Puller	125
Figure 135 - Effect of tip angle on profile of electrospray needle	125
Figure 136 - Fused Silica Grinder Version 1 Design	126
Figure 137 - Fused Silica Grinder Version 2 Design	127
Figure 138 – Fused Silica Grinder Version 3 Design	128
Figure 139 - Image of Fused Silica Grinder Version 3	128
Figure 140 - Fused Silica Grinder Version 4 Design	129
Figure 141 - Final Fused Silica Grinder (Left) and the Electrospray Tips generated (Right)	129
Figure 142 – Fused Silica Electrospray Needle Reproducibility.....	130
Figure 143 - Prototype Orbitrap Schematic with Omnitrap System and two PUPP systems ²⁰⁵	132
Figure 144 - Tandem MS Internal Encoded Calibration Workflow.....	133
Figure 145 - Antibody Digestion Workflows using PUPP System	133
Figure 146 - PUPP-DART-MS Schematic.....	135
Figure 147 - Microdroplet Concentration Effect	142
Figure 148 - Effect of different levels of solvation on activation energy	143
Figure 149 - Rapid Diffusion in Microdroplets.....	145
Figure 150 – The Hydrazone Reaction	152
Figure 151 - Microdroplet Accelerated Hydrazone Reaction Spectra - ESI(-) ..	154

Figure 152 - Offline Microdroplet Synthesis Setup	155
Figure 153 - Keto vs Enol Products	155
Figure 154 - Hydrazone Synthesis with E/Z Isomer Formation	156
Figure 155 - Effect of LED Irradiation on Isatin Phenylhydrazone LC-MS	156
Figure 156 - Effect of LED Irradiation on ¹ H NMR Spectrum of Isatin Phenylhydrazone	157
Figure 157 - Shift in E/Z Isomer Ratio Over Time observed for Microdroplet Accelerated Hydrazone Product	157
Figure 158 - LC-MS for Sprayed and Unsprayed Hydrazone Reaction Solution	158
Figure 159 - The Pechmann Condensation	159
Figure 160 - Pechmann Reaction Mixture ESI Spectra Obtained.....	160
Figure 161 - Offline Synthesis Schematic	161
Figure 162 - Pechmann Reaction Conversion Ratio vs Desolvation Gas Temperature	162
Figure 163 - Pechmann Reaction Conversion Ratio vs Desolvation Gas Temperature with Correction Factor Applied	163
Figure 164 - Test #1 - Identification of Products.....	165
Figure 165 - Test #2 - Confirmation of True Microdroplet Effect.....	166
Figure 166 - Test #3 - Determine the Yield for Online Microdroplet Synthesis	168
Figure 167 - Test #4 - Determine the Yield for Offline Microdroplet Synthesis	169
Figure 168 - Triton QS-15 Structures	198
Figure 169 - Jeffamine M600 Structures	198
Figure 170 - ESI Cal Tuning Mix Component Structures	199
Figure 171 - Human Plasma Spectra obtained via PUPP and ESI	201
Figure 172 - Human Plasma Internal Calibration	202
Figure 173 - Sequential Ionisation Effect (Waterfall Plot)	205
Figure 174 - Diclofenac in Acetonitrile - Intra-Day repeatability	207
Figure 175 - Terfenadine in Acetonitrile - Intra-Day repeatability	207
Figure 176 - Reserpine in Acetonitrile - Intra-Day repeatability.....	207

Figure 177 - Isatin Phenylhydrazone Carbon and Nitrogen Numbered.....	211
Figure 178 - ¹ H NMR Spectra for E and Z Isatin Phenylhydrazone.....	212
Figure 179 - Intensity of Reactant and Product Peaks vs Desolvation Gas Temperature.....	213
Figure 180 - Pechmann Bulk Synthesis Screening.....	214
Figure 181 - Pechmann Microdroplet Synthesis Screening.....	214

Tables

Table 1 - Elemental Composition of Stainless-Steel Plate (Carbon Excluded) ...	56
Table 2 - Elemental Composition of Stainless-Steel Plate (Carbon Included)....	56
Table 3 - Needle Types & Specifications.....	60
Table 4 - Electrospray Needle Types Tested.....	67
Table 5 - Orange Juice - Compounds Identified.....	90
Table 6 - Human Plasma - Lipid Peaks Identified.....	93
Table 7 - Component Confirmation LC-MS Method.....	109
Table 8 - Summary of Fused Silica Grinder Designs.....	126
Table 9 - Overview of Scale Up Microdroplet Synthesis.....	147
Table 10 - UPLC-UV/MS Method.....	149
Table 11 - Pechmann ESI Settings.....	160
Table 12 - Linear vs Looped Microdroplet Synthesis Systems.....	161
Table 13 - Overview of Ionisation Sources.....	200
Table 14 - Human Plasma Analysis Instrument Settings.....	202
Table 15 - Human Plasma Lipid ESI-MS/MS Data.....	202
Table 16 - Beer Peaks and Assignments.....	204
Table 17 - Origins of Beer Analysed.....	204
Table 18 - BMSS Study Sample Components.....	205
Table 19 - BMSS Mixture (Acetonitrile) Data for PUPP-Orbitrap.....	205
Table 20 - BMSS Mixture (Surine) Data for PUPP-Orbitrap.....	206

Table 21 - BMSS Study Participant Overview	206
Table 22 - Fused Silica Grinder Version 4 Parts List	208
Table 23 - Isatin Phenylhydrazine LC-MS/MS Fragmentation Data	209
Table 24 - Changes in Chemical Shift observed from Z to E Isatin Phenylhydrazine	212

Abbreviations

Abbreviation	Meaning
ABS	Acrylonitrile butadiene styrene
ACN	Acetonitrile
AGC	Automatic gain control
AMI	Acoustic mist ionisation
AMUSE	Array of Micromachined Ultrasonic Electrospays
AP	Atmospheric Pressure
APCI	Atmospheric Pressure Chemical Ionisation
ASAP	Atmospheric Solid Analysis Probe
BASIC	Bruker Acquisition Sequence for Instrument Control
BMSS	British Mass Spectrometry Society
CCD	Charge Coupled Device
CCS	Collisional Cross Section
CE	Capillary Electrophoresis
CEM	Chain Ejection Model
CID	Collision Induced Dissociation
CRM	Charge Residue Model
CSV	Comma Separated Value
DART	Direct Analysis in Real Time

DC	Direct Current
DESI	Desorption Electrospray Ionisation
DMSO	Dimethyl sulfoxide
ECD	Electron Capture Dissociation
EESI	Extractive Electrospray Ionisation
EFF	Electro-flow Focusing
EI	Electron Ionisation
EIC	Extracted Ion Chromatogram
ESI	Electrospray Ionisation
ESSI	Electrosonic Spray Ionisation
ETD	Electron Transfer Dissociation
FA	Formic Acid
FD	Field Desorption
FT	Fourier Transform
FTICR	Fourier Transform Ion Cyclotron Resonance
FTMS	Fourier Transform Mass Spectrometry
FWHM	Full Width Half Maximum
GC	Gas Chromatography
GUI	Graphical User Interface
HCD	Higher-energy C-Trap Dissociation
HDF5	Hierarchical Data Format
HF	Hydrofluoric Acid
HILIC	Hydrophilic Interaction Chromatography
HPLC/UPLC	High/Ultra Performance Liquid Chromatography
HV	High Voltage
ICR	Ion Cyclotron Resonance

ID	Internal Diameter
IEM	Ion Ejection Model
IHSS	International Humic Substances Society
IMS	Imaging Mass Spectrometry
IMS	Ion Mobility Mass Spectrometry
IPA	Isopropyl Alcohol
IR	Infrared
IRMPD	Infrared Multiphoton Dissociation
IRMS	Isotope Ratio Mass Spectrometry
LC	Liquid Chromatography
LED	Light Emitting Diode
LESA	Liquid extraction surface analysis
MALDI	Matrix Assisted Laser Desorption Ionisation
MD	Microdrop
MDD	Microdrop Dispenser
MMA	Mean Mass Accuracy
MS	Mass Spectrometry
NMR	Nuclear Magnetic Resonance
OD	Outer Diameter
PC	Phosphatidylcholine
PCA	Principle Component Analysis
PDA	Photodiode-Array Detection
PDMS	Polydimethylsiloxane
PEG	Polyethylene glycol
PESI	Probe Electrospray Ionisation
PTFE	Polytetrafluoroethylene

PUPP	Porous Ultrasonic Piezoelectric Plate
REIMS	Rapid Evaporative Ionisation Mass Spectrometry
RF	Radio Frequency
RMS	Root Mean Squared
RPM	Revolutions Per Minute
SAWN	Surface Acoustic Wave Nebulisation
SEC	Size Exclusion Chromatography
SEM	Scanning Electron Microscopy
SESI	Secondary Electrospray Ionisation
SID	Surface Induced Dissociation
SRFA	Suwannee River Fulvic Acid
TD	Thermal Desorption
TIC	Total Ion Chromatogram
TOF	Time-of-Flight
TTL	Time to Live
UASI	Ultrasonic Assisted Spray Ionisation
UV	Ultraviolet
VI	Virtual Instrument
ZDV	Zero Dead Volume

Section A: Ionisation Source Development

Mass Spectrometry (MS) has become one of the most powerful tools available for solving analytical problems in a variety of different applications. It has been established as a workhorse for both routine analysis and advanced research, and within both fields the need for higher performing instrumentation continues to grow.

The ionisation source of the mass spectrometer acts as the critical interface between the sample and the instrument itself. Herein, research undertaken to develop and systematically characterize novel droplet-on-demand ionisation sources and ionisation source adaptations is presented. The capability of one of the systems in specific application areas has been explored, and the data generated during this process is presented. After this, the tools and software created to support the development of the ionisation source are presented. Finally, suggested next steps in this research are presented in detail.

Chapter 1: Introduction, Aims & Experimental

This chapter provides the reader with the fundamental principles in mass spectrometry necessary to understand the research undertaken. Herein, the main principles of mass spectrometry, the mass analysers used during this research and finally in-depth analysis of the current ionisation sources available is provided.

1.0 Mass Spectrometry Principles

The ability for a mass spectrometer to successfully analyse a complex sample is determined by three main parameters: mass accuracy, resolution and dynamic range. Mass Accuracy is a measure of the measured m/z (mass to charge ratio) of a compound relative to the exact m/z , which is calculated from the known isotopic masses of the elements of the periodic table. This is usually expressed as parts per million (ppm):

$$\text{Mass Error (ppm)} = \frac{m_{\text{spectrum}} - m_{\text{exact}}}{m_{\text{exact}}} \times 10^6 \quad \text{Eq. 1}$$

Mass spectrometers are routinely calibrated to ensure high mass accuracy, in a process which is generally performed by the analysis of a calibration mixture, containing a series of molecules across a wide mass range for which the exact m/z is known. Mass calibration is discussed in further detail in Section 1.1.

$$\text{Peak Resolution} = \frac{m/z}{\Delta m}$$

$$\Delta m = \text{FWHM}$$

FWHM = "Full Width Half Maximum" - This is the width of the peak at half of the peak height

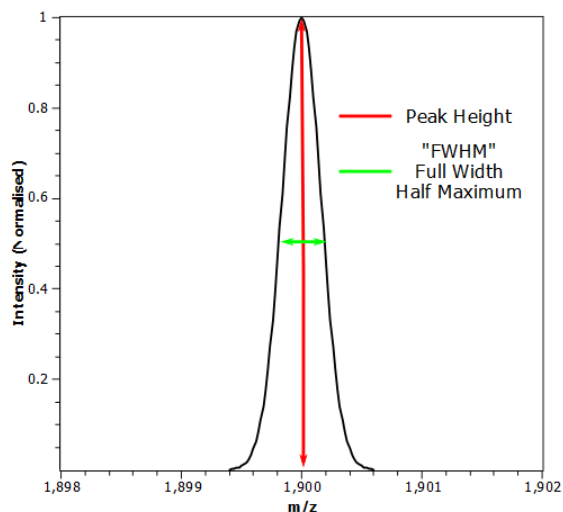


Figure 1 - Peak Resolution (FWHM)

The resolution of a peak within a mass spectrum is a mathematical description of the peak shape itself, with high-resolution peaks being narrow and low-resolution peaks being wide. It is measured as the m/z of the peak divided by the full width

of the peak measured at half the maximum (FWHM), which has been shown visually in Figure 1. High mass resolution is needed for analysis where isotopic fine structure is needed, or alternatively elemental composition determination is necessary. Figure 2 shows a series of spectra (simulated using enviPat Web¹) for Myoglobin (Equine) at different levels of resolution, with only the high resolution able to reveal the isotopic distribution.

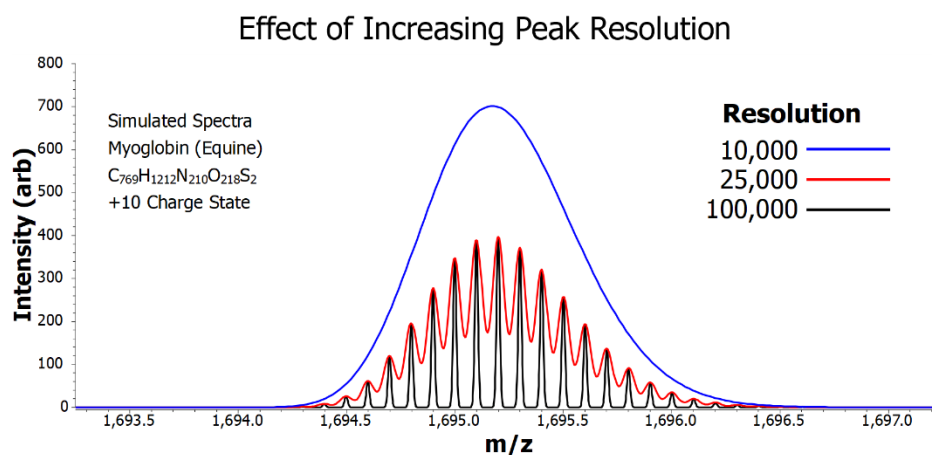


Figure 2 - Effect of increasing peak resolution

The commonly accepted definition for the dynamic range of a mass spectrometer is the sample concentration range over which the signal obtained is proportional to the concentration of the analyte. However, it is more accurate to define the dynamic range of the instrument to include the interaction of all the subsystems of the mass spectrometer.

The detector of the mass spectrometer has its own dynamic range related to the ion currents it can detect. This can be by direct interaction, as is the case for Time of Flight (TOF) analysers, whereby the ion population directly impacts on the surface of the detector. Alternatively, it can be indirect interaction, as is the case for Fourier transform mass analysers which monitor the image current. Ultimately, the dynamic range of the complete mass spectrometry system is limited by the fundamental dynamic range of the detection system.

However, ions that are detected must first be created in the ionisation source, before being transferred through various pumping stages, ion optics and mass analysers before reaching the detector. These systems all have their own inherent transfer efficiencies and ion population limits, which therefore effect the dynamic range of the overall system. Some of these parameters can be controlled or tuned by the user to ensure maximum transfer efficiency or to adjust the ion population available for eventual detection. High performance instruments are commonly designed to provide a high dynamic range, because this is crucial when performing

analyses on complex mixtures which commonly exhibit a wide range of analyte concentrations within an individual sample.

High performing mass spectrometers show strength in all of these areas; mass accuracy, peak resolution and dynamic range. This allows users to make confident assignment of peaks and distinguish between peaks with similar m/z ratios, all over a wide concentration range.

1.1 Mass Recalibration

In order to generate mass spectrometry data which can be assigned with a high degree of confidence, it is crucial that these instruments achieve high mass accuracy. Mass accuracy is a measure of how close the m/z of the peak you obtain in a given spectrum is to the true m/z of the molecule you are analysing, the difference between the two is referred to as the "mass error". Mass error is commonly reported in two units: daltons or parts per million (ppm), the equations of which are both given below in Eq. 2 and Eq. 3. In addition to this, mean mass accuracy (MMA) and root mean squared (RMS) mass accuracy are often presented in the literature as a method of giving an indication in the quality of the data generated, which are shown in Eq. 4 and Eq. 5.² However, MMA and RMS MA are limited in their usefulness when assessing an entire dataset, as the mass error is often dependent on the m/z value. Therefore, applying a single unit of mass accuracy across a large number of datapoints has its limitations, and therefore carries the risk of giving the reader a false impression of the accuracy across the mass range.

$$\text{Mass Error (Da)} = m_{\text{spectrum}} - m_{\text{exact}} \quad \text{Eq. 2}$$

$$\text{Mass Error (ppm)} = \frac{m_{\text{spectrum}} - m_{\text{exact}}}{m_{\text{exact}}} \times 10^6 \quad \text{Eq. 3}$$

$$\text{Mean Mass Accuracy (ppm)} = \sum \frac{|E_{\text{ppm}}|}{n} \quad \text{Eq. 4}$$

$$\text{RMS Mass Error (ppm)} = \sqrt{\frac{\sum (E_{\text{ppm}})^2}{n}} \quad \text{Eq. 5}$$

When assigning molecular formula to peaks within a mass spectrum, high mass accuracy is one crucial aspect required to underpin confident assignments, good mass accuracy is achieved by performing a mass recalibration. When performing the analysis of a low number of known molecules across a narrow mass range,

good mass accuracy and therefore confident assignment can be obtained using a single point mass calibration. When performing the analysis of unknown samples, particularly complex mixtures which have a high number of peaks across a wider mass range, the calibration solution chosen should have several peaks spread across the mass range of interest.

Performing mass recalibration requires one or more internal standards of known mass (m/z) to be analysed. There are two forms of mass recalibration which are commonly performed: external and internal mass (re)calibration. External recalibration is performed prior to the sample analysis and requires the user to analyze a standard solution in a separate data collection run. Using the values generated by this analysis, recalibration can be performed and the data stored as a recalibration file for the instrument to use in subsequent sample analysis. This process is time consuming, and means that confidence in data decreases over time after recalibration is performed, due to instrument drift, lowering the mass accuracy.

Internal recalibration however, does not require any data collection to be performed prior to sample analysis. Instead, the internal standard is analysed with the sample itself, either by spiking the sample solution to be analysed or by using a system which introduces the internal standard to the mass spectrometer through an additional ionisation system, such as the Waters LockSpray system. Internal recalibration is then performed retrospectively after the analysis is complete.

Internal recalibration offers a series of advantages over external recalibration, making it the method of choice for experiments where high mass accuracy is crucial. As mentioned, internal mass recalibration is performed for every sample, and therefore negates the issue of instrument drift over time. Furthermore, internal recalibration ensures that the internal standard ions and the analyte of interest ions share an increased number of instrument conditions which increases the mass accuracy generated relative to external methods.^{3,4} This includes conditions which cannot be positively controlled by the user, including pressure, temperature, degree of inlet contamination etc.

The mass accuracy of peaks obtained using Fourier Transform Mass Spectrometry (FTMS) instruments can change from scan to scan because of fluctuations in the ion population in the mass analyser. This is referred to as the space-charge effect, whereby the electric field associated with ions in the cell cause shifts in the oscillation frequencies, and hence shifts in the observed m/z of identical ions between scans.^{5,6} The effect is magnified by the number of ions present in the

cell, and the charge the ions carry. Unless accounted for, this space charge effect limits the mass accuracy observed, regardless of the trapping parameters being identical between runs. Internal mass recalibration can correct for the space-charge effect, as internal standard ions and sample ions coexist in the cell during analysis, and therefore experience identical shifts in the oscillation frequency due to the identical space charge effect they experience.

Finally, when performing mass recalibration it is important to consider the calibration solution being used. Good calibration solutions provide multiple peaks across the mass range of interest. Compounds which form clusters are a good example of this, such as Cesium Iodide, Trifluoroacetic Acid or Sodium Formate.⁷⁻¹⁰ Alternatively, polymer series with regular repeating units also provide the same benefit, Polyethylene Glycol and Polyethylene oxide are all good examples of these which are routinely used in recalibration.^{11,12} Although recalibration can be performed using internal standards which provide very few peaks across a small mass range, this is less likely to provide a good calibration relative to an internal standard which covers the mass range of interest.^{13,14}

1.1.1 Mass Recalibration Calculations

The first stage of recalibration is to determine the relationship between the mass error in parts per million (ppm) and the m/z of the internal standard peaks. This relationship is typically a second order polynomial for most mass analysers, the general format of which is given in Eq. 6. Figure 3 illustrates this relationship for an example internal standard solution of Triton QS-15 analysed on our quadrupole time of flight mass spectrometer, and the equations for the line of best fit is given in Eq. 6. and Eq. 7.

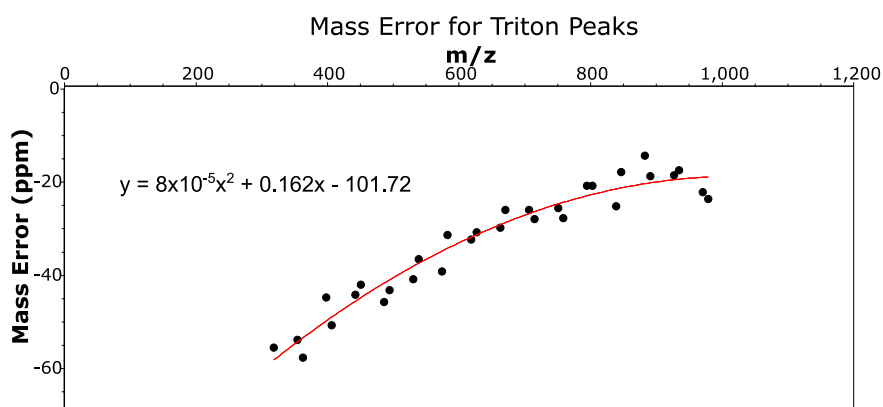


Figure 3 – Mass Error vs m/z for a Spectrum of Triton QS-15

$$\text{Mass Error Curve} = ax^2 + bx + c \quad \text{Eq. 6}$$

$$\text{Mass Error (ppm)} = (7.899 \times 10^{-5})(x)^2 (0.16195)(x) - 101.7192 \quad \text{Eq. 7}$$

Now that the mass error curve has been calculated, it is possible to use this function to correct the sample peaks across the mass range. Figure 4 shows the mass error (in ppm) for a series of sample peaks across the mass range.

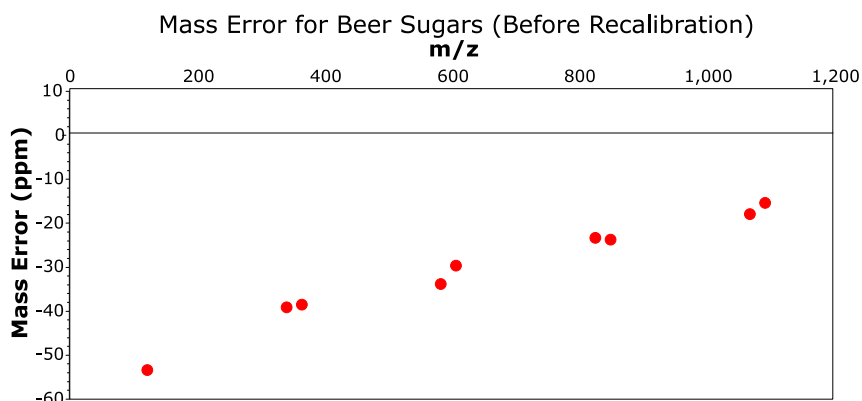


Figure 4 – Mass Error for Beer Sugars (Before Recalibration)

By inputting the spectral values for our sample peaks, it is possible to predict the mass error for a peak at a given mass to charge ratio using the calibration curve. This can be done by inputting a sample spectral value into the calibration curve equation. This has been done in Eq. 8 for a trisaccharide sugar of spectral mass 543.1133 m/z.

$$\begin{aligned} & \text{Predicted Mass Error (ppm)} \\ & = (7.899 \times 10^{-5})(543.1133)^2 (0.16195)(543.1133) - 101.7192 = -37.0605 \text{ ppm} \quad \text{Eq. 8} \end{aligned}$$

In order to perform the recalculation, it is necessary to simplify and rearrange Eq. 3 to make the exact mass the subject. This is shown in the following sequence of equations:

$$\text{Mass Error (ppm)} = \frac{m_{\text{spectrum}} - m_{\text{exact}}}{m_{\text{exact}}} \times 10^6 \quad \text{Original Mass Error Calculation (Eq. 3)}$$

$$\frac{\text{Mass Error (ppm)}}{10^6} = \frac{m_{\text{spectrum}} - m_{\text{exact}}}{m_{\text{exact}}} \quad \text{Both sides are divided by } 10^6 \text{ to eliminate this from the right-hand side.}$$

$$\frac{\text{Mass Error (ppm)}}{10^6} = \frac{m_{\text{spectrum}}}{m_{\text{exact}}} - \frac{m_{\text{exact}}}{m_{\text{exact}}} \quad \text{The right-hand side is broken up into two fractions}$$

$$\frac{\text{Mass Error (ppm)}}{10^6} = \frac{m_{\text{spectrum}}}{m_{\text{exact}}} - 1$$

The equation is simplified as one of the fractions is equal to 1

$$\frac{\text{Mass Error (ppm)}}{10^6} + 1 = \frac{m_{\text{spectrum}}}{m_{\text{exact}}}$$

1 is added to both sides to remove the -1 from the right-hand side

$$\frac{\left(\frac{\text{Mass Error (ppm)}}{10^6}\right) + 1}{m_{\text{spectrum}}} = \frac{1}{m_{\text{exact}}}$$

Both sides are divided by the spectral mass, leaving the exact mass as the only dependent on the right-hand side

$$\frac{m_{\text{spectrum}}}{\left(\frac{\text{Mass Error (ppm)}}{10^6}\right) + 1} = m_{\text{exact}}$$

The equation is inverted to make the exact mass the subject of the equation

The final equation we are left with shows the corrected mass, although due to the recalibration the corrected mass is much closer to the true value, the correction almost never generates a perfect mass accuracy. Therefore, the equation should be presented as it is in Eq. 9, with the corrected m/z ($m_{\text{corrected}}$) as the subject:

$$\frac{m_{\text{spectrum}}}{\left(\frac{\text{ppm}}{10^6} + 1\right)} = m_{\text{corrected}} \quad \text{Eq. 9}$$

Inputting the value of our spectral mass and the mass error calculated from the calibration curve, we can determine the corrected mass of our analyte:

$$\frac{543.1133}{\left(\frac{-37.0605}{10^6} + 1\right)} = m_{\text{corrected}} = 543.13342880 \text{ m/z}$$

Using the mass error equation, we can determine the mass error of our corrected spectral value as follows:

$$\text{Mass Error (ppm)} = \frac{m_{\text{corrected}} - m_{\text{exact}}}{m_{\text{exact}}} \times 10^6$$

$$\text{Mass Error (ppm)} = \frac{543.13342880 - 543.1327480}{543.1327480} \times 10^6 = 1.2535 \text{ ppm}$$

By performing a mass recalibration, the mass error has been significantly reduced, an effect that is observed across the mass range, Figure 5 shows the mass error

values for our Beer analytes before and after the recalibration is performed, and the improvement in mass accuracy is clear.

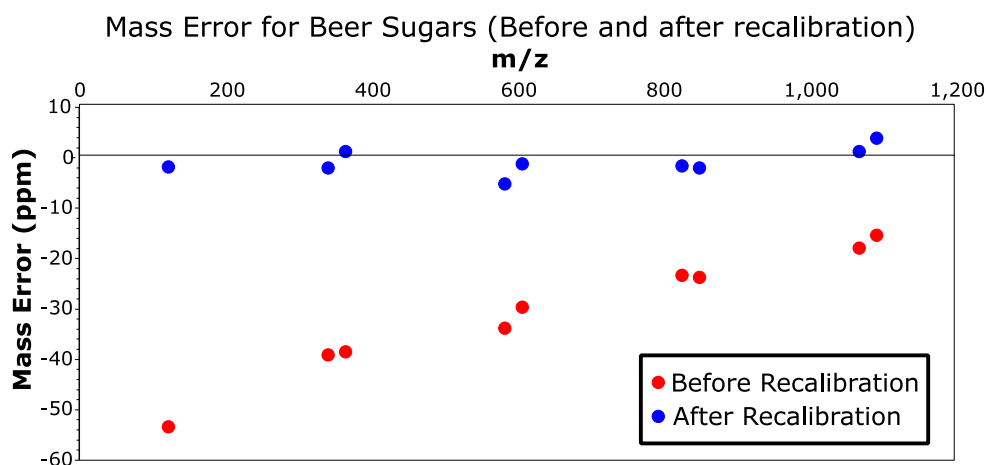


Figure 5 – Mass Error for Beer Sugars (After Correction)

The ionisation source developed during this project was designed in-part to generate reliable and robust data which is suitable for use with custom software, written as part of this project, to perform encoded internal recalibration which is discussed in detail in Chapter 4. There are however other ambient ionisation sources which offer different methods of performing recalibration which have been previously published, and Section 1.5 is dedicated to discussing these.

1.2 Instrumentation

The focus of the work described in this section of the thesis was the development and characterization of a specific class of ion source. However, any ion source for mass spectrometry must be coupled to a system that incorporates one or more mass analyzers. Throughout this project, a variety of different mass analyser types were used, from a variety of different manufacturers. And, although a complete fundamental description of the operation of these mass analyzers is not required, a top level introduction to the general principles which provides enough context and detail necessary to understand the work conducted in this project is beneficial.

1.2.1 Quadrupole Time-of-Flight Mass Spectrometry

The majority of the early development work was performed on a Waters Xevo G2-XS Quadrupole Time-of-Flight (Q-TOF) instrument, a schematic of which can be seen in Figure 6.

Quadrupole Time-of-Flight (Q-TOF) Schematic

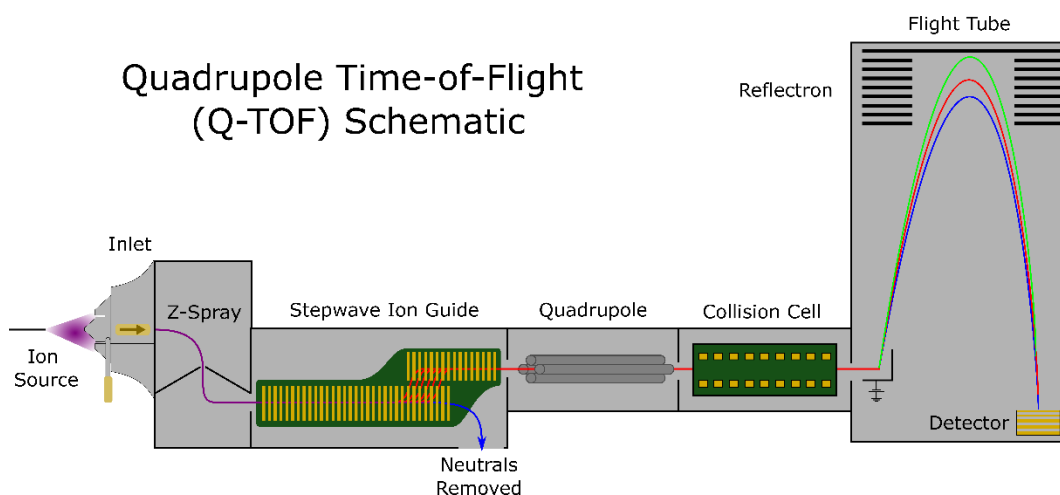


Figure 6 – Quadrupole Time-of-Flight Mass Spectrometer

After sample ionisation from the ionisation source (electrospray ionisation shown), charged ions enter the mass spectrometer through a Z-Spray inlet, where neutrals are pumped away, whilst ions are drawn into the instrument. The sample beam enters the StepWave ion guide, an ion optics system which is used to further eliminate neutrals and other contaminants from the beam entering the mass spectrometer, ensuring that only ions are passed further into the mass spectrometer. The Stepwave consists of a series of ring-shaped electrodes, which guide charged ions up and into the next stage, whilst neutral molecules and incompletely desolvated droplets, which are unaffected by the electrode rings, are pumped away.^{15,16} Although the specific example shown is the case for the Waters instrument shown, the general principle of the sample beam entering a series of ion optics to remove solvent and neutrals is the case for almost all Q-TOF mass spectrometers.

The ion beam then enters the quadrupole, a mass analyser comprising of four parallel rods, where the rods opposing each other are paired. Each pair of rods has a radio frequency (RF) voltage applied, with the two pairs in opposite phase from one another. In addition, a DC offset is applied to the two pairs of rods.¹⁷

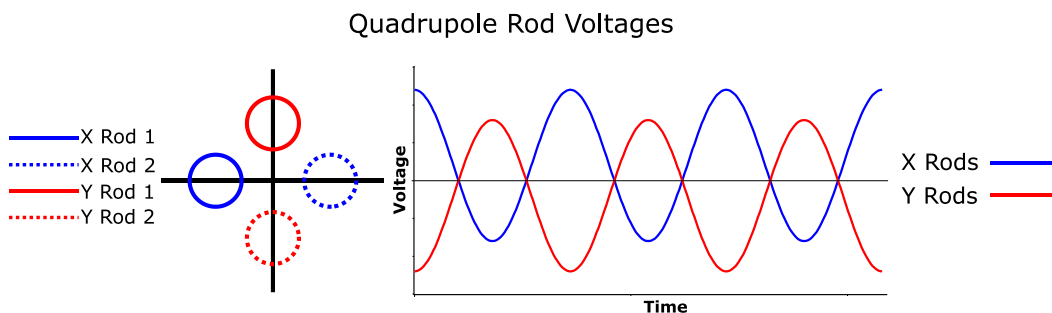


Figure 7 – Quadrupole Rod Positions & Voltages

Ions passing through the quadrupole will either have a stable trajectory, and will successfully navigate through the quadrupole and further into the instrument, or have an unstable trajectory, therefore impacting against the rods where they will discharge and pass no further into the instrument. The Mathieu equations, which are given in Eq.10, predict whether an ion of a given m/z has a stable trajectory through the quadrupole¹⁸:

$$\begin{array}{lll}
 U = \text{DC Potential} & m = \text{Ion Mass} \\
 \text{(Volts)} & \text{(kilograms)} \\
 a_x = \frac{8zU}{mr_0^2\Omega^2} & V = \text{RF Potential} & r_0 = \text{Quadrupole Radius} \\
 & \text{(Volts)} & \text{(metres)} \\
 q_x = \frac{4zV}{mr_0^2\Omega^2} & z = \text{Ion Charge} & \Omega = \text{Radial Frequency} \\
 & \text{(Coulombs)} & \text{(radians per second)}
 \end{array}
 \tag{Eq.10}$$

The trajectory of an ion is considered stable if the Mathieu parameters (a_x and q_x) fall within the stable region of the Mathieu stability diagram (Figure 8).¹⁸

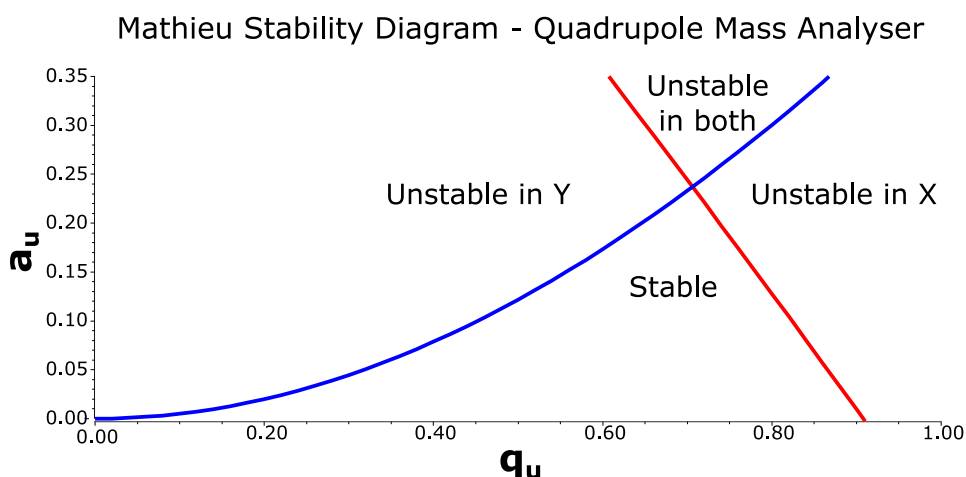


Figure 8 – Quadrupole Mathieu Stability Diagram

After ions pass through the quadrupole, they are then transferred into the collision cell. If the appropriate voltage is supplied, ions are accelerated along the length of this cell and collide with neutral gas; the kinetic energy is transferred into

internal energy, which builds up until it results in the fragmentation of the precursor ion into product ions, in a process known as collision induced dissociation (CID).^{19,20} When the instrument is not performing tandem mass spectrometry, this system is set so that the ions pass through the collision cell at lower energy, and without building up enough internal energy to result in fragmentation.

The Time-of-Flight mass analyzer is the final stage of the instrument, which calculates the m/z of an ion based on the length of time taken to pass through the flight tube and reach the detector. The reflectron was introduced to TOF systems to overcome the initial differences in kinetic energy ions possess when entering the flight tube.^{21,22} Ions with higher kinetic energy will pass further into the reflectron, whilst those with lower kinetic energy will not pass as deeply into the reflectron, thereby reducing the difference in flight time of ions with identical m/z caused by differences in their kinetic energy, improving mass resolution.

1.2.2 Orbitrap Mass Spectrometry

Orbitrap mass analysers are a form of Fourier Transform Mass Spectrometer (FTMS), capable of giving high performance mass accuracy (sub ppm) and resolution ($>100,000$).^{23,24} The mass analyser consists of a central spindle electrode held at a high potential of the opposite polarity to that of the ions for analysis, and a barrel shaped outer electrode which is held at near ground potential.

Although commercial mass spectrometers containing Orbitrap mass analysers vary slightly in their components, a general schematic can be seen in Figure 9 for a Thermo Fisher Q-Exactive system, which has the orbitrap mass analyser labelled. This system uses a quadrupole for initial ion selection. Fragmentation is performed via higher-energy collisional dissociation (HCD), which occurs in a multipole ion trap adjacent to the C-Trap. HCD does not suffer from the low mass cut off associated with ion trap CID because it is being undertaken in a multipole rather than a quadrupole/linear ion trap, making it a powerful tool for isobaric labelling experiments which produce low mass reporter ions.²⁵⁻²⁹

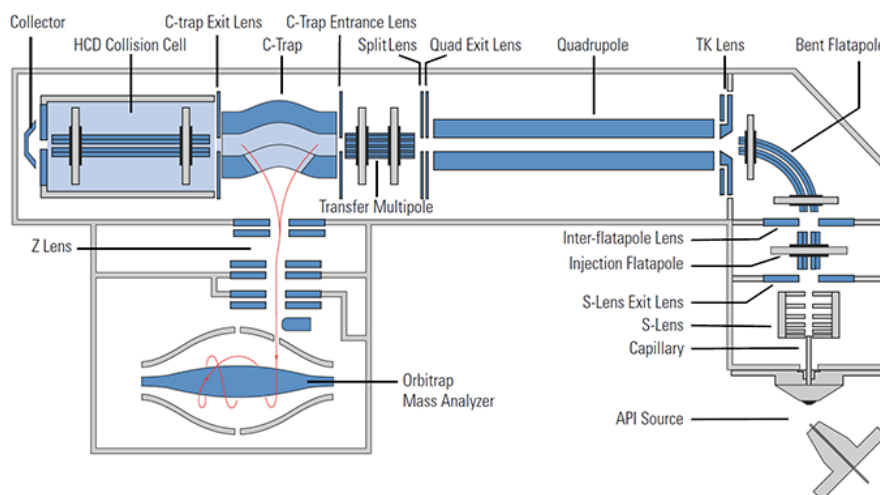


Figure 9 – Q-Exactive Orbitrap Mass Spectrometer (reprinted with permission from Thermo Fisher)

Prior to entering the Orbitrap, ions are sent to the C-Trap. The C-Trap dampens the motion of the ion cloud and focuses the ion packet in the axial direction, this ensures that all ions enter the orbitrap at the same time, and therefore ions of an identical m/z move coherently along the orbitrap mass analyser enhancing the image current.³⁰

Ions are injected with a high kinetic energy (several kiloelectronvolts) through a hole in the outer electrode, where they begin to orbit around the central electrode.³¹ Although the ion is attracted to the central electrode due to its high potential and opposing polarity, the ion does not impact with it and instead begins its orbit around it due to the high kinetic energy the ion is injected with.³² This effect is akin to a satellites ability to orbit the earth at high speed despite the gravitational pull of the earth.

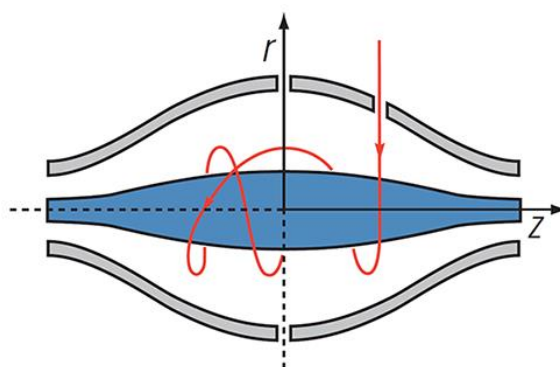


Figure 10 – Ion Motion in Orbitrap Mass Analyser Cell (reprinted with permission from Thermo Fisher)

In addition to their oscillation around the central electrode, the ions also move axially along the direction of the electrode itself, Figure 10 shows the general

motion of ions within an orbitrap, with the axial movement along the central electrode being displayed as the movement along the z-axis.³³ The frequency with which ions move along this axis is proportional to the square root of the inverse of the mass to charge ratio.³⁴

$$\omega = \sqrt{\left(\frac{q}{m}\right)k}$$

Eq. 11

$\omega = \text{Frequency}$
 $q = \text{Charge}$
 $m = \text{Mass}$
 $k = \text{Harmonic constant of the axial potential}$

The outer electrode is split into two halves, and as ions move back and forth along the z-axis they induce a charge difference between the two electrodes. The two halves of electrode are connected through a differential amplifier. This amplifies the image current flowing between the two electrodes, and the signal is digitized to generate a transient. The transient is then Fourier transformed to generate a frequency spectrum, with each ion of a given m/z generating a signal at the corresponding frequency, according to the relationship given in Eq. 11. Finally, a mass calibration function is applied to the frequency spectrum to generate a mass spectrum.

1.2.3 Fourier Transform Ion Cyclotron Resonance Mass Spectrometry

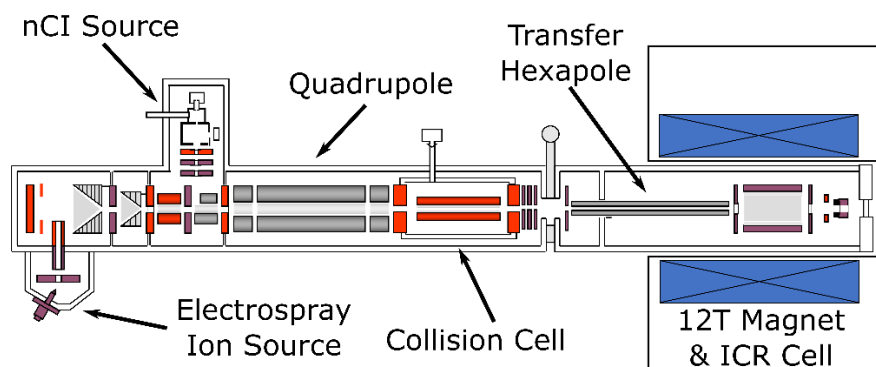


Figure 11 – Bruker solarix FT-ICR Schematic (reprinted with permission from Bruker)

Fourier Transform Ion Cyclotron Resonance Mass Spectrometry (FT-ICR-MS) is a class of mass analyser routinely capable of low parts-per-billion (ppb) mass accuracy and resolving powers well over 1,000,000.³⁵⁻³⁸ FT-ICR instruments offer the highest resolving powers, with the largest, “21 Tesla” class (referring to the magnetic field), reporting resolving powers of just under 40,000,000, for a 300s transient of reserpine.³⁹ The high resolving power, mass accuracy and high variety of fragmentation techniques typically available for commercial FT-ICR

instruments, make them well suited for the analysis of complex mixtures and high mass molecules such as proteins or antibodies.

The ICR mass analyser, often referred to as the ICR Cell, consists of a series of plates which form a cylindrical shape. The number of plates may vary depending on the ICR cell design, and for the purposes of this explanation a simplified model using only 6 plates, made up of three pairs as shown in Figure 12, will be used. In the 6 plate design example shown, two of these are the “end plates” of the cylinder, and are referred to as the trapping plates; these plates are set to a slightly higher potential than the plates forming the body of the cylinder which generate an axial electric trapping field, E . The remaining four plates make up the cylinder itself, and consist of two detection plates and two excitation plates, each pair of plates sit opposite to each other. The entire cell is housed within a superconducting magnet which gives a spatially uniform magnetic field, B , which is directed along the z-axis of the ICR cell.

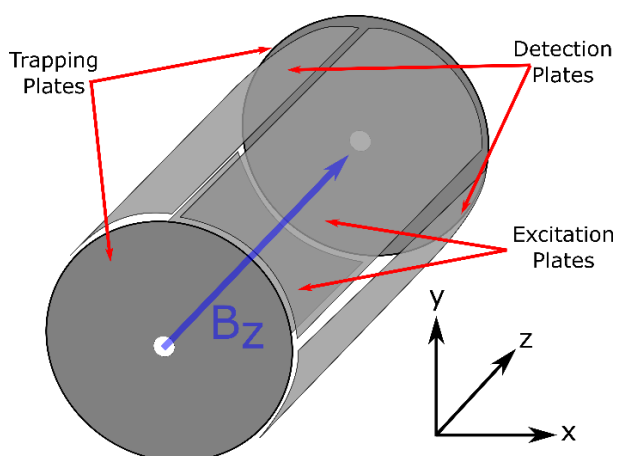


Figure 12 – FT-ICR Cell Structure

Ions entering the magnetic field experience a “Lorentz Force” causing the ion to orbit in a circular motion along the magnetic field axis, referred to as the cyclotron motion, which is described in Eq. 12.⁴⁰ According to this equation, all ions of a given mass to charge ratio have identical cyclotron frequencies, regardless of the ion’s velocity.

$$\omega_{cyc} = 2\pi f_{cyc} = \frac{qB}{m} \quad \text{Eq. 12}$$

The ions also experience motion along the Z-axis of the ICR cell, which is caused by the electric field generated by the trapping plates, known as the trapping motion.⁴¹ The electric field used to generate this trapping effect also generates an electric field in the XY plane of the ICR cell, resulting in ions to be pushed outwards, towards the excitation and detection plates. This causes an orbital

motion around the z-axis of the cell, referred to as the Magnetron Motion. The Cyclotron motion and the Magnetron motion have been displayed visually in Figure 13.

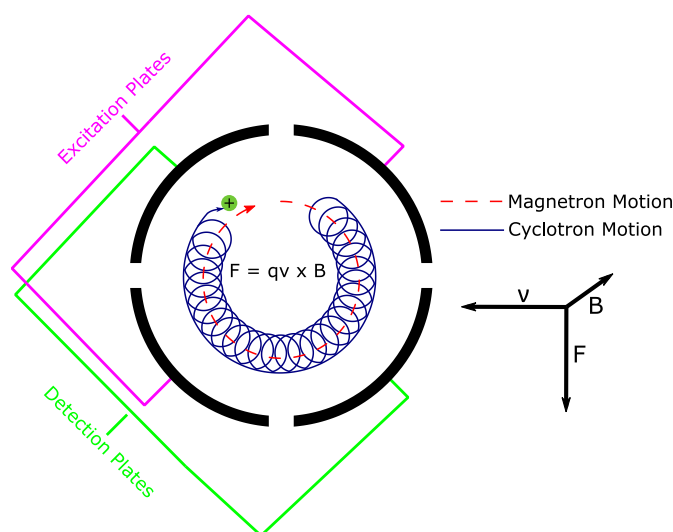


Figure 13 – Ion Motion inside an FT-ICR Cell

Improvements to the design of the ICR cell increased the resolution and the instrument dynamic range, allowing for better analysis of complex mixtures which contain many thousands of compounds at concentrations which vary by several orders of magnitude. Previously, ICR cells created non-ideal fields, resulting in ion cloud dephasing and “comet-like” structures, which ultimately led to a disappearance of signal over time during analysis.⁴² This was overcome by designing cells which decouple the cyclotron, magnetron, and axial motions from one another. This allowed for longer transients to be collected (therefore higher resolution) and higher trapping potentials allowing more ions in the trap (and therefore a higher dynamic range). The cell inside the Bruker 12T solariX FT-ICR used during this project, designed by Nikolaev et al., is an example of a cell which does this.⁴³

Ion detection occurs when the ion packet passes by the detector plates (highlighted in green in Figure 13), inducing a charge difference between the two plates, referred to as an image current. This image current is plotted as a function of time, creating a transient. The mass spectrum is generated by performing a Fourier Transform on the time domain transient and then applying a (frequency to) mass calibration function. Typically for FT-ICR instruments either the Frankl (Eq. 13) or Ledford (Eq. 14) calibration functions are used, and the two provide ultimately identical results.⁴⁴⁻⁴⁶

$$\text{Francl Calibration: } \frac{m}{z} = \frac{A_{\text{Francl}}}{\omega_o + B_{\text{Francl}}} \quad \begin{array}{l} A_{\text{Francl}} = eB \\ B_{\text{Francl}} = \frac{V_T \alpha}{B a^2} \end{array} \quad \text{Eq. 13}$$

$$\text{Ledford Calibration: } \frac{m}{z} = \frac{A_{\text{Ledford}}}{\omega_o} + \frac{B_{\text{Ledford}}}{\omega_o^2} \quad \begin{array}{l} A_{\text{Ledford}} = eB \\ B_{\text{Ledford}} = \frac{eV_T \alpha}{a^2} \end{array} \quad \text{Eq. 14}$$

The excitation plates are used to permit signal collection through the detection plates. Without contribution from the excitation plates, the signal produced by ions as they are initially trapped in the cell suffers from two effects. The first is that the cyclotron motion of the ions is extremely small, and therefore has such a small effect on the detection plates that the signal is too low to be useful.^{47,48} In addition, ions of identical m/z do not orbit coherently around the cell, and therefore the potential difference induced by each ion passing by a detection plate is cancelled out by an ion of identical m/z on the opposing plate.⁴⁹ Applying a RF frequency sweep to the excitation plates overcomes both of these limitations. Ions of a given cyclotron frequency (and therefore m/z), will only become excited by a specific RF frequency, and therefore as the sweep is applied different m/z will become excited. The excitation causes two effects: the ions' oscillation radii increases, and ions of identical m/z begin to orbit the ICR cell coherently.

1.3 Ionisation Sources

In order for a mass spectrometer to be able to manipulate and detect analytes, the analyte molecules must be presented in the form of gas phase ions. The subsystem of a mass spectrometer that produces these ions is known as the ionisation source. Ionisation Sources are referred to as either "hard" or "soft" depending on the amount of fragmentation that molecules undergo upon their ionisation. Electron ionisation (EI) is the classic example of a hard ionisation source that spontaneously causes high fragmentation, which it does by depositing energy in excess of the ionisation potential of the molecule, causing bond cleavage. EI is generally restricted to the ionisation of molecules small enough to be easily thermally vaporised, because it is used to ionise molecules already in the gas-phase. This, along with the lack of intact molecular ion observed through EI are notable disadvantages, and since the introduction of much softer ionisation techniques which can ionise much larger molecules, such as electrospray ionisation (ESI) and matrix assisted laser desorption ionisation (MALDI), EI is generally only used for the analysis of volatile, low molecular weight compounds during gas chromatography analysis.

More recently, since the introduction of desorption electrospray ionisation (DESI) by Cooks and co-workers in 2004, there has been a further shift towards the introduction of ionisation techniques which are performed in ambient conditions, often in open air environments.⁵⁰ This opened up the possibility for the analysis of samples which are unsuited to low pressure environments, and also allowed users to perform the analysis of native surfaces, often with little or no sample preparation. In most cases, the success of an ambient ionisation source stems from its ability to transfer gaseous ions generated at atmospheric pressure into the MS vacuum through the inlet.

1.3.1 Electrospray Ionisation (ESI)

Electrospray Ionisation (ESI) is one of the most common soft ionisation techniques, particularly in the analysis of biological samples, due to its ability to analyse non-volatile components, with low fragmentation, allowing for analysis of intact large biological molecules. Although the system works as a standalone technique by permitting direct infusion of samples into the source, it is most commonly directly coupled with separation techniques such as high-performance liquid chromatography (HPLC), hydrophilic interaction chromatography (HILIC) or capillary electrophoresis (CE).

A solution containing the sample of interest is passed through a needle, held at a high potential ($\approx 1.5 - 6.0$ kV) relative to the inlet of the MS. The polarity of the ions produced matches that of the polarity of the needle. When the needle is held at a positive potential, the counter ions are drawn to the counter electrode, where they are neutralized, whilst the positive ions in the solution pass through the needle, congregating in the meniscus at the needle tip. The electrostatic attraction between the charges on the surface of the liquid and the grounded inlet of the mass spectrometer overcomes the surface tension of the liquid, forming a "Taylor cone".⁵¹ The apex of the Taylor cone is the least stable, and this ultimately breaks up into a plume of highly charged microdroplets.⁵² This process has been shown in Figure 14:

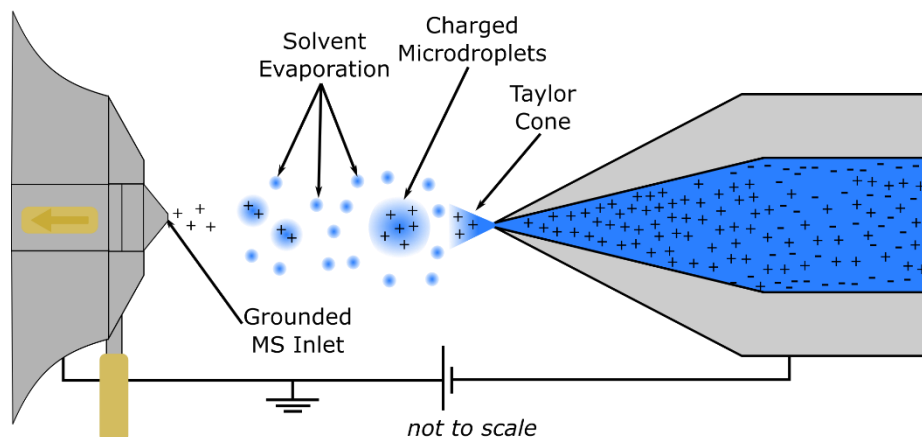


Figure 14 - Electro spray Ionisation (ESI)

The initial microdroplet formed has a high surface area to volume ratio, and consequently the rate of solvent evaporation is high. The droplet continues to decrease in size as solvent evaporates, forcing point charges at the surface of the droplet closer together.⁵³ Eventually, the droplet reaches the Rayleigh Limit, when the repulsive force between point charges on the surface of the microdroplet becomes great enough to overcome the surface tension of the droplet itself.⁵¹ The Rayleigh Limit (Q_r) can be defined using Eq. 15.⁵⁴ The result is that the droplet breaks up into smaller charged droplets, in a process termed a Coulombic explosion.

$$Q_r = 8\pi(\epsilon_0\gamma R^3)^{1/2} \quad \text{Eq. 15}$$

$\epsilon_0 = \text{Electric Permittivity}$
 $\gamma = \text{Surface Tension}$
 $R = \text{Droplet Radius}$

The mechanism of forming the final gaseous ions for ESI is still being developed, despite many decades of research and argument. Three main models have been proposed: the Ion Ejection Model (IEM), the Charge Residue Model (CRM) and the Chain Ejection Model (CEM).^{55,56} IEM is the process by which the electric field surrounding a microdroplet is so strong that the ion is simply ejected from the droplet surface as a gaseous ion. The CRM is the formation of an ion through continuous evaporation of the solvent, until only the analyte ion remains. Finally, the CEM model is mostly only applicable for multiply charged molecules with a linear structure, such as denatured proteins or polymers. This model is based on the principle of a long chain with multiple charge points along its structure which is found on the surface of a microdroplet. As one end of the linear chain begins to eject from the droplet surface, charge is transferred from the droplet onto the chain, forcing the chain away from the droplet surface further until the entire chain

is ejected from the droplet as a multiply charged gaseous molecule. It is likely that all three of these mechanisms play a role in the ionisation of analytes, with the relative contribution of each varying depending on the analyte size, structure and polarity.

1.3.2 Direct Analysis in Real Time (DART)

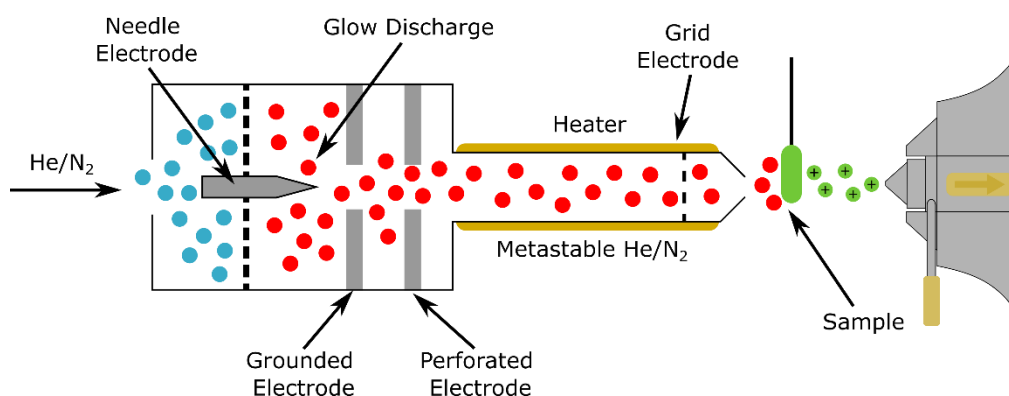


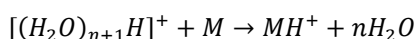
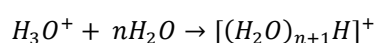
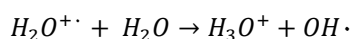
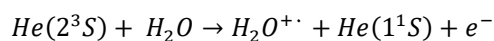
Figure 15 - Direct Analysis in Real Time (DART)

Direct Analysis in Real Time (DART) was first introduced through a patent in 2003, with a publication by Cody et al. following in 2005.^{57,58} The system works by passing a carrier gas (Helium, Nitrogen or Argon for example) over a needle held at a several kilovolts. The voltage is sufficiently high that it generates a glow discharge with a grounded electrode in front of the needle, which the carrier gas interacts with, generating a mixture of ions, electrons, and excited-state (vibrational or electronic) neutral atoms and molecules.

The mixture of species then passes through a perforated electrode to remove ionized species.⁵⁹ The remaining excited state carrier gas molecules/atoms are passed through a heater, before exiting and interacting with the sample, for which no prior sample preparation is necessary. The gas is heated to aid the thermal desorption process of the sample, this typically can be between 50°C and 500°C depending on the volatility of the sample.

There are several mechanisms by which sample ionisation can occur depending on multiple factors including the polarity, the carrier gas, the sample proton affinity and ionisation potential, the presence of additives or dopants to the sample, and the analyte concentration.⁶⁰ The simplest ionisation mechanism is Penning Ionisation, the general equation for which is given below in Eq. 16.⁶¹ Energy is transferred from the excited-state carrier gas species to the analyte, which has a lower ionisation potential than the energy of the excited-state carrier

gas. The general equation for the Penning Ionisation mechanism which occurs when Helium gas is used is also given (Eq. 17). The reaction does not occur directly between gas and sample, but instead creates uses a metastable excited state Helium ($He(2^3S)$) to ionize water molecules, which subsequently undergo proton-transfer with the analyte.⁶²⁻⁶⁴



Eq. 17

Thanks to the lack of sample preparation and rapid nature of analysis, DART has been extensively used in a wide variety of applications, including food quality, pharmaceutical screening, explosive detection and analysis of inks in fraud cases.⁶⁵⁻⁶⁸

1.3.3 Desorption Electrospray Ionisation (DESI)

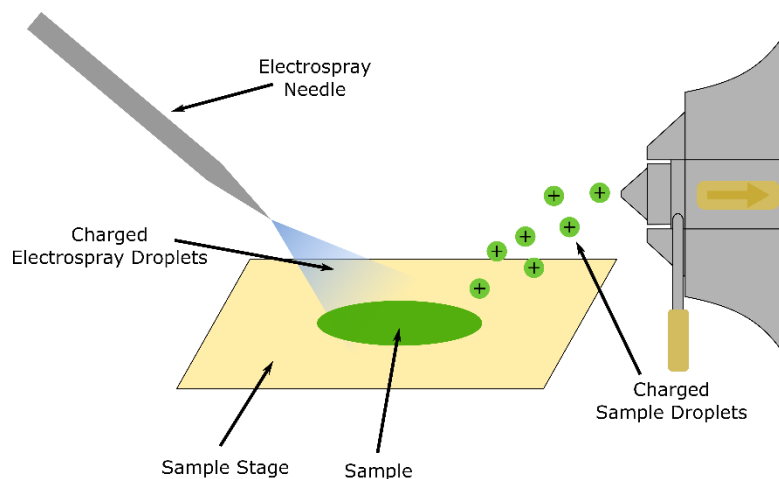


Figure 16 - Desorption Electrospray Ionisation (DESI)

Desorption Electrospray Ionisation (DESI) is one of the earliest ambient ionisation techniques reported. During DESI, an electro sprayed plume of charged microdroplets impacts the sample of interest, as shown in Figure 16. The ionisation mechanism of DESI follows a "droplet pickup" model, whereby the highly charged droplets form a thin layer on the surface of the sample, into which sample compounds dissolve. The subsequent bombardment of the sample with further charged microdroplets from the electro spray plume generates secondary charged

droplets containing the dissolved sample compounds, which are then directed towards the MS inlet for analysis.⁶⁹ Gaseous ions are formed, following one or more of the proposed mechanisms of ionisation (IEM, CRM or CEM) discussed for electrospray previously in Section 1.3.1. The system produces similar multiply charged ions to those of electrospray, making it a strong method for the analysis of high mass molecules. The plate on which the sample sits is usually mounted on an XY controllable stage, which moves allowing for the analysis of multiple different sample spots or to collect imaging data of biological samples.

Rapid sampling is crucial within chemical analysis laboratories, for the purposes of quality control, reaction screening, reaction optimization and screening pharmaceutical candidate molecules through assays. DESI, thanks to its ability to screen thousands of samples in a short space of time, has been applied to these tasks for a variety of applications, including pharmaceutical fingerprinting of tablets for harmful components, analysis of biological samples for biomarkers of disease, and detection of explosives on surfaces.⁷⁰⁻⁷³

1.4 Droplet-on-Demand Ionisation Sources

Droplet-on-Demand (DoD) ionisation sources are those through which droplets (or in some cases a single droplet) are generated only when an appropriate pulse is applied to trigger droplet generation. The duration of the pulse can be accurately controlled, allowing for short bursts of very low volumes of sample. When performing analysis where only a limited amount can be sampled, such as forensic analysis samples or analysis of rare and expensive artefacts, this could be highly advantageous compared to continuous flow ionisation methods. As will be discussed throughout, many DoD ionisation sources decouple the droplet formation and charging process, which allows for greater control over the droplet formation process. Herein a series of DoD ionisation sources are described, including their applications and, where applicable, their limitations.

1.4.1 Acoustic Mist Ionisation (AMI)

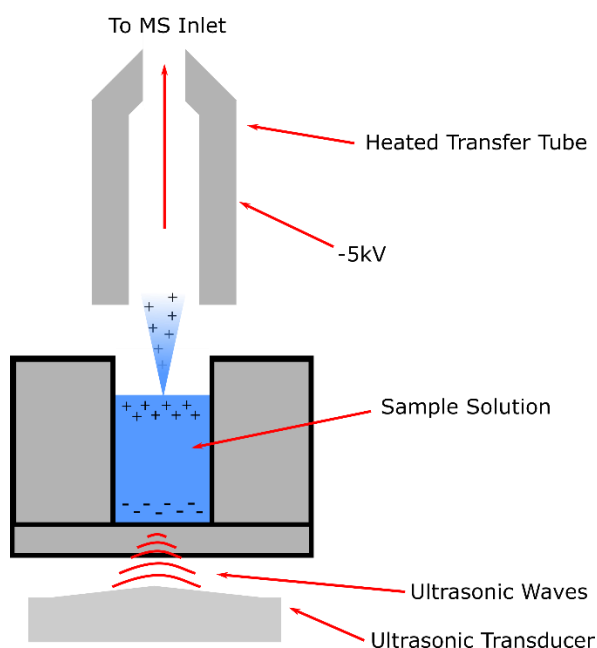


Figure 17 - Acoustic Mist Ionisation (AMI)

Acoustic Mist Ionisation (AMI) is an example of an ultrasonic based droplet-on-demand ionisation source, capable of performing high throughput screening of samples.^{74,75} Samples are stored in a microplate, above which is a heated transfer line held at a high potential, inducing a charge separation in the sample well.⁷⁶ Charged microdroplets are then generated through acoustic waves generated by an ultrasonic transducer beneath the microplate. The acoustic wave travels through the liquid reservoir where, if the acoustic energy is sufficient, it will overcome the surface tension of the liquid, causing it to nebulize.⁷⁷ The charged microdroplets generated subsequently pass through the heated transfer line for MS analysis. The system is shown visually in Figure 17, which shows the lack of direct contact between the transducer and the sample, reportedly reducing chances of sample carryover and reducing analysis time.⁷⁸

The system's ability to perform the rapid screening of samples is well presented in the literature, which is achieved by loading samples into a microplate mounted onto an XY stage, allowing the system to rapidly move from sample to sample.

There have been various reported cases of AMI being used for the screening of samples, optimization of reaction conditions, small and large molecule medicinal candidate screening, quality control and biological sample screening.⁷⁹⁻⁸² The sampling rate of the system has reached an impressive 6 samples per second in

a high throughput screening analysis reported, whilst still maintaining baseline separation between samples peaks.⁸³

1.4.2 Surface Acoustic Wave Nebulisation (SAWN)

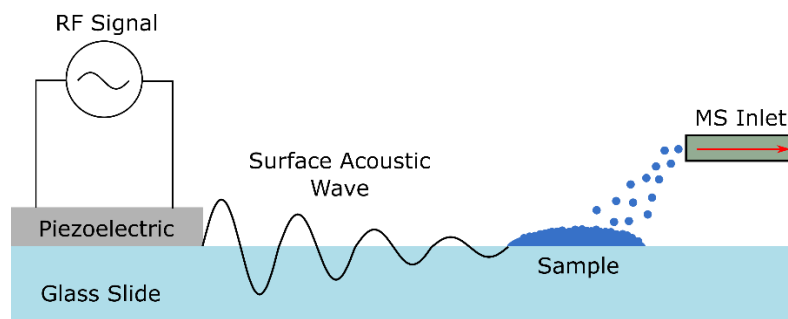


Figure 18 - Surface Acoustic Wave Nebulisation (SAWN)

Surface Acoustic Wave Nebulisation (SAWN) was first presented in 2010 as an effective method of analyzing samples for which only a low volume was available.⁸⁴ The system used no pumps or interconnecting devices, and therefore a small volume of sample could simply be pipetted onto the glass surface for analysis. Figure 18 shows a schematic of the main components of the system.

A piezoelectric transducer generates a surface acoustic wave in the glass slide onto which it is mounted; energy from this acoustic wave is transferred into the sample solution, a droplet of which is found further along the glass slide. The energy transferred overcomes the surface tension of the sample, causing it to nebulize.⁸⁵ Unlike conventional ionisation sources, which induce ionisation through applied potential differences, the SAWN system is capable of generating ions through microscopic fluctuations in the charge distribution of the bulk liquid.⁸⁶⁻⁸⁸ Despite the lack of charge being induced, the ions generated by SAWN tend to be multiply-charged, similar to those generated by ESI.⁸⁴ However, the signal obtained via SAWN is significantly enhanced by using an electrode to introduce a charge in the liquid.⁸⁹

One of the biggest advantages to SAWN is the minimal fragmentation which occurs, allowing for the analysis of intact proteins, and even cells.⁹⁰ Moreover, the lack of fragmentation for SAWN means that analysis of degradation products can proceed with additional certainty that the degradation products did not form during the analysis procedure.⁹¹ This lack of fragmentation is attributed to the lower internal energy ions generated by SAWN compared to conventional electrospray ions.⁹²

1.4.3 Array of Micromachined Ultrasonic Electrospays (AMUSE)

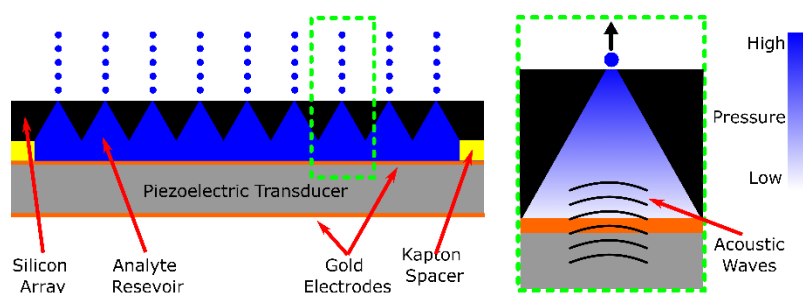


Figure 19 - Array of Micromachines Ultrasonic Electro spray (AMUSE)

Array of Micromachined Ultrasonic Electrospays (AMUSE) Ionisation is an ultrasonic based ionisation device, which also overcomes the limitations associated with conventional electro spray type ionisation sources by decoupling droplet formation and charging.^{93,94} The device, shown in Figure 19, consists of a piezoelectric transducer which generates ultrasonic waves in a sample. The ultrasonic waves generate a high-pressure gradient at the nozzles of an array of cones, which cause droplet ejection.⁹⁵ Droplet charging is performed by a gold electrode held at several hundred volts, which makes direct contact with the sample. Although, as noted when performing the analysis of peptides and proteins using the system, good signal can be obtained without the use of an applied voltage through the random distribution of charges in bulk solutions.^{93,96}

1.4.4 Ultrasonic Assisted Spray Ionisation (UASI)

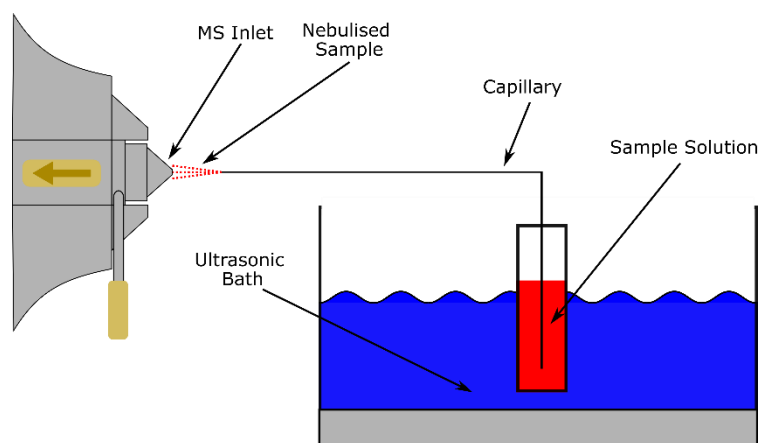


Figure 20 - Ultrasonic Assisted Spray Ionisation (UASI)

Ultrasonic Assisted Spray Ionisation (UASI) is another example of an ionisation source which uses ultrasonic waves to nebulise the sample, which has been successfully applied to the analysis of small organic molecules and proteins.⁹⁷ The sample is stored in an appropriate vial which sits in an ultrasonic bath, a piece of

equipment routinely found in almost every laboratory.⁹⁸ A capillary passes from the sample to just in front of the MS inlet, sample is continuously drawn through by capillary action. The applied ultrasonic frequency causes the sample to nebulise at the tip of the capillary and induces acoustic cavitation within the sample, whereby bubbles form and rapidly collapse.⁹⁹ This formation and subsequent collapse of the bubbles is an extremely violent process, inducing local temperature maximums of several thousand kelvin, enough to transfer ions into the gas phase.⁹⁷ Although ionisation is not induced through an applied voltage, there is a significant increase in the signal observed when the capillary is grounded relative to the MS inlet compared to when the capillary is not grounded.

1.5 Ion Sources for Improved Mass Accuracy

As mentioned, internal recalibration is the most effective method of ensuring high mass accuracy, most commonly performed by spiking the sample of interest with internal standards. This approach is labor-intensive, and frequently adopts a trial-and-error method to determine an appropriate concentration. Moreover, performing internal recalibration by spiking additional components into the sample opens the possibility of preferential ionisation of either sample or calibrant. This can be caused by differences in the hydrophobicity of different components (more hydrophobic molecules preferentially sit on the surface of a droplet, where the surface charges are, and therefore tend to have better ionisation coefficients), along with differences in the location and number of charging sites and the gas phase acidity/basicity of the components.¹⁰⁰⁻¹⁰²

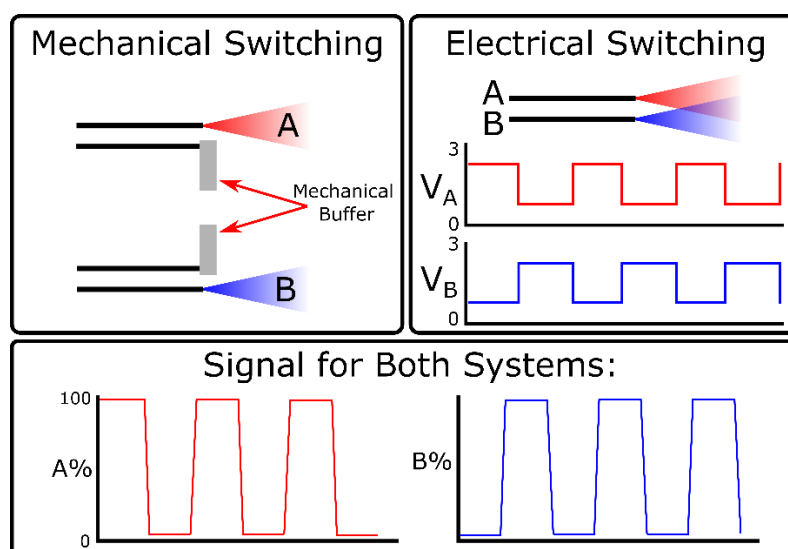


Figure 21 - Examples of Mechanically and Electrically Switched Dual Electro spray Systems

There are a small number of previously published of ionisation sources and adaptations to ion sources which are designed to perform internal recalibration without the need to spike samples directly. Many of these ionisation sources involve the use of dual-sprayers, whereby one emitter sprays the sample whilst the other is set to introduce a calibrant solution. The dual-spray systems cannot have both emitters simultaneously active due to the repulsive forces between the two highly charged plumes. Therefore, dual-spray systems mostly rely on electrical or mechanical switching to alternate between calibrant and sample ions to avoid this repulsion, schematic examples of which are given in Figure 21.¹⁰³⁻¹⁰⁶ Moreover, when using electrically switched electrospray type emitters, there is a minimum distance between the two emitters which must be kept to ensure no unwanted discharge between the active tip (at high voltage) and the inactive tip (grounded).¹⁰⁷ Although the use of multiple sprayers is being discussed in the context as a mass recalibration tool here, their use is not limited to calibration, with multiple spray systems being used to perform ion/ion reactions within ion traps.¹⁰⁸⁻¹¹¹

Much of the work around dual-electrospray ionisation sources was published by Muddiman et al., who tested their system(s) in a variety of different genomic and proteomic studies, achieving good mass accuracy values throughout.¹¹²⁻¹¹⁵ They used a dual-spray system which operated through a mechanical switching mechanism, and coupled the system to an FT-ICR Mass Spectrometer. After a significant improvement in sprayer switching time (from 300 milliseconds to 50 milliseconds), they were able to exploit the hexapole accumulation of ions to trap a single ion cloud containing both sample and calibrant, which could then subsequently be sent to the ICR cell for analysis.¹¹⁶

Li et al. presented the first dual spray system which was able to have both sprayers in the same alternating current field, and therefore able to simultaneously spray.⁴ The device was able to achieve good mass accuracy values for the analysis of components in urine (a complex matrix), with mean mass accuracy values as low as 1 ppm for positive mode and 3 ppm for negative mode.

Overall, the number of ionisation sources which are designed with the focus of improving mass accuracy are limited, in part due to the associated difficulties of introducing sample and calibrant sprays simultaneously to the mass spectrometer. Those that have been reported have shown some good success, particularly those which focus on the development of dual electrospray systems. However, the need to explore further work in this area remains clear.

1.6 Summary

Developments in ionisation sources over the last two decades have sparked a new chapter in the way mass spectrometry analysis would be conducted. There has been a significant number of publications and research performed focusing on the development of new ionisation techniques and the application of these systems for increasingly complex samples, a subset of which have been discussed. The advantages of ambient ionisation sources in sample preparation and analysis time over conventional methods are clear, rapidly increasing their popularity in the broader scientific community as a key tool for analysis in a broad range of applications.

In conjunction with the ionisation source development, there has been significant progress in the quality of data generated by instruments. Both manufacturers and researchers are continuously pushing the capabilities of instrument peak resolution and mass accuracy, driven by a need to be able to confidently assign molecular formula to complex samples containing hundreds of thousands (if not millions) of peaks. FTMS instruments are clearly paving the way in this development, routinely achieving sub ppm mass accuracy, and resolving powers well into the millions.

The development of more advanced instruments with ever higher resolving powers, reveals more and more molecular (e.g. biochemical) complexity in samples. However, this resolution improvement must be coupled to improvements in the calibration of instrumentation to ensure sufficient confidence in peak assignment to permit this complexity to be appropriately understood in its context. The vast majority of the ionisation sources developed to provide improved mass accuracy have been dual electrospray based. This thesis discusses the development and characterization of a novel droplet-on-demand ultrasonic ionisation source which aims to improve mass accuracy for complex analysis.

1.7 Aims

This research project aims to achieve the following:

1. Investigate and evaluate potential ultrasonic nebuliser-based systems which could be used as droplet-on-demand ionisation sources for improved mass accuracy
2. Undergo a development process through 3D printed components and engineered components to optimise system(s) for best signal obtainable
3. Develop programmatic control over the system(s) to perform automatic internal recalibration of spectra
4. Demonstrate the ion source's ability to work on a series of different mass analyser types and mass spectrometer manufacturers
5. Evaluate the ion source's performance as an internal mass recalibration tool
6. Investigate additional potential applications of the ion source

Herein, this thesis describes the research and development process undertaken for ionisation source development and characterization.

1.7.1 Internal Encoded Recalibration and Duty Cycle

If a sample and a mass calibrant are both introduced into the mass spectrometer in a steady state manner, then it can be hard or impossible to distinguish between the sample signal and the mass calibrant signal in complex samples. Internal encoded recalibration is a method for encoding the calibration function within the sample dataset, through introducing the mass calibrant in a controlled manner at defined points during the sample analysis. If the calibration signal is encoded in the signal, then it is possible to demodulate the mixed signal to positively identify the spectral peaks originating from the calibrant. Demonstrating a successful internal encoded recalibration capability was one of the primary aims of the ionisation source developed during this thesis.

In addition to encoding the calibrant signal, another key benefit of any droplet-on-demand ionisation source is to be able to modulate the volume of the calibration solution introduced into the mass spectrometer. The observed signal given by the mass spectrometer is directly related to the volume of solution generated by the ionisation source during the ion accumulation period, and therefore developing an ionisation source which gives fine control over the volume

of calibrant solution sprayed will allow the strength of the mass calibrant signal to be altered on-the-fly.

One method for modifying the volume of sample solution analysed per spectrum is to adjust the duty cycle of the nebuliser - the duty cycle, in this case, being the proportion of the ion accumulation time during which the nebuliser operates. The theoretical effect of varying the duty cycle on the signal has been shown visually in Figure 22. The dashed black line on each graph indicates an example scan taken by the mass spectrometer (in this case set to take a scan every 100 milliseconds). The colored regions indicate a period in which the nebuliser is active, with blank regions indicating the nebuliser inactive. As the duty cycle decreases, the proportion of time between scans where the nebuliser is active is decreasing, and therefore a decrease in signal can be expected. Assuming that there is a linear relationship between the duty cycle and the signal, a theoretical calibration curve can be drawn using this information, shown within Figure 22.

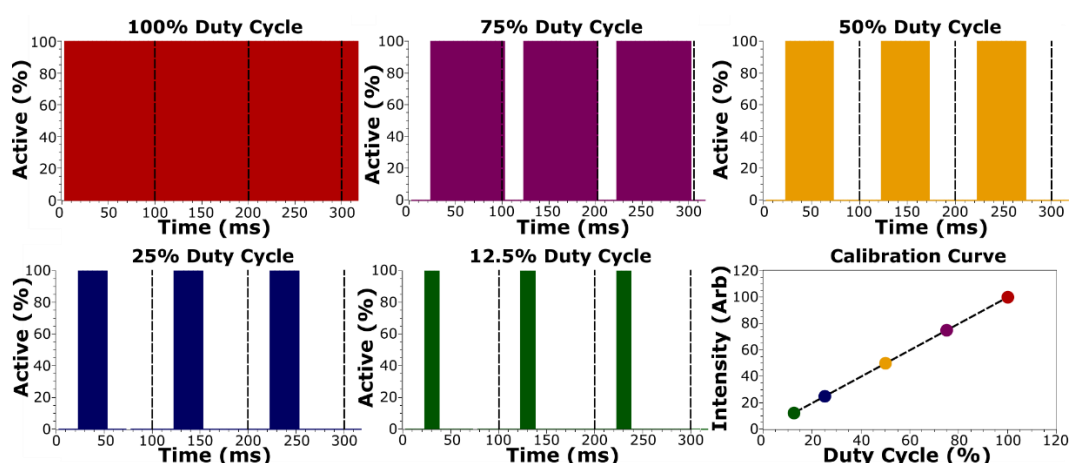


Figure 22 - Theoretical PUPP Duty Cycle Control & Calibration Curve

Vertical dashed lines indicate when a scan is performed on the mass spectrometer. The coloured regions indicate when the nebuliser is active, and white regions indicate the nebuliser is inactive. An increase in the amount of time the nebuliser is active between scans theoretically leads to an increase in the signal, as indicated by the calibration curve shown.

1.8 Experimental

The following section gives an overview into the equipment, chemicals, instruments, and software used throughout this project.

1.8.1 Equipment

A Microdrop Control Unit (MD-E-3011), Microdrop Inkjet Nozzle (50 μm , MD-K-130-020) and Microscope Lens (10 x Zoom, MD-Z-503) were purchased from Microdrop Technologies GmbH (Norderstedt, Germany). All high-speed images of the droplet formation process of the Microdrop system were taken using a MD-O-

539-USB - XiQ USB 3.0 SuperSpeed Compact Camera, purchased from Microdrop Technologies GmbH (Norderstedt, Germany). The high voltage power supply (Model PS350/5000V-25W) was purchased from Stanford Research Systems (Sunnyvale, CA, USA). The 3D printer used was an Ultimaker S3 (Utrecht, Netherlands), and unless specified printing was done using ABS Filament purchased from Ultimaker and RS Components (Corby, UK). Two types of Porous Ultrasonic Piezoelectric nebulizer Plates were used. The 756-Hole plates were extracted from Donut Air Humidifiers purchased from Amazon (amazon.co.uk, London, UK). The 1-, 7- and 19-Hole plates (KS-W13.8-162K1D3W) were custom manufactured by Dongguan Cosson Electronic Plastic Company (Guangdong, China) and were supplied by a collaborator for this project. XY Controllable Mini Milling Tables were manufactured by Poweka (Shenzhen, China), and purchased via Amazon. The XYZ 3-Axis Manual Linear Stage was manufactured by Jecste (China) and purchased via Amazon (London, UK). Details about the Custom-Built Fused Silica Grinder can be found in the Chapter 5, whilst the fused silica used for generating ESI Tips (TSP075375, ID = 75 μm , OD = 363 μm) was purchased from CM Scientific (Silsden, UK). The ESI Needle used during the early stages of the project was removed from a Micromass Quattro Micro Mass Spectrometer, Micromass was purchased by Waters Corp in 1997 (Manchester, UK).

1.8.2 Chemicals

Triton QS-15 and Jeffamine M-600 were purchased from Sigma-Aldrich (Gillingham, UK). ESI Tuning Mix was purchased from Agilent (Santa Clara, CA, USA). LC-MS Water was produced using a Thermo Fisher (MA, USA) Barnstead Nanopure Analytical UV System. Unless specified otherwise, all general lab reagents and solvents were obtained through Sigma-Aldrich (Gillingham, UK).

It should be noted, that at various stages three different solutions were used to perform recalibration functions, these are Triton QS-15 (an anionic polyethylene glycol based-surfactant), Jeffamine M-600 (a polypropylene glycol-based surfactant) and an Agilent ESI Tuning Mix (comprised mostly of a perfluorinated phosphazene series), all of which gave different numbers of peaks at different m/z ranges.^{14,117} The proposed structures of Triton QS-15, Jeffamine M-600 and the Agilent ESI Tuning Mix have been given in Figure 168, Figure 169 and Figure 170 respectively.

1.8.3 Instrumentation

Throughout the project, various mass spectrometry instruments were used, below is a list of these and the institutions who kindly agreed for their use during the project.

- Waters Xevo G2-XS Q-TOF Mass Spectrometer (Waters Corp, Manchester UK)
 - *School of Science & Technology, Nottingham Trent University*
- ABSciex TripleTOF 6600+ Mass Spectrometer (ABSciex, Macclesfield, UK)
 - *John van Geest Cancer Research Centre, Nottingham Trent University*
- Thermo Q-Exactive Plus Hybrid Quadrupole-Orbitrap Mass Spectrometer (Thermo Fisher, MA, USA)
 - *Ion Beam Centre, University of Surrey*
- Bruker solariX 12T FT-ICR Mass Spectrometer (Bruker Corporation, MA, USA)
 - *Scottish Instrumentation and Resource Centre for Advanced Mass Spectrometry, University of Edinburgh*
- JEOL JSM-7100F Thermal Field Emission Electron Microscope (JEOL, Tokyo, Japan)
 - *School of Science & Technology, Nottingham Trent University*
- Olympus BX51 Microscope with Leica MC190 HD Camera (Olympus, Tokyo, Japan)
 - *School of Science & Technology, Nottingham Trent University*
- Thermo Fisher Q-Exactive HF Orbitrap (Thermo Fisher, MA, USA)
 - *M4I Division of Imaging Mass Spectrometry, Maastricht University, the Netherlands*

1.8.4 Software

Initial processing of data collected on the Waters Q-TOF was performed via the MassLynx v4.1 Software provided by Waters Corporation (Milford, MA, USA).

Later, data collected on all instruments was processed via custom programming written in LabVIEW 2020, a software development environment from National Instruments (Austin, TX, USA). In order to be able to do this, in most cases, the mass spectrometry data file format was converted to mz5.¹¹⁸ This was done using

Proteowizard's MSConvert tool (Palo Alto, CA, USA).¹¹⁹ More information on the programming written as part of this project can be found in Chapter 5.

3D Printing designs were generated using FreeCAD, an open-source software tool available on GitHub. The .STL files created in FreeCAD were then generated into .3mf files readable by the printer via Ultimaker Cura (Utrecht, Netherlands).

The waterfall figures were generated using MATLAB R2020b software by MathWorks (Natick, MA, USA). The camera used to collect images of the Microdrop emitter droplet generation process was controlled by XIMEA CamTool v4.2 (Münster, Germany).

Chapter 2: Microdrop System Development

This chapter introduces the Microdrop system as an effective method of generating microdroplets on demand. The mechanism of microdroplet generation is initially presented, followed by details on the various ways the system was adapted into a functioning ionisation source. Proof of concept data is presented for some of the key features of the Microdrop system, followed by an overview of the advantages and disadvantages of the system as an ionisation source. In the appendix of this thesis is a summary of all the ionisation sources versions used throughout this project to assist the reader with understanding the development process.

2.0 Ion Source - Microdrop

The first ionisation source developed used a piezoelectric inkjet printing device developed by Microdrop Technologies. Li et al. provide an excellent summary of the various types of piezoelectric inkjet devices, including a classification system based on their method of generating droplets.¹²⁰ The Microdrop system discussed here falls into the category of a "squeeze type", and has previously been published as a method of performing ionization.^{121,122}

A system near identical to the Microdrop was used to inject plumes of highly charged droplets into an ion mobility cell, in order to perform investigations into the preference of different small molecules to undergo the Ion Evaporation Model (IEM) ionization mechanism through "Time of Ionization Spectrometry".¹²¹ The scope of this investigation does not focus on the ionization source or optimization of the ion source, and instead uses the ability to generate individual droplets (or plumes of droplets) on demand to perform ionization mechanism studies.

Earlier work conducted at the University of Edinburgh demonstrated the capability of the Microdrop system to perform droplet-on-demand ionization, of e.g. biomolecules (Bovine Insulin), coupled to an Orbitrap.^{122,123} Triggers taken from the Orbitrap enabled the droplet generation and ion accumulation events to be synchronized, and the authors also mention the ability to vary the number of droplets generated during the ion accumulation events to alter sample peak intensities on demand.

The system had a number of features which made it an appealing starting point for the ion source development considering the aims of the project stated previously. These features include the ability to control the number of droplets generated, and the frequency at which they are dispensed.

This chapter describes the general principle of the system, which is already established in the literature. After this, number of different methods of performing ionization were tested, and their performance and suitability for internal encoded recalibration are compared. Previous studies have demonstrated the Microdrop system as an ionization source without presenting any systematic characterisation for different methods of performing ionization, to my knowledge this is the first study of its kind.

2.1 Microdrop System Structure

The Microdrop system consists of a glass capillary encased in a piezoelectric actuator. The tip of the glass capillary has a diameter of 50 μm , which approximately translates to the size of the droplet emitted. The liquid sample to be dispensed is stored in a 4 mL glass vial, and is transferred into the glass capillary through a PTFE sample line via capillary action and a headspace pressure supplied into the glass vial. Figure 23 shows the internal components of the Microdrop system. The piezo actuator is driven by a series of electrical pulses, which are regulated and delivered by the Microdrop control system. The droplet formation process revolves around the expansion/contraction of the piezoelectric actuator, which in turn generates pressure waves inside the glass tubing, leading to the formation of a droplet at the tip of the capillary.¹²⁴ The Microdrop controller can be used either through the touchscreen interface, or through serial commands.

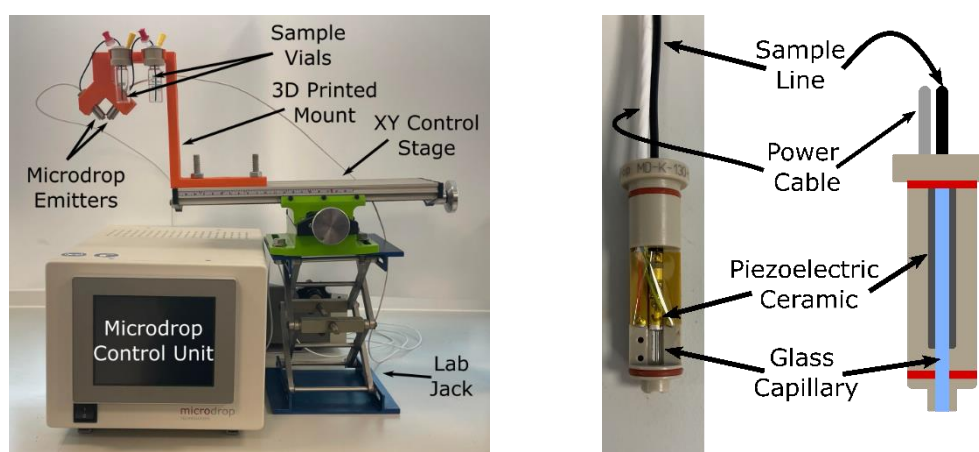


Figure 23 – Overall Microdrop system (Left) and Internal Components of Microdrop Unit (Right)

The system has two modes of operation: a “Single Pulse” and a “Triple Pulse” droplet ejection method. The “Single Pulse” method, shown in Figure 25, provides pulses of consistent voltage and length, with a delay between individual pulses.

Good quality droplet formation is dependent on the tuning of the pulse voltages, when the voltages are not tuned the system generates a “splutter” of droplets from the emitter, whilst a good quality tune produces a clearly defined single droplet. Figure 24 shows the difference in quality of droplet(s) formed when the tune is good quality (left) and poor quality (right).

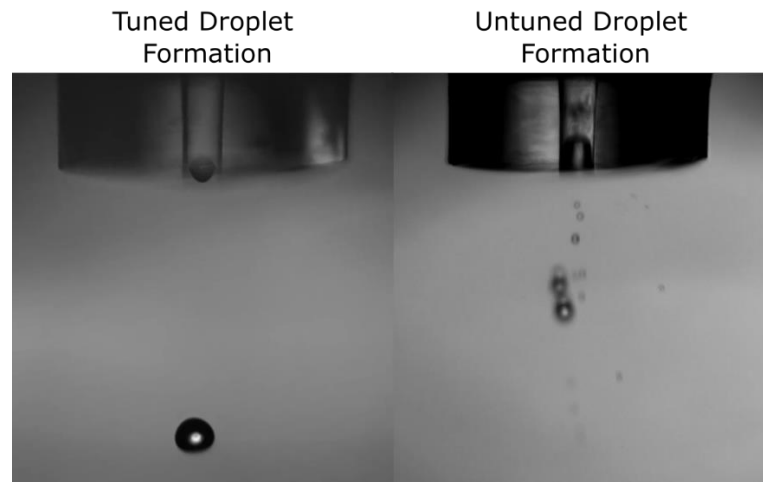


Figure 24 - Difference in quality of droplet formation when Microdrop system is tuned and untuned

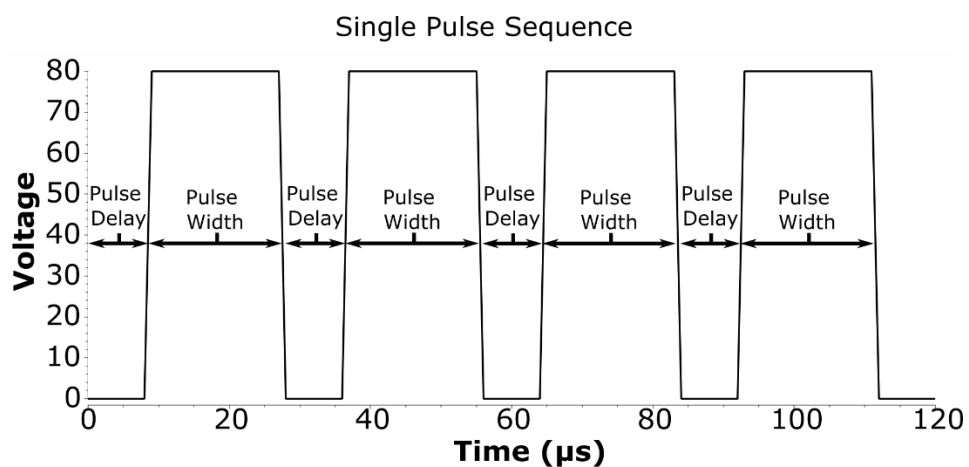


Figure 25 - Microdrop Single Pulse Emission Sequence

The “Triple Pulse” method has three distinct pulses, the first and final of which are typically positive voltages, whilst the middle is typically a negative voltage. Figure 26 shows a triple pulse configuration which generated good quality droplets and was subsequently used for much of the data collection performed in triple pulse mode. One cycle of the three individual pulses results in the ejection of a single microdroplet, which according to the manufacturer is approximately half the diameter of a droplet ejected from a “Single Pulse” method.

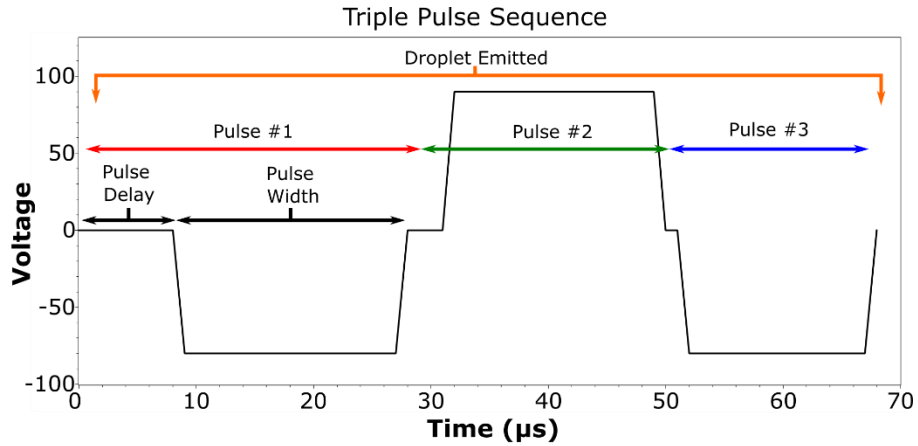


Figure 26 - Microdrop Triple Pulse Emission Sequence

The system has a user-defined frequency (Hz) at which droplets are ejected ranging between 1-6000 Hz. The system can be set to run at this frequency continuously, or to provide a defined burst of n droplets at the specified frequency. The system therefore can be set to eject a single droplet, enabling analysis of very low volumes of sample. When the settings are well tuned, the Microdrop system generates droplets of a very consistent diameter, and therefore the volume of sample dispensed per second (when Microdrop is used in continuous mode) or total volume dispensed (when Microdrop is set to generate a defined number of droplets) can be accurately calculated using Eq. 19 and Eq. 20. The volume of each droplet is fairly low, with a single droplet of 25 μm diameter corresponding to just to 8.2 picolitres of sample.

$$\text{Droplet Volume } (V) = \frac{4}{3}\pi r^3 \quad \text{Eq. 18}$$

$$\text{Volume Dispensed per second } (\text{pL s}^{-1}) = \frac{\frac{4}{3}\pi r^3}{1000} \times \text{Hz} \quad \text{Eq. 19}$$

$$\text{Total Volume Dispensed } (\text{pL}) = \frac{\frac{4}{3}\pi r^3}{1000} \times n \quad \text{Eq. 20}$$

r = Capillary Radius in μm

Hz = Droplet Frequency

n = Number of Droplets Generated

The droplet formation process was visualized using a CCD camera with a 10x microscope lens, together with a strobe light and monitor. Through varying the strobe delay, the process of droplet formation and emission from the glass capillary can be viewed as part of the process for tuning of the relevant pulse voltages and durations to achieve good quality droplet formation. Figure 27 shows an example droplet formation and ejection captured using this system.

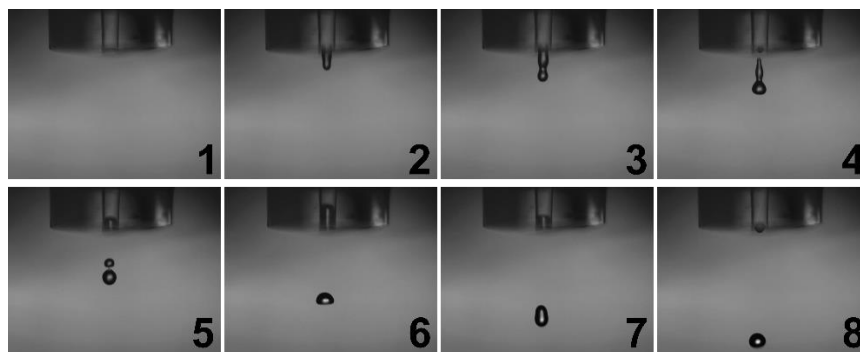


Figure 27 - Microdroplet formation process

Although the Microdrop system emits a stream of single droplets, rather than a widespread plume of droplets more akin to that of electrospray, it is not necessary for the droplet stream to be directed into the orifice of the MS inlet. Good signal can be achieved with the droplet stream directed slightly away from the inlet. There are two possible explanations for how this occurs, the first is that signal is achieved through the formation of smaller satellite droplets, which are observed in similar acoustic droplet formation techniques.¹²⁵ These smaller satellite droplets do not follow the same linear path as the main droplet, and therefore are likely to be responsible for the signal obtained when the pathway of the main droplet does not enter the MS inlet. The second possible explanation is that highly charged droplets can produce Taylor cones directly from the droplets itself when they approach the grounded MS inlet, known as Rayleigh Jets.¹²⁶⁻¹²⁸ These small Taylor cones generate small highly charged droplets which then subsequently enter the MS inlet, generating signal. However, this latter explanation is only applicable for the signal observed when the microdroplets generated have a high charge induced in them through an external power supply, and this does not need to be the case in order to observe signal when the microdroplet stream is directly slightly away from the inlet.

2.2 Microdrop Ion Source Development

Through the development stage of the Microdrop ion source a series of different configurations and designs were tested. Each prototype was initially tested using a single Microdrop system, some of which were further developed to try to introduce an additional, second Microdrop system. In addition, a series of different mechanisms of charging the microdroplets were tested, including mechanisms which charge the sample liquid before droplet formation, and those which aim to charge a droplet which has already been formed. Each design used a custom 3D Printed support mechanism to hold the appropriate ion source components in place.

2.2.1 Ion Source 1.0 - Single Microdrop into MS Inlet (MDD)

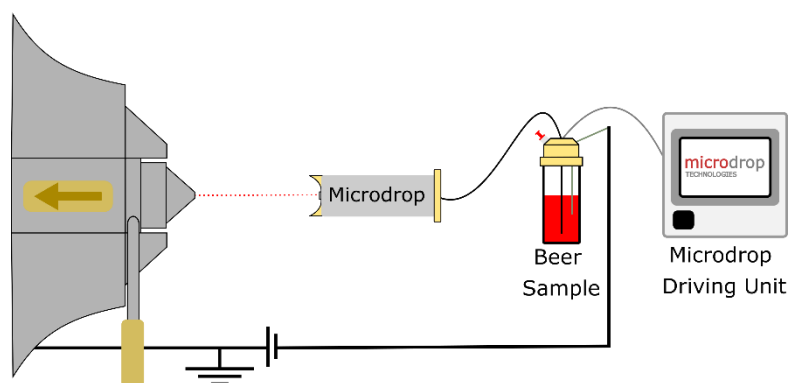


Figure 28 - Ion Source 1.0 - Single Microdrop directly into MS Inlet

The first iteration of the ion source had a single Microdrop system held horizontally, with the droplet stream directed towards the MS Inlet (See Figure 28). Although signal could be obtained without inducing charge in the sample, the signal was significantly enhanced through the use of a high voltage power supply. Charge was induced through a 0.40 mm diameter stainless steel wire which was suspended in the sample storage vial and attached to the high voltage (HV) supply.

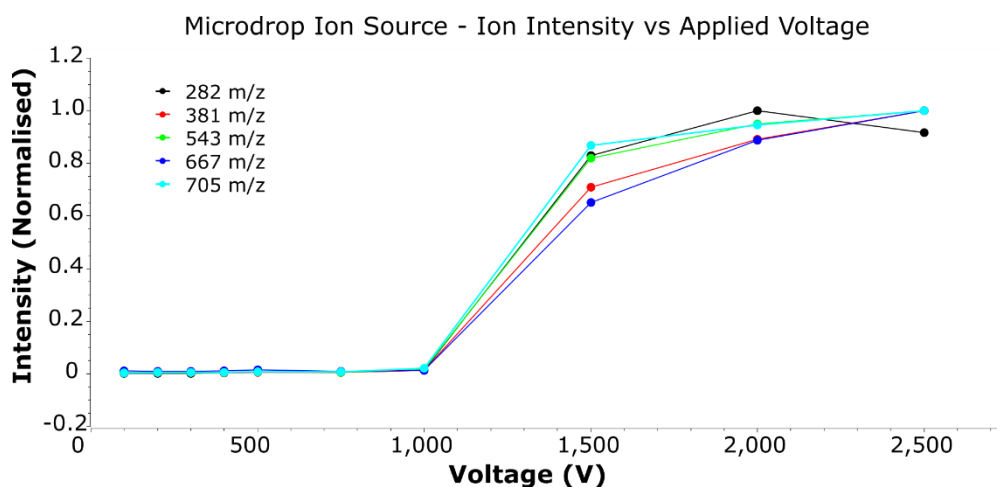


Figure 29 - Microdrop Ion Source - Ion Intensity vs Applied Voltage

The improvement in signal by inducing charge can be seen in both Figure 29 and Figure 30. Keeping the droplet frequency constant, but varying the voltage applied to the sample storage vial, there is a clear increase in signal at 1500V, which is shown in Figure 29. Whilst Figure 30 shows the effect on total ion chromatogram (TIC) signal when the power supply is switched on/off. This improvement in signal is likely to be caused by two effects of introducing charge; highly charged microdroplets undergo coulombic explosions and therefore iteratively produce

smaller droplets with a high charge density, and charged droplets are much more likely to be drawn towards the grounded MS inlet.

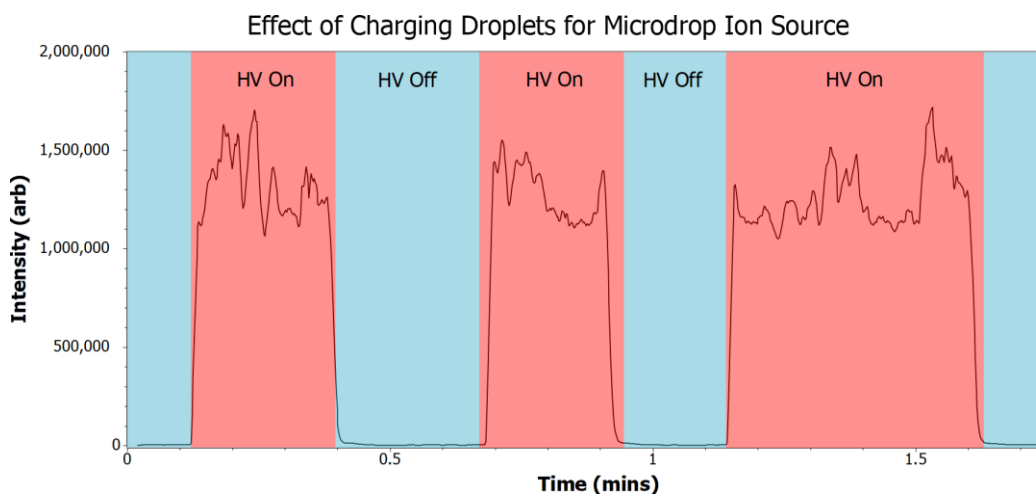


Figure 30 - Effect of Charging Droplets on Microdrop Signal

The system gave a strong signal across the mass range of interest, and it was clear that sensitivity could be easily adjusted through control of the droplet ejection frequency (Hz). Although the signal is not consistent when the HV is switched on, this can be attributed to the system not being optimized at this early development stage, and other possible external factors including airflow disrupting the flight path of the droplets entering the MS inlet.

Figure 31 shows the relationship between the frequency and the signal generated for a series of oligosaccharide peaks seen in a beer sample. Confirmation of this linear relationship promotes the use of the ion source as a system which can systematically alter the intensity of sample/calibrant ions as discussed in Section 1.7.1, and follows similar work published within the group using microdroplet dispensers.¹²²

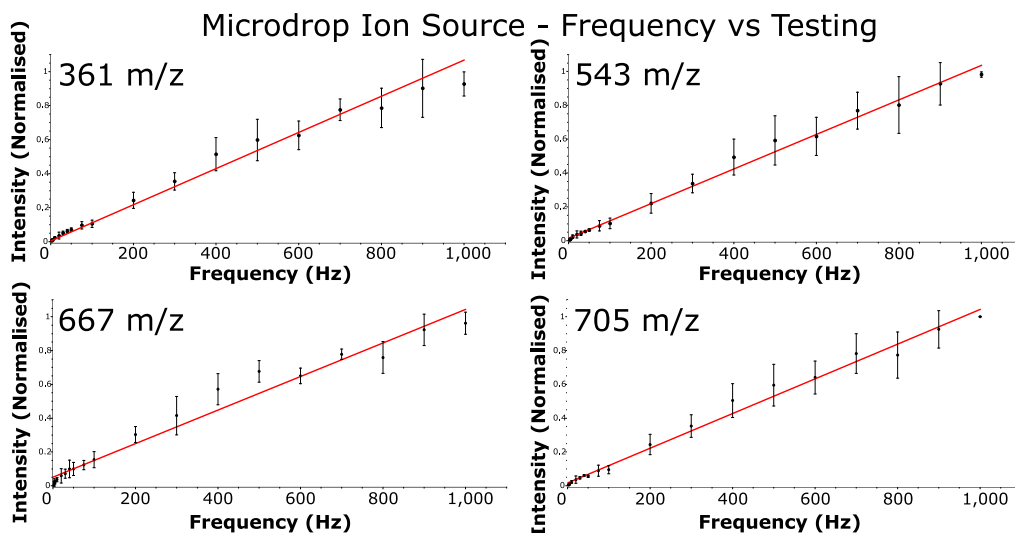


Figure 31 - Microdrop Frequency vs Intensity Relationship

2.2.2 Ion Source 2.0 - Double Microdrop into MS Inlet (MDD²)

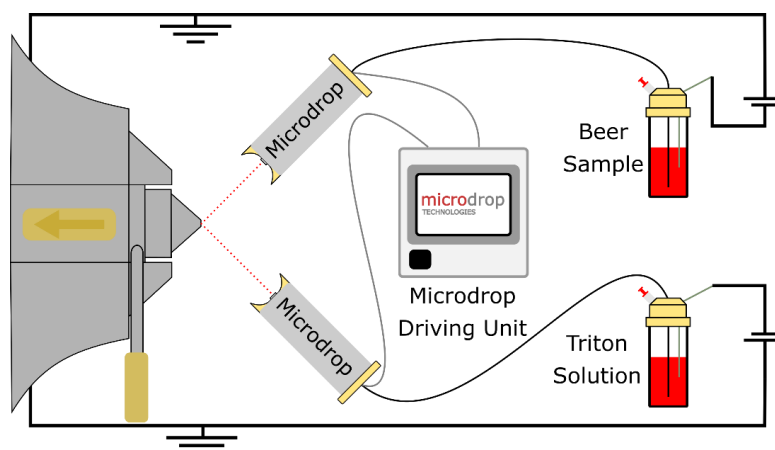


Figure 32 - Ion Source 2.0 - Double Microdroplet directly into MS Inlet

The next prototype sought to introduce a second microdroplet stream into the MS inlet. Both Microdrop systems were charged in the same manner, through a stainless-steel wire in the sample vial. However, consistent signal from both Microdrop streams could not be maintained due to the droplet streams interfering with each other. This interference can be attributed to the repulsive force of two highly charged droplet streams of the same polarity.

The interference could be seen visually, as when both power supplies were switched on, the droplet streams would repel each other, generally resulting in one of the streams being directed away from the inlet, as shown in Figure 33. This is a common occurrence within dual spray-based systems, and is generally overcome through the use of either electrical or mechanical switching between the two sprays.^{4,104,129} Dual electrospays have been used without the need for

any electrical or mechanisms, however, the calibrant and samples plumes are directed into the instrument via different inlets.^{130,131}

Holding only one of the microdroplet streams at a high potential was tested to try to overcome this issue. In theory, this would allow both microdroplet streams to meet prior to the MS orifice, and through droplet mixing this would enable both the Beer and Triton sample to mix in highly charged droplets. However, this resulted in signal dominance for whichever sample was held at a high potential, likely due to insufficient mixing.

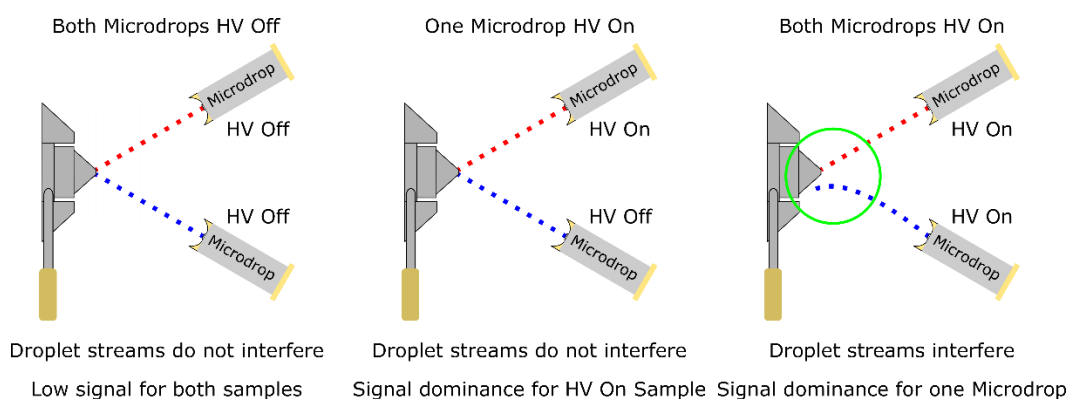


Figure 33 - Interference observed between highly charged Microdrop streams

2.2.3 Ion Source 3.0 - Single Microdrop into ESI Stream (MDD-ESI)

Figure 34

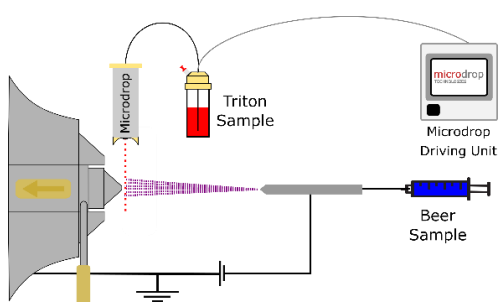


Figure 34 - Single Microdrop directed into ESI Plume

Figure 35

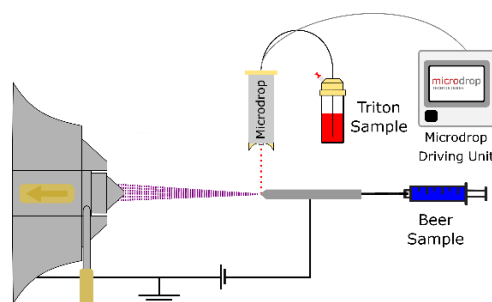


Figure 35 - Single Microdrop directed onto ESI Needle Tip

In order to avoid the droplet stream repulsion issues experienced between two highly charged droplet streams, methods to charge both droplet streams simultaneously were investigated. The first stage of this would be to determine whether signal could be obtained when introducing the Microdrop stream into the path of electrospray plume, or coming into contact with the tip of a highly charged electrospray needle. There have been various ionization sources previously

reported where ultrasonic-generated microdroplets are mixed with electrospray-style plumes to great success.^{132,133}

The original focus of the ionization source was to develop a system which could introduce a calibrant of choice into a series of defined sample spectra on demand. As discussed in 1.7.1, this would allow the generation of high accurate mass data through encoded internal recalibration. The system schematics can be seen in Figure 34 and Figure 35, which show the ESI generating a plume of sample (Beer) microdroplets. This would produce a steady stream of sample signal, into which the calibrant (Triton QS-15) signal could be introduced through the Microdrop system.

Initially, the Microdrop stream was introduced to the ESI stream immediately prior to the MS inlet as shown in Figure 34, in the hope that the ESI plume and the Microdroplet stream would undergo droplet mixing and therefore introduce charge to the Triton sample. However, this simply resulted in a complete loss of signal. Although an investigation would need to be performed to determine the cause, this is possibly due to the significantly larger Microdrop droplets ($\approx 50 \mu\text{m}$) pushing the much smaller electrospray droplets ($\approx 1\text{-}5 \mu\text{m}$) away from the MS inlet.

Greater success was achieved through introducing the Microdrop stream directly onto the electrospray needle tip, as shown in Figure 35. A similar approach was taken by Yu et al., who used a near identical piezoelectric microdroplet generation system coupled to a probe electrospray system.¹³⁴ In their work, they used a probe to directly sample cells. The piezoelectric device would subsequently deliver solvent onto the probe, extracting metabolites from the cell, which would subsequently be probe electrosprayed.

In our approach, short bursts of Triton introduced by the Microdrop would land onto the needle, where they would subsequently co-electrospray with the beer solution. Figure 37 shows a comparison of an EIC obtained for a beer sugar, which is consistent throughout the analysis, and an EIC for a Triton peak, which shows significant increases in intensity when the Microdrop system is triggered to deliver a short burst of microdroplets onto the needle tip. Figure 36 shows the spectra obtained from this dataset, the spectra containing Triton signal only are obtained by performing a background subtraction using a region where the Microdrop system is not active.

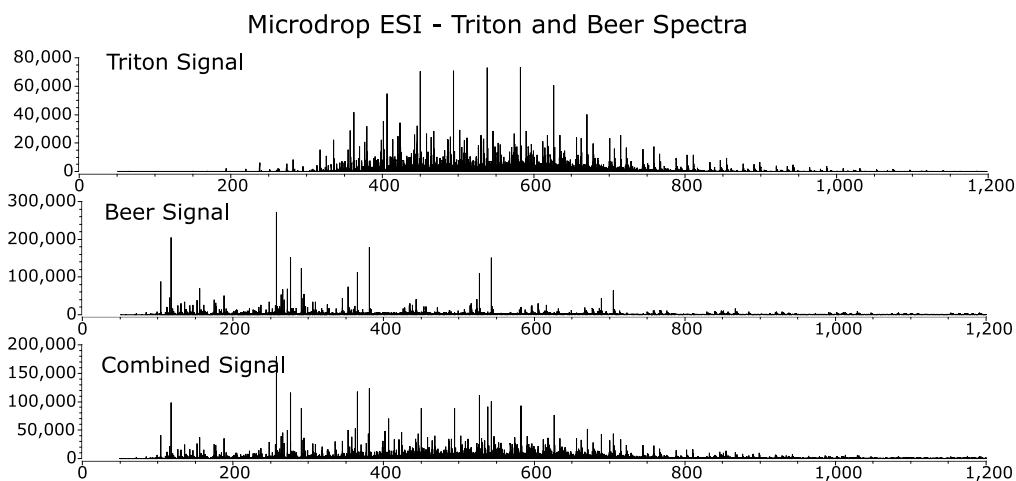


Figure 36 - Spectra obtained from ESI Microdrop Dataset

Although this method gave greater sensitivity, the depletion of the Triton signal had a significant delay. As can be seen in Figure 37, the signal would rapidly rise after the system is triggered to generate microdroplet(s), but then would slowly deplete. An ideal system would give much sharper peaks in calibrant signal, and therefore were only visible for short bursts after the system is triggered. This issue is likely caused by the volume of calibrant deposited onto the electrospray needle, which is significant enough that the electrospray continues to introduce calibrant into the plume long after the microdroplet generation event. This is a significant limitation of this system, and significant investigative work would need to be undertaken in order to avoid this.

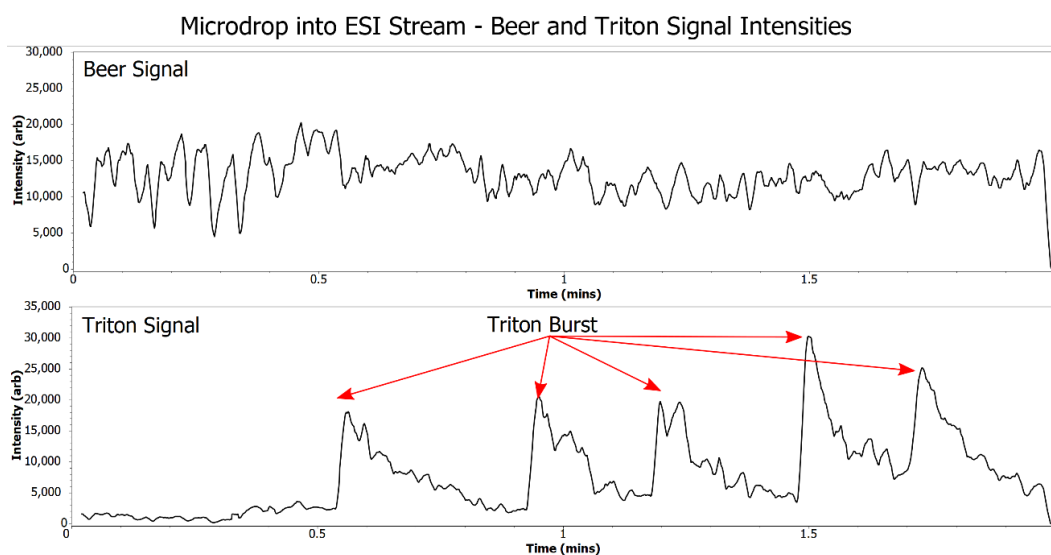


Figure 37 - ESI Analysis of Beer with Microdrop Triton Calibration Peaks

2.2.4 Ion Source 4.0 - Single Microdrop onto Needle (MDD-PESI)

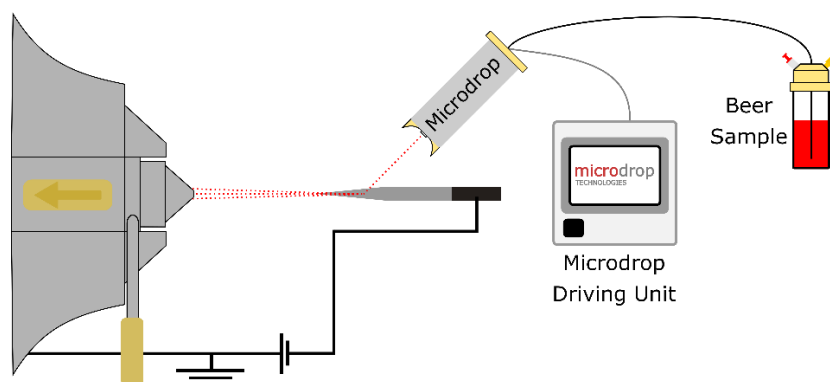


Figure 38 - Single Microdrop onto Needle

Although directing two Microdrop systems directly at the MS inlet (discussed in Section 2.2.2) was not successful, alternative routes to using two Microdrop systems were explored. This included depositing droplets generated onto a needle held at a high voltage, which would then electro spray from the tip, in a similar manner to that adopted by Yu et al. discussed previously.¹³⁴ This would be akin to the Probe Electro spray Ionisation (PESI) system, a commercially available ionisation source which operates by dropping a needle held at ground into a sample well, before applying a HV to the needle, causing an electro spray from the tip.

By avoiding the use of two charged droplet streams, and instead using a single charged needle from which two neutral streams of microdroplets could mix and co-electro spray, there would be no issue between the microdroplet streams interfering with each other. To test this system, a single Microdrop system was set to deposit onto an electro spray needle, as shown in Figure 38. The electro spray needle used was taken from a Micromass Triple Quadrupole Mass Spectrometer and was used as a standalone needle without spraying any sample from the emitter tip.

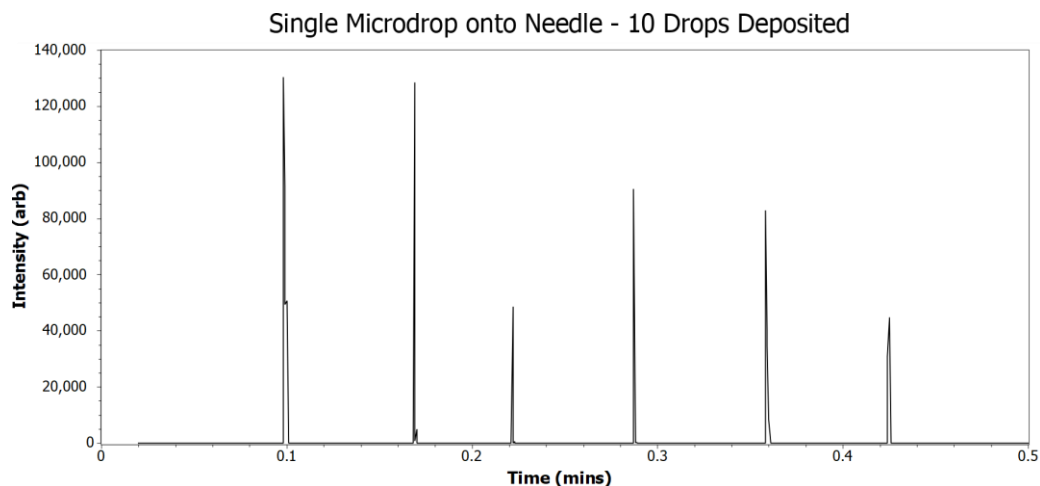


Figure 39 - Single Microdrop onto Needle EIC

Through approximating the droplet size to that of the glass capillary diameter, it is possible to calculate the size and volume of the droplets being ejected. This information, combined with the number of droplets ejected and the concentration of the triton sample ($1.0 \mu\text{g/mL}$), could then be used to calculate the total mass of triton introduced in these short bursts, shown in Eq. 21.

$$\frac{\left(\frac{4}{3}\pi 25^3\right)}{10^6} \times 1.0 \mu\text{g mL}^{-1} = 82 \text{ femtograms} \quad \text{Eq. 21}$$

The system showed good sensitivity, comfortably able to detect bursts of just 82 femtograms of Triton as shown in Figure 39. Averaging across a short peak gives the spectra showing the easily identifiable signal obtained for Triton, shown in Figure 40.

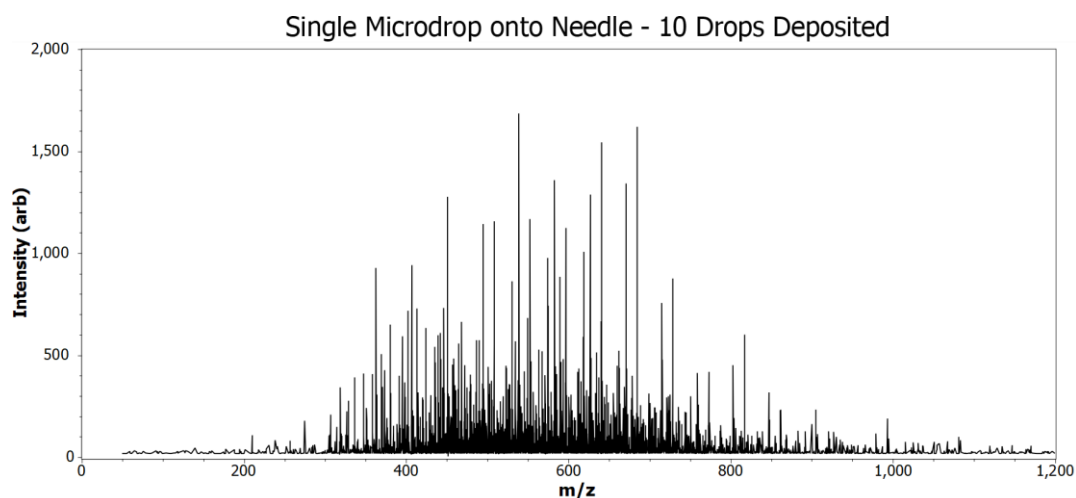


Figure 40 - Single Microdrop onto Needle Triton Spectra

2.2.5 Ion Source 5.0 - Double Microdrop onto Needle – MDD²-PESI

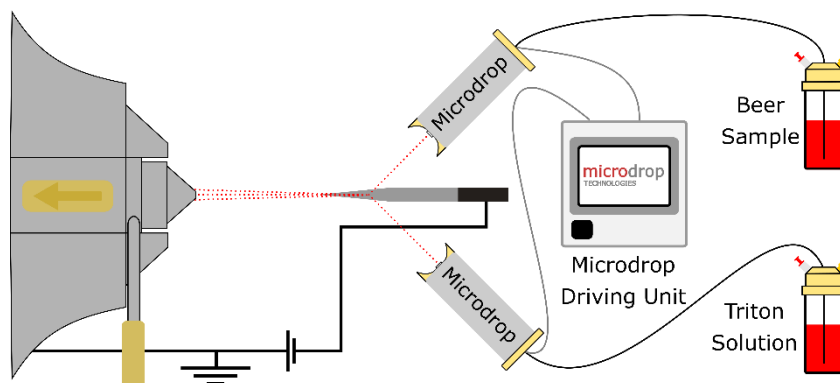


Figure 41 - Double Microdrop onto Needle

Naturally, the final step was to determine whether two Microdrop streams could be introduced onto the needle tip and subsequently co-electrosprayed into the MS inlet. Initially it proved difficult to introduce two narrow streams of microdroplets onto the small needle. Various system designs were developed and tested to avoid this issue, including spraying onto larger surface areas which still enabled the subsequent co-spray to be performed (including a Carbon Fiber Ionisation and Paperspray Ionisation systems). Neither of these systems were successful, with both either not spraying consistently enough or resulting in poor sensitivity.

Through improved design of new 3D printed parts, it was possible to co-spray onto the original needle tip, which gave excellent sensitivity. Images and a schematic of the set up are given in Figure 41 and Figure 42. This system allowed for the continuous spray of one sample, and the introduction of the other in short bursts. Initially, the Microdrop spraying the beer sample was sprayed to give a continuous signal, although care was needed to ensure that the volume of beer being ejected from the Microdrop did not outweigh the volume being electrospayed, in order to avoid a build-up of liquid on the needle tip. The number of Triton microdroplets and the frequency at which they were ejected could be adjusted to increase or decrease sensitivity.

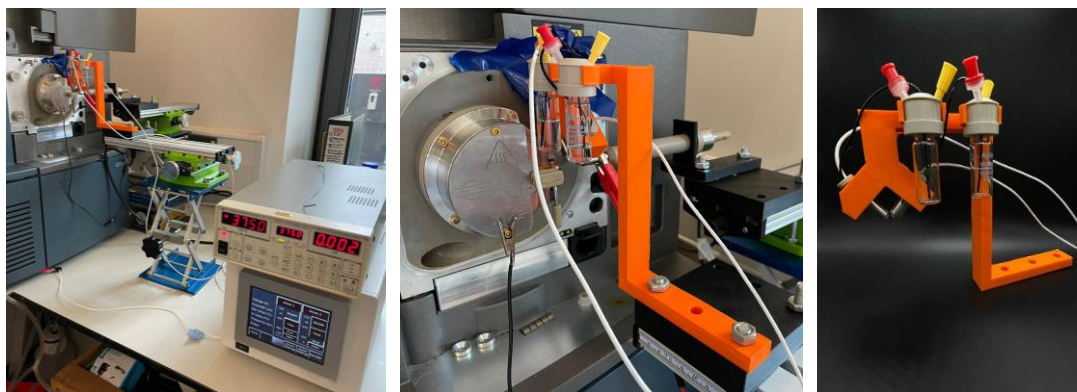


Figure 42 - Ion Source 5.0 Design Images

Figure 43 shows an example dataset collected using this system. The Microdrop containing Beer was sprayed continuously at a frequency of 75 Hz, which gave a consistent MS signal. Although small dips in the extracted ion chromatogram for the beer can be seen at the time points where the Microdrop system is active, this is not actually a drop in observed beer signal, and instead the result of some shifts in the dominant adduct formed, which are explained and discussed in detail in Chapter 4. Triton was introduced in 5 Drop bursts at a frequency of 100 Hz (therefore taking 50 milliseconds to spray the entire volume ejected). The system showed excellent sensitivity for the triton sample introduced, easily able to detect 131 picograms of Triton for each burst, shown in Figure 43.

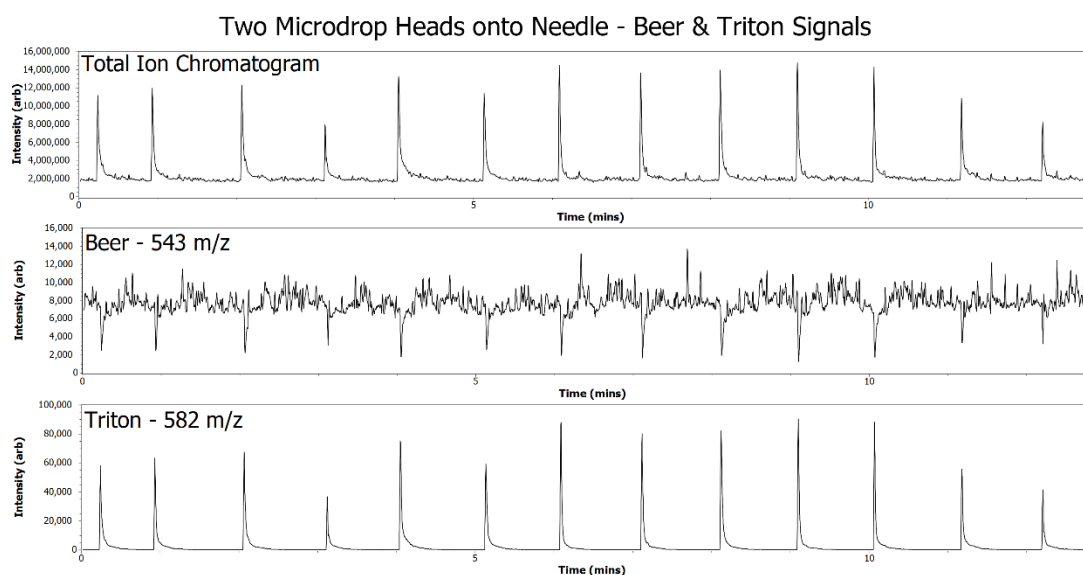


Figure 43 - Two Microdrop Heads onto Needle - Beer & Triton Signal

2.3 Microdrop System: Limitations

The Microdrop system has clearly demonstrated its potential as a tool for ambient ionisation, capable of introducing calibrant into an analysis procedure on demand. However, as the system underwent development the limitations for its use as an ionisation source became clear, some of which were fundamental limitations of the nature of the Microdrop system and could therefore not be changed. These limitations included:

- **Sample Loading Speed** - The sample is stored in a 4 mL vial, with the sample being drawn into the system via capillary action. This is a slow and ineffective method of sample loading, which renders the system unsuitable for rapid analysis or changing calibrant easily.
- **Droplet Size** - Droplets generated are approximately equal to half the diameter of the capillary (50 μm). To increase signal, a smaller droplet size is necessary, and the systems lowest possible capillary diameter offered by the manufacturer is 30 μm .¹³⁵ In addition, the droplet size needs to be significantly reduced in order to avoid the slow depletion of the Microdrop signal observed, whereby the volume of calibrant introduced by the Microdrop is large enough that the calibrant signal takes a significant length of time to dissipate off of the ESI needle.
- **Cost** - The system is expensive, and therefore maintenance/replacements are expensive, reducing the appeal of the system to users

Because of these reasons therefore, development of the Microdrop system was stopped in favor of pursuing alternative acoustic based droplet generating devices, which are subsequently discussed in the next chapter

Chapter 3: PUPP System Development

This chapter introduces the PUPP system (Porous Ultrasonic Piezoelectric Plate) as a replacement for the Microdrop system presented in Chapter 2. The PUPP system overcomes the inherent limitations of the Microdrop discussed previously. This chapter begins by characterizing the PUPP and shows the mechanisms of droplet formation. Focus then shifts onto the development of the PUPP as an ionisation device, of which a number of different design iterations were found to be successful. Proof-of-concept data is shown for a number of important features of the ionisation source, which are the foundation for the applications shown in Chapter 4.

3.0 Ion Source - PUPP

In order to overcome the limitations of the Microdrop system discussed in Chapter 2, it was necessary to switch to a different form of ultrasonic droplet generating device. The system chosen to explore is henceforth referred to throughout this thesis as a Porous Ultrasonic Piezoelectric Plate (PUPP), which falls under the category of a “bend type” piezoelectric inkjet printing device, according to the Li et al. classification system mentioned in Chapter 2.¹²⁰

Research has investigated the mechanisms of near identical devices, often proposing their potential use in medical inhalation therapy.^{136,137} Their most popular application however is in humidifier systems, where they are used to generate mists of liquids, sometimes with the addition of specific aromas. Their functionality as an ionisation source is clear and has been shown in previous publications which use this system, which are discussed later in this chapter. They are a low-cost method of generating microdroplets consistently and of a smaller diameter than the Microdrop system, which through simple electronic adaptations can be controlled to generate defined bursts of microdroplets.

3.1 PUPP System

The PUPP system uses an ultrasonic nebulizer to generate a fine mist of microdroplets for a liquid sample dispensed on top of a plate containing micropores. The PUPPs used throughout this project consist of a stainless-steel plate attached to a piezoelectric transducer ring. At the centre of the stainless-steel plate are a series of cone shaped pores, the number of which depends on the specification of the plate being used. Although there are other designs available for these systems, such as a square stainless-steel plate with a transducer offset to one side (Figure 44 - Right), throughout this project the

circular PUPPs (Figure 44 – Left) were used for ion source development. PUPPs containing 1, 7, and 19 holes were custom manufactured and supplied by a collaborator (Vibrat-Ion Ltd, UK), and PUPPs with 756 pores were extracted from commercially available donut humidifiers (Amazon, UK).

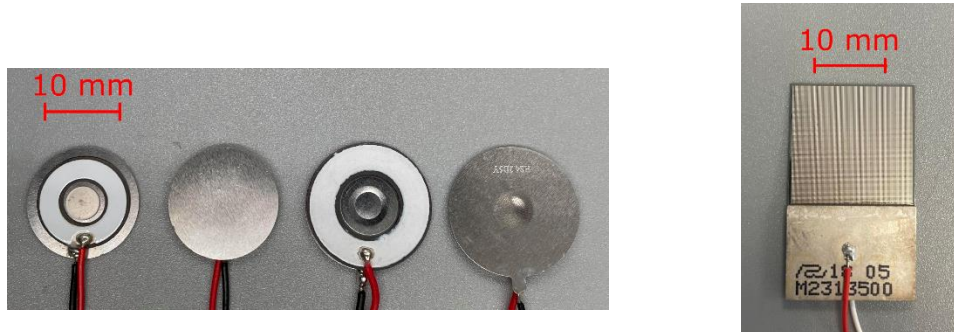


Figure 44 - PUPPs with Scale

Left - 1-, 7- and 19-Hole plate design. Right - 756-Hole plate design
 Right - PUPP with ultrasonic transducer offset to one side of the plate

The diameter of the droplet expelled is proportional to the diameter of the pore, which for all the specification of plates used is ~ 5 micrometers. As the pore size is consistent between the plates, the volume of solution sprayed is therefore proportional to the oscillation frequency and the number of pores the stainless-steel plate has.

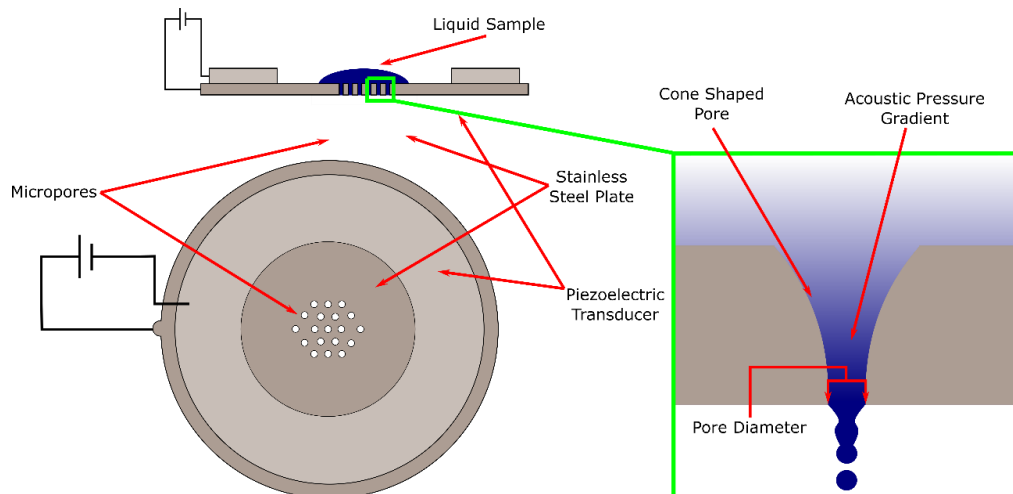


Figure 45 - PUPP Schematic

The piezoelectric transducer ring is driven by an alternating current voltage, which causes the ring to vibrate at an ultrasonic frequency (and therefore the stainless-steel plate also). Droplet formation and ejection is driven by vibration of the stainless-steel plate. Liquid sample is dispensed onto the plate itself, and does not pass through the pores due to surface tension when the system is inactive.

When the system is in operation, and the plate vibrates, liquid sample is forced into the pores as the plate bends towards the sample, creating a high-pressure gradient at the cone orifice, shown in Figure 45. A droplet is subsequently ejected as the plate bends in the opposite direction. The overall process has been shown visually in Figure 46 as a schematic, whilst photographs of active PUPPs can be seen in Figure 47.

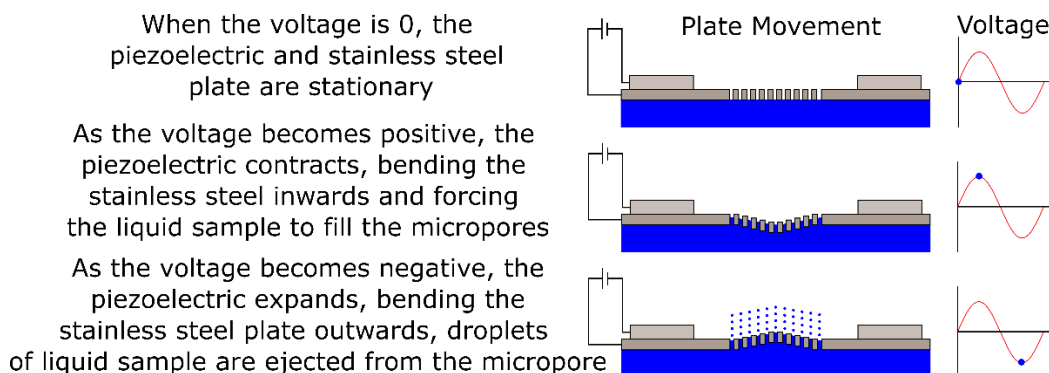


Figure 46 - PUPP Mechanism of Droplet Ejection

The PUPP device is capable of generating a uniform distribution of small droplets ($\approx 5 \mu\text{m}$), and is approximately 1000-fold cheaper than the Microdrop system. Finally, the easy and open access to the sample side of the PUPPs allows rapid loading or unloading of samples; a process which was not possible through the Microdrop system.

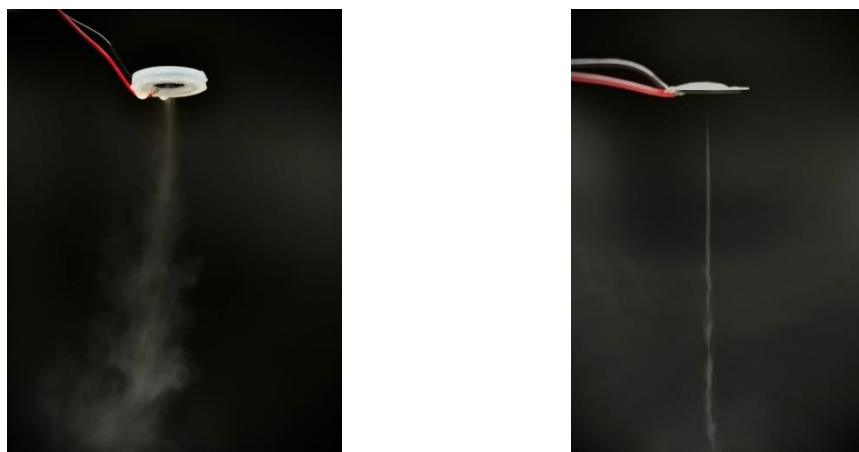


Figure 47 - PUPP in Operate Mode

(Left - 756-Hole PUPP spraying water, Right - 7 Hole PUPP in operation.)

Studies have investigated how careful control over the PUPP plate characteristics can be used to optimize their performance, such as pore pitch, the thickness of the stainless-steel plate and the diameter of the pores.¹³⁶⁻¹³⁹ The optimization of these characteristics may lead to further performance gains to a developed

ionisation source. However, as shown later in this chapter, the majority of the successful PUPP ionisation devices used a secondary ionisation mechanism to generate droplets which entered the inlet of the mass spectrometer. Therefore, optimization of the PUPP was not performed at this early development stage of the system, as it is unlikely to have a significant effect on the results generated.

This style of nebulizer has already been applied to mass spectrometry by coupling the nebulizer with electro-flow focusing (EFF) to form an extractive electrospray ionisation system (EESI) for the isotopic analysis of inorganic metal ions in synthetic fingerprints, gunshot residue and soil samples.¹³³ The system (shown in Figure 48) consists of a capillary held at a high potential to create a highly charged solvent stream. Concentric laminar gas flow is used to focus the droplet stream through a small orifice in a grounded plate held close to the capillary. The solvent stream immediately breaks up into charged microdroplets due to the nature of the electric field between the capillary tip and the grounded plate. The charged microdroplets are directed towards the MS at a slight angle, interacting with the nebulizer sample plume just 5 mm in front of the MS inlet. The system demonstrated good levels of sensitivity, detecting sub nanogram levels of inorganic ions in very small sample volumes (microliter).

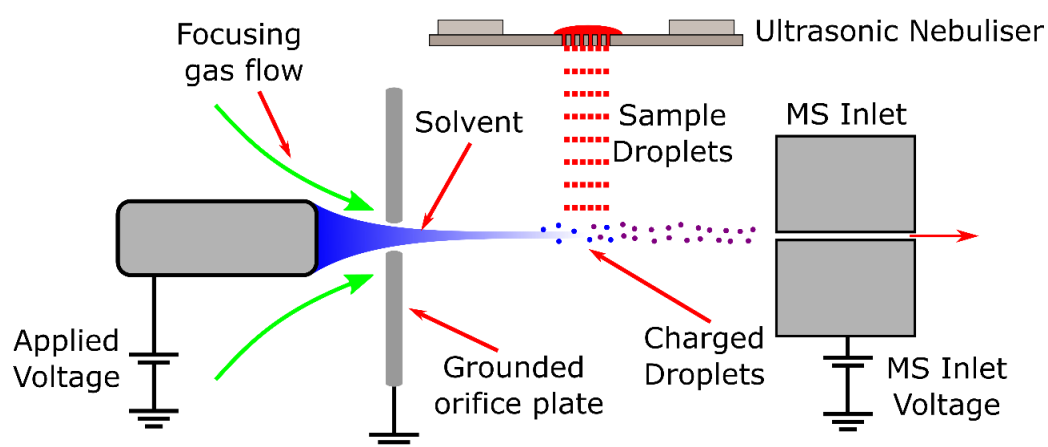


Figure 48 - Extractive Electrospray Ionisation coupled to Ultrasonic Nebulisers for Analysis of Inorganics

Note: Schematic recreated using schematic shown in Forbes et al. 2014¹³³

The same research group who performed the inorganic analysis described also adapted the nebulizer to work in conjunction with a Venturi pump to direct the droplets past a needle held at high potential, where the droplets become charged through corona discharge.¹⁴⁰ The system was successfully shown to be able to detect a range of volatile explosives, narcotics and chemical vapors. The venturi system enabled the collection of a significant proportion of the plume generated

by the nebulizer, and therefore minimizing the waste of sample. This is crucial for the analysis of high value samples for which only low volumes can be obtained.

3.1.1 Duty Cycle Control of PUPP

One of the major benefits of the Microdrop system was its ability to generate a specified number of droplets, even allowing for the generation of a single droplet, for analysis, per mass spectrum. As mentioned previously, control over the number of droplets generated per mass spectrum enabled a series of ion source applications to be explored, and replicating this ability through the PUPP system would be crucial to its success

Although the PUPP system was designed for continuous generation of microdroplets, control over the number of microdroplets generated per mass spectrum was achieved through the creation of customized electronic circuits. Working with collaborators at Ystumtec Ltd. (now Vibrat-Ion Ltd.), appropriate electronics with the capabilities required for this application were sourced and designed. The electronics were themselves controlled by an Arduino system, and the LabVIEW program that controlled the whole system via this Arduino was developed as part of this project.

Two systems were generated: the first of which controlled the duty cycle of the PUPP by altering the duration of time the plate was active for, and another through the use of a circuit board which generated individual pulses to the piezoelectric, and therefore how many droplets were generated. The former of these systems, which enabled control of the plate to spray for as little as 1 millisecond, allowed consistent pulses of a known length, which could then be controlled further by use of PUPP systems with differing number of pores. Through the Arduino controlled system, individual droplets could be generated when using a PUPP with a single pore, as one droplet would be generated through this with each pulse.

3.1.2 Scanning Electron Microscope Analysis of PUPP

In order to determine the shape and diameter of the PUPP pores, images of the different plate types were collected using a scanning electron microscope (JEOL JSM-7100F). In addition, these images were taken to confirm the number of pores present in the piezo plates extracted from Donut Humidifiers, which was confirmed as being 756 using these images. The images confirmed that the pores were cone shaped, and that the orifice where the droplet is emitted from which controls the droplet size, is 5 μm . Figure 49 shows a selection of the images collected using the SEM.

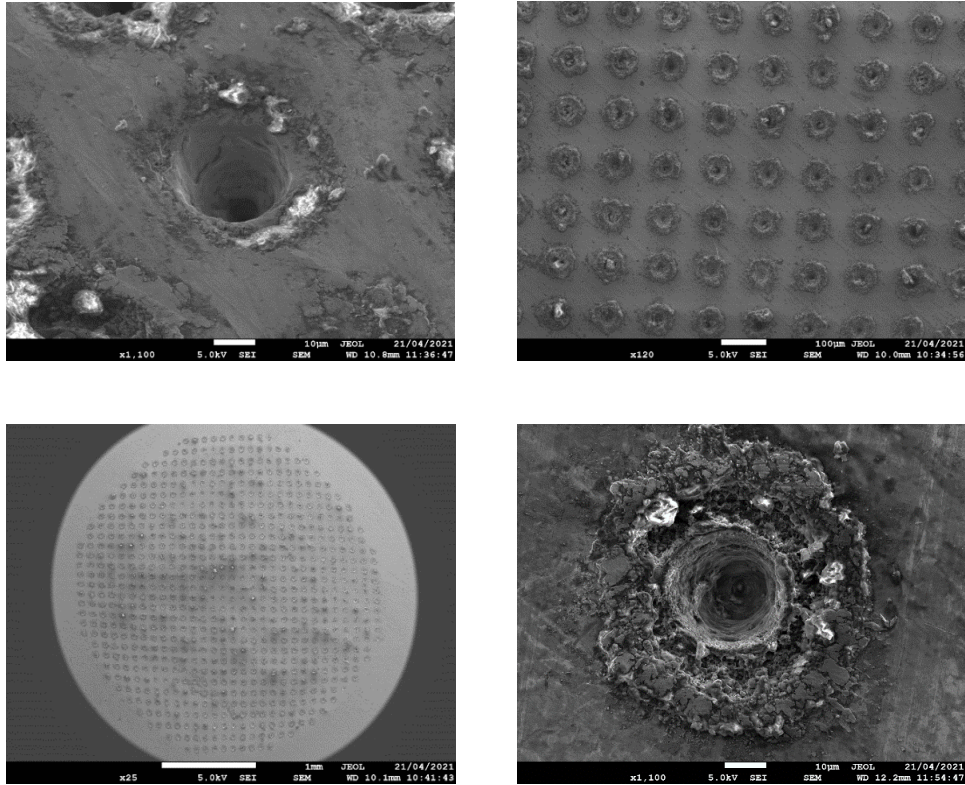
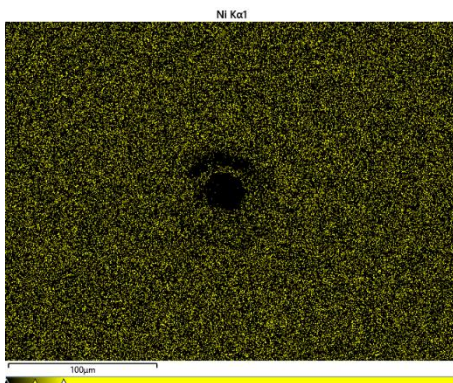


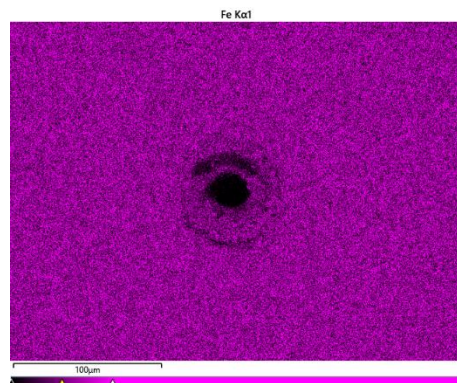
Figure 49 - Scanning Electron Microscope Images of PUPPs

3.1.3 Elemental Analysis of Plates via SEM-EDS

The elemental composition of the piezoelectric plates was determined through energy-dispersive X-Ray spectroscopy (EDS) performed on a scanning electron microscope (SEM). Although Carbon is shown to be a contribution to the plates, it becomes clear that the carbon content is concentrated in the pore itself (likely the result of contamination from previous samples), and can therefore be removed from the elemental composition. Figure 50 shows the EDS-SEM mapping images collected, with Table 1 and Table 2 showing the elemental composition of the stainless-steel plate.



A) Nickel



A) Iron

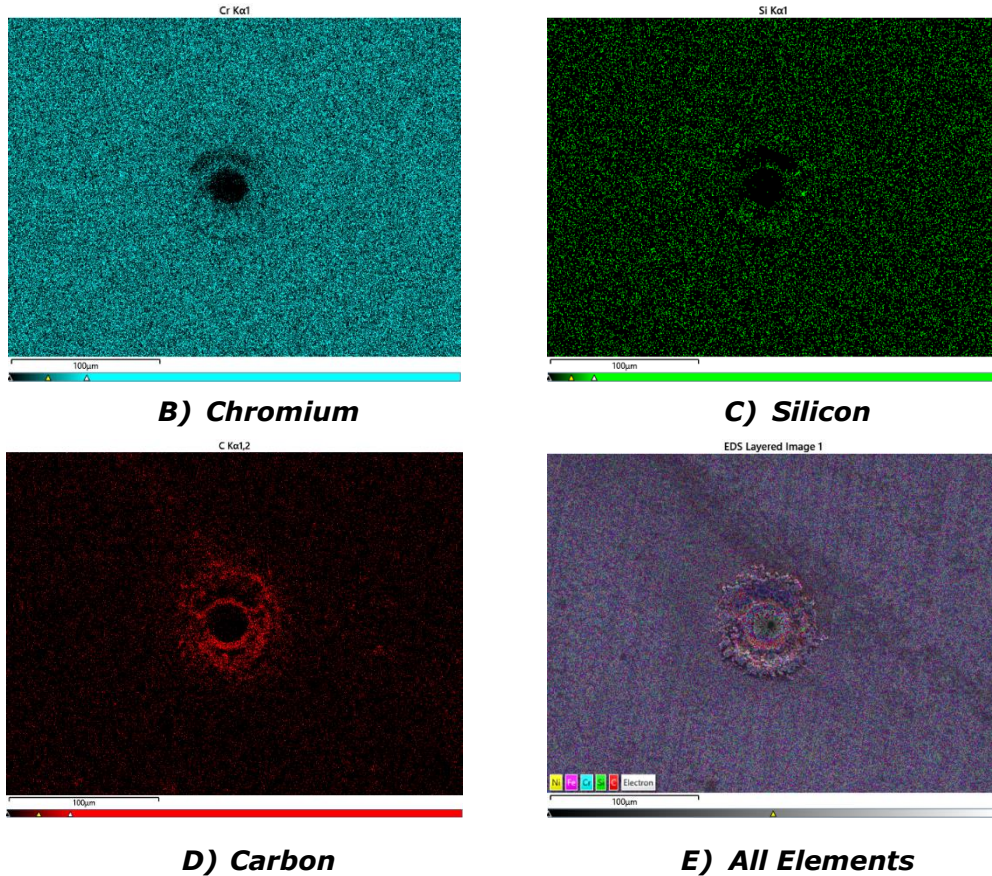


Figure 50 - Elemental Mapping of 1-Hole PUPP by Energy-Dispersive X-Ray Spectroscopy

Table 1 - Elemental Composition of Stainless-Steel Plate (Carbon Excluded)

Element	Atomic %	Weight %
Si	0.83	0.42
Cr	20.50	19.38
Fe	71.20	72.30
Ni	7.47	7.97

Table 2 - Elemental Composition of Stainless-Steel Plate (Carbon Included)

Element	Atomic %	Weight %
Si	0.60	0.39
Cr	15.13	18.02
Fe	52.37	66.98
Ni	5.46	7.34
C	26.44	7.27

3.2 PUPP Ion Source Development

The PUPP system went through various iterations of development, including testing various ionisation mechanisms which could be used, the introduction of additional components giving finer control over the positioning of the PUPP to allow for better optimisation and more consistency, and allowing for the system to be controlled via software or trigger signals given by instruments. Herein the

development process along with some preliminary data collected to determine the system performance is discussed.

3.2.1 Ion Source 6.0 - Single PUPP into MS Inlet (PUPP)

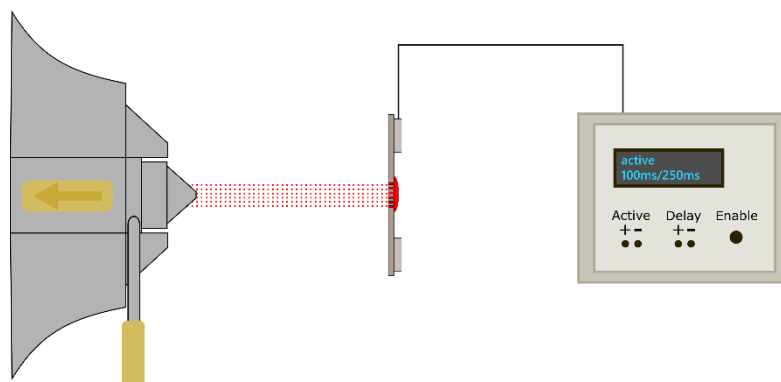


Figure 51 - Single PUPP Directly into Inlet

Early testing on the PUPP system was done with the plume being directed towards the MS inlet with no additional voltages being applied, in a similar approach to the early testing performed on the Microdrop. Despite the lack of voltage, the system gave a signal in both positive and negative mode, which was attributed to the random distribution of charge within a solution. The system gave an overall low signal, although peaks were observed across a wide mass range, Figure 52 shows a butterfly averaged spectrum for signal of beer collected using the system.

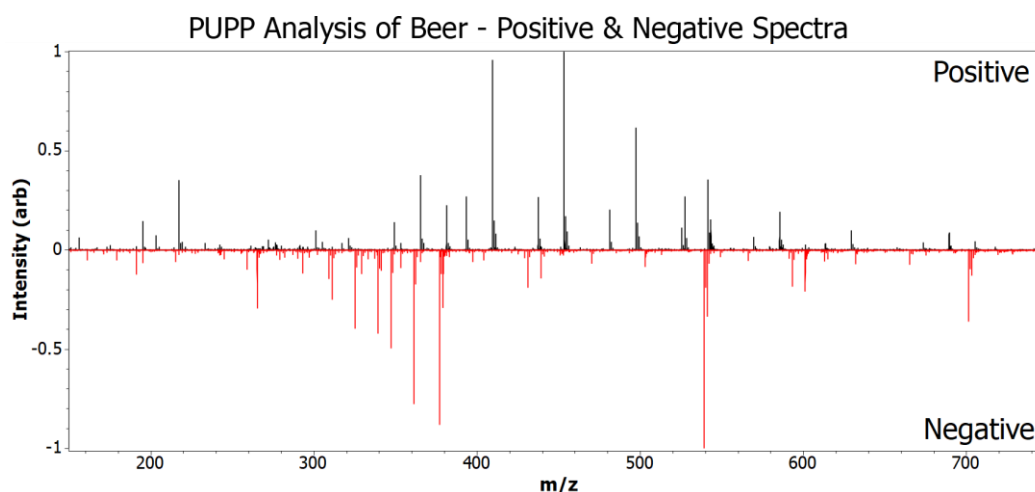


Figure 52 - PUPP Analysis of Beer - Positive & Negative Spectra

This variation of the ion source was tested on the Waters Q-TOF and the Q-Exactive Orbitrap (shown in Figure 53) the latter of which gave a much better signal. The coupling of the ion source to both instruments is discussed in 3.3.

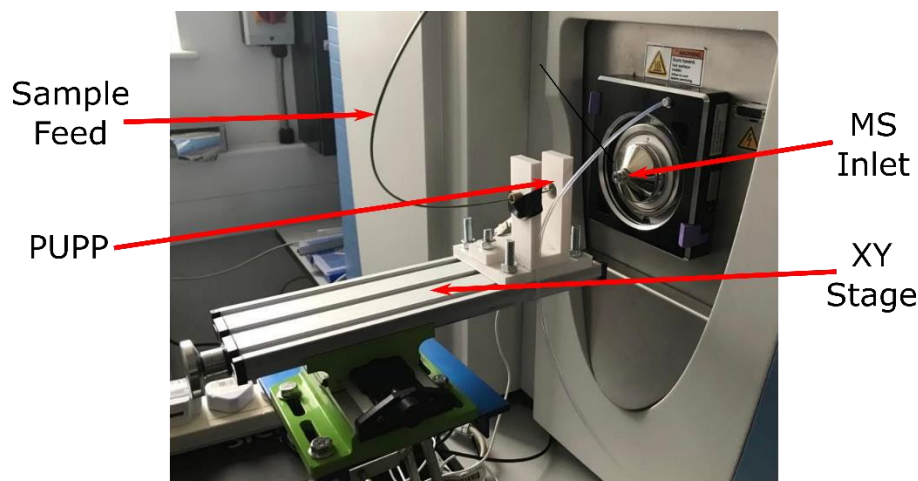


Figure 53 - PUPP coupled to Thermo Q-Exactive Orbitrap

This system configuration suffered from a number of issues, the first of which is the lack of signal repeatability. Figure 54 shows a representative chromatogram for the signal obtained for beer analysis using the setup shown in Figure 51. There were a variety of factors which likely contributed towards this, and these were identified as systematic limitations which would need to be overcome to improve reproducibility. The first of these hypothesized was that variations in the air flow of the surrounding laboratory environment (caused by air conditioning or movement of people) affected the directionality of the microdroplet plume. This would cause microdroplets to enter the MS inlet on some occasions but not others.

In addition, the PUPP was held in a vertical position to ensure the plume was directed horizontally towards the inlet (see Figure 51), which in turn meant that the solution was pipetted onto a surface which was held at 90°. This caused the sample solution to repeatedly fall down the plate, causing inconsistent droplet generation (and therefore signal), particularly for solutions which had low surface tension.

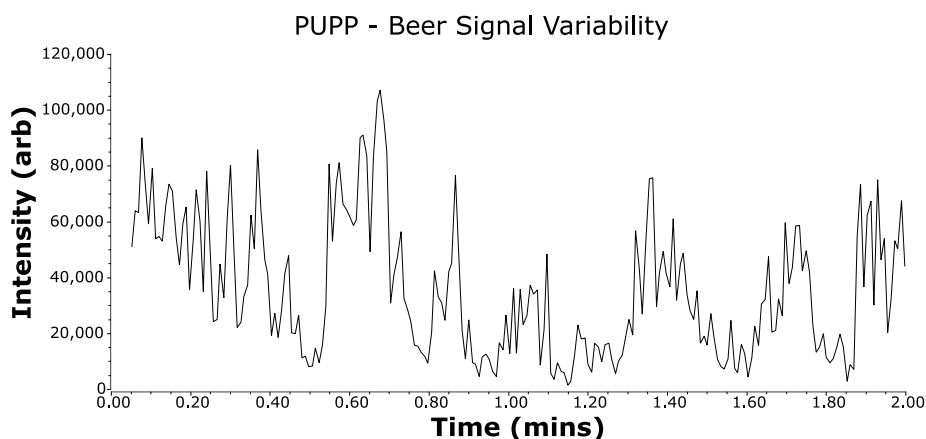


Figure 54 - Inconsistent PUPP Total Ion Chromatogram

Sample loading and lack of droplet charging were not issues observed when pointing the Microdrop system directly at the inlet (see 2.2.1); however, they would be solved relatively easily by switching to a system which used the PUPP to dispense the sample onto a secondary form of ionisation, such as a sharp tipped probe or electrospray needle. This would allow the PUPP to be held horizontally, allowing for easy sample loading regardless of the surface tension of the solution, and the ability to charge secondary sample droplets.

3.2.2 Ion Source 7.0 - Single PUPP onto Needle (PUPP-PESI)

Many of the limitations the PUPP suffers from when spraying directly into the inlet can be overcome by using the PUPP as a tool to dispense samples onto a needle (shown in Figure 55). This would be akin to the MDD-PESI system discussed in 2.2.4, which used a needle raised to a high voltage to generate an electrospray from the tip. Commercial PESI systems give a high degree of sensitivity, and are able to perform rapid analysis of various sample types. Much like the PESI, this PUPP-PESI-MS system would not be suitable for the addition of calibrants to a sample being infused through conventional MS systems, but would have potential applications in the rapid analysis of samples (see Chapter 4).

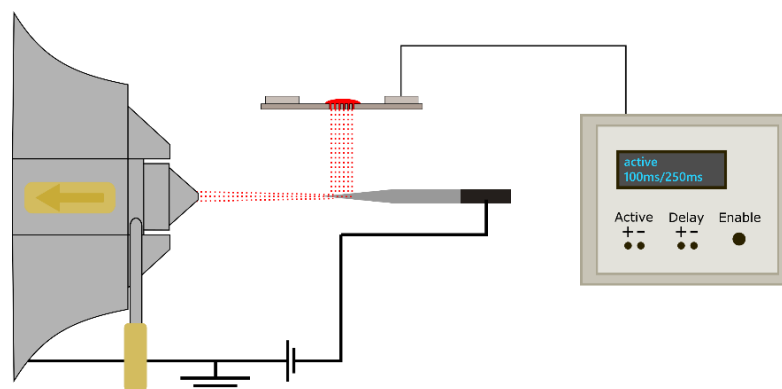


Figure 55 - Single PUPP onto Needle

As part of the system development, a number of needle types were tested, including sewing needles, an Atmospheric Pressure Chemical Ionisation (APCI) needle, medical syringe needles, acupuncture needles and carbon fibre brushes, summarised in Table 3. Previous work within the research group had looked at using an APCI probe to perform post-ionization. Inspiration was taken from previous work conducted with the use of Carbon Fibre brushes as a tool to generate fine electrospray droplets.¹⁴¹ Each method of post-ionization was successful.

Table 3 - Needle Types & Specifications		
Needle Type	Manufacturer	Details
Acupuncture	SEIRIN	No.02 (∅ 0.12) x 30mm
Syringe Needle	Appleton Woods	21 Gauge x 38 mm
Sewing Needle	Cork International	Sewing Machine Needles x 45 mm
APCI Needle	Waters	Corona Discharge Pin #700005346
Carbon Fibre Brush	Easy Composites	0.13 mm (#CF-TOW-3K-100)

3.2.3 Ion Source 8.0 – Single PUPP into ESI Spray (PUPP-ESI)

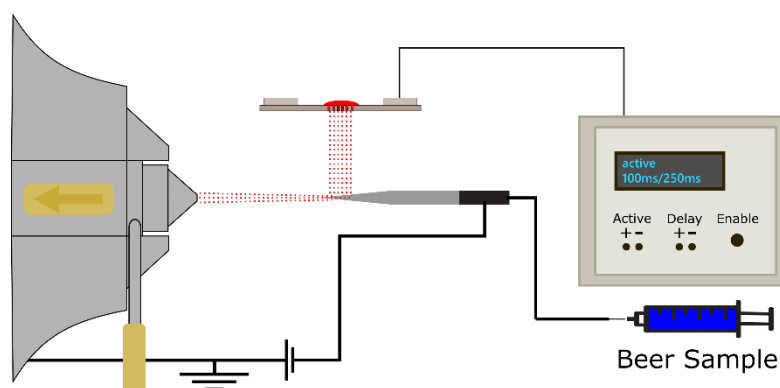


Figure 56 - Single PUPP into ESI Spray

The next iteration of the ion source tested was set up to deposit sample droplets onto the tip of an ESI needle which was spraying a second sample, as shown in Figure 56, together with an image of the setup in Figure 57. At this stage, additional control was gained over the position of the PUPP relative to the ESI needle through the use of an XY stage (a mini milling table) and 3D printed components. Control of the position which the PUPP plume impacted on the ESI needle allowed for the optimization of the PUPP signal.

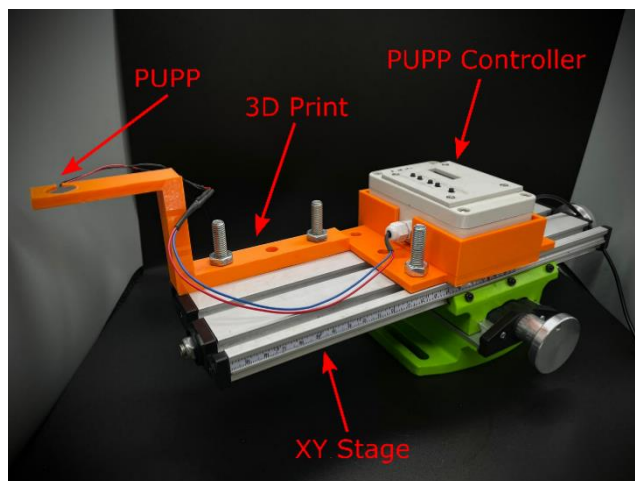


Figure 57 – Ion Source Prototype Design

This system was highly successful, and gave a good strength of signal and consistency in the peaks dispensed by the PUPP. Figure 58 and Figure 59 show extracted ion chromatograms for the Triton dispensed by the PUPP and the Beer sprayed through the ESI needle respectively. Despite the size of the plume, the PUPP has no detrimental impact on the signal given by the ESI.

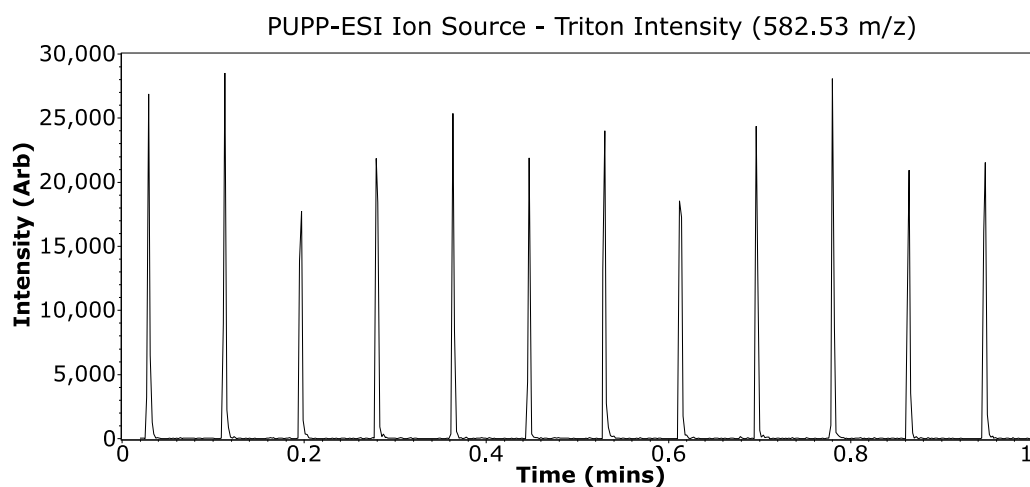


Figure 58 - PUPP-ESI Ion Source - Triton Intensity

*Note: 17 Hole PUPP Plate running at 160ms on/4840ms off. Triton 50 µg/mL.
Beer 100 x Dilution ESI 0.02 mL/min.*

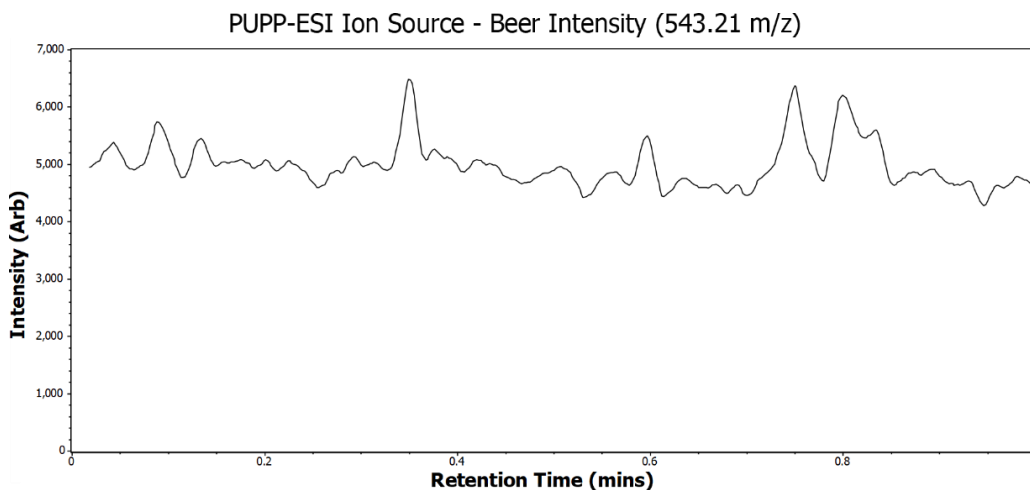


Figure 59 - PUPP-ESI Ion Source - Beer Intensity

*Note: 17 Hole PUPP Plate running at 160ms on/4840ms off. Triton 50 µg/mL.
Beer 100 x Dilution ESI 0.02 mL/min.*

As discussed in 1.7.1, and subsequently shown in in Chapter 2 for the Microdrop dispenser-based ionisation sources, it is possible to vary the duty cycle of the PUPP system itself, theoretically giving independent control over the strength of the signal observed within spectra. This was done by collecting chromatograms for each duty cycle value and generating an extracted ion chromatogram for the Triton signal generated by the PUPP. The extracted ion chromatograms were then integrated to find the area of each peak generated by the PUPP ($n = 12$ for each chromatogram), the average of these peak areas was then plotted to generate Figure 60.

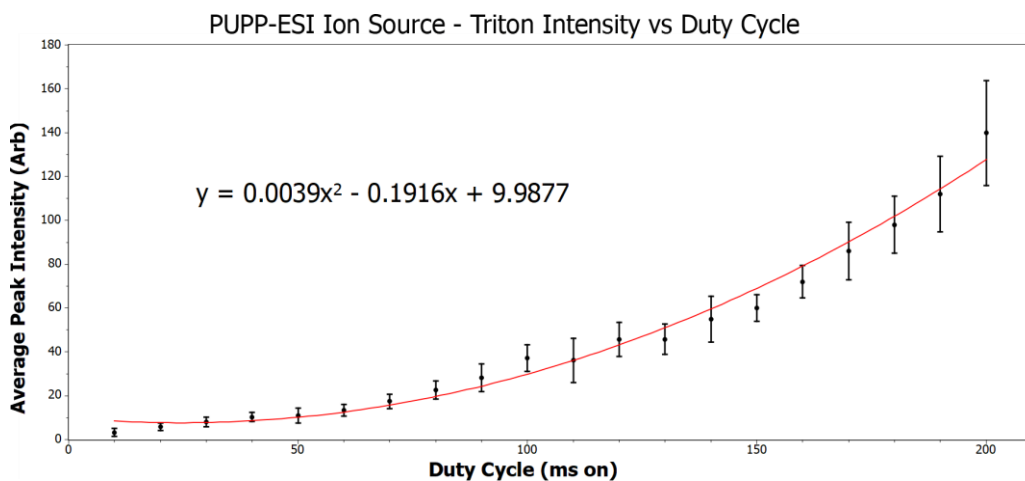


Figure 60 - PUPP-ESI Ion Source - Triton Intensity vs Duty Cycle

The relationship shows a clear positive correlation between the duty cycle and the intensity of the peak, indicating that the system is suitable for modulation of the

signal through varying the duty cycle of the PUPP. However, the relationship is not linear, instead following a 2nd order polynomial curve (selected heuristically, purely to highlight the trend). This is possibly due to the thin layer of liquid which develops after the PUPP deposits solution onto the electrospray tip. As the PUPP solution co-electrosprays, the deposited solution flows towards the needle tip, replenishing the material which has been sprayed. If the layer of solution on the electrospray tip is thicker (as is the case here for higher duty cycles), then the flow towards the needle tip is likely to flow faster. Thin layers of deposited solution on the other hand are less likely to easily flow towards the electrospray tip, and therefore a non-linear solution replenishing process effects the volume of solution deposited by the PUPP and the volume of that solution that co-electrosprays. This hypothesis would suggest that as a greater volume of solution is deposited, the effect is less severe as all duty cycles deposit a sufficient volume of solution onto the needle to negate the resistance of the replenishing flow, and this is observed within the data which shows a much more linear response after approximately 120 milliseconds, as shown in Figure 61.

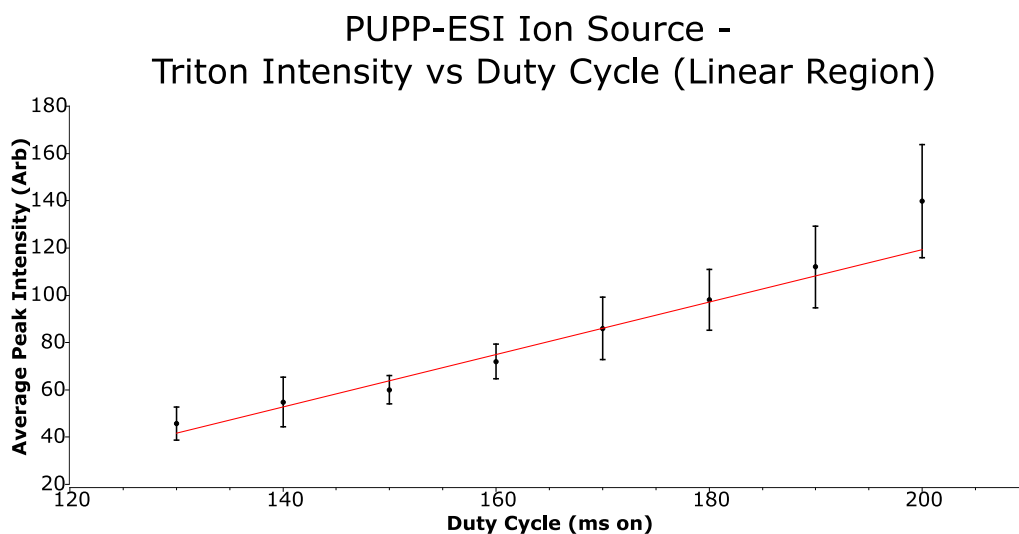


Figure 61 - PUPP-ESI Ion Source - Triton Intensity vs Duty Cycle (Linear Region)

3.3 Application onto different Mass Spectrometers

There are a variety of different mass spectrometers currently available from manufacturers, with each manufacturer using a different inlet design to transfer ions into the mass spectrometer. In order to demonstrate the versatility of the ionisation source, and to collect good quality data in different applications, the system was used in combination with a variety of different mass spectrometer types and manufacturers. At different stages of the ionisation device's development, the system(s) were applied to Waters, Thermo Fisher, ABSciex and

Bruker instruments, which included Q-TOF, Orbitrap and FT-ICR Mass Analysers. Within the appendix, a summary of each ionisation source and which system(s) it was tested with is given. Each mass spectrometer presented its own individual set of challenges, each of which were overcome through rigorous development, which is discussed in the following sections.

3.3.1 Waters Xevo G2-XS Q-TOF

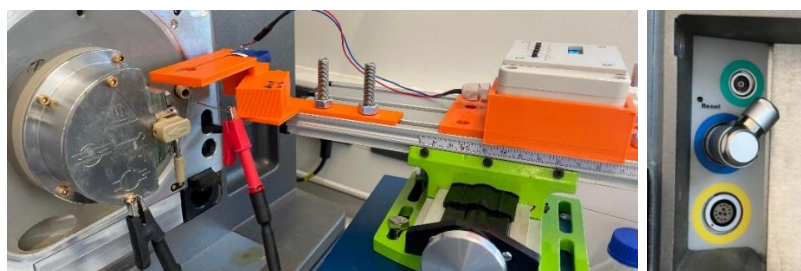


Figure 62 – Ion Source Version 7.0 coupled to Waters Xevo G2-XS Q-TOF

The majority of the development work was performed with a Waters G2-XS Q-TOF Mass Spectrometer. The electrospray ion source door was removed to allow access to the MS inlet. Ordinarily, the system is unable to run without a door present and the interlock sealed. However, this was overcome through the use of an adapted plug placed in the options cable (blue) slot which contained a series of resistors and by overriding the source door interlock switches. The system was then set to operate in Nanospray mode, and all gases switched off.

Although not necessary for most applications, the ion source could be set up to be synchronized with the Q-TOF by using an external trigger, which has been discussed in detail in 3.4.1.

3.3.2 ABSciex Triple TOF 6600

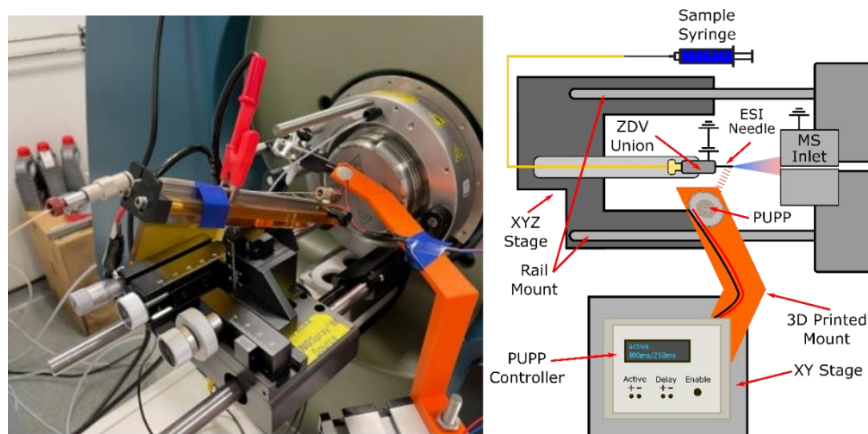


Figure 63 - PUPP Setup with Sciex TripleTOF 6600

Development of a system which works in front of a Sciex system proved to be the most difficult of the systems tested. The system uses a nanospray mounting rail system, which must be locked into place for the mass spectrometer to be operational, and therefore a design was necessary which would work alongside this. The PUPP was introduced from the side using a custom 3D printed part, and sprayed onto a metal ESI capillary. Beer was chosen as the sample sprayed through ESI, whilst Triton was chosen as the mass calibrant introduced via the PUPP to perform internal encoded recalibration, explained in 1.7.1. As shown in Figure 64, the PUPP gave a very strong signal, however, the signal causes a drop off in signal obtained for the ESI, therefore suggesting the plume is too intense, or the angle of approach of the plume negatively impacted the quality of the ESI spray. Further optimization of the system would be necessary to avoid this issue, in addition to making this a single unit which mounts onto the front of the Sciex inlet.

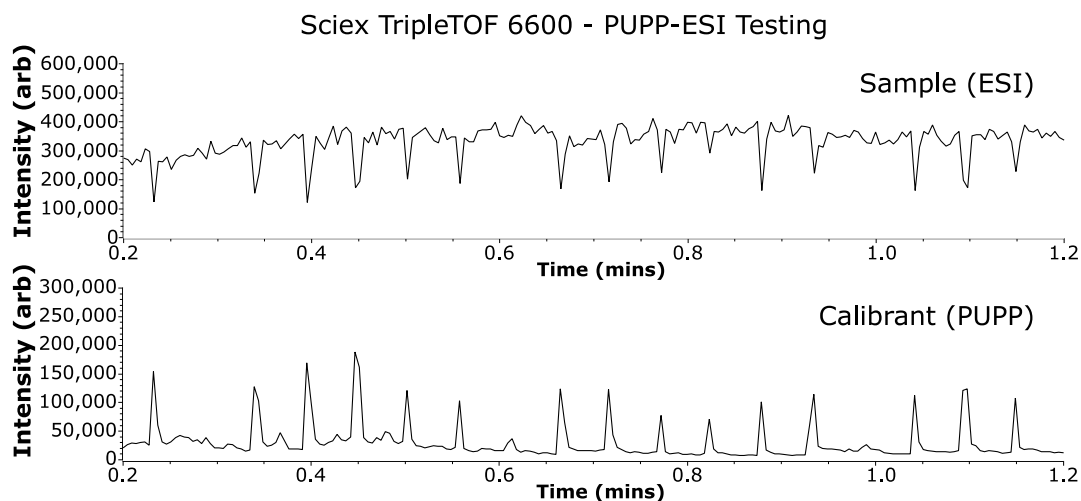


Figure 64 - Sciex TripleTOF 6600 Ion Source Testing

Top: Sample (ESI) signal showing drops in intensity when PUPP is active, indicating PUPP is interfering with ESI signal. Bottom: Calibrant (PUPP) signal showing peaks of intensity where PUPP is active

3.3.3 Bruker solariX 12T FT-ICR

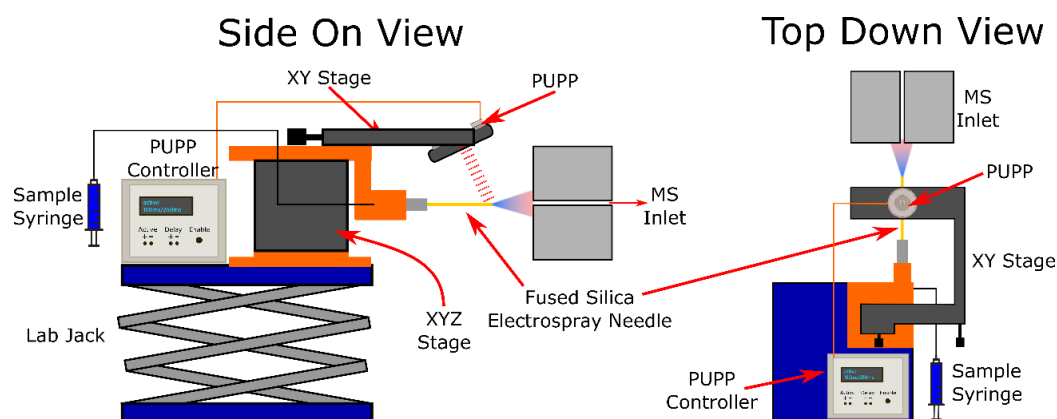


Figure 65 - PUPP-ESI Set up Schematic on Bruker solariX FT-ICR

The PUPP-ESI ion source was applied to a Bruker solariX 12T FT-ICR at the University of Edinburgh, the schematic of which can be seen above in Figure 65. This system differs slightly to previous mass spectrometer inlets, in that the electro spray needle is held at ground, whilst a potential is applied to the inlet. Most commonly, the electro spray needle is held at a potential with the inlet grounded, although this presented no issues to the set-up of the ion source. Improvements were made to gain the most out of the system, the first of which was the ability to bolt the lab jack down onto the surface to provide additional stability for the electro spray signal.

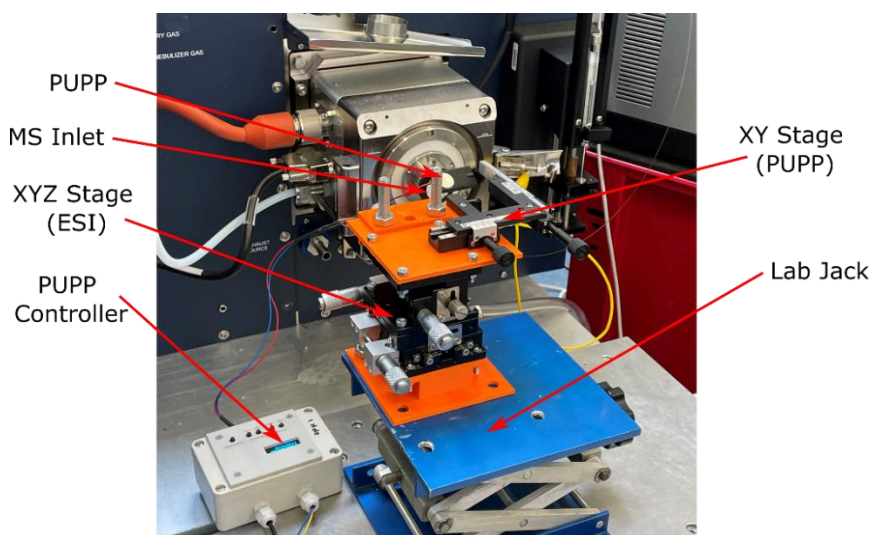


Figure 66 – Photograph of PUPP-ESI Set up on Bruker solariX FT-ICR

Further improvements to the electro spray signal were made through testing different varieties of electro spray and nano spray needles. The original system used a Waters metal capillary as an electro spray needle, which had an ID of 127 μm . When using the Waters Q-TOF for development testing this gave a good signal, which appeared stable. However, when applying this to the Bruker system

the signal was lower than anticipated compared to other spray based ambient ion sources which had been run on the same system.

In order to gain sensitivity and reproducibility in the signal, the decision was made to test fused silica emitters. Two new emitters were compared to the original metal capillary, details of all three can be found in Table 4. The first of these was a New Objective PicoTip fused silica capillary, with a 75 μm ID and a conductive coating on the emitter tip. The second of these was a needle, custom made using a fused silica grinder, with a 75 μm ID and no conductive coating. Further details of the fused silica grinder used can be found in Chapter 5. Another difference between needles was the tip diameter, the custom-made emitters maintained a 75 μm ID all the way to the tip, whilst the PicoTip tapered at the end giving an 8 μm tip diameter.

Needle Type	Manufacturer	Product Number	ID (μm)	Tip Size (μm)
Metal Capillary	MS Tech Solutions	CAP0021	127	127
PicoTip - Coated	New Objective	FS360758CE5	75	8.0
Custom Made - Uncoated	Polymicro Technologies	TSP075375	75	75

Both needles offered improvements in signal compared to the metal capillary, likely due to the quality of the tip shape generating an improved electric field for the generation of a Taylor cone. Despite the smaller tip size of the PicoTips, no significant difference in signal was noticed between the PicoTip and the custom-made fused silica emitter. The limitations of the PicoTip were the fragility of the emitter, which was prone to both blockage and breakage due to its smaller size. No such issues were observed for the custom-made fused silica emitter.

Despite the lack of conductive coating present on the custom-made fused silica tips, a good signal could be obtained from the PUPP, although more careful adjustment of the piezo droplet impact location was necessary to generate signal. When using metal capillaries, there is much more flexibility in the droplet impact location, because the outside of the capillary was held at a high potential. The liquid could previously impact the either the bulk or the tip of the needle, and the wetted emitter would electro spray regardless. This is the founding principle of Probe Electro spray Ionisation (PESI), whereby a needle is dipped into the sample liquid, and electro spray from the tip when a high voltage is applied. When using a non-conductive fused silica emitter, the PUPP plume would need to impact on

the very tip of the needle in order to mix with the conductive liquid being electrosprayed, as shown in Figure 67.

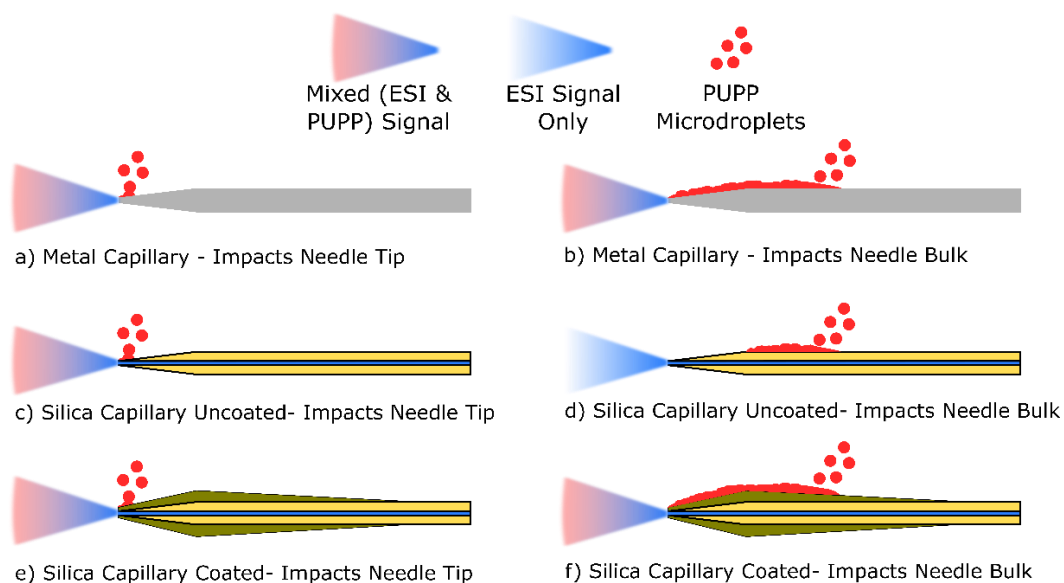


Figure 67 - Effect of PUPP Plume Impacting on Different Needle Types

In order to generate signal, the fused silica tips also needed to be much closer to the instrument compared to the previously used metal capillary, and due to the shape of the Bruker inlet this required an engineering solution to allow the PUPP plume to impact on the needle tip. All other mass spectrometer manufactures inlets tested prior had cone shaped inlets, and therefore had adequate space for the PUPP to sit perpendicular to the electrospray emitter, the Bruker inlet is a flat surface however and therefore does not allow the PUPP to sit this close to the needle when the needle is so close to the inlet. This was solved through the introduction of a pivot point on the PUPP holding mechanism (seen in Figure 68), held in place through a grub screw, enabling the angle of spray to be adjusted accordingly.

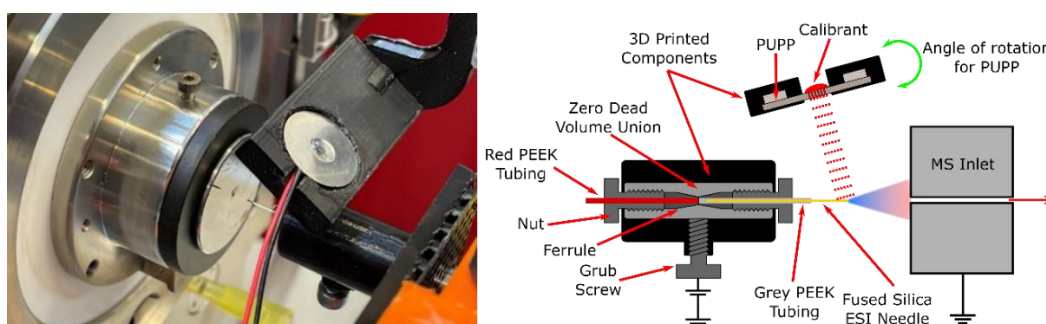


Figure 68 - Pivot System generated for Bruker FT-ICR Inlet Shape

Finally, coupling the PUPP-ESI system had limitations in its repeatability due to the nature of ion accumulation and detection on the Bruker solarix FT-ICR MS, compared to previously used mass spectrometers. The original PUPP system was activated manually by the user, and the spray duration and time between sprays controlled by a manual input. However, FT-ICR instruments undergo short accumulation periods to generate ion packages, which are then subsequently sent to the ICR cell for analysis, generating a transient of length n . In order to generate high resolution mass spectra, longer transients are required which are often much longer than the ion accumulation time.

If the plume generated from the PUPP does not fall within the ion accumulation period, then the calibrant or sample being introduced via PUPP will not be visible in the mass spectrum generated. Alternatively, problems also arise when a varying portion of the PUPP plume is collected within the ion accumulation period, as this will vary the intensity of the PUPP calibrant/sample peaks between scans. This therefore affects the overall ion population for each scan, resulting in mass shifts between peaks through the space charge effect. This effect can be seen in Figure 69. Across the x-axis is the m/z ratio, intensity shown as a heatmap, with the scan number shown on the y-axis. If there had been no variation in ion population between each spectrum then the peak shown at approximately 440.268 m/z would appear at the same mass. However, as the ion population varies between spectra there is a clear shift in the observed m/z throughout the analysis.

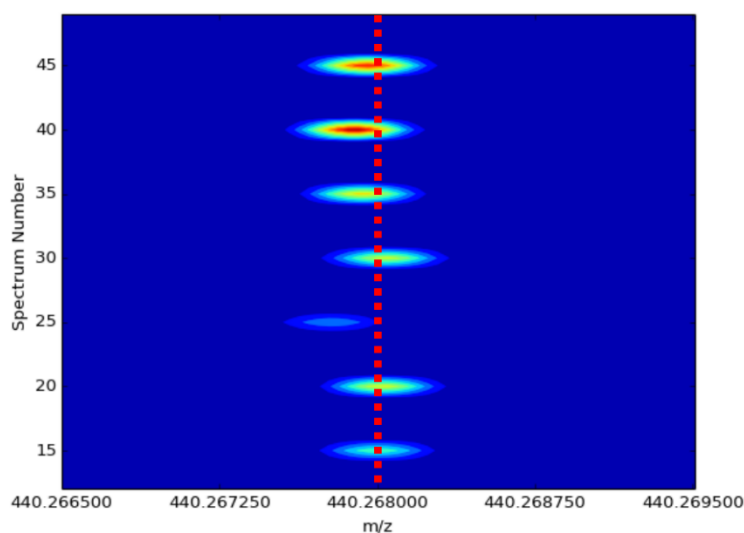


Figure 69 - Variance in mass and intensity of the PUPP signal

This was overcome by upgrading the driver electronics of the PUPP system to include an external trigger system, which is discussed in detail in Section 3.4. In summary, the introduction of a trigger system allowed the PUPP to be activated by a signal generated from the MS when the ion accumulation period was

beginning. This therefore allows for more consistent volume of the PUPP plume to enter during the ion accumulation period, and therefore a more consistent ion population for each scan, reducing the mass shift observed because of the space charge effect. The reduced variance in intensity (and by extension m/z) can be seen for Figure 70 relative to the variance observed in Figure 69.

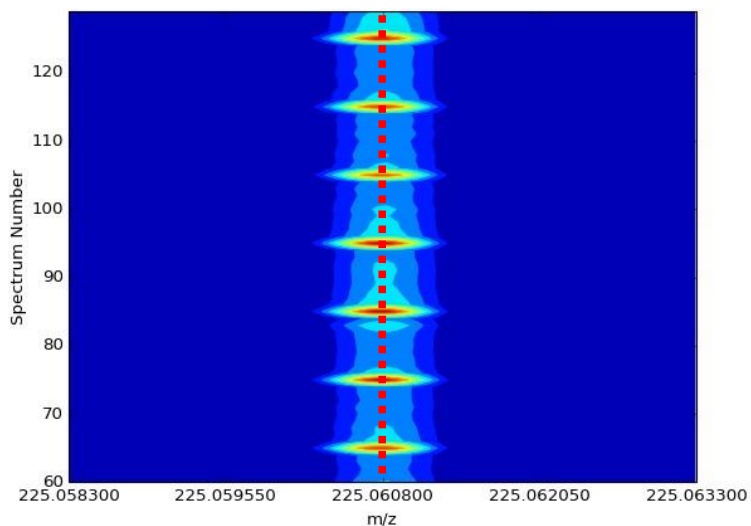


Figure 70 – Reduced variance in both mass and intensity after introduction of trigger system

In addition to the improvements made by synchronizing the ionization source with the mass spectrometer, further improvements were made through an external collaborator (Vibrat-Ion Ltd, UK). Figure 71 shows this final version of the ionization source used for testing on the Bruker FT-ICR.

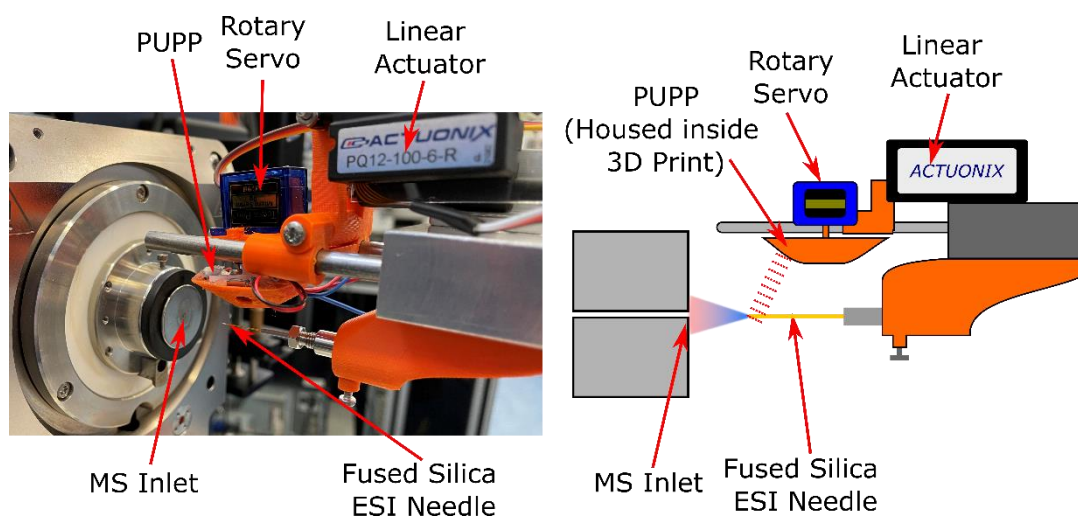


Figure 71 – Updated PUPP-ESI Set Up on Bruker solariX FT-ICR

These improvements including using linear actuators to give fine motor control over the Z position of the ESI needle and the PUPP, a rotary servo to give control over the X/Y position of the PUPP relative to the ESI needle and mounting the

entire system on rails to minimize movement between analysis runs when changes were made to the system. The Arduino used to power the PUPP and the associated electronic controls was mounted onto the rail.

3.3.4 Thermo Fisher Q-Exactive Orbitrap



Figure 72 - PUPP coupled to Thermo Fisher Q-Exactive Orbitrap

The earliest version of the PUPP based ionisation source, whereby the PUPP sprays directly into the MS inlet, was coupled to a Thermo Orbitrap Q-Exactive as part of a collaboration with the University of Surrey. The system used 3D printed components to hold the PUPP in-line with the inlet, and a XY manipulator for fine adjustment. Good signal was achieved for a mixture of samples (including beer and the BMSS pharmaceutical mixtures).

A much more developed version of the ion source (the PUPP-ESI) was successfully coupled to a Thermo Fisher QE-HF Orbitrap Mass Spectrometer. This was achieved by mounting the system to the front of the MS using a custom base plate, which was attached to a Thermo Nanospray source mount. This can be seen below in Figure 73. The MS inlet itself was not that of a standard Q-Exactive HF Orbitrap, but was instead a MALDI/ESI Injector (Spectroglyph LLC, USA). To ensure that the ionization source spray time was aligned with the ion accumulation period of the mass spectrometer, a trigger system was used, which has been discussed in detail in Section 3.4.

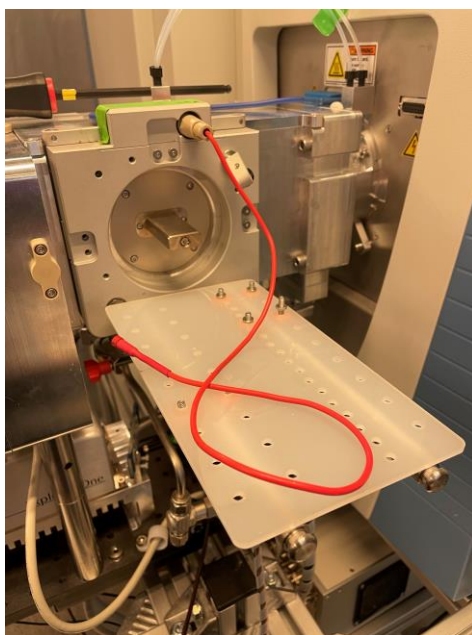


Figure 73 - Custom Base Plate for Thermo Q-Exactive Ion Source

The ion source used an identical system to the final version which was coupled to the Bruker FT-ICR discussed previously in 3.3.3, which included the upgrades to the hardware to give fine motor control over both the ESI and the PUPP system.

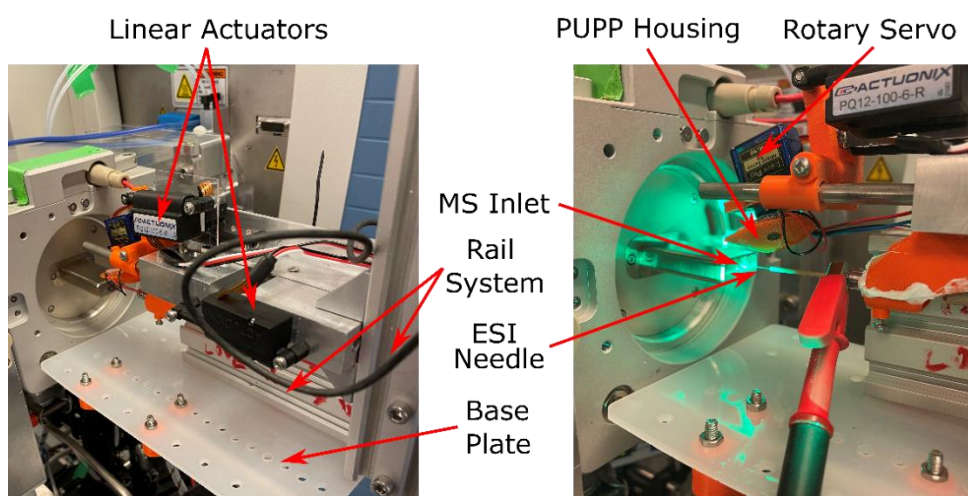


Figure 74 - Ion Source coupled to Thermo Fisher Q-Exactive HF Orbitrap

3.4 Instrument Synchronization

A trigger is a signal (such as a TTL or Time to Live pulse) given by an instrument after a certain event is completed. Mass spectrometers can accept triggers from external sources to gain information about processes starting or finishing, for example, an LC can emit a trigger when an injection is completed which would subsequently begin the data acquisition process of the mass spectrometer for an LC-MS analysis.

In the context of the ionisation source's ability to deliver calibrant (or sample) ions into the mass spectrometer consistently, the ability to use a trigger to synchronize the PUPP system and the mass spectrometer event sequence is crucial, particularly for Fourier-Transform based instruments (namely, FT-ICR and Orbitrap).

In an Orbitrap for example, the system performs an ion accumulation event before each scan, whereby ions are collected for a fixed period of time (e.g. 20 milliseconds). Alternatively, ions can also be collected until a predefined charge capacity of the ion trap is reached, at which point ions are sent to the Orbitrap for analysis, this is commonly known as "Automatic Gain Control" or "AGC".

This introduces two major hurdles to the ion source:

1. Only ions which enter the ion trapping cell during the ion accumulation period are sent for analysis
2. When AGC is being used, the ion accumulation period for FT based instruments is commonly a variable length of time based on when the ion trap reaches the pre-defined charge capacity

The importance for the two systems to be synchronized is given in Figure 75, which shows a simplified sequence of events which an FT-MS instrument performs for a series of scans. In the example given, the ion accumulation event varies in length, reflecting the effect observed when the system runs in AGC mode.

The top row shows the activity of the PUPP when the system is not synchronized with the MS, and is therefore set to spray at defined intervals of time. The PUPP activity does not align with the ion accumulation events shown in orange, and therefore a number of the PUPP sprays miss the ion accumulation period, and some (the final scan for example) only a portion of the PUPP burst is performed when the ion accumulation event occurs.

The bottom row shows the activity of the PUPP when the system uses a trigger given by the mass spectrometer when the ion accumulation event begins. Each

PUPP burst now aligns with the ion accumulation event, and therefore no material is wasted by spraying when the ion accumulation is off.

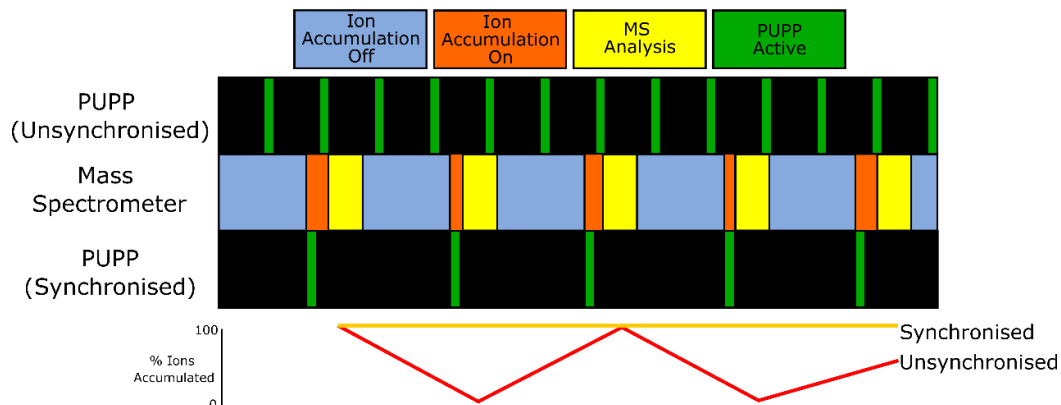


Figure 75 - PUPP Synchronization with FT-MS Instruments

When performing analysis on TOF based instruments, this synchronization is less critical. These systems do not use ion accumulation events, and instead all ions which enter the MS are sent to the TOF for analysis, although some are lost due to transmission efficiency. So long as the scan rate is known, then the duty cycle of the PUPP can be maintained regardless on when the PUPP is triggered. Figure 76 demonstrates that if Eq. 22 is satisfied, the PUPP will be active for the same length of time for each scan.

$$\begin{aligned}
 \text{Delay between PUPP Bursts (ms)} &= (s \times n) - P_A & s &= \text{scan rate (ms)} & \text{Eq. 22} \\
 & & n &= \text{PUPP every } n^{\text{th}} \text{ scan} & \\
 & & P_A &= \text{PUPP Active Length (ms)} &
 \end{aligned}$$

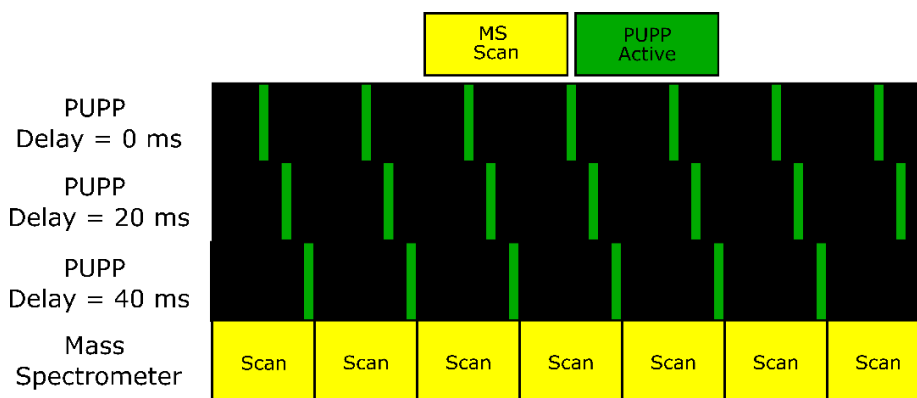


Figure 76 - PUPP Synchronisation with TOF Instruments

3.4.1 Q-TOF Trigger

Synchronization of the PUPP system with Q-TOF mass spectrometers is not a practical option because of the scanning rate of Q-TOF systems. Most Q-TOF mass spectrometers typically run scans every 100 milliseconds or less (The Xevo G2-

XS Q-TOF used for development throughout this project for example can collect scans every 19 milliseconds), and therefore spectra are recorded at a faster rate than the nebulizer can be controlled.

However, there is still a need to extract a trigger from the mass spectrometer for synchronizing the system when coupled to a separation technique such as LC, HILIC or SEC. This trigger would enable users to trigger the PUPP system at specific points in a chromatographic run.

The overall flowchart of the trigger process has been outlined in a flowchart in Figure 77. In summary, the LC system was set to wait for a contact closure signal to be received, rather than being controlled by the MassLynx software. Injection(s) would be written and submitted via the LC software using the conventional process, after which the system would wait to receive a contact closure to begin the LC-MS run.

LabVIEW code constructed allowed the user to submit a list of retention times and spray durations (ms), which would control when to activate the PUPP and for how long. The user would then run this code, which would send a contact closure via an Arduino to the MS, beginning the LC-MS method and data acquisition process. In addition, the Arduino would send contact closure signals to activate the PUPP system at appropriate times/spray lengths according to the user-controlled PUPP method.

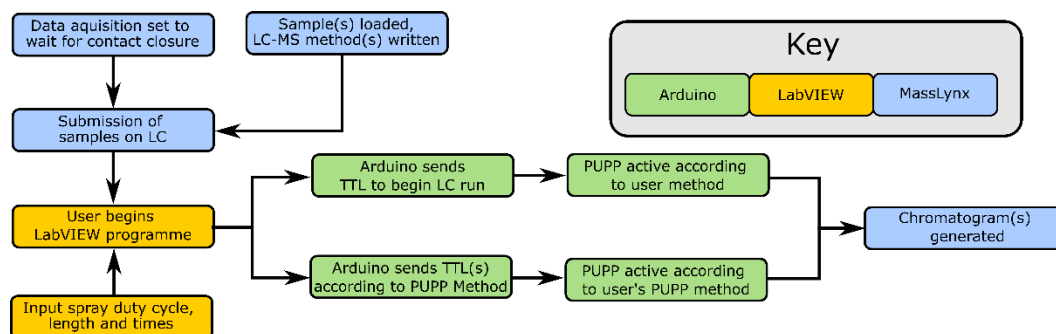


Figure 77 - Waters LC-MS PUPP Trigger Flowchart

3.4.2 Orbitrap Trigger

The system used to synchronize the ion source to the ion accumulation period of the Q-Exactive HF Orbitrap is shown in Figure 78. The system uses the same contact closure signal which is sent to an FTMS Booster (Spectroswiss Sàrl, Lausanne, Switzerland) to ensure synchronized data collection.

The FTMS Booster is an advanced data acquisition system which works in parallel with the built-in instrument manufacturer data acquisition system for FTMS mass

spectrometers. On the Orbitrap, the booster works by splitting the signal obtained from the standard differential amplifier, so that the signal is recorded simultaneously by the thermo electronics but is now also digitized by the oscilloscope built into the booster unit. The booster collects the full (unreduced) transient at a higher digitization rate than the Thermo electronics. This unlocks absorption mode data for the user, which achieves higher peak resolution than conventional magnitude mode data. In addition, the FTMS booster allows Orbitrap users to record longer transients than otherwise possible through the Thermo software limits.

The contact closure is sent from the Q-Exactive every time the ion accumulation period begins. This contact closure signal is fed into a T-Splitter, which allows the same signal to be sent to a pulse generator (Stanford Research Systems, DG535). The pulse generator subsequently sends a TTL pulse (3.3V, Dwell Trigger, 10 microsecond pulse length) to the Arduino of the ion source.

Although the Arduino receives a TTL pulse for every scan the Q-Exactive takes, this does not mean that the ion source will be activated for every scan. The ion source is set to activate every n^{th} scan (therefore every n^{th} TTL pulse received) based on user-controlled parameters.

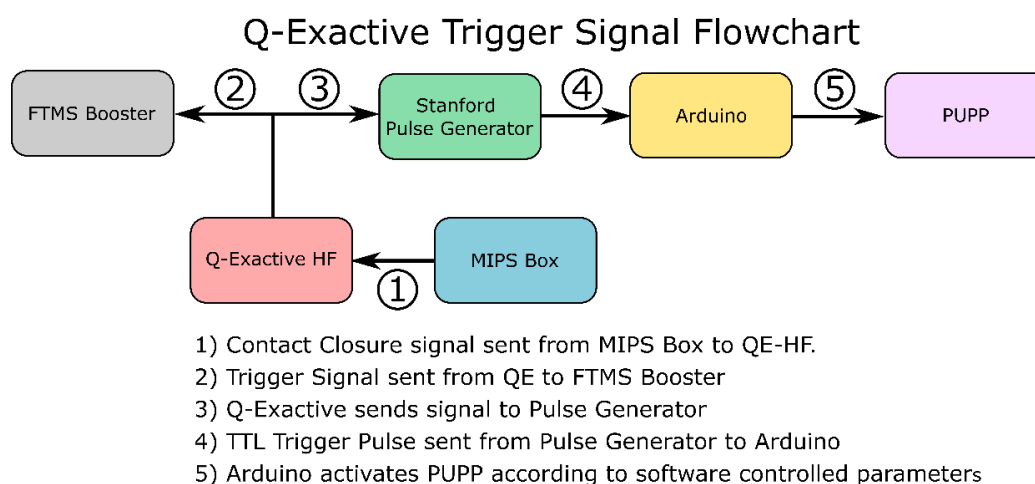


Figure 78 - Q-Exactive HF Orbitrap Triggers Flowchart

3.4.3 FT-ICR Trigger

During data acquisition, the event sequence of a Bruker solariX FT-ICR is controlled via pulse programming, referred to as BASIC (Bruker Acquisition Sequence for Instrument Control). The solariX uses text files containing event keywords to perform functions in the appropriate sequence, these keywords are linked to an event definition. Events are regarded as either “constant” or “conditional”. Constant events are required for all modes of acquisition, an

example of this would be "DETECTION", and these events are always compiled into the event sequence. Conditional events are controlled by user selected settings in the GUI (Graphical User Interface) of the software, and therefore are only compiled into the event sequence, if necessary, based on the settings chosen by the user. An example of a conditional event therefore would be "ECD" which can be switched On/Off based on the needs of the experiment the user is performing.

Within the Application Note "Pulse Programming in solariXcontrol"¹⁴² published by Bruker, a tutorial for extracting a trigger from the instrument is given. The application note gives a list of all the TTL pulses available from the solariX instrument, the pulse of interest for this application is the "setnmr4(31)", which is the only user accessible pulse on the AUX interface (specifically PIN35) located just above the inlet of the mass spectrometer. The BASIC system allows for the input of up to 5 custom user events, and following the tutorial given within the pulse programming manual "USER_EVENT_1" was written as shown in Figure 79. This generates a 5-millisecond pulse (TTL low to high) immediately after the "ION_QUENCH" event, during which ions from the previous scan are ejected from the cell.

```
# USER_EVENT_1_KEY:
USER_EVENT_1.lines = 2
USER_EVENT_1.1 = " 5m setnmr4|31 ; set TTL high for
d500"
USER_EVENT_1.2 = " 1u setnmr4^31 ; set TTL low"
```

| = sets TTL level high
^ = sets TTL level low
m = milliseconds
u = microseconds

Figure 79 - solariX FT-ICR Trigger User Event

3.5 Summary

The PUPP system has been shown to be a system capable of delivering small volumes of calibrant or sample for analysis. Proof of concept data has been shown for the ability to control the signal intensity by varying the duty cycle of the PUPP. In addition, data has been shown which demonstrates the PUPP's ability to generate sharp bursts of signal, the signal for which rapidly depletes after the PUPP is activated. The system overcomes the limitations discussed for the Microdrop ion source discussed in Chapter 2, summarized in the table below.

Microdrop Limitation	PUPP Evaluation
<i>Slow sample loading speed</i>	The PUPP system has an open-air sample delivery, enabling the user to pipette sample directly onto the plate, and rapidly change between sample/calibrants being used
<i>Large droplet size (50 μm)</i>	The PUPP system produces much smaller microdroplets, approximately 5 μm in diameter
<i>High cost</i>	PUPP System is significantly lower cost than the Microdrop system, by approximately 3 orders of magnitude

The next stage of the ionisation source was to perform proof of concept testing for encoded internal recalibration of complex organic matter samples, which is subsequently discussed in the next chapter. Through the development and testing of the ionisation source, a number of different applications were tested, including Rapid Screening of Samples, Adduct Modification and Component Confirmation.

Chapter 4: Ion Source Applications

As shown in Chapter 3, the versatility of the PUPP system allows for multiple variations of the ion source (PUPP, PUPP-PESI, and PUPP-ESI). The ability to easily interchange the hardware used and rapidly load the sample/calibrant onto the piezo means the system can easily be adapted for a variety of different applications.

4.0 Ion Source Applications

Herein, the different applications of the ionisation source are shown. Initially, the original focus of the ion source, encoded internal mass recalibration, is shown. This was applied to the analysis of a complex sample, Suwannee River Fulvic Acid. All three ion source variations were successfully applied to the rapid analysis of different samples, including beer, fruit juices, human plasma and a pharmaceutical mixture, data for all is shown herein. Finally, two further applications are presented which were found during the development process of the ionisation source; on demand adduct modification and component confirmation, the theory of which and proof of concept data are shown.

4.1 Encoded Internal Mass Recalibration

Confident assignment of peaks in complex mass spectra for unknown samples is a difficult task. Accurate mass across the spectrum is crucial, and the most effective approach to obtaining this is through internal mass recalibration, for the reasons described previously in Chapter 1. The most common method is to spike the sample with calibrant; however, this is a labor-intensive process which requires matching the concentration of the calibrant to the unknown sample (usually performed through trial and error) and can lead to the unwanted suppression or enhancement of sample ions. In addition, detection of the calibrant peaks is often performed manually by the user along with the recalibration function, a process which can be difficult and can easily lead to misassignment of calibrant peaks in complex spectra. Figure 80 shows a spectra region containing a calibrant peak and a sample peak at nearly identical masses (0.004 m/z apart), which if manually assigned could easily be misassigned. Finally, spiking a sample with internal calibrant means that all sample spectra contain the calibrant peaks, which are otherwise unwanted when reporting spectral data.

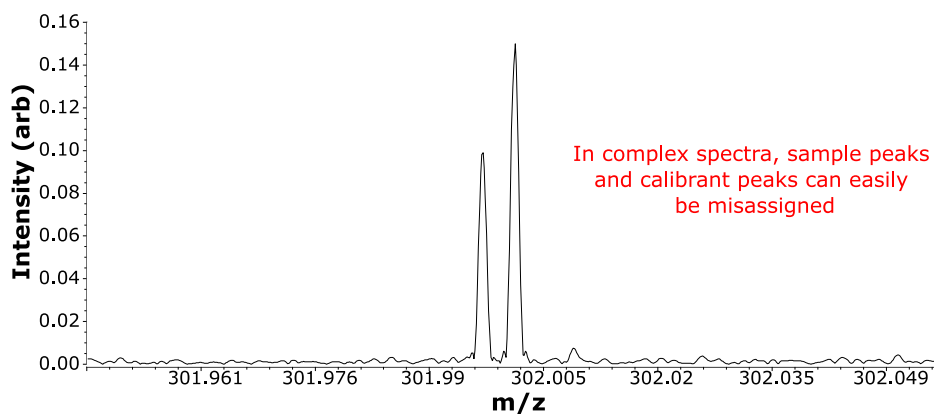


Figure 80 - Calibration peak with a complex mass spectrum region

There are a variety of ionisation sources which have been developed that have been used to generate sample and calibrant ions separately without the need to spike the sample, most of which are focused on the use of dual electrosprays, which have been discussed in Chapter 1.

The PUPP system can introduce calibrant into the spectrum on demand, which can be either be automatic (through use of a trigger) or manually controlled (by the user). The user can set the system to introduce calibrant at specified points, for example during pre-defined points or regular intervals during LC runs or direct infusion data collection. Regardless of the method used, the resulting dataset contains a mixture of spectra which only contain peaks associated with the sample and spectra which contain a mixture of both sample and calibrant peaks.

The introduction of calibrant at known points in time (and therefore known spectra) is referred to as encoding the calibrant signal in the dataset. This encoding enables software to detect which peaks in the mixed spectra are calibrant peaks and which are sample peaks. These calibrant peaks are then used to perform an internal recalibration function across the relevant mass range, and this same function can then be applied to the spectra which contain sample peaks only. This is the overall principle of generating encoded internal recalibration data.

There are other benefits to using the PUPP system to perform mass recalibration. For example, the PUPP system allows for the adjustment of the intensity of the calibrant in the spectra through control of the PUPP duty cycle, for which proof of concept data has been shown in Chapter 3. Moreover, because the PUPP facilitates the rapid loading of different samples, the system can also therefore be used to change between calibrants by the user. Therefore different solutions can be easily screened to find the one which gives peaks across an appropriate mass range for the sample being analysed. Alternatively, if the choice of concentration for the calibrant is significantly out of range, and duty cycle adjustment cannot account

for this alone, then a more dilute calibration solution can easily be introduced. Finally, for applications which require the use of isotopically labelled mass calibration standards, the PUPP calibration uses a much smaller volume for calibration, therefore reducing material costs.

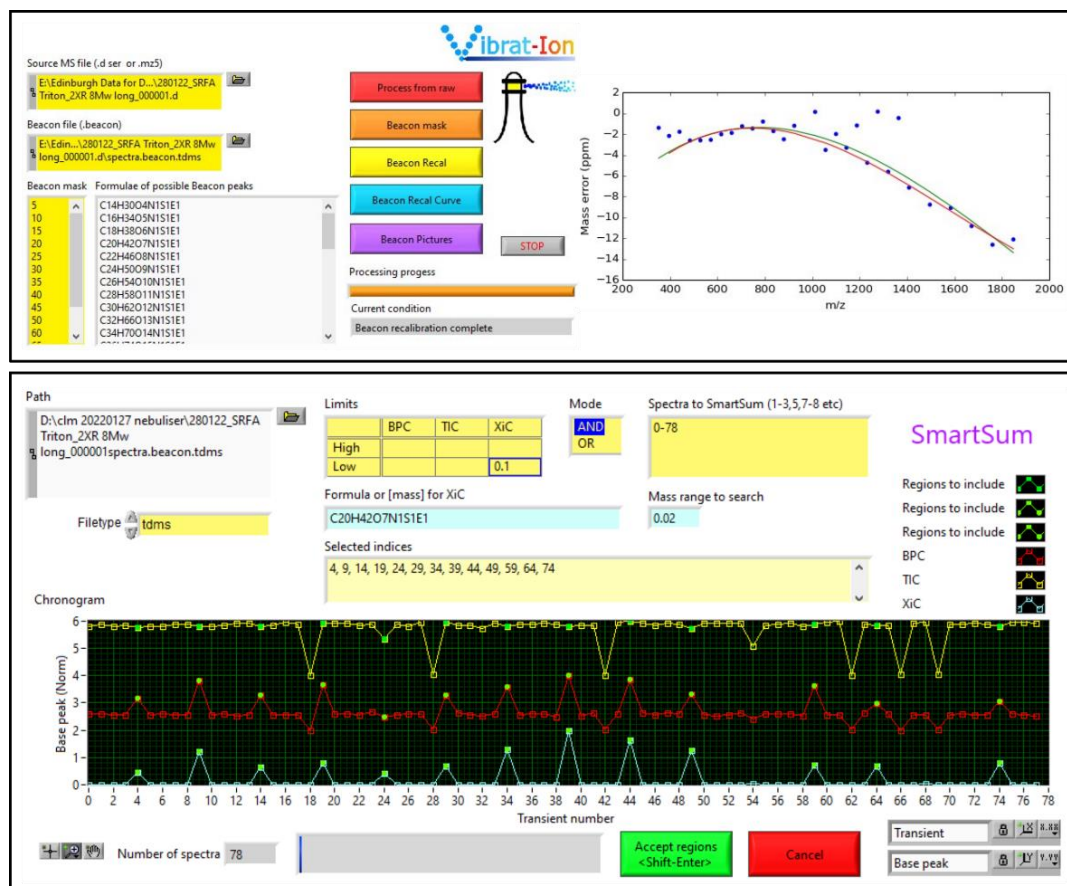


Figure 81 – “Beacon” Software User Interface (Vibrat-Ion, UK)

Main user interface (Upper) and the Beacon Mask sub panel interface (Lower)

In order to perform internal encoded recalibration, Beacon software (Vibrat-Ion Ltd., UK) was used, the user interface of which is shown in Figure 81. Programmatically, the system works by using a predetermined list of chemical formula peaks for the internal calibrant, thus generating a list of expected m/z peaks. The system then seeks them out by finding the peaks within the spectra (within $\pm m/z$ 0.5) that best reflect the calibrant pattern (patterned correlation). In addition to generating a calibrated file, the system also generates a recalibration function graph and images to show the calibrant ion intensity heatmaps. Finally, because the calibration function performed is stored within the recalibrated file, the calibration can be retrospectively accessed, which in some cases may be useful during data auditing in order to justify why the calibration peaks used were chosen.

An overview of the programmatic workflow of the Beacon software has been given in Figure 82. Figure 83 shows region of a mass spectrum containing a calibrant ion, identified using the software. The red spectrum shown is the raw spectrum, the black spectrum is generated after a wavelet decomposition of the raw spectrum, and finally the blue line indicates a peak identified as calibrant.

Error! Reference source not found.

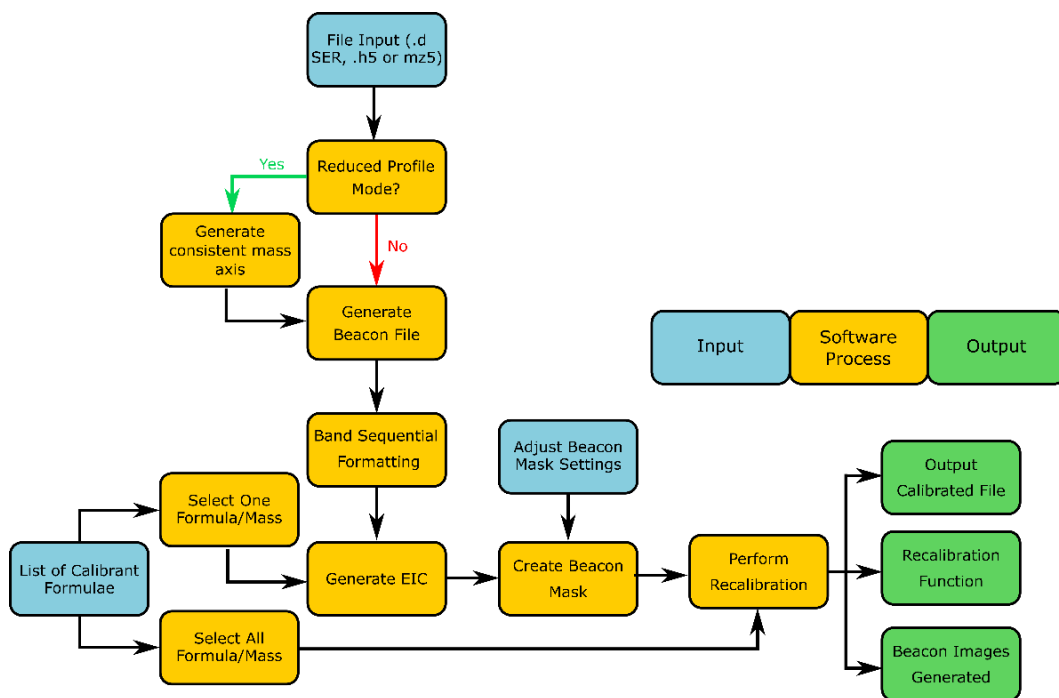


Figure 82 - Internal Recalibration Programmatic Workflow

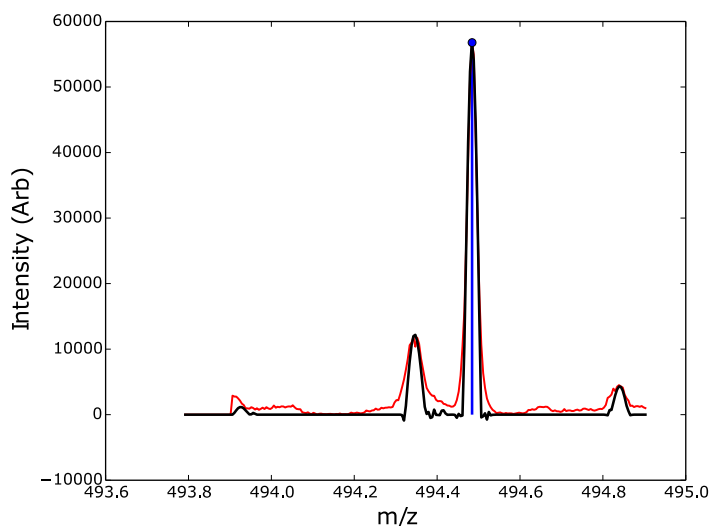


Figure 83 - Peak Detection of Internal Calibrant using Beacon software

The Beacon software can differentiate between which peaks originate from the electrosprayed sample and which originate from the calibrant delivered in bursts from the PUPP. Figure 84 shows an example of the software performing this task

for an analysis of Beer, with the PUPP introducing Triton QS-15 as the mass calibrant. Figure 84a shows a mixed spectra containing both sample and calibrant peaks, Figure 84b shows a spectrum where only the calibrant is present. Crucially, the spectra shown in Figure 84b matches that of Figure 84c, which shows a spectrum containing the peaks which have been identified as calibrant and extracted from a mixed spectrum. Finally, Figure 84d shows a zoomed in region of the spectra, showing calibrant peaks plotted in blue and sample peaks plotted in red overlaid one another.

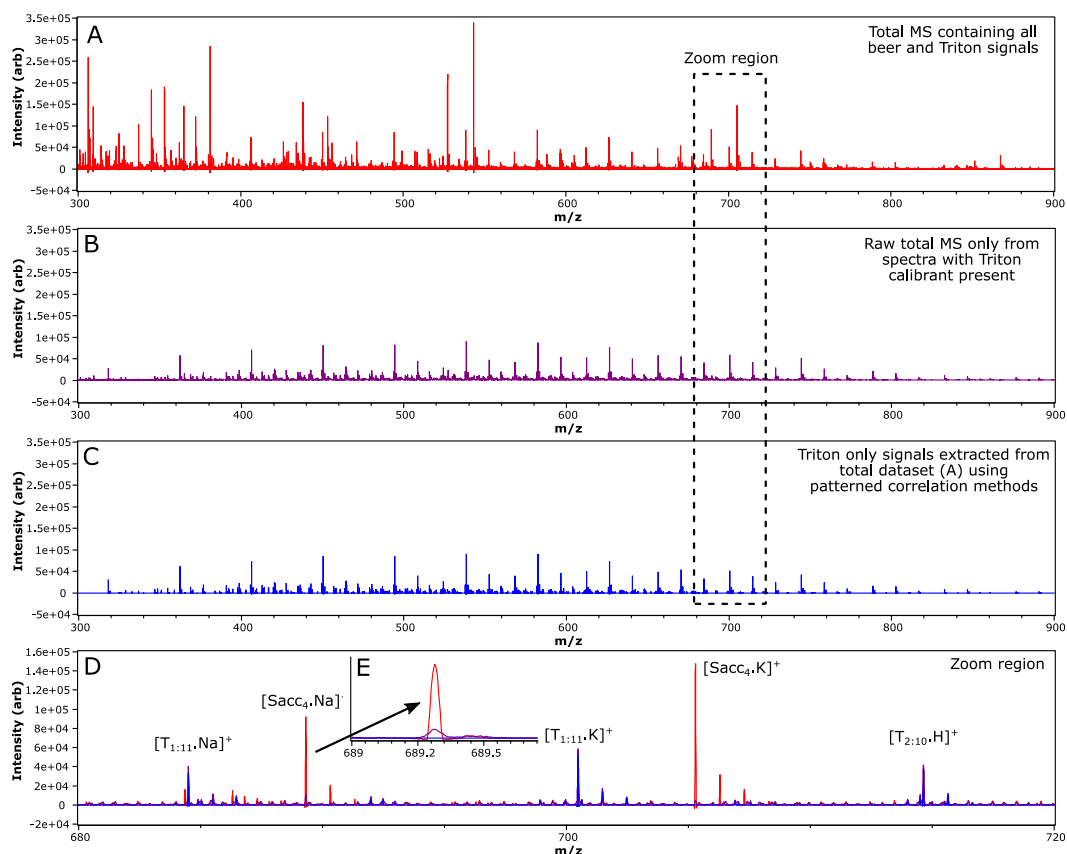


Figure 84 - Automatic Peak Detection of Calibrant (Triton) from Analysis of Beer Samples using Beacon software

The calibrant peaks are then used to perform an internal recalibration algorithm across the entire mass spectrum. With each spike in calibrant used to calibrate all spectra until a new calibration spike is detected. Although there are various methods which can be used to visualize the calibrant signal, the best method to spot the calibrant pattern is through generation of a heat map, as shown in Figure 85. Here, the Y-axis shows the Spectrum # (time), whilst the m/z is plotted on the X-axis. The intensity of the heat map is generated through the intensity of the corresponding m/z peak, which gives a clear pattern akin to a beacon light flashing

on/off. Herein, the use of the PUPP system to perform internal encoded recalibration is shown for real world complex samples.

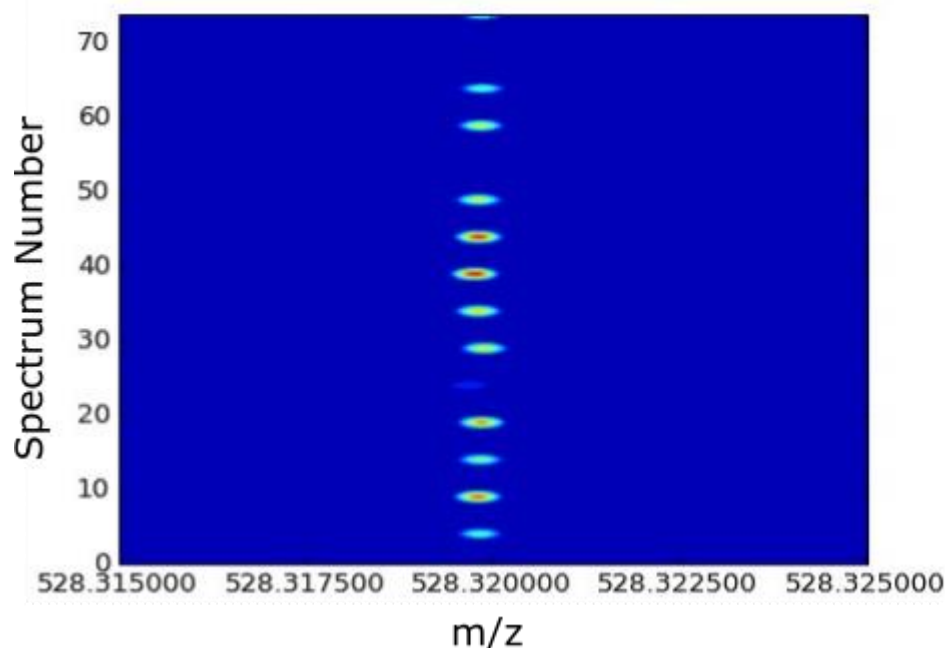


Figure 85 - Internal Calibrant Peak Intensity - "Beacon Effect"

4.1.1 Complex Organic Matter Analysis - Suwanee River Fulvic Acid

The Suwanee River, located in the Okefenokee National Wildlife Refuge (GA, USA) has a very high concentration of natural organic matter. The International Humic Substances Society (IHSS) collects samples of the river to create standards of the organic matter.¹⁴³ In the most recent sample collection in 2014, 36,890L of filtered river water were processed by reverse osmosis, cation exchange, freeze drying and homogenization to generate over 6 kg of organic matter.¹⁴⁴ Standards of the organic matter are available to purchase for analysis, and they have become a common sample reported for mass spectrometry due to the complex nature of the spectra obtained.¹⁴⁵⁻¹⁵¹

Experimental:

SRFA Standard II was purchased from the IHSS. The sample was prepared by dissolving in 50:50 ACN:H₂O to a final concentration of 0.1 mg/mL. The sample was directly infused using a syringe pump at 80 μ L/hr, through a 75 μ m ID Ground Fused Silica ESI Needle. Analysis was performed in negative mode, with the inlet held at +2200V, and the ESI needle grounded.

The Bruker solariX 12T FT-ICR was set with an ion accumulation time of 200 ms. To achieve maximum resolution the system was ran in 2ω mode. The ion source

was synchronized with the FT-ICR using a trigger system, the method for which is given in 3.4.3. The calibrant chosen was Triton QS-15, a PEG based series of polymers which give calibrant peaks across a wide mass range. This was prepared at 0.1 mg/mL in 50:50 H₂O:ACN. The Triton QS-15 solution was pipetted onto the PUPP manually, which was set to spray for 50 ms every 5th scan.

Results:

Figure 86 shows a spectrum for the SRFA sample and a spectrum containing SRFA and Triton. The peaks of Triton extend far beyond the region of interest for SRFA, however there are sufficient peaks within the mass range to perform confident mass recalibration.

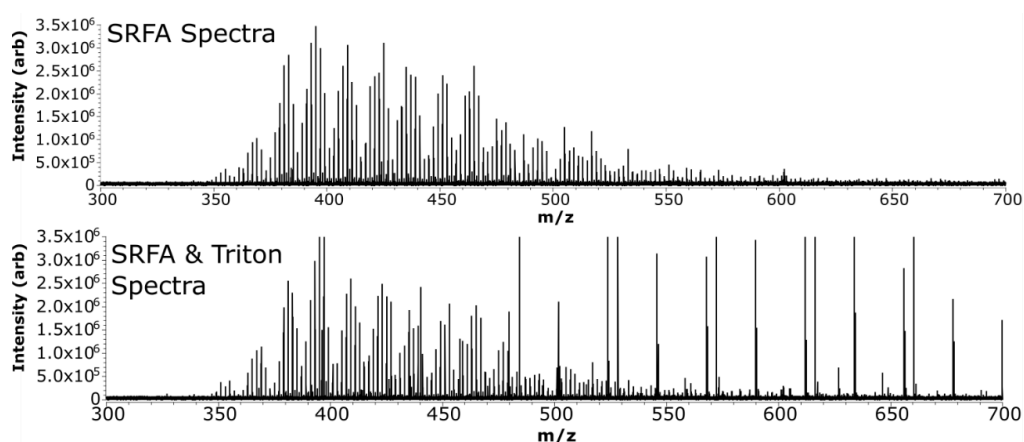


Figure 86 - SRFA spectra (Top) and SRFA spectra with Triton calibrant (Bottom)

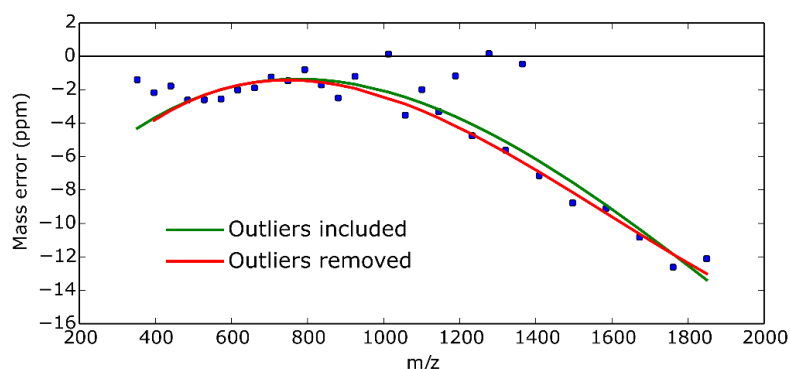


Figure 87 - Mass Error vs m/z plot for Triton QS-15 calibrant

Note: Two calibration curves are shown. The green curve includes the calibration points which do not match the overall trend of the calibration points. The red curve is the result when those outliers are removed.

Figure 87 shows the recalibration function generated by the Beacon software. In this example, the system has generated a second recalibration function whereby the outliers have been automatically removed. This recalibration function is applied to the whole mass spectrum. Figure 88 shows the mass errors obtained

for SRFA peaks identified using Autopiquer (part of the AutoVectis software package – Spectroswiss Sàrl, Lausanne, Switzerland) with and without internal encoded recalibration.¹⁵²

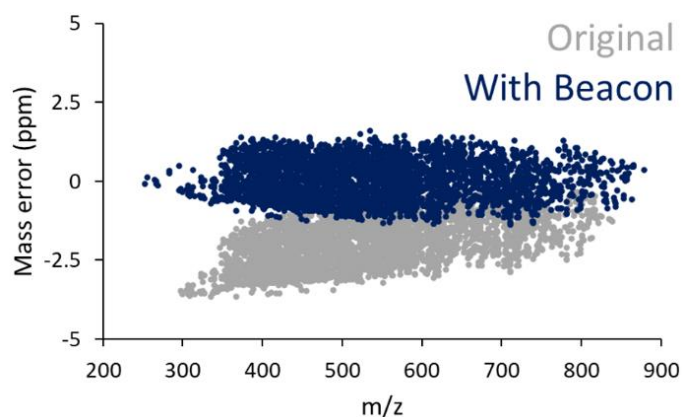


Figure 88 – SRFA - Mass error with and without encoded internal mass recalibration

4.2 Rapid Sample Analysis

In Chapter 1, a series of ionisation sources were presented which can perform rapid analysis of samples, such as DESI, AMI, and DART. Their ability to do this makes them suitable for a variety of high throughput applications, including reaction screening, reaction condition optimization and quality control.

The PUPP system can be used for the rapid analysis of a low number of samples where immediate screening feedback would be beneficial, such as in a synthetic chemistry lab for product confirmation. The system can be set up to manually load the sample onto the PUPP using an autopipette, triggering the PUPP spray mechanism for a user defined period of time. The system can then generate an averaged mass spectrum for this sample. This is how rapid screening was performed for all of the following applications discussed. In order to scale up the system to higher throughput, the introduction of a liquid handling robot would be necessary, which is discussed in Chapter 6. Herein, data is presented for the rapid analysis of Beer, Fruit Juice, Human Plasma and Pharmaceutical samples.

4.2.1 Rapid Sample Analysis - Beer

Beer contains a highly complex mixture of inorganic salts, carbon dioxide, alcohols and more than 800 organic compounds, with many of these organic compounds make up characteristics of the flavor of the beer.^{153,154} During the brewing process, long-chain polysaccharides from the grain are hydrolyzed to form individual sugar units (glucose, sucrose and maltose) along with short chain oligosaccharides, which are typically between 3 and 10 sugar units long. The majority of the sugar units are then fermented into alcohol using yeast, leaving behind the longer

chained oligosaccharides which cannot be fermented by most yeast strains. The quantity and relative ratios of these different length oligosaccharides is a key component in many of the various characteristics of beer.

The ability to perform rapid fingerprint screening of beer is an important industrial process. It is a cost-effective method of screening the authenticity of products, which gives added confidence to consumers.¹⁵⁵ There have been a variety of methods which have been adopted to perform high throughput screening of beer varieties, including DART, Direct Infusion ESI, GC-IRMS, LC-MS, HPLC-UV-Vis and, FT-IR and Headspace GC-MS etc.¹⁵⁶⁻¹⁶³ The complexity of the sample data generated through these methods means that the majority of these studies rely on data analysis tools, such as Principal Component Analysis (PCA) to confidently assess the data generated.

Six bottled beers, of various classes (Stout, IPA, Ale), were purchased from a local supermarket. Prior to analysis, the samples were diluted 10-fold in 80:20 H₂O:MeOH + 0.1% FA. The PUPP-PESI set up was used for analysis. Samples were manually pipetted onto the PUPP, which was then manually activated to generate the sample plume. The sample plume was deposited onto an APCI needle, which caused the subsequent electro spray towards the MS inlet. Figure 89 shows the TIC obtained for the analysis of the samples, which was completed in under 2 minutes.

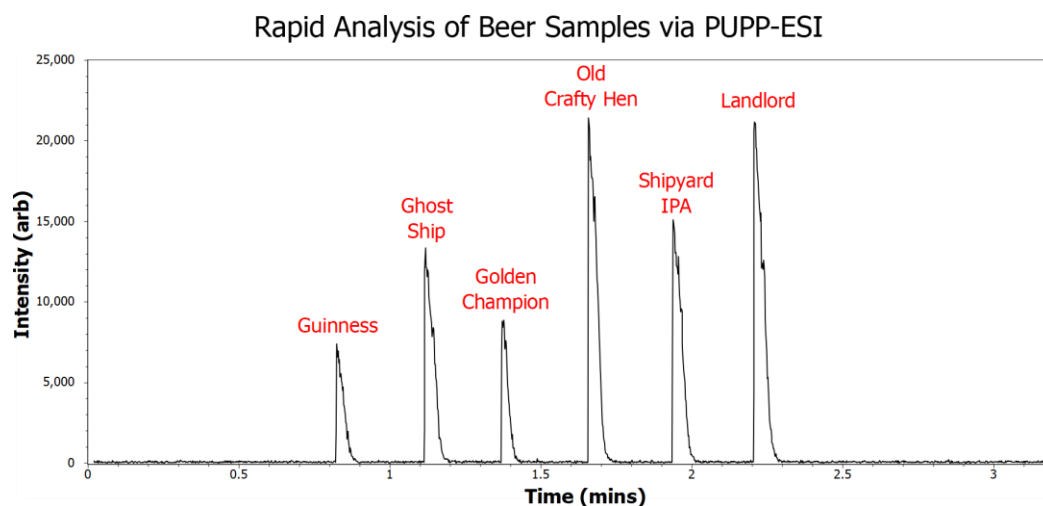


Figure 89 - TIC for Rapid Analysis of Beers

Average spectra were generated for each beer by summing the spectra generated across the sample peak width. Figure 90 shows a spectrum collected for one of the beers with the oligosaccharide components labelled, this data is also shown in Table 16 in the Appendix.

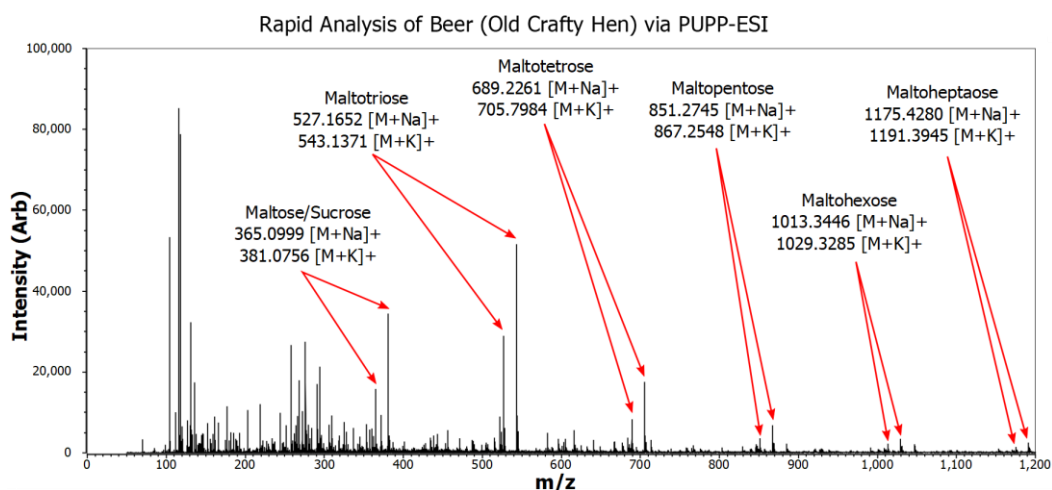


Figure 90 - Extracted Spectrum for "Old Crafty Hen" Sample taken during Rapid Analysis testing

To demonstrate the quality of the data obtained via the PUPP system, 29 beer samples (15 Pale, 9 Dark and 5 Malt) were purchased from local supermarkets and online stores, these were analysed by both ESI and PUPP-PESI. Principle component analysis (PCA) was then performed to determine if the data was of sufficient quality to group light, dark and malt beers. PCA has been used previously to distinguish between these beer types before using electrospray ionisation.¹⁵⁴

Beer samples were diluted 10-fold in 80:20 H₂O:MeOH + 0.1% FA before analysis. For electrospray analysis, the samples were infused at 100 µL/min. PUPP analysis was performed using the PUPP-PESI style set up (see 3.2.2) with an APCI needle as the probe. Spectra were generated by taking an average. PCA was performed using software specially developed in LabVIEW (see Chapter 5), using the Machine Learning Toolkit. Average spectra were generated for each sample, which were normalized to reduce any influence of overall intensity and focus on the relative distribution of peaks in the spectra. The results of both PCA analysis tests are shown in Figure 91 and Figure 92.

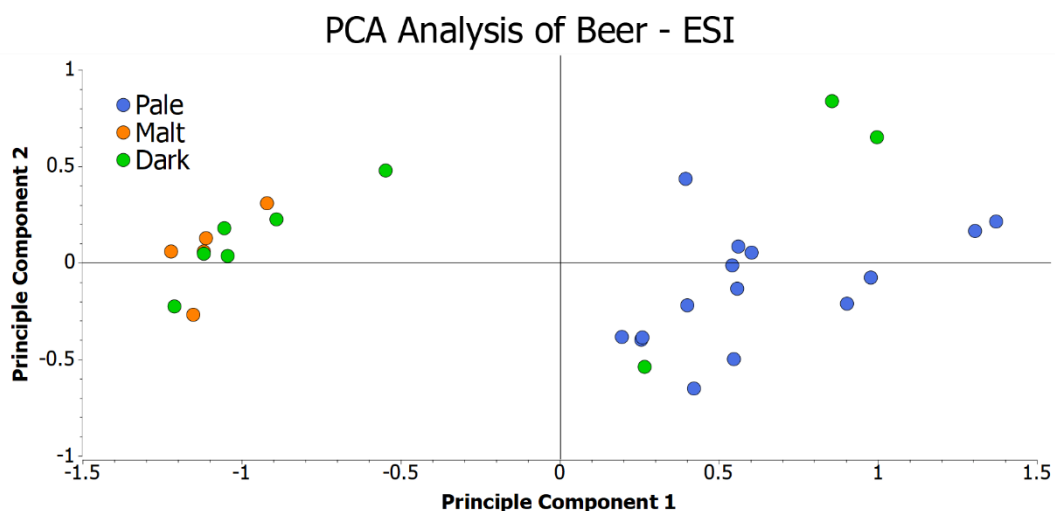


Figure 91 - PCA Analysis of Beer via ESI

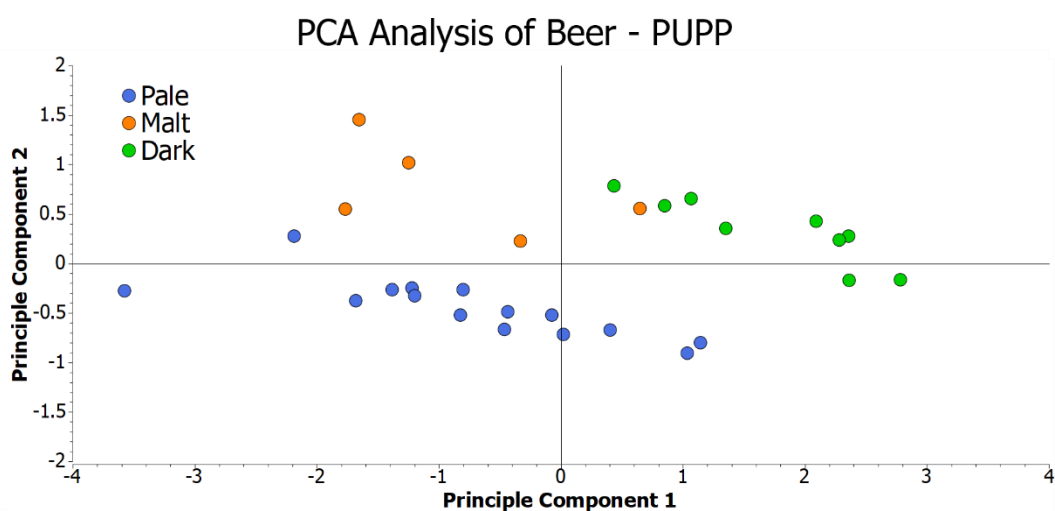


Figure 92 - PCA Analysis of Beer via PUPP

As shown, the PUPP data shows a good ability to distinguish between the different beer types, akin to that shown in the literature.¹⁵⁴ Unlike in the ESI spectra collected during this study, the malt and dark beers are mostly distinguishable from one another via the PUPP PCA analysis, however, there still remains some overlap between the two. Further development of the system, the addition of sample clean up methods and introducing more data into the PCA analysis would allow the system to better distinguish between dark and malt beers.

4.2.2 Rapid Sample Analysis – Juice

As mentioned, ambient ionisation techniques are being more frequently shown to be an effective screening method to ensure the highest standards of food/drink safety and authenticity. Beverages are routinely screened for pesticides, illegal additives, and dyes by mass spectrometry.¹⁶⁴⁻¹⁶⁷ Most frequently however these methods use sample extraction/clean up and separation techniques for analysis,

in part because of the complex sample matrix and low sensitivity for residues necessary. Ambient mass spectrometry systems offer an alternative, whereby samples can be analysed directly with minimal sample extraction/clean up. To demonstrate the potential ability of the PUPP-PESI system to perform rapid analysis of samples, a series of juice concentrate samples were analysed to show the speed and range of standard compounds found in fruit juices detected using the system.

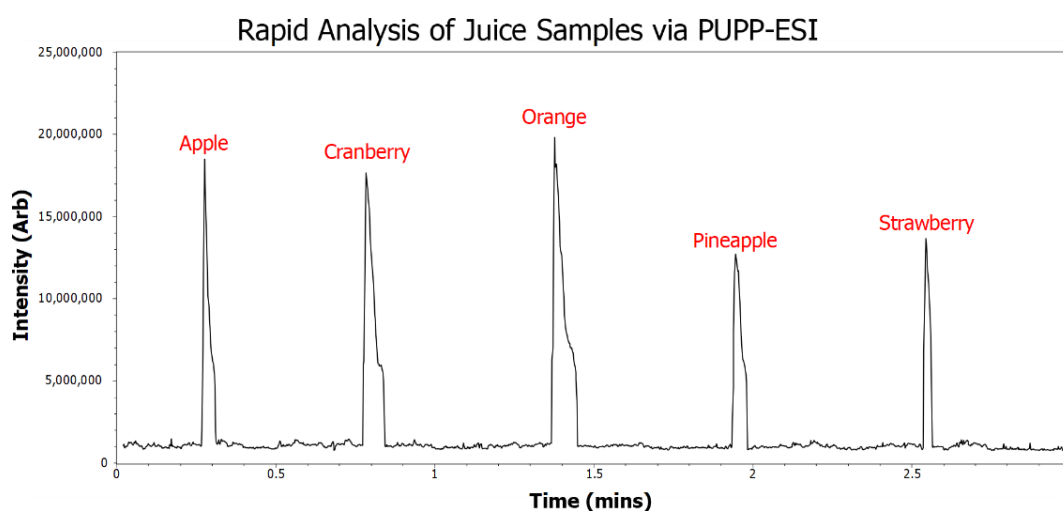


Figure 93 - TIC for the Rapid Analysis of Juices

A series of juice concentrate samples (Apple, Cranberry, Orange, Pineapple and Strawberry flavors) were analysed via the PUPP system to further demonstrate the rapid analysis potential of the ion source. The samples were diluted 100-fold in 50:50 H₂O:MeOH + 0.1% FA. 5 μ L of each juice sample was manually transferred onto the PUPP via pipette, the entire volume of which was subsequently sprayed for analysis. The resulting TIC can be seen in Figure 93, average mass spectra were generated over the period for which the piezo was active, and subsequently analysed. The peaks identified for Orange Juice have been shown in Table 5 as an example, and a region of the spectra obtained for this sample has been given in Figure 94.

Table 5 - Orange Juice - Compounds Identified		
m/z	Component	Adduct
144.0939	Proline Betaine	[M+H] ⁺
273.0780	Naringenin	[M+H] ⁺
130.0795	N-methyl-proline	[M+H] ⁺
182.0489	Tyrosine	[M+H] ⁺

203.0455	Glucose	[M+Na] ⁺
219.0213	Glucose	[M+K] ⁺
277.1000	Glucosylglycerol	[M+Na] ⁺
365.1077	Maltose/Sucrose	[M+Na] ⁺
381.0796	Maltose/Sucrose	[M+K] ⁺
409.1874	Ethylmaltoside	[M+K] ⁺
527.2823	Maltotriose	[M+Na] ⁺
543.1371	Maltotriose	[M+K] ⁺
689.2261	Maltotetraose	[M+Na] ⁺
705.2432	Maltotetraose	[M+K] ⁺

Again, the system shows its capability at performing rapid screening of samples with complex matrices minimal sample preparation. However, further studies in this area would need to take a more focused look at whether the system gave the required sensitivity to perform screening on a more targeted approach, such as pesticide residue analysis. Most pesticide residue analysis methods use an extraction technique when performing analysis at such low concentrations (sub mg/kg levels), and rapid techniques such as QuEChERS (quick, easy, cheap, effective, rugged, and safe) may be best suited for this system to maintain speed of analysis whilst maximizing sensitivity.

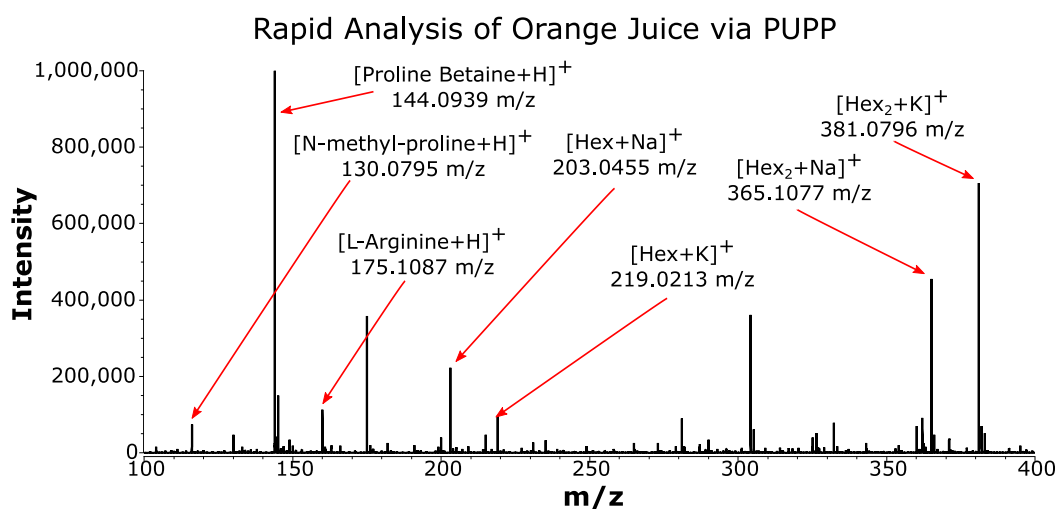


Figure 94 - Extracted Spectrum for Orange Juice Sample taken during Rapid Analysis

4.2.3 Rapid Sample Analysis – Human Plasma

Rapid analysis within a clinical setting has enormous potential benefits for laboratories, clinicians and most importantly patients. The turnaround time for laboratory results in many settings can have a direct impact in the quality-of-care

patients receive, and therefore the demand for rapid testing methods and instrumentation is increasing.¹⁶⁸ Ambient mass spectrometry has been shown to be an efficient method of doing this for several clinical applications, perhaps most notably the introduction of the rapid evaporation ionization mass spectrometry (REIMS, or iKnife) system which can be used in-vivo for rapid diagnosis of tissue during surgery.¹⁶⁹⁻¹⁷¹

Therefore, it felt necessary to demonstrate that low volumes of biological sample could be analysed via the PUPP system. Human plasma was selected for this, with the aim of identifying and characterizing some of the major glycerophospholipids present. Abnormal lipid metabolism is related to a number of diseases, including cancers, type II diabetes and Alzheimer's. DESI, MALDI, REIMS and PESI have all previously been successfully used to characterize the structure of glycerophospholipids in various biological samples.¹⁷²⁻¹⁷⁷

Although further studies focusing on the use of the PUPP system for identifying abnormal lipid behavior for specific diseases would be needed, the focus of this project is to show evidence that the PUPP system would be suitable for the rapid analysis of lipids in a complex biological sample such as plasma.

Experimental:

Human plasma was analysed on a Q-Exactive HF Orbitrap Mass Spectrometer. The transient length was 256 ms, automatic gain control (AGC) was used with a maximum ion accumulation time of 300 ms. No sample preparation was performed on the plasma. 10 μ L of plasma was transferred onto the PUPP by pipette, and the piezo was switched on to spray the entire sample (approximately 25 seconds). Beer was infused at 7 μ L/min through an ESI needle, and this would be used to retrospectively perform an internal mass recalibration on the results. An average spectrum was taken across the region where the piezo was active for processing.

Results

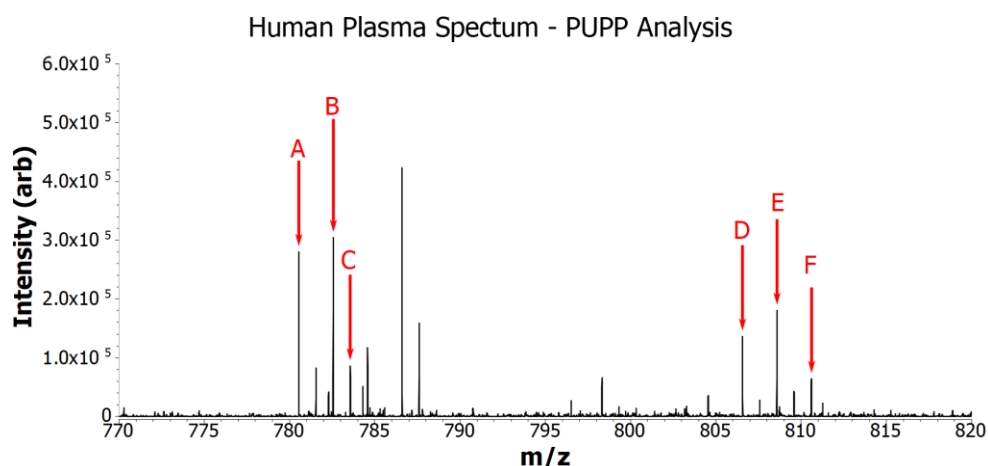


Figure 95 - Human Plasma Spectra - Lipid Peaks Identified

The spectra obtained from the plasma sample can be seen in Figure 95 with the lipid peaks identified labelled, the corresponding assigned molecular formula for each peak can be seen in Table 6. Although fragmentation data was not collected during the PUPP analysis, a sample of the plasma was subsequently subjected to MS/MS analysis via ESI using an Exploris 480 Orbitrap system. The extraction method and MS/MS spectra are available in the Appendix. Extraction and analysis were performed by collaborators at Maastricht MultiModal Molecular Imaging Institute (M4i), Maastricht University. This data has been subsequently used as complimentary data to confirm the identity of the lipid species observed via the PUPP. Internal recalibration of the data was performed using the beer solution which was continuously sprayed through the ESI needle, this recalibration has been shown in the appendix.

Table 6 - Human Plasma - Lipid Peaks Identified

ID	Peak mass (m/z)	Lipid Type	Assignment	Formula	Mass Error (ppm)
A	780.5504	Glycerophospholipid	PC 34:2	C ₄₂ H ₈₀ NO ₈ PNa	2.412
B	782.5684	Glycerophospholipid	PC 34:1	C ₄₂ H ₈₂ NO ₈ PNa	0.429
C	784.5841	Glycerophospholipid	PC 34:0*	C ₄₂ H ₈₄ NO ₈ PNa	-0.015
D	806.5684	Glycerophospholipid	PC 36:3	C ₄₄ H ₈₂ NO ₈ PNa	1.331
E	808.5816	Glycerophospholipid	PC 36:2	C ₄₄ H ₈₄ NO ₈ PNa	2.012
F	810.5997	Glycerophospholipid	PC 36:1	C ₄₄ H ₈₆ NO ₈ PNa	0.469

**Note: Fragmentation data not available for this peak due to other peaks being within the precursor isolation window. PC = Phosphatidylcholine*

4.2.4 PUPP-PESI - Sequential Ionisation Effect

Sequential Ionisation is an effect observed in conventional PESI, which has also been observed when in some cases when analysing samples using the PUPP-PESI. Sequential ionisation describes how analytes are sprayed sequentially based on their surface activity, surface active analytes are sprayed initially, whilst ions with a lower surface activity remain behind in the main droplet on the probe.¹⁷⁸ Over a short space of time, once the high surface activity analytes become depleted, analytes with a lower surface activity begin to spray.

This effect is clearly observed when using the PUPP to rapidly dispense samples onto certain probes held at high voltage. Figure 96 shows the extracted ion chromatogram for different ions observed in the beer sample, and Figure 97 (also shown as a waterfall plot in the appendix) shows how the spectra changes over time. Initially, contaminant surfactants and other molecules are visible, but within just over one hundred milliseconds the profile of the mass spectrum changes completely, and the sugars present in beer, a much lower surface-active set of molecules, dominate the spectrum. This effect was only observed when investigating acupuncture needles (No.02, \varnothing 0.12 x 30 mm) and hypodermic needles as potentially low cost and readily available PESI probes. The literature observes that this effect is commonly observed for titanium needles (such as acupuncture needles), which is attributed towards their rough surface.

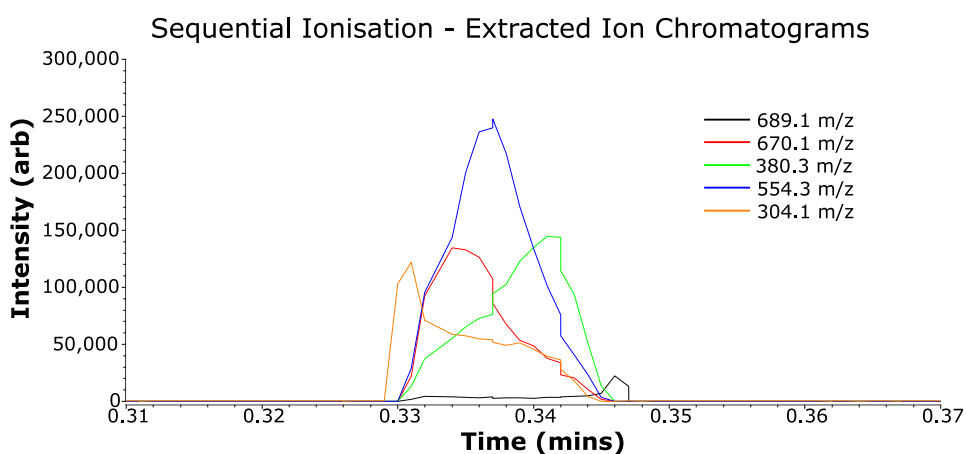


Figure 96 - Extracted Ion Chromatograms showing the sequential ionisation of analytes

Sequential ionisation allows for the analysis of typically less surface-active molecules whilst avoiding the suppression surface active molecules. By comparison for example, when performing the analysis of beer via conventional

ESI, the relative intensity of longer chained oligosaccharides is much lower compared to the intensities obtained via PUPP-PESI.

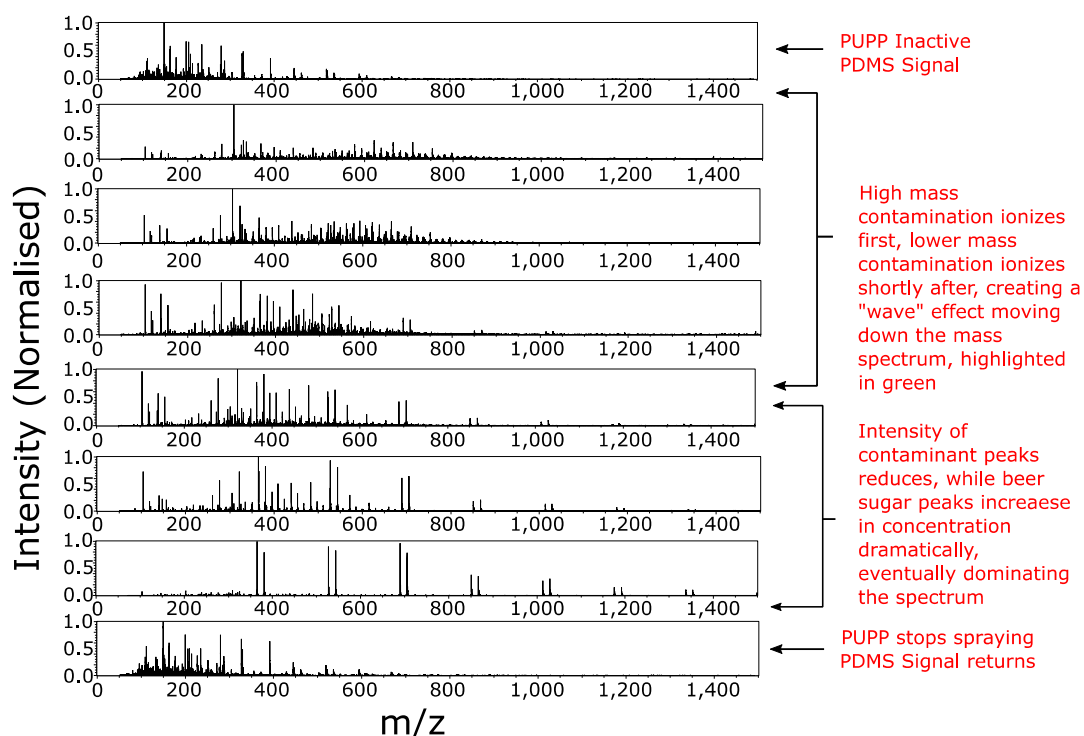


Figure 97 - Sequential Ionisation Effect

4.2.5 Carryover Effect

The major limitation of the PUPP system is the carryover effect observed. There are two possible causes for carryover using this system: carryover originating from the PUPP itself and carryover originating from contamination of the needle.

Figure 98 shows the carryover when performing the rapid analysis on a series of juices, using the PUPP system combined with an APCI needle. An extracted ion chromatogram is shown for one of the sugar peaks, with the blank performed at the beginning giving a negligible signal as expected. After the subsequent analysis of five juice samples, the PUPP is rinsed with a wash solvent, before reanalysis of a blank sample. The intensity of the blank is significantly greater than before the juice samples were analysed, and only returned to the expected level after the 10th spray is performed.

The PUPP system developed by Forbes et al. discussed in Chapter 3 also suffered from carryover issues, and spray of 5 blank samples between "live" samples was used to minimize this effect.¹³³ Similar methods would be necessary for this system to avoid carryover, which would be detrimental to high throughput analysis of samples. Although a manual cleaning method of spraying a blank sample multiple times was easily adopted for the analysis discussed in this thesis, a more

rigorous cleaning method would need to be adopted for high throughput analysis. This is discussed further in Chapter 6, where the capability of the system when coupled to liquid handling robot systems is discussed.

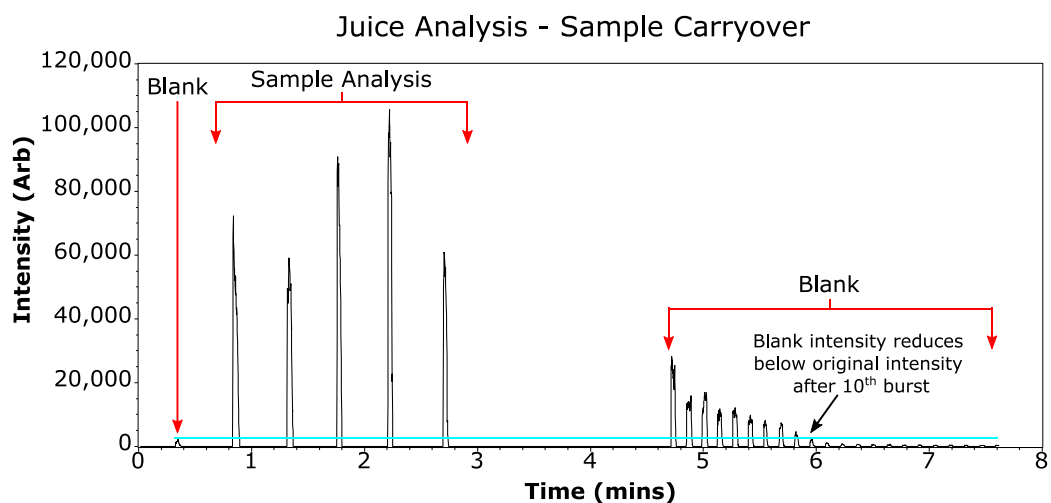


Figure 98 - Carryover effect observed during rapid analysis of juices

4.2.6 PUPP-PESI Polysiloxane Background Signal

When performing rapid analysis using the PUPP-PESI set up with a hypodermic needle as the probe, it was noticed that when the PUPP system was inactive, a spectrum was obtained which did not match that of any sample analysed previously. Figure 99 shows the spectra obtained, and the Polysiloxane series which the peaks were identified to. This signal was not observed for the other needle types tested during this project, such as APCI, sewing needle and acupuncture. The spectrum clearly shows a pattern of peaks which are 74 Daltons apart, which is attributed as the siloxane $[\text{Si}(\text{CH}_3)_2\text{O}]_n$ series.

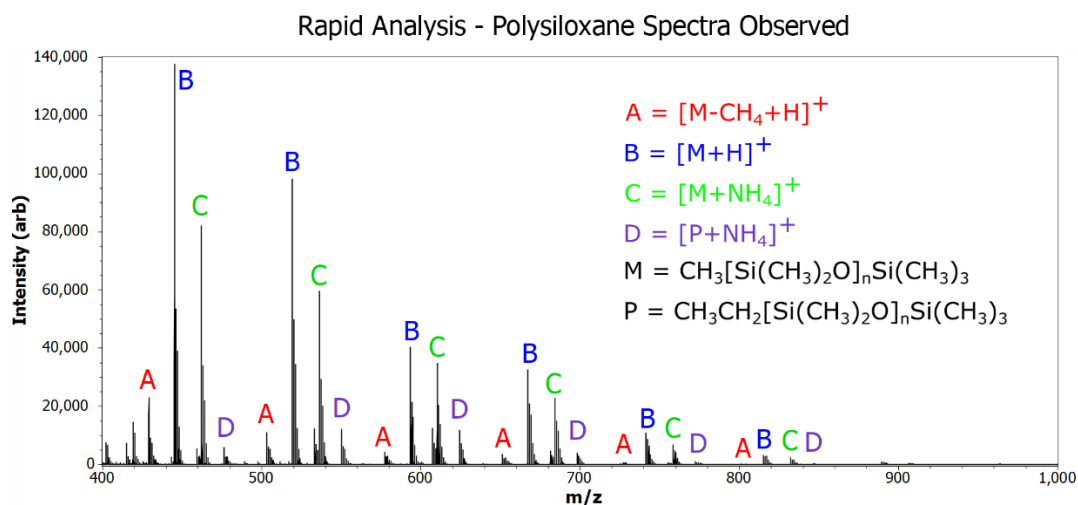


Figure 99 - Polysiloxane Contaminant Spectra

The source of this contamination was initially unclear, and work was conducted to establish the cause. This included testing various different types of needles (see Chapter 3) and a thorough cleaning of the Q-TOF ion source and step-wave, both of which made no impact on the strength of the signal obtained. The compounds identified in the spectra have however previously been reported as a contaminant when performing ambient mass spectrometry.¹⁷⁹ Work by Schlosser and Volkmer-Engert presented the contamination of nanospray signals which interfered with the analysis of peptides. Their work attributed the signal as contamination from the external laboratory environment, where cyclic siloxanes are used in cosmetic products (e.g., deodorants or hair products), air conditioning systems and paints used on walls.¹⁷⁹

The signal detected during our rapid analysis experiments was only present when the PUPP was inactive, and therefore can be attributed to being when the needle is dry. This suggests that the contamination is occurring through a form of corona discharge, identical to that observed in the Scholler and Volkmer-Engert study. Two methods were employed in their study to eliminate the signal given by the siloxane compounds, the first of which was to reduce the distance between the nanospray tip and the instrument inlet from 1 cm to 1 mm. Reducing the distance between the needle and the inlet induces electrical discharge before any change in the siloxane signal is observed.

The second method was to use a flow of nitrogen gas and have the nanospray tip perpendicular to the MS inlet. This is not possible when using the PUPP with a needle for probe electrospray, as the gas flow would detrimentally interfere with the flow of the PUPP microdroplets.

The presence of PDMS peaks does not adversely affect the spectra obtained when the PUPP is active and sample is being analysed, and therefore does not present a significant problem which needs to be overcome. Instead, as the molecular formula of the siloxane peaks has been identified, the peaks obtained can be used to perform internal recalibration in a similar manner for the encoded internal recalibration, the results of which can be seen in in Figure 100 for the rapid analysis of beer samples. The improvement in mass accuracy is clear, however, as this signal is caused by the laboratory environment, this is not a practical consideration for the ion source, and instead internal recalibration should be performed using a dual PUPP system onto a needle, with one PUPP delivering sample and another delivering calibrant.

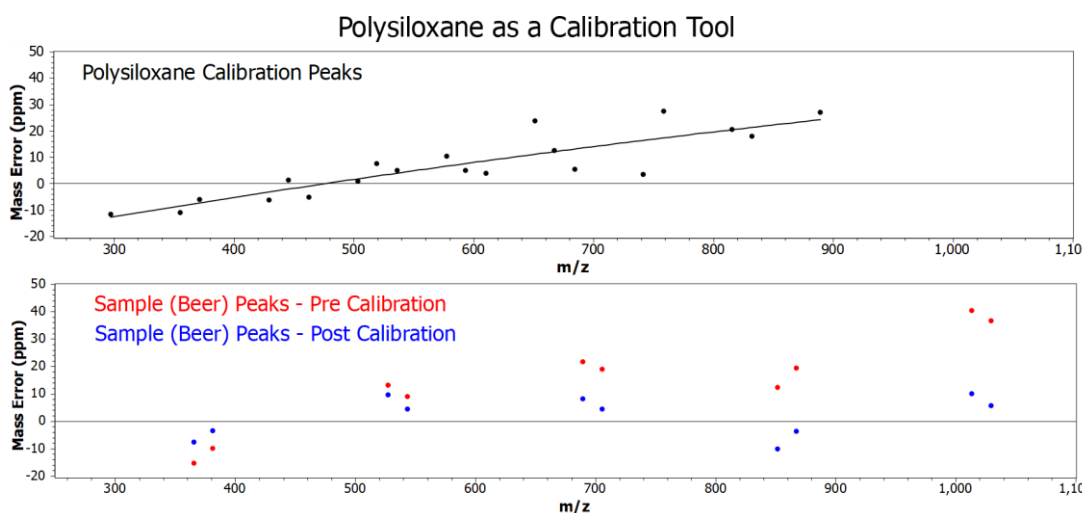


Figure 100 - Using Polysiloxane Contamination as a Calibration Tool

4.2.7 Rapid Analysis - BMSS Ambient Ionisation Study

As shown during Chapter 3, the PUPP system can be used as a standalone ionisation source without the need for any additional mechanism of ionisation. In order to test the sensitivity and repeatability of the system, the ionisation source was tested as part of a collaboration with the University of Surrey. The system was benchmarked as a standalone ionisation source by performing analysis that followed the protocols given in the British Mass Spectrometry Society (BMSS) Ambient Ionisation Special Interest Group Interlaboratory Study II.^{180,181} This study was set up by the BMSS in order to give an overview on the robustness and repeatability of different ambient ionisation sources.

ASAP, DART, DESI, LESA, SESI, TD-CDI, AP-MALDI and Paperspray were all tested, with some having more than one dataset submitted. These ionisation sources were each tested on different instrumentation too, including Orbitrap, TOF, Q-TOF, Single Quadrupole and Triple Quadrupole instruments. Further details on the ionisation sources studied are summarized in Table 21 in the Appendix. The PUPP data work was not collected as part of the study itself, which took place before the PUPP project began, but this data collected following the study protocol and retrospectively compared to the data presented in the report itself.

Spare sample vials not used by one of the participant institutions of the study were donated for the purposes of analysis using the PUPP system. The study used two samples, each containing the same 8 small organic molecules (see Table 18 in the appendix). One sample was prepared in acetonitrile and the other in Surine, a synthetic urine matrix. The two mixtures were analysed on a Thermo Q-Exactive

Orbitrap and a Waters Xevo G2-XS Q-TOF using the same setup in order to provide some interlaboratory comparison of the PUPP data.

Each solution was set to spray directly into the MS inlet, and average chromatograms were taken across the region where the PUPP was active. Figure 101 shows a summary of which compounds were detected using different ionisation sources. The PUPP system performed well relative to other ionisation sources, detecting 7 out of 8 analytes using the Orbitrap and Q-TOF. The exception was Ibuprofen, which could only be detected using negative mode on the Orbitrap, and was not detected at all using the Q-TOF. The poor detection of Ibuprofen was observed for many other ionisation sources (particularly spray-based techniques), and the report attributes this due to the low gas phase basicity of Ibuprofen relative to other analytes.

Summary of Ion Source Analyte Detection using Acetonitrile Solutions									
Institute	Ion Source	Para	Para-d ₄	Ibu	Diclo	Colch	Terf	Reser	Eryth
AIS03	ASAP	Green	Green	Green	Green	Green	Green	Green	Red
AIS04	DART	Green	Green	Green	Green	Green	Green	Green	Green
AIS05	ASAP	Green	Green	Green	Green	Green	Green	Green	Green
AIS06	TD-CDI	Green	Green	Green	Green	Green	Green	Green	Red
AIS08	DART	Green	Green	Green	Green	Green	Green	Green	Green
AIS09	Paperspray	Yellow	Yellow	Yellow	Yellow	Green	Green	Green	Green
AIS11 A	ASAP	Green	Green	Red	Green	Green	Green	Green	Red
AIS11 B	ASAP	Green	Green	Green	Green	Green	Green	Green	Green
AIS12	LESA	Green	Green	Red	Green	Green	Green	Green	Green
AIS13	ASAP	Green	Green	Green	Green	Green	Green	Green	Green
AIS14 A	ASAP	Green	Green	Green	Green	Green	Green	Green	Green
AIS14 B	ASAP	Green	Green	Green	Green	Green	Green	Green	Green
AIS14 C	SESI	Green	Green	Red	Green	Green	Green	Green	Green
AIS14 D	ASAP	Green	Green	Green	Green	Green	Green	Green	Green
AIS14 E	ASAP	Green	Green	Green	Red	Green	Green	Green	Green
AIS16	ASAP	Green	Green	Green	Green	Green	Green	Green	Red
AIS19	DESI	Green	Green	Red	Green	Green	Green	Green	Green
AIS20 A	DART	Green	Green	Green	Green	Red	Red	Red	Red
AIS20 B	DART	Green	Green	Green	Green	Green	Green	Red	Red
AIS23	DART	Green	Green	Red	Green	Green	Green	Green	Green
AIS24	AP-MALDI	Yellow	Yellow	Red	Red	Green	Green	Green	Green
Orbitrap	PUPP	Green	Green	Blue	Green	Green	Green	Green	Green
Q-TOF	PUPP	Green	Green	Red	Green	Green	Green	Green	Green

Figure 101 - BMSS Solution Analysis - Pharmaceutical Mixture in Acetonitrile

Note: Green = Detected, Yellow = Interfered Species, Red = Not Detected, Blue = Detected in negative mode only

The data also follows a similar trend for the Surine analysis. The matrix suppression causes many of the compounds to not be detected relative to the acetonitrile solution, and a similar effect is observed for the PUPP system. The Orbitrap data showed that the same 7 analytes could be detected, but the

protonated species suffered a significant matrix suppression. However, for the majority of the analytes, detection of Sodium and/or Potassium adducts was observed. Table 19 and Table 20 in the appendix give a full list of the ions detected for both the Acetonitrile and Surine samples for the Orbitrap data.

Summary of Ion Source Analyte Detection using Surine Solutions									
Institute	Ion Source	Para	Para-d ₄	Ibu	Diclo	Colch	Terf	Reser	Eryth
AIS03	ASAP	Green	Green	Red	Red	Green	Green	Green	Green
AIS04	DART	Green	Green	Red	Red	Green	Green	Red	Green
AIS05	ASAP	Green	Green	Red	Green	Green	Green	Green	Green
AIS06	TD-CDI	Green	Green	Red	Red	Green	Green	Green	Red
AIS08	DART	Negative	Negative	Green	Green	Green	Green	Green	Green
AIS09	Paperspray	Yellow	Yellow	Yellow	Yellow	Yellow	Green	Yellow	Yellow
AIS11 A	ASAP	Green	Green	Red	Red	Red	Green	Green	Red
AIS11 B	ASAP	Green	Green	Green	Green	Green	Green	Green	Green
AIS12	LESA	Red	Red	Red	Red	Green	Green	Green	Green
AIS13	ASAP	Green	Green	Red	Green	Green	Green	Green	Green
AIS14 A	ASAP	Green	Green	Red	Green	Green	Green	Green	Green
AIS14 B	ASAP	Green	Green	Red	Green	Green	Green	Green	Green
AIS14 C	SESI	Green	Green	Red	Green	Red	Green	Green	Green
AIS14 D	ASAP	Green	Green	Red	Red	Green	Green	Green	Green
AIS14 E	ASAP	Green	Green	Red	Red	Red	Green	Green	Green
AIS16	ASAP	Green	Red	Red	Green	Green	Green	Green	Green
AIS19	DESI	Red	Red	Red	Red	Green	Green	Red	Red
AIS20 A	DART	Green	Green	Red	Red	Red	Red	Green	Red
AIS20 B	DART	Green	Green	Red	Red	Red	Green	Red	Red
AIS23	DART	Red	Red	Red	Red	Green	Green	Green	Green
AIS24	AP-MALDI	Yellow	Red	Red	Red	Green	Green	Green	Green
Orbitrap	PUPP	Green	Green	Red	Green	Green	Green	Green	Green
Q-TOF	PUPP	Red	Red	Red	Red	Green	Green	Green	Green

Figure 102 - BMSS Solution Analysis - Pharmaceutical Mixture in Surine

Note: Green = Detected, Yellow = Interfered Species, Red = Not Detected, Blue = Detected in negative mode only

As mentioned, one of the main aims of the BMSS study was to assess the repeatability of different ambient ionisation techniques. This was done by each institute analysing the same sample several times over three days. This experiment was repeated for the PUPP to assess the repeatability and to enable comparison against other ionisation techniques. Average spectra were generated across the region of highest intensity. Analysis was performed 5 times on each day, over three consecutive days. The same instrument settings were used for each analysis, and a fresh vial was used for each day's analysis as per the protocol of the report. The report explains that the participating labs had the option to submit chromatograms, for which the repeatability was assessed by extracted ion chromatogram peak area, or processed spectra, for which spectral peak intensity was used. The PUPP generates a continuous spray, and therefore an integrated

peak area could not be used. Therefore, processed average mass spectrum were used for all repeatability tests.

Sample 1 - Paracetamol Intra-Day Repeatability

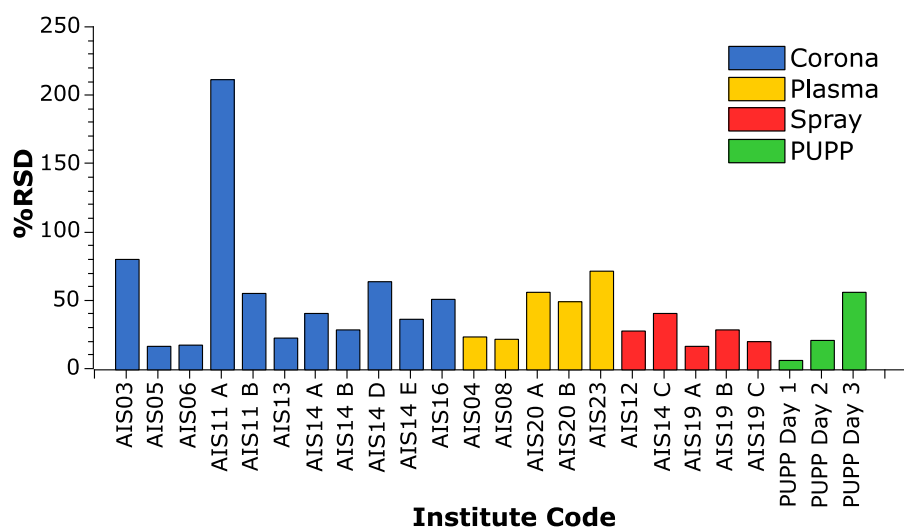


Figure 103 - Paracetamol in Acetonitrile - Intra-Day repeatability

Figure 103 shows the intra-day repeatability for paracetamol compared to the other ionisation sources. The data collected for the PUPP is shown for each day, for which a clear day to day variation could be observed. There are a number of factors which likely contributed towards this variability – including day to day variations in the position of the PUPP and the consistency of the spray plume entering the inlet due to air flows in the lab environment. Repeatability for three other analytes (Terfenadine, Diclofenac and Reserpine) are given in the appendix, which all show similar results to the paracetamol data.

However, the BMSS report notes that variability between instruments is difficult to compare because of the differences in sample preparation, instrument, techniques and whether integrated peak area of spectral peak intensity were used. However, a fairer comparison can be drawn for the ratio of Paracetamol to Paracetamol-d₄ in the spectrum. The intra-day repeatability of this ratio is shown in Figure 104, and the inter-day repeatability in Figure 105.

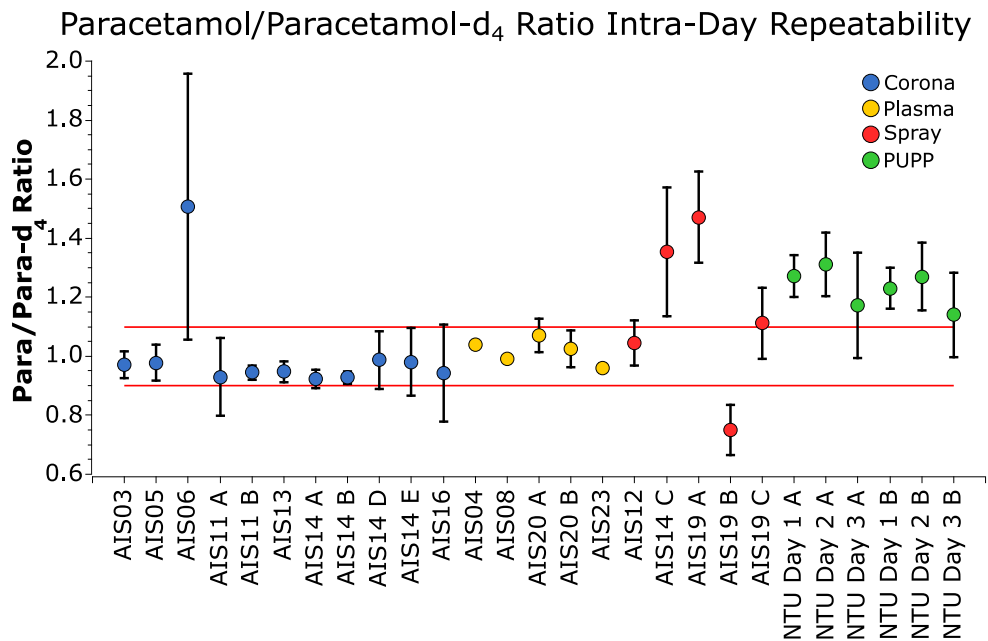


Figure 104 - Paracetamol/Paracetamol-d₄ Ratio - Intra-Day Repeatability
Note: Consensus range is indicated by red lines (1.01 ± 0.06)

The Paracetamol/Paracetamol-d₄ ratio for the PUPP is consistently higher than the majority of the ambient ionisation sources. However, this is also observed for other spray-based techniques (red), where there is a significant variability and outside of the range of the report consensus value. Within the BMSS report, it is noted that this is due to a variability in the observed intensities of the [M+H]⁺ and [M+Na]⁺ species. AIS19 A uses the [M+H]⁺ species only, AIS19 B is the [M+Na]⁺ only, which both fall outside the consensus value. When the combined intensity of the two species is used however, the observed ratio is much closer to the consensus value. This effect is also observed for the PUPP system for both the intra-day (Figure 104) and inter-day (Figure 105) data. PUPP dataset A uses the ratio of the [M+H]⁺ species, whilst PUPP dataset B shows the ratio of the summed [M+H]⁺ and [M+Na]⁺ species. Using the ratio brings the value closer to the consensus, but it is still outside of the specified range (1.01 ± 0.06).

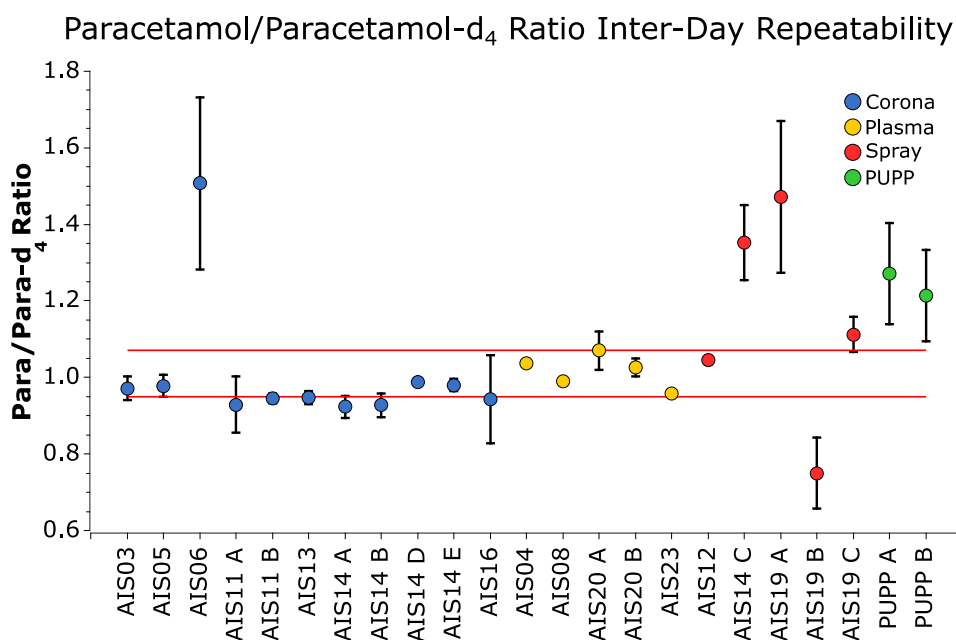


Figure 105 - Paracetamol/Paracetamol-d₄ Ratio - Inter-Day Repeatability
Note: Consensus range is indicated by red lines (1.01 ± 0.06)

Overall, the PUPP system performed well, particularly when compared to other spray-based ambient ionisation techniques. The PUPP showed good levels of sensitivity, and only failed to detect the Ibuprofen in the acetonitrile sample. The Surine sample caused matrix suppression which meant that 4 of the analytes could not be detected using the Q-TOF, but the same 7 were still detected with the Orbitrap. The repeatability of the system was strong, although this data is less useful due to the variations in data reporting (intensity vs peak area) and instrument. However, the PUPP did perform well compared to other spray-based techniques when looking at the ratios of analytes to the internal standard (Paracetamol-d₄), indicating a good level of repeatability. The ratio obtained through the PUPP falls outside of the consensus range, however as mentioned in the BMSS study report this is a feature commonly observed using spray-based ionisation sources.

4.3 Adduct Modification

Tandem mass spectrometry is a vital tool in the analysis of both large and small molecules for the determination of their structure, or the structure of impurities, forced degradation products and metabolites. There are a variety of techniques available to perform this fragmentation, including collision induced dissociation (CID), surface induced dissociation (SID), electron capture dissociation (ECD), electron transfer dissociation (ETD) and infrared multiphoton dissociation (IRMPD).¹⁸²⁻¹⁸⁶

Through the differences in their mechanisms, different fragmentation patterns are observed for identical molecules. Obtaining as much structural information about a molecule by subjecting it to different fragmentation techniques would be ideal, but would be a highly time-consuming process, and is therefore not practical. The choice of adduct for an ion has a clear effect on the fragmentation pattern observed.¹⁸⁷⁻¹⁹⁴ The majority of this work is applied to polymers, which can be difficult to ionise or fragment, and therefore frequently require the sample to be manually doped with metals to generate the desired adducts. However, adduct induced changes in fragmentation patterns have also been observed for pharmaceutical and peptides.^{187,195}

The PUPP is capable of rapidly introducing solutions into an ESI stream, and therefore is capable modifying the composition of the solution being electrosprayed. In theory, this system can therefore be used to rapidly alter the charge carrying species of an analyte, by spraying solutions containing the target metal carrying species.

This effect was originally observed as an artefact of the early encoded internal recalibration system testing. During analysis, Beer was continuously electrosprayed, with an internal standard solution of Triton QS-15 being introduced in bursts via the PUPP. When observing the spectrum of the Beer, it became clear that when Triton was introduced to the sample, there was a shift in the relative intensities of the Sodium and Potassium adducts of the sugars, favoring the Sodium at the points when Triton was present. Figure 106 shows the ratio of Sodium to Potassium as a function of time, clear and consistent spikes in the ratio can be seen at regular intervals when the PUPP is active.

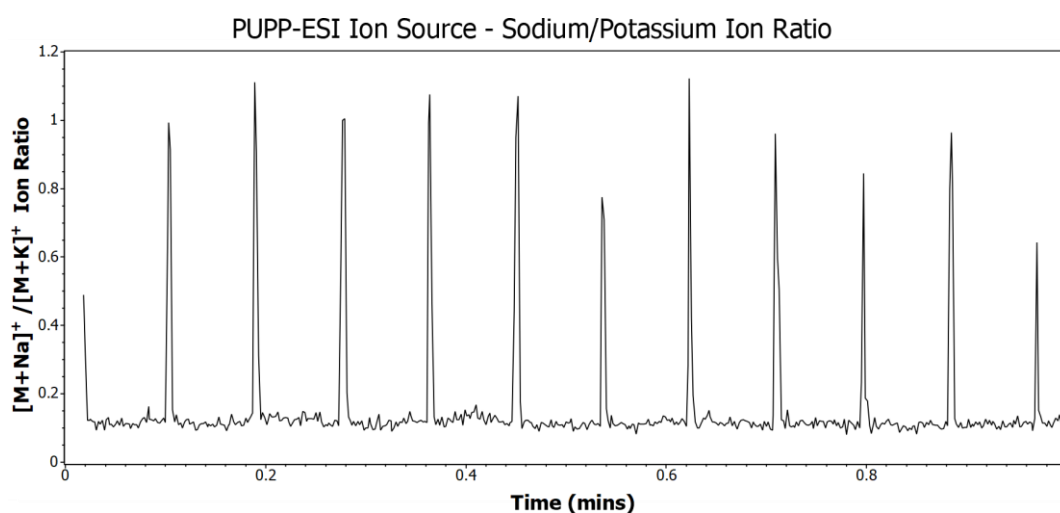


Figure 106 - PUPP-ESI Ion Source - Sodium/Potassium Adduct Ratio

Representative spectra for when the PUPP is inactive (left) and when the PUPP is active (right) are shown in Figure 107, which show a clear shift in the relative intensity of the Sodium adduct to the Potassium adduct for a sugar peak in the beer.

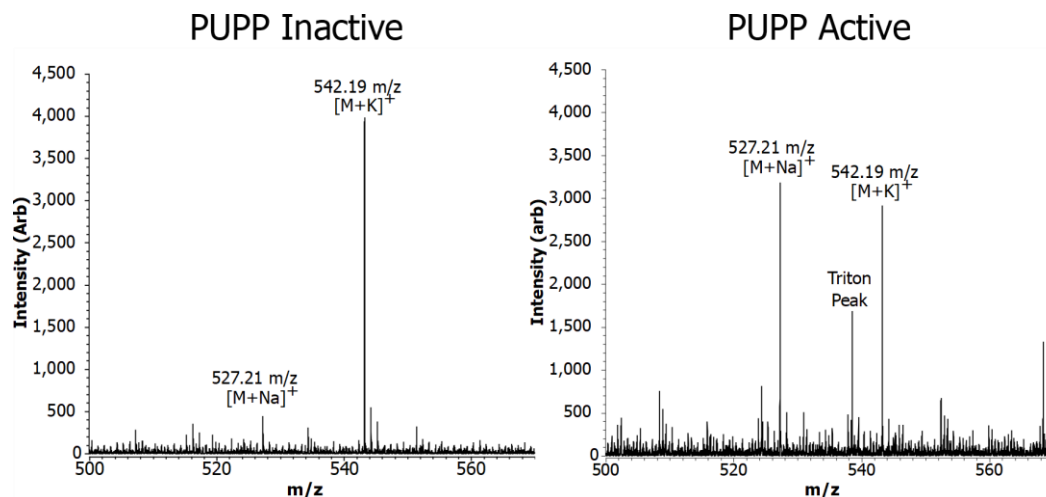


Figure 107 - Shift in Sodium/Potassium Adduct Ratio caused by Triton Burst

Spectra on the left is when PUPP is inactive, and therefore no Triton present in spectra. Spectra on the right shows the effect on the Sodium/Potassium ratio when the PUPP is active.

After this effect was observed, work was conducted to determine if the system could be used to deliberately control the adduct observed within spectra. This was performed for the analysis of beer again, using the PUPP-ESI system. Beer is continuously electrosprayed as before, whilst the PUPP introduces an aqueous solution containing the target charge carrying metal species, in this case a Lithium Chloride. Figure 108 shows the ratio of the intensity of the Lithium adduct to the sum of the adducts commonly observed in beer, Sodium and Potassium, calculated using Eq. 23. The PUPP duty cycle has been set up to introduce a 50-millisecond burst of 1000 ppm Lithium Chloride solution every 5000 milliseconds. There are clear peaks in the intensity of the Lithium adduct, showing the successful change in the dominant charge carrying species for this sugar. Figure 109 shows the change in the mass spectrum obtained when the PUPP is inactive (top), and when the PUPP is active (bottom).

$$\text{Adduct Ratio} = \frac{I_{[M+Li]^+}}{I_{[M+Na]^+} + I_{[M+K]^+}} \quad \text{Eq. 23}$$

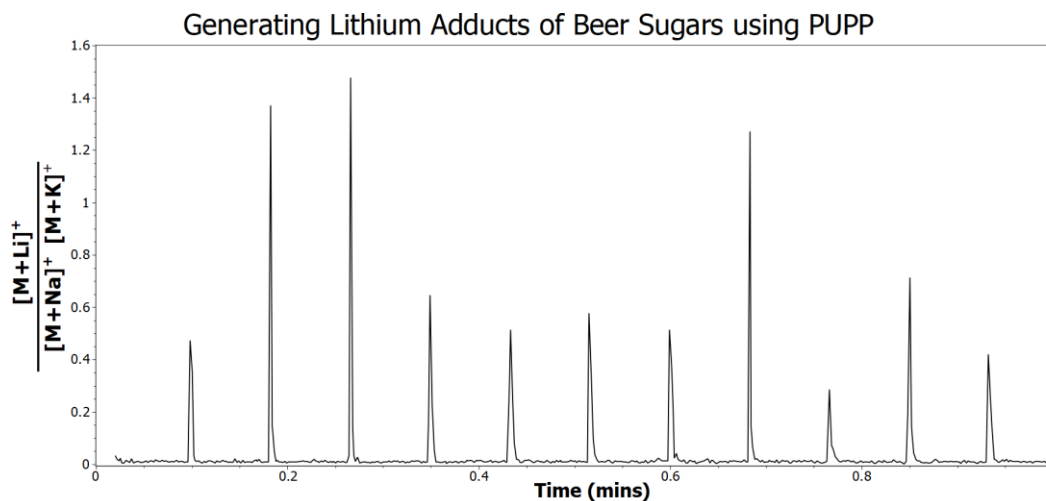


Figure 108 - Relative Intensity of Lithium Adducts of Beer Sugars

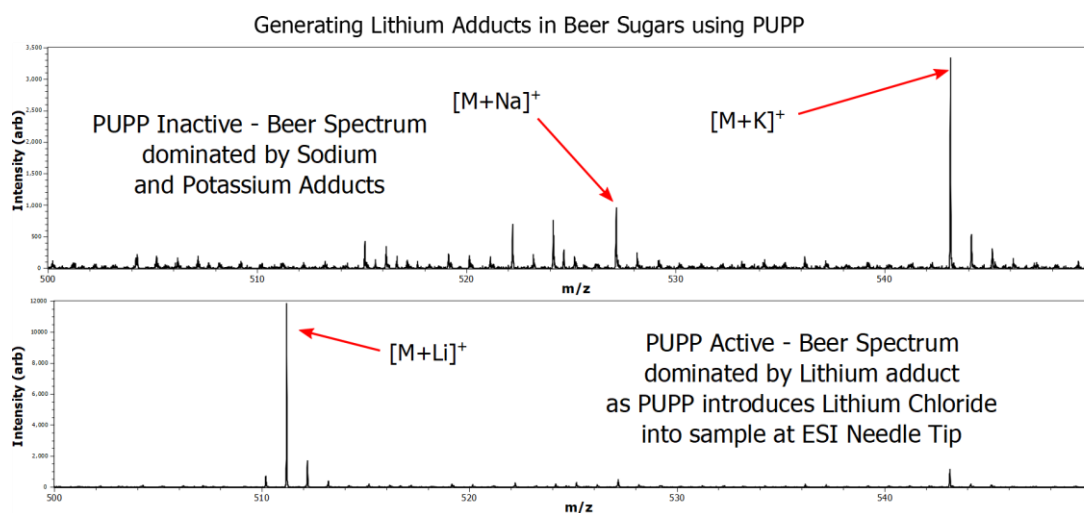


Figure 109 - Effect of introducing Lithium Chloride into Beer via PUPP

This process has also been performed to generate Silver adducts by introducing a 100 ppm Silver Nitrate solution into the ESI stream. Figure 110 and Figure 111 show this effect, with the generation of the two peaks of near equal intensity separated by 2 Da ($[M+^{107}\text{Ag}]^+$ and $[M+^{109}\text{Ag}]^+$) characteristic of the isotope distribution generated by silver adducts.

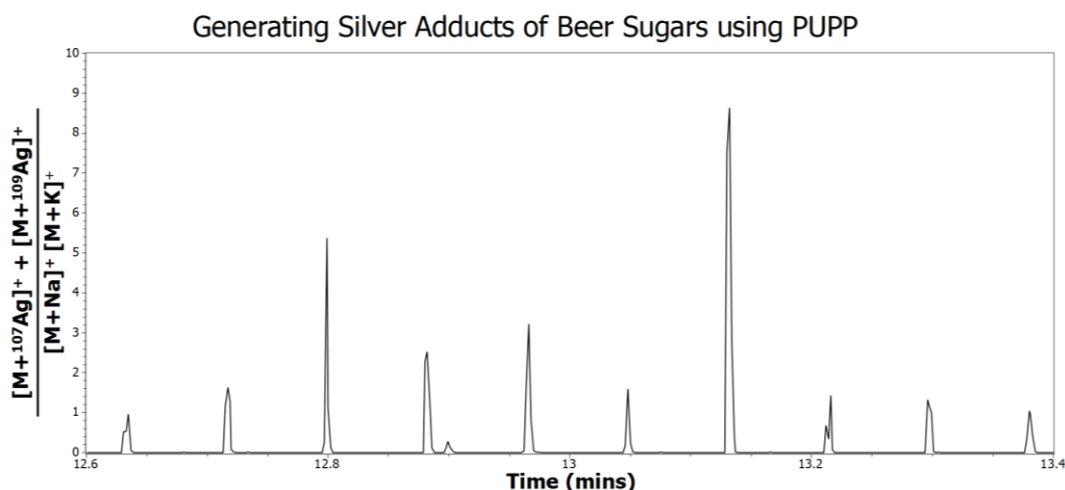


Figure 110 - Relative Intensity of Silver Adducts of Beer Sugars

This data shows the clear potential for rapid switching between adducts of choice. However, the system would need to be tested using samples which are known to exhibit different adduct induced changes in fragmentation pattern and using a variety of different fragmentation techniques which were not available during the course of this project.

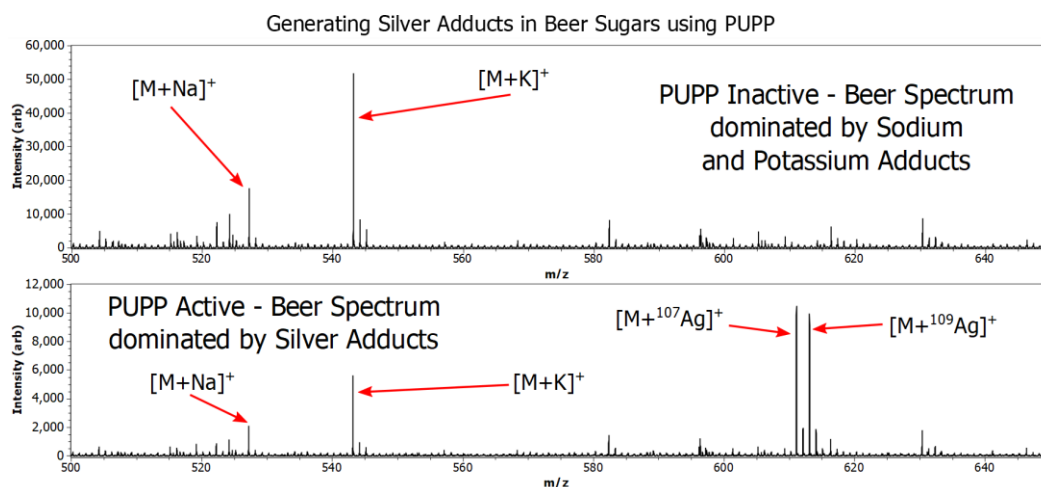


Figure 111 - Effect of introducing Silver Nitrate into Beer via PUPP

4.4 Component Confirmation

By introducing small volumes of known compounds into direct infusion MS/MS or LC-MS/MS data, the presence of components can be confirmed by observing the effect on the product ions obtained. This is achieved through a process called “overspraying”, whereby the PUPP introduces small bursts of a target compound. If compounds of identical mass either coelute or are analysed by direct infusion, the presence or absence of specific target compounds can be determined by plotting the intensities of the fragments. Fragments which correspond to the target

compound being oversprayed by the PUPP will see a rise in intensity when the PUPP is active, whilst the fragments of other compounds will not see an increase.

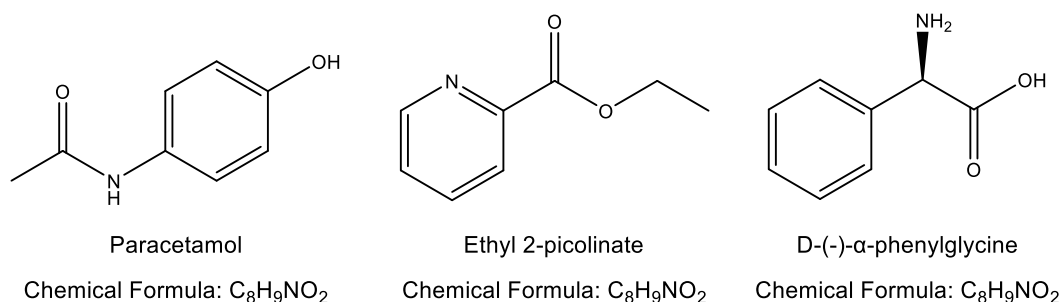


Figure 112 - Structure of Paracetamol, Ethyl 2-Picolinate and D-(-)-α-phenylglycine

Proof of concept data was collected using Paracetamol, and two other components which had an identical molecular formula (and therefore identical molecular masses); Ethyl 2-picolinate and D-(-)-α-phenylglycine. The structures of these compounds are given in Figure 112, together with the unique fragmentation pattern each compound demonstrated via direct infusion in Figure 113.

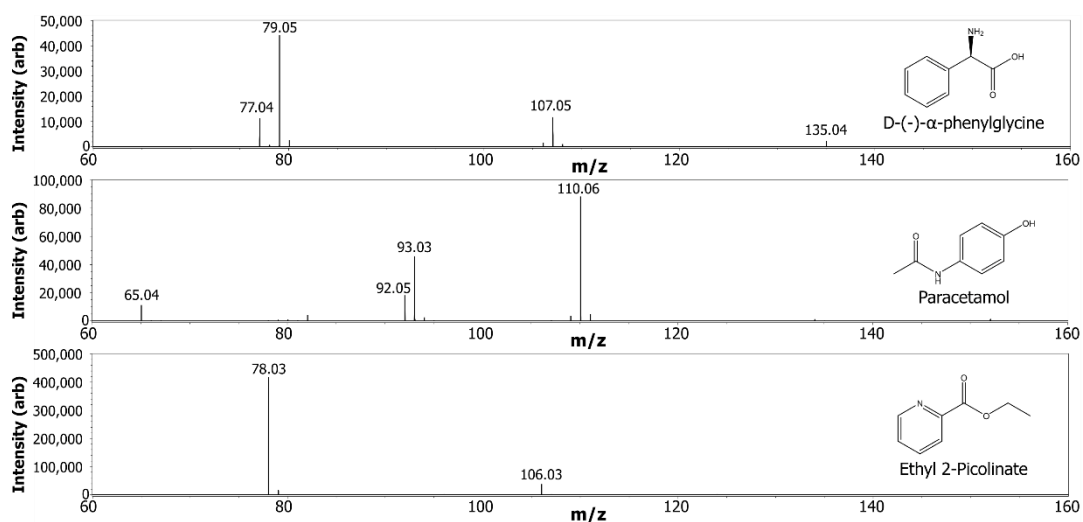


Figure 113 - Compound Fragmentation Patterns

Experimental:

Direct Infusion: A mixed solution of Paracetamol (10 $\mu\text{g/mL}$), D-(-)-α-phenylglycine (10 $\mu\text{g/mL}$) and Ethyl 2-picolinate (1 $\mu\text{g/mL}$) was prepared in MeOH. The solution was infused directly into the MS at 5 $\mu\text{L/min}$ through a 75 μm Fused Silica Electrospray Needle. A 19 Hole PUPP was set to spray a solution containing Paracetamol only (100 $\mu\text{g/ml}$) for 50 ms every 10,000 ms.

LC-MS: A mixed solution of Paracetamol (50 $\mu\text{g/mL}$), Ethyl 2-Picolinate (100 $\mu\text{g/mL}$) and D-(-)-α-phenylglycine (100 $\mu\text{g/mL}$) was prepared in MeOH. As

discussed in the results, for the final dataset the post-column flow was split using an LC-MS flow splitter, which was done to reduce the flow into the fused silica electrospray needle used. The LC-MS method used is shown in Table 7. A 19 Hole PUPP was set to spray for 300 ms every 4500 ms during the LC-MS dead volume (up to approximately 1 minute).

Table 7 - Component Confirmation LC-MS Method			
Needle	75 µm Fused Silica Electrospray Needle		
Injection Volume	2 µL		
Column	Raptor C18, 2.7 µm, 100 x 2.1 mm		
Mobile Phase A	H ₂ O:MeOH:FA 90:10:0.1		
Mobile Phase B	MeOH:FA 100:0.1		
Time (mins)	%A	%B	Flow Rate (mL/min)
0.00	80.0	20.0	0.300
1.00	80.0	20.0	0.300
2.00	20.0	80.0	0.300
10.00	20.0	80.0	0.300
12.00	80.0	20.0	0.300
13.00	80.0	20.0	0.300

4.4.1 Confirmation using Direct Infusion

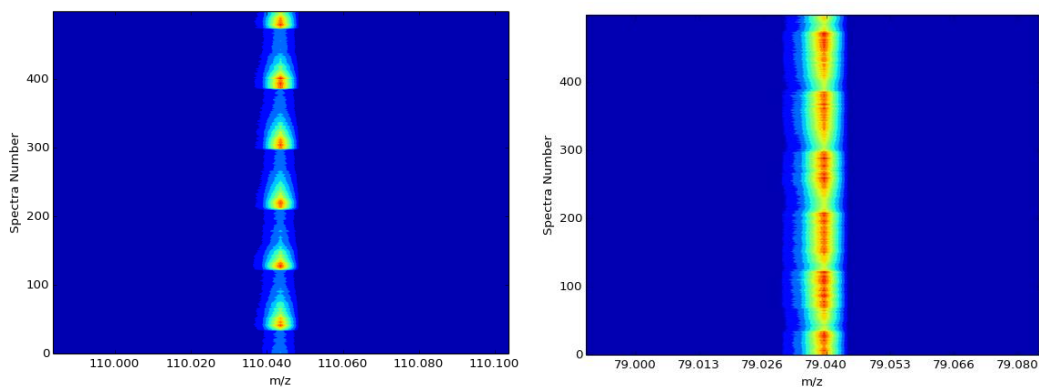


Figure 114 - Intensity Heatmap for different component fragments

Component confirmation can be performed when performing direct infusion of a solution containing multiple components. The PUPP introduces Paracetamol into the mixed solution being analysed, and therefore fragmentation peaks which correspond to Paracetamol increase in intensity when the PUPP is active, whilst little or no effect is seen to other fragmentation peaks. This enables the easy distinction between fragmentation pattern of Paracetamol, and fragmentation of other components. Heatmaps generated for two fragmentation peaks are given in Figure 114, with the left hand side (110.04 m/z, Paracetamol fragment) clearly showing an intensity pattern which matches that of the PUPP cycle, whilst the right

hand side (79.040 m/z, D-(-)- α -phenylglycine fragment) shows small reductions in intensity when the PUPP is active caused by charge competition.

4.4.2 Confirmation using LC-MS Dead Volume

Data was collected to demonstrate the systems effectiveness when coupled to an LC system. When analysed via LC-MS/MS, a solution containing these three components gives a set of three LC peaks at different retention times. However, without running each component as an individual LC-MS standard, or infusion of each component individually to obtain its fragmentation pattern, it is difficult to determine which peak corresponds to each compound. This is particularly the case when LC-MS peaks coelute. The PUPP system is able to introduce the compound of interest during the dead time of the LC injection, which serves as a much more rapid method to determine the fragmentation pattern of the component of interest. The bursts of signal introduced via the PUPP will only be present in the product ion signal(s) which correspond to the component of interest. Currently, the LC-MS dead volume is an underused period of data collection within LC-MS, and therefore is an ideal period of time to perform component confirmation.

Initially, the fused silica electrospray needle was coupled to the LC-MS directly. However, using the conventional LC method for the Waters ESI source, the flow was too high for the ESI needle. This was reduced by directly reducing the LC-MS flow rate of the system to 0.100 mL/min, which had significant detrimental effect on the chromatography, as shown in Figure 115. The PUPP was activated during the LC-MS dead volume, spraying a standard solution of paracetamol. Despite the poor chromatography, the bursts of intensity from the PUPP are only observed for the fragments which match that of paracetamol as expected (110.11 m/z in this example).

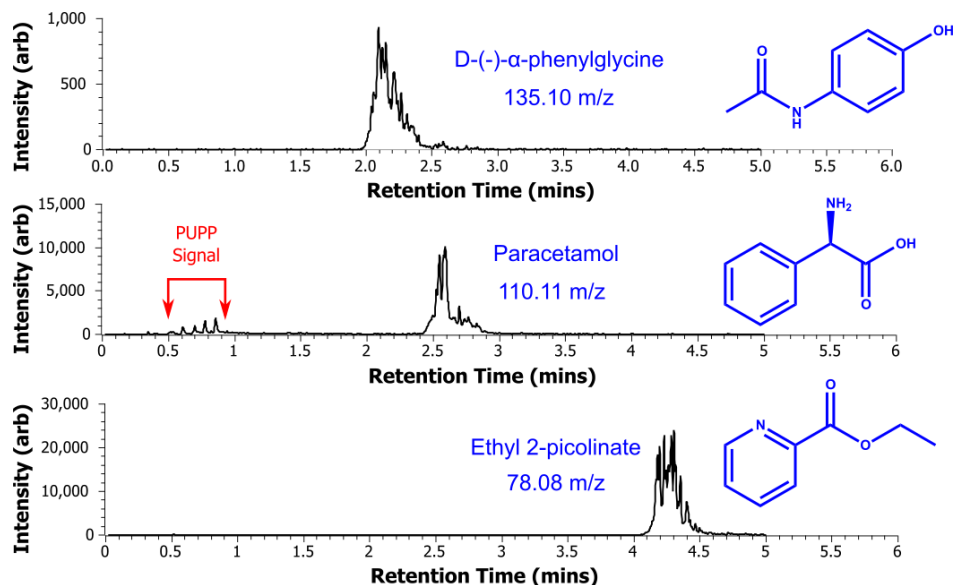


Figure 115 - Paracetamol delivered via PUPP during the LC-MS/MS Dead Time

The chromatography was improved through the use of a flow splitter. Due to the high pressures of the UPLC system, it was necessary to reduce the pressure of the flow splitter by using wider bore PEEK tubing to obtain a good flow to the fused silica electrospray needle, which caused some peak broadening. The results of this are shown in Figure 116, where the chromatography is significantly improved to that of Figure 115.

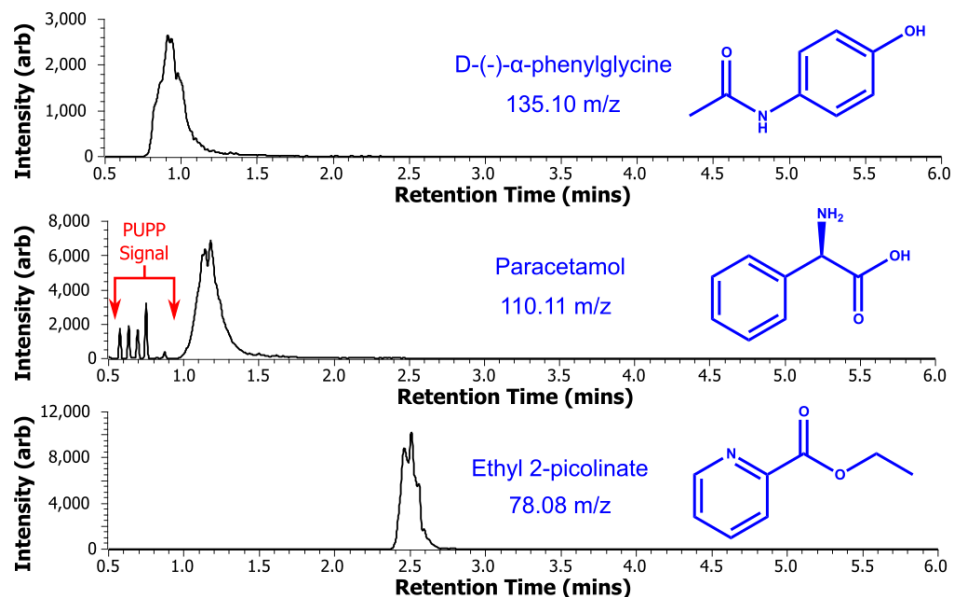


Figure 116 - Paracetamol delivered via PUPP during the LC-MS/MS Dead Time with flow splitter

4.4.3 Confirmation during LC-MS peak elution

The alternative to performing component confirmation during the LC-MS dead time is to perform it during the elution of the LC-MS peak itself. In theory, this would generate an LC-MS peak which has spikes in intensity where the piezo is switched on/off. However, this presents a series of technical challenges which the ionisation source is not currently capable of overcoming, and for reasons discussed herein is likely to be overcome. The difficulties associated with this have been shown by generating artificial piezo data which has been used in conjunction with a genuine LC-MS peak of a typical shape/intensity. Figure 117 shows an ideal example of this pattern across an LC-MS peak.

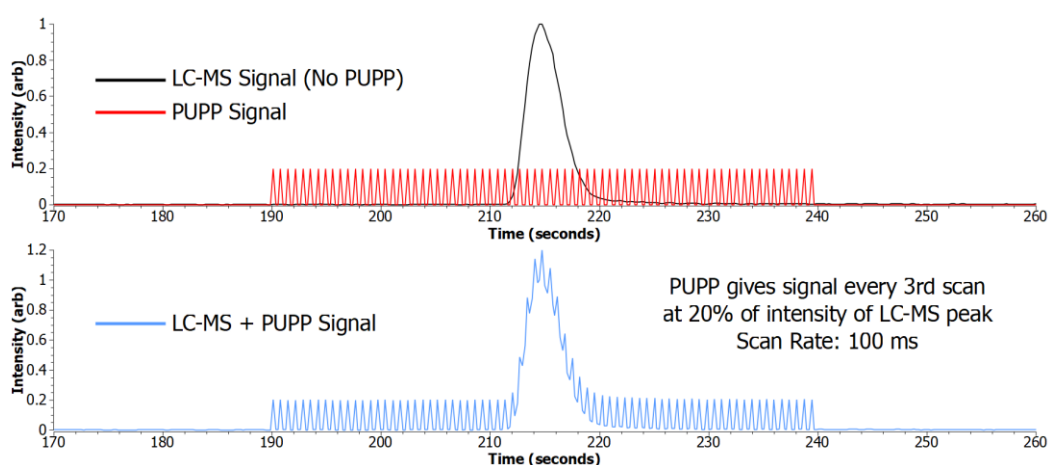


Figure 117 - Simulated chromatogram showing how the PUPP signal could interact with the LC-MS peak signal

However, the example above represents a perfect example of this, and there are a variety of factors which can easily affect this signal. To start, this is a high intensity LC-MS peak, and one which is relatively wide at 10 seconds. Better chromatography or smaller peak size could easily result in the signal from the PUPP dominating over the LC-MS peak itself.

In addition to the differences in the LC-MS peak affecting the data, the settings of the PUPP can also have a negative impact. The intensity of the signal from the piezo must not be too low relative to the LC-MS peak, otherwise the bursts of intensity are not easily observed across the peak. The reverse is true for the PUPP signal dominating over the LC-MS peak, which can cause issues in observing the shape of the LC peak itself. Both of these scenarios have been shown in Figure 118.

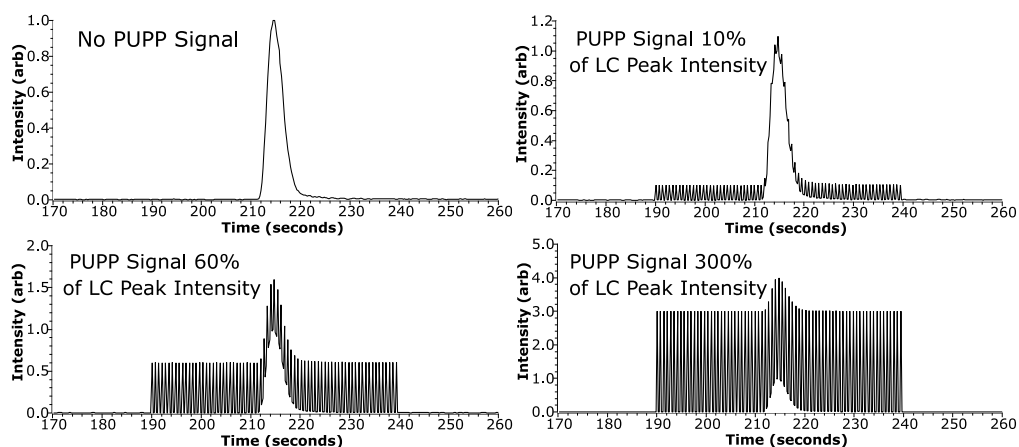


Figure 118 - Simulated Chromatograms to show the effect of increasing the signal obtained for the PUPP on the LC-MS peak obtained

In addition, the frequency of the PUPP spray would need to be suitable for the LC-MS peak. Too infrequent, and the PUPP burst could miss the LC-MS peak all together, too frequent and you get a signal which makes the true shape of the LC-MS peak difficult to observe. This scenario has also been shown in Figure 119.

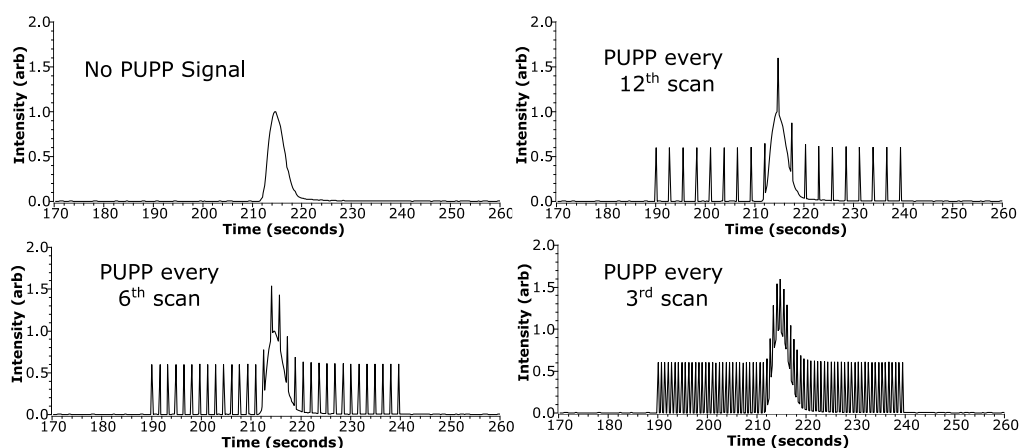


Figure 119 - Simulated Chromatograms to show the effect of increasing the frequency of the PUPP peaks on the LC-MS peak

In addition to the difficulties associated with getting the PUPP optimized, this all assumes the peak retention time and shape is known in advance, which for unknown samples is not possible, and even for known samples is likely to have some degree of variance based on the performance of the LC column. Therefore, component confirmation during the LC-MS dead volume is the most practical solution.

4.5 Summary

The PUPP ionisation source has been shown capable of perform a variety of different applications. The original focus of the ion source, performing encoded

internal recalibration, has been demonstrated on different complex organic matter samples. Mass calibrated data can be automatically generated using significantly reduced workflows, allowing users to perform higher confidence peak assignment for batches of complex spectra.

In addition, the ion source has also shown its capability to perform a variety of other functions, requiring only minor modifications to software or hardware at most. Beer, fruit juices and human plasma and pharmaceutical mixtures were all subjected to rapid analysis via the PUPP-PESI system. The Beer samples were characterized into light, dark and malt via PCA analysis using the PUPP-PESI system and ESI, and their respective performances compared. The human plasma analysis was performed to show the potential application of the system in a clinical setting, and a number of lipids were successfully identified without the aid of sample preparation or system optimization.

On-the-fly adduct modification was shown via the system, enabling rapid switching between the conventional adducts observed for sample solutions to alternative adducts, which could be a powerful tool for rapidly generating different fragmentation patterns based on the adduct of choice.

Component confirmation for tandem mass spectrometry data is shown through the use of overspraying. Three compounds with identical molecular formulae (and therefore identical mass) were analysed by LC-MS/MS and direct infusion MS/MS. The PUPP introduced a small volume of one target compound, which by monitoring the changes in fragment peak intensity during analysis could be used to confirm the presence of the target compound in a complex mixture.

Chapter 6 gives in-depth discussions around some of the future developments for some of these applications. Although these applications are beyond the scope of this project, they demonstrate the wealth of possibilities which the PUPP system could be adapted to and the theoretical benefits these systems would bring.

Chapter 5: Tools Developed

In modern instrumental analytical chemistry, whether you are a user or a developer, the ability to be able to make physical tools to aid in your sample preparation or software tools to automate data processing or visualization is highly valuable. During this project I have developed a wide range of different tools (both physical and software) to support my research. Herein, some of the tools are presented as an illustration of this.

5.0 Software

The software tools developed can be split into two categories: those for hardware control and data processing. All were written in LabVIEW (NI, Austin Texas, USA).

Control of the ion source hardware was necessary to ensure that the system generated consistent and appropriate data, and to synchronize the ionisation source with the mass spectrometer.

The data processing tools were necessary to perform or automate functions which would be extremely time-consuming to undertake manually, or difficult or impossible to achieve through conventional software packages available from instrument manufacturers or open-source programmes online. Most of the programmes written as part of this PhD are available online at <https://github.com/HarryTaylor1296/PhD-Thesis-Code>. This work has been made available to help others in the field who are beginning to process their data using LabVIEW.

5.1 LabVIEW Introduction

LabVIEW is a programming environment developed by National Instruments, which uses the programming language "G". This language differs from the most commonly used programming languages (Python, C++, R, MATLAB etc.) because it is a graphical language rather than a text-based language. Programmes written in LabVIEW are displayed as a diagram, with functions being displayed as symbolic nodes and variables being passed between those functions by wires. The Block Diagram contains the "code", whilst the user interface, where inputs can be controlled and outputs displayed, is the "Front Panel". Figure 120 shows a basic program used to perform a simple mathematical function. Programmes written in LabVIEW are referred to as "Virtual Instruments" or "VIs".

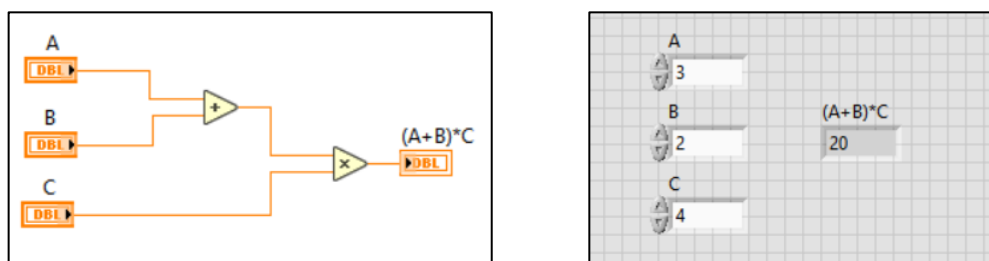


Figure 120 - LabVIEW Block Diagram (Left) and the Front Panel User Interface (Right)

Text based programming languages execute code in a sequential format; they perform actions in order from top to bottom. LabVIEW is a dataflow language and

so “code” operates non-sequentially, whereby all inputs begin simultaneously, after which specific actions within a program will execute once all relevant inputs to that particular node or function are present. This difference is shown in Figure 121, which shows identical functions written in MATLAB (left) and LabVIEW (right). In the MATLAB code, Line 5 and 6 are performed sequentially, before performing the final sum in Line 7. In LabVIEW however, the functions $A+B$ and $C+D$ will be computed in parallel, the final multiplication will begin when both inputs are filled. The inherently parallelized nature of the operation of LabVIEW code can make it difficult to describe the mode of operation of programmes written for this project.

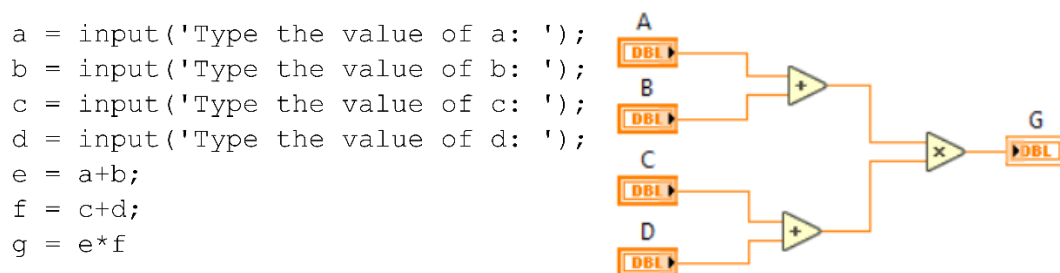


Figure 121 - Identical Basic Functions in MATLAB (Left) and LabVIEW (Right)

All programming was performed in LabVIEW. Although no block diagram code is shown in the main bulk of the thesis, the code itself is available through the GitHub link given previously.

5.2 Data Processing Tools

5.2.1 “Mezzo” – Reading mz5 format files

Every mass spectrometry vendor uses their own file format – in fact some vendors have multiple different file formats. Therefore, the general workflow used for processing mass spectrometry datafiles in this project involved first converting the vendor specific files to the standard mz5 interchange format.¹¹⁸ This approach then avoids the need to write multiple programmes capable of reading the various raw file formats from each different mass spectrometry vendor (Thermo, Bruker, Waters, ABSciex etc.).

There are many other, more common, interchange formats – e.g. mzML and mzXML and mzData. However, mz5 benefits by using an HDF5 (Hierarchical Data Format) file format, and therefore overcomes the storage space requirements and read/write speed limitations associated with more common XML based interchange formats.¹¹⁸

Conversion of vendor specific files into mz5 is a standard feature of the well-known MSConvert tool, part of the Proteowizard package. The MSConvert toolkit is freely available and therefore easily accessible to all users.¹¹⁹

I developed a tool, called “Mezzo”, in LabVIEW, to read and process the data contained in the mz5 format files. Mezzo uses the h5LabVIEW2 LabVIEW add-on, to read, write and perform other functions on the HDF5 based file format of mz5 files, in LabVIEW.¹¹⁹ This tool is called Mezzo because it is used to read mz5 files, but also because it sits in the middle of other tools that I describe later.

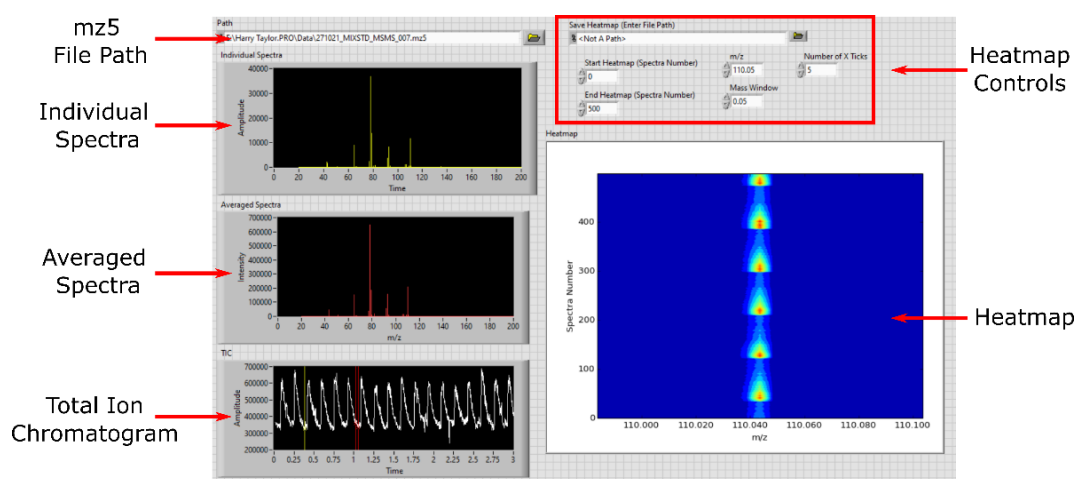


Figure 122 - User Interface for Waters File Reading Software

Mezzo can load an mz5 file and then extract:

- Individual mass spectra
- Averaged mass spectra
- The Total Ion Chromatogram
- Hyperslabs/subsets of the data – e.g. all mass spectra between two time points; or all data for a given mass range at all timepoint; or the chronogram for a single mass or small mass range.

These outputs can be viewed in the user interface of Mezzo, but can also be passed to other functions that simply call Mezzo to read the mz5 data. The general user interface for Mezzo is shown in Figure 122. Heatmaps were generated using the Advanced Plotting Toolkit, another freely available add-on toolkit for LabVIEW. The speed of the software and the memory footprint was helped greatly through the use of the HDF5 “Hyperslab” tools, permitting the software to only read data which was necessary for the task the user requests, rather than the entire dataset.

5.2.2 “Transcend” – Viewing and process transient data

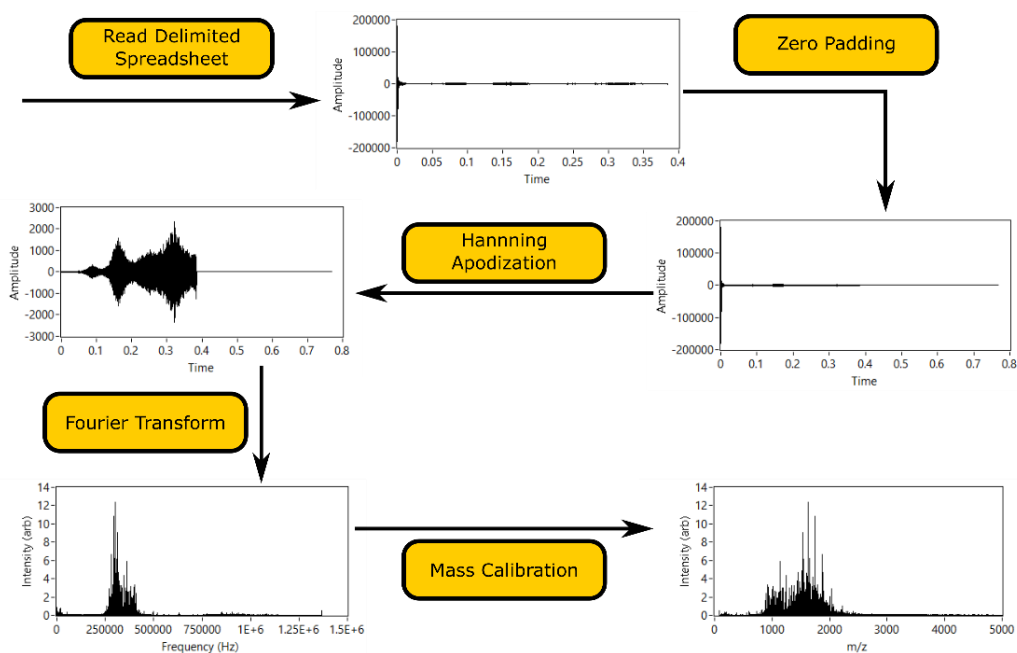


Figure 123 - Processing Raw Transients in LabVIEW Workflow

The ability to process raw transients was not critical to the project at any stage, however a VI was developed in order to gain a further understanding on the workflows necessary to generate mass spectra from raw transients. Transient data was provided in a .CSV file format (this is a Spectroswiss Sarl file format used for Orbitrap transients) can be read and processed using this VI, the workflow for which is shown in Figure 123. The number of zero paddings is controlled by the user interface (shown in Figure 124). The first zero pad applied adds sufficient zeros to the transient to make the transient length up to a power of 2, and all subsequent zero paddings double the length of the transient. Apodization (a Hann window was implemented in this case) is applied to reduce Gibbs oscillations. After this, the transient is Fourier-transformed to produce a frequency spectrum. The frequency spectrum is subsequently mass calibrated (using a mass calibration factor extracted from the file) to generate the mass spectrum.

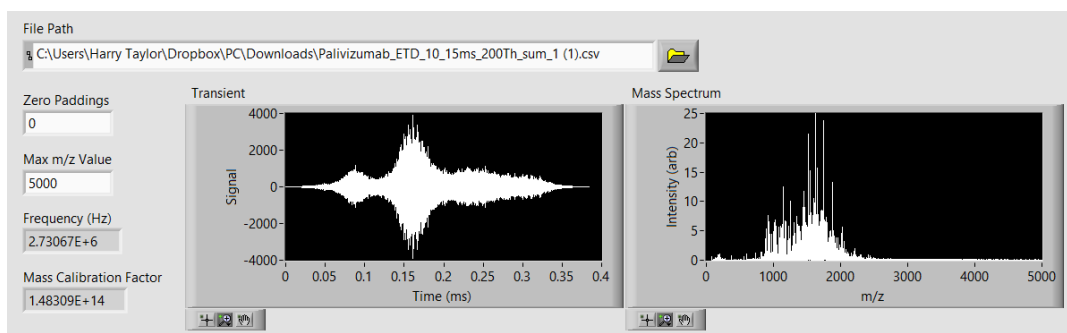


Figure 124 – Transcend – User Interface

5.2.3 “THRASHer” - Baseline Calculation (THRASH Algorithm)

Calculating Baseline Workflow

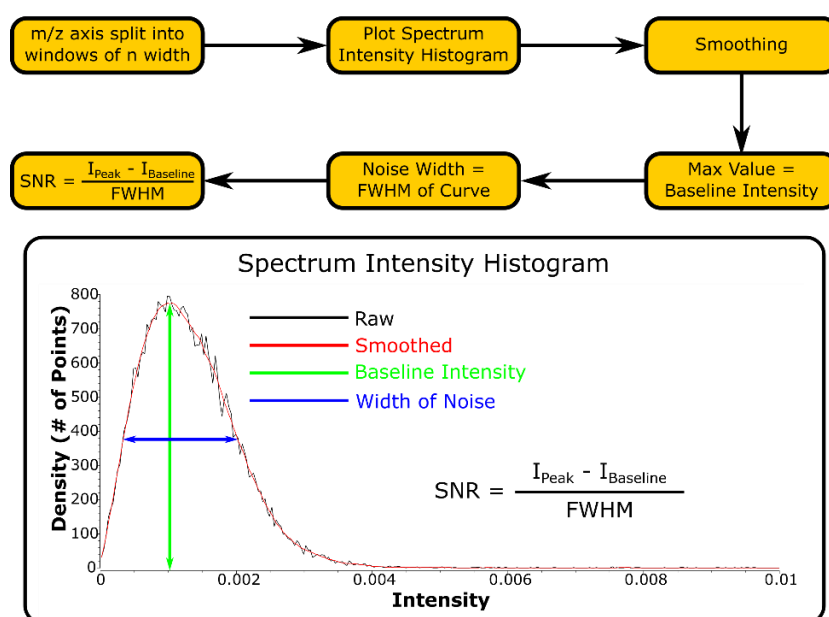


Figure 125 - Calculating Baseline Workflow and Spectrum Intensity Histogram

Peak detection for complex spectra is difficult because when there are many peaks across a narrow mass range it is difficult to generate an appropriate noise level to be used for detection. There are various methods of performing this adopted by different peak detection algorithms such as the n-Sigma, root mean squared, THRASH and Autopiquer methods.^{152,196}

In order to be able to perform good quality peak detection for complex spectra, a LabVIEW VI was constructed which closely followed the THRASH algorithm approach, the workflow for which has been shown in Figure 125.¹⁹⁶ In short, the algorithm splits the mass axis into short windows (generally 4 m/z), and a histogram of the number of points at each intensity is generated, an example of which is given in Figure 125. The highest point (the mode) of this distribution is taken as the baseline intensity, and the magnitude of the noise is the full width at half maximum (FWHM) of the histogram peak. Peak detection is then performed

using the peak detection VI given in the signal processing package in LabVIEW. Using this algorithm, the S/N of a peak is defined as:

$$S/N = \frac{I_{Peak} - I_{Baseline}}{FWHM} \quad \text{Eq.24}$$

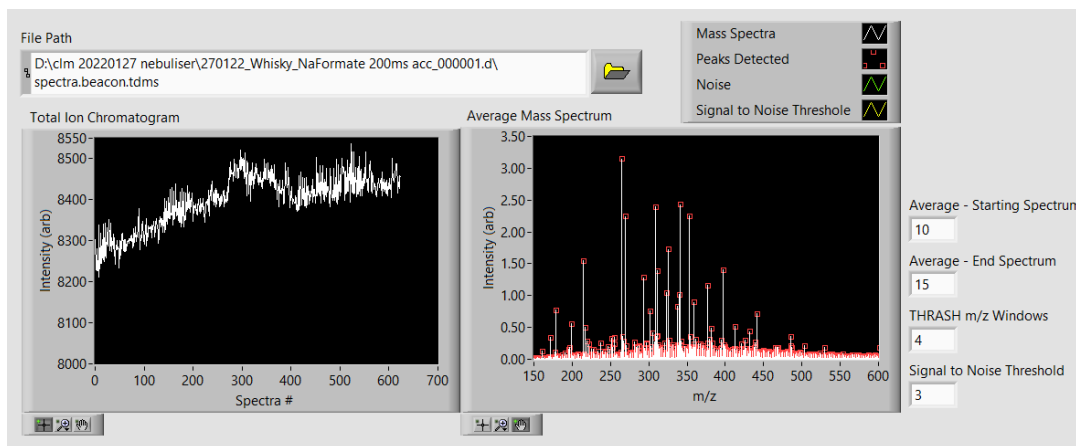


Figure 126 – THRASHer - User Interface

The algorithm can be used to perform peak detection on individual spectra, either as part of a larger workflow package or as an individual program. Figure 126 shows the algorithm working as an individual workflow package, whereby TDMS files are read and a summed spectra is subjected to peak detection. Figure 127 shows the peaks detected across a 0.25 m/z window.

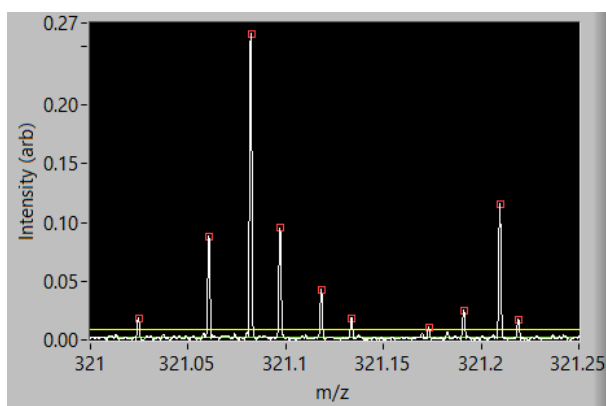


Figure 127 – THRASHer - Peaks Detected over a 0.25 m/z Window
Signal to Noise Ratio Threshold for peak detection is shown in yellow. The noise level is shown in green. Peaks detected are highlighted with a red box.

Figure 128 –

5.3 Hardware Control

Further code was written at various stages during the ion source development to enable control and synchronisation of hardware. Much of this work was performed during the early stages of using a trigger from the mass spectrometer to synchronise droplet generation with ion accumulation. Herein, the LabVIEW controls used to perform this early development work are shown.

5.3.1 "MISSI" – Microdrop Ion Source System Interface

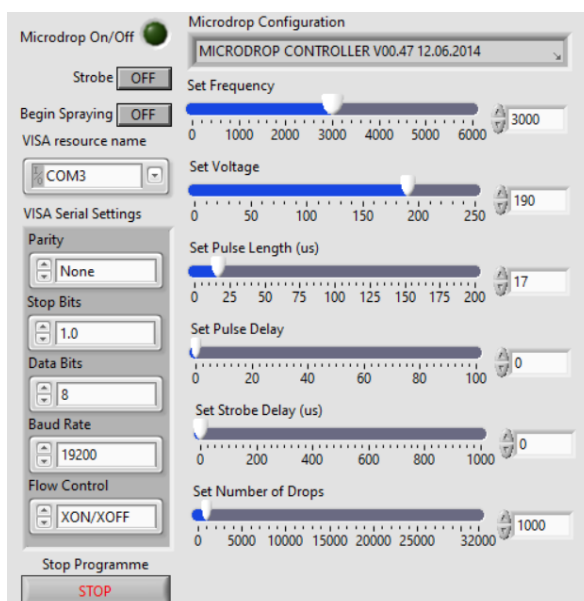


Figure 129 - Microdrop Control User Interface

The Microdrop system, discussed during Chapter 2, was controlled through LabVIEW software written as part of this project, named "MISSI." – *Microdrop Ion Source System Interface*. This was developed with the initial aim to synchronize the Microdrop system with the mass spectrometer. However, due to the limitations associated with the system (see Chapter 2), development was stopped and focus shifted towards the PUPP system. Regardless, an overview of the software is given here to inform future research focused on this system.

The Microdrop system can be externally controlled through an RS232 port at the back of the Microdrop control unit. Syntax commands (a list of which was supplied by the manufacturer) are sent to the control unit through the LabVIEW software, which uses the LabVIEW VISA sub-VIs to deliver each command when triggered to do so according to controls on the user interface (Figure 129).

5.3.2 "Ion-Sync" - Q-TOF Trigger

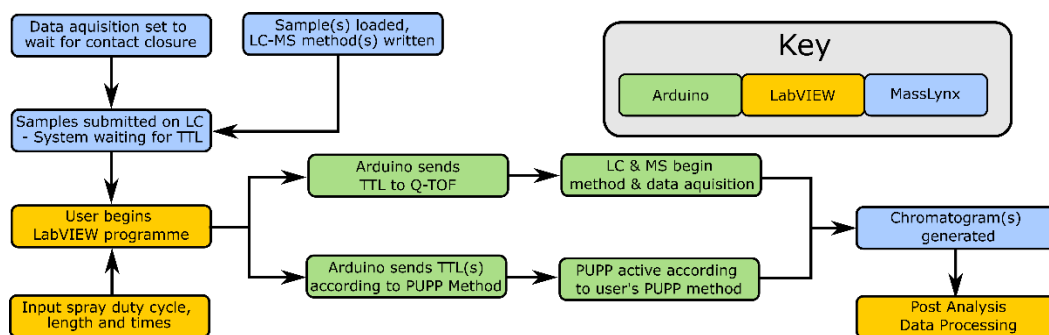


Figure 130 - PUPP Trigger System for Waters LC-MS System

As discussed previously in Chapter 3, for many applications it is crucial to synchronise the PUPP system and the corresponding mass spectrometry system. When coupling to Fourier-Transform based MS systems this is to minimise the variability in the number of ions delivered by the PUPP system between scans, thereby reducing the space charge effect. However, for other applications it may be necessary to couple the PUPP system to the beginning of MS data acquisition events.

The PUPP system was coupled to a Waters Xevo G2-XS Q-TOF and Waters Acquity UPLC System through the use of an Arduino Uno, all of which was controlled by custom LabVIEW code, named "Ion-Sync". Ion-Sync used tools from the LINX (MakerHub) add-on to send and receive contact closures from the Arduino. The workflow for the software can be seen in Figure 130, and the user interface can be seen in Figure 131.

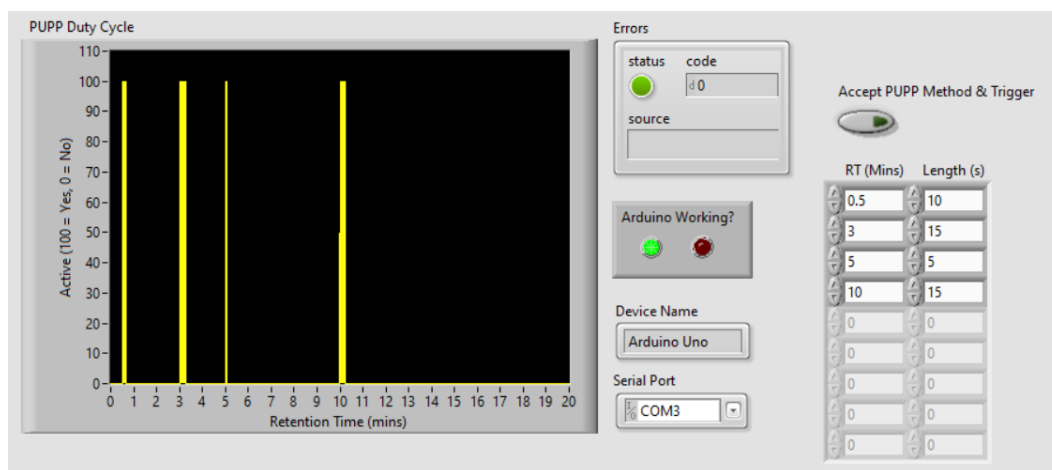


Figure 131 – Ion-Sync User Interface

5.4 Custom Fused Silica Grinder

Much of the data collected during this project used the PUPP system in conjunction with a custom electro spray system. In the early stages of the ion source development, the need to be able to generate fused silica electro spray needles was identified. Although commercially available fused silica electro spray tips are available, the cost of these is significant, and therefore they are not a sustainable resource for cost effective research and development. Therefore, as part of this PhD, it was necessary to explore and develop a method by which fused silica electro spray needles could be developed which would provide highly sensitive and reproducible data without significant cost.

Currently, there are three main techniques employed to generate electro spray needles from fused silica: etching with hydrofluoric acid (HF), glass pulling and mechanical grinding. Each of these give a different profile of needle, shown in Figure 132.



Figure 132 - Fused Silica Electro spray Needle Methods

During etching, the fused silica is dipped into concentrated hydrofluoric acid, which slowly removes the fused silica material. The surface tension of the solution leads to the generation of a small meniscus which travels up the length of the silica.¹⁹⁷ Water is pumped through the fused silica to prevent HF from entering and etching the interior. The rate of etching is proportional to the volume of acid coating the fused silica, and this is shown in Figure 133. This technique generates parallel tips, whereby the inner diameter of the capillary remains constant throughout the length of the tip. There are several issues with this technique, including the very slow throughput (fabrication of a needle can take up to two hours) and the environmental and safety risks associated with using concentrated hydrofluoric acid.

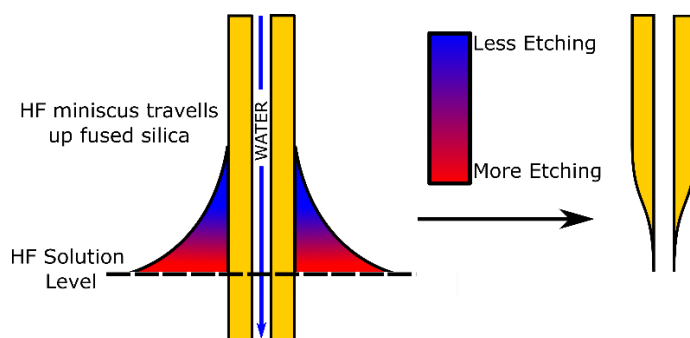


Figure 133 - Fused Silica Etching with Hydrofluoric Acid

Alternatively, a glass puller can be used to generate electro spray needles. The capillary is set up so that it experiences a constant pulling force and the silica is heated until the capillary is softened, at which point the capillary is pulled apart forming two very narrow tips as shown in Figure 134.^{198,199} Unlike etching, the system generates tapered tips, whereby the inner diameter of the capillary narrows towards the end. This system also has its limitations, including the formation of tips which are extremely fragile and prone to blockages and in many cases the unwanted generation of asymmetrical shaped tips.

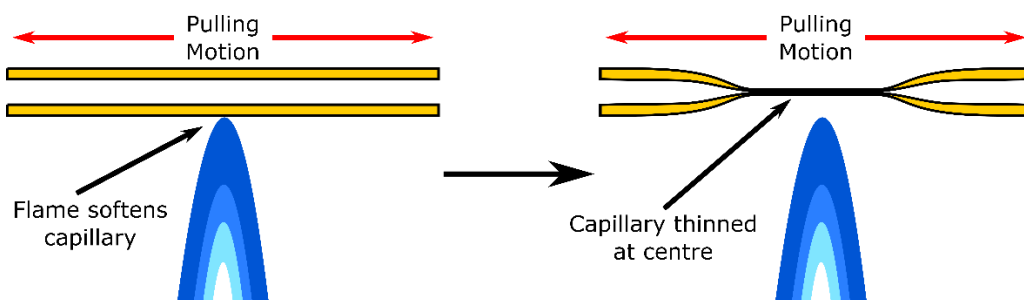


Figure 134 - Fused Silica Pulling with Glass Puller

Finally, electro spray tips can be generated through mechanical grinding.²⁰⁰⁻²⁰⁴ The fused silica and the grinding material are both rotated, and the capillary is pressed against the material at a controlled angle. This system leads to the generation of parallel tips, but allows for a level of control over the tip angle (Figure 135). This is a fast and repeatable method of generating electro spray needles, which does not require the use of chemicals that pose a significant risk to the user.

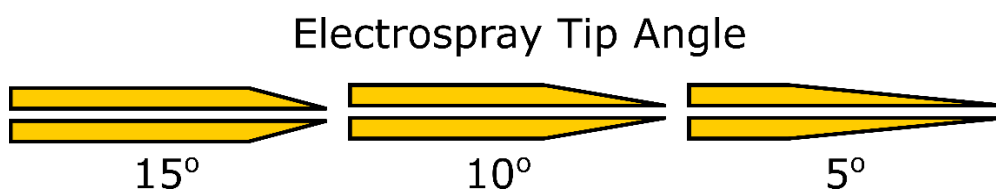


Figure 135 - Effect of tip angle on profile of electro spray needle

Mechanical grinding was therefore identified as the best method for creating fused silica electro spray needles. Initially this was done using a custom grinding system at the University of Edinburgh, and to be able to repeat this process in-house a similar system was generated through a mixture of 3D printed parts and commonly available low-cost components. Similar systems have been published previously, and generate excellent quality of sprays which deliver highly sensitive and consistent signal.²⁰⁰

Herein, the development of a new low-cost 3D printed fused silica grinder is shown. The system went through 4 iterations of design, which are summarized below in Table 8.

Version Number	Lapping Film Motor	Fused Silica Motor	Generated usable ESI Needles?
1	Dremel	Dremel	No
2	Dremel	Mini Motor	No
3	Mini Motor	Mini Motor	Yes
4	Mini Motor	Mini Motor (Pulley)	Yes

5.4.1 Fused Silica Grinder – Version 1

The initial design, shown in Figure 136, consisted of two rotary devices, one which held the fused silica through 1/16" OD 0.015" ID Grey PEEK tubing mounted into a mini drill chuck, the second held the lapping film used to grind the fused silica. Both the rotary devices were mounted onto mini milling machine tables to give fine motor control over the positions of the two rotary devices. The angle of the fused silica could be customized using a R axis mount, which would allow for control of the angle of the tapered tip. Finally, a USB camera fixed to a mount was used enabled the user to visualize the process more clearly via a monitor.

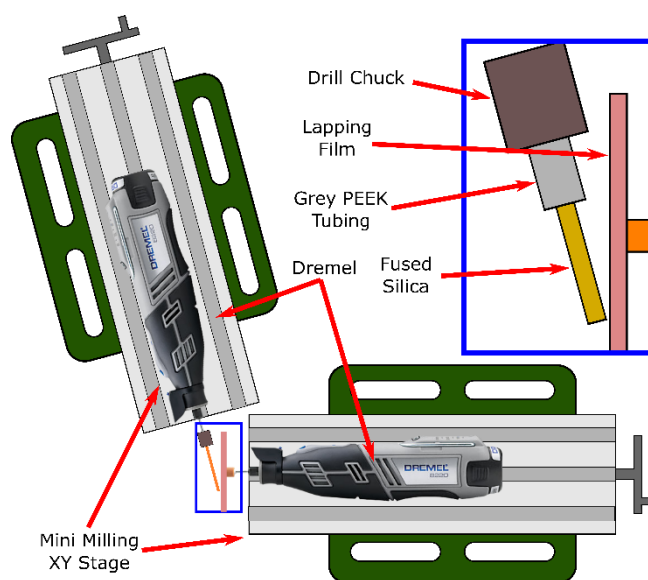


Figure 136 - Fused Silica Grinder Version 1 Design

This system did not give enough control over the angle of approach for the fused silica, and therefore lead to inconsistent tip angles. Moreover, the design was overall too bulky and difficult to have the fine control necessary to generate good quality tips. Finally, although significantly cheaper than purchasing a glass puller

system for example, the cost of the system was overall high because of the need for two rotary devices, two XY stages and an R-axis stage.

5.4.2 Fused Silica Grinder – Version 2

The second design improved the system significantly in the areas of fine control, cost, and overall size of the system. This was done by replacing one of the rotary devices with mini motor and a simple electronic circuit board (powered by 2 x AA Batteries) which the user could use to control the rotation speed. The fused silica was mounted into the system using a mini drill chuck which was secured onto the shaft of the mini motor. Improvements in user control over the tip grinding angle was gained through use of a guide rail and angle adjustment notches.

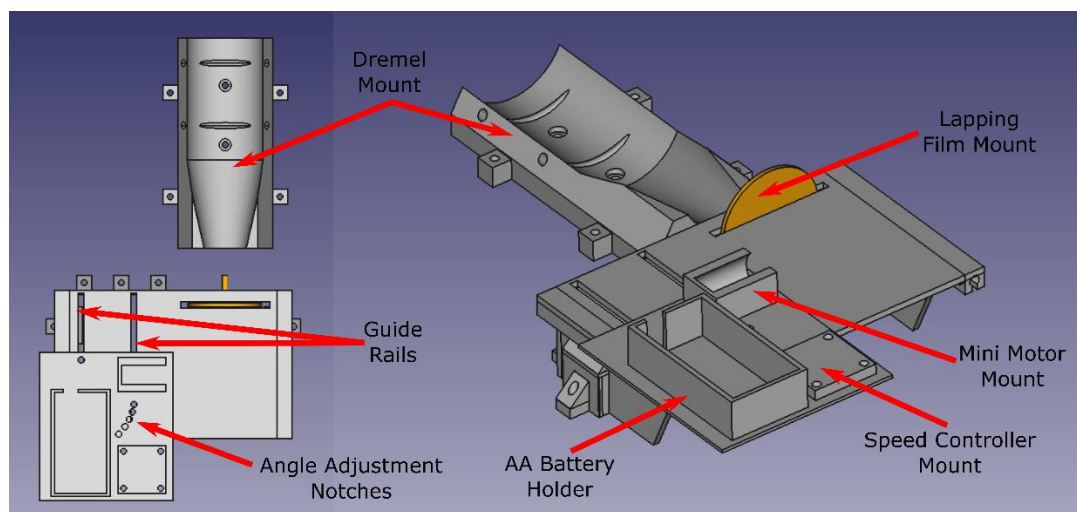


Figure 137 - Fused Silica Grinder Version 2 Design

However, the system remained too bulky to reproducibly generate electrospay needles of good quality. In addition, it still required the use of a rotary device, the lowest speed setting for which made it difficult to have fine control over the grinding process, made the system significantly larger and required mains power for use.

5.4.3 Fused Silica Grinder – Version 3

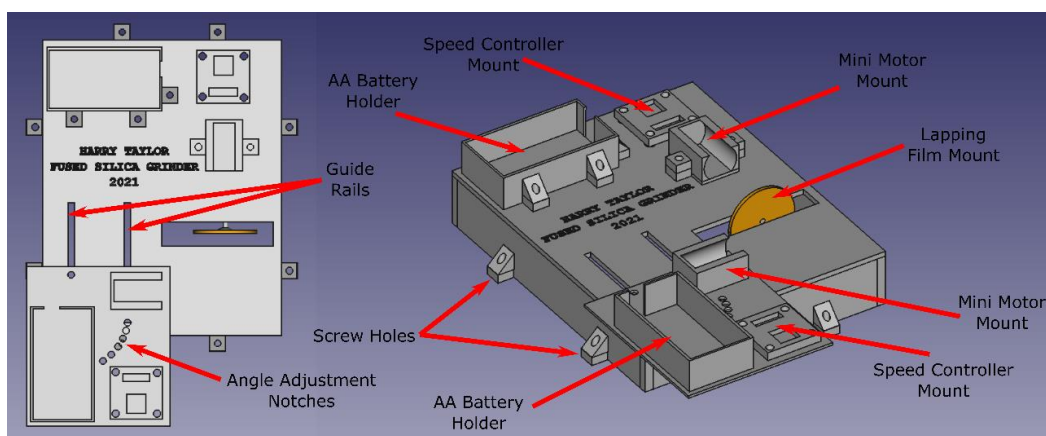


Figure 138 – Fused Silica Grinder Version 3 Design

Version 3 of the fused silica grinder (shown in Figure 138 and Figure 139) replaced the rotary device holding the lapping film with another battery powered mini motor. The lapping film was attached to a 3D printed disk, which was held in place by a mini drill chuck attached to the motor. The system showed good repeatability at making fused silica electrospray tips, images taken through a microscope can be seen in Figure 138 – Figure 139.

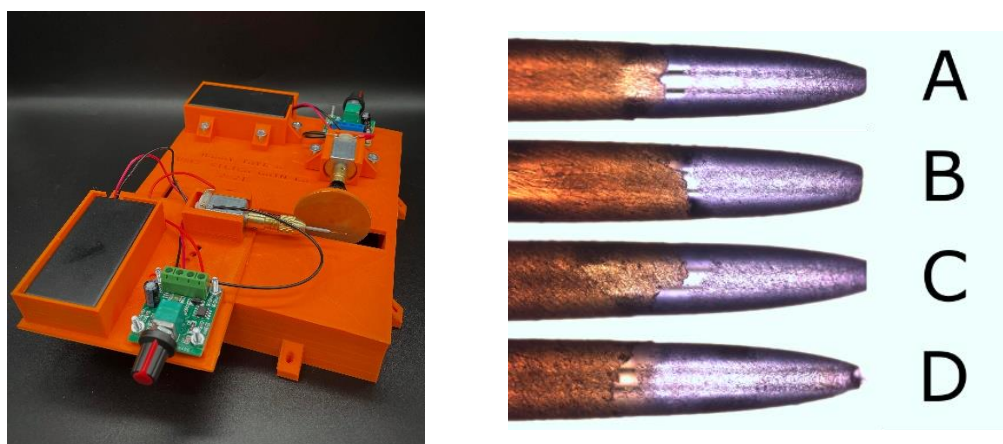


Figure 139 - Image of Fused Silica Grinder Version 3

Although control over the tip grinding angle was achieved, the system did not allow for smooth movement of the tip towards the grinding material, and therefore made it difficult to apply consistent pressure when grinding. Moreover, the speed at which electrospray tips were made was limited by the fact that the fused silica had to be pre-cut to length, and manually inserted into the drill chuck each time.

5.4.4 Fused Silica Grinder – Version 4

The final version of the fused silica grinder (shown in Figure 140 and Figure 141) saw two major improvements on the usability of the device. Firstly, the rail system was removed, allowing the user to grind the electrospray tips with more flexibility.

Secondly, a pulley system was introduced onto the fused silica rotator, which allowed the user to continuously feed a reel of fused silica into the device, overcoming the limitation of previous designs which required the user to pre-cut the fused silica to length for each tip. This significantly reduced the time taken between electrospray tips.

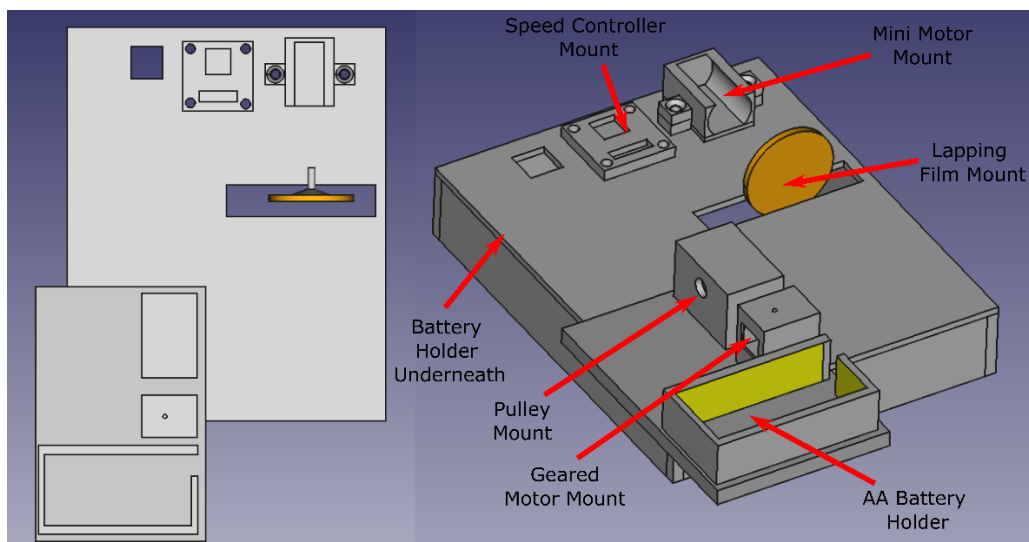


Figure 140 - Fused Silica Grinder Version 4 Design

When switching to a pulley-based system it became apparent that the mini drill chuck provided insufficient grip on the PEEK tubing, therefore allowing the fused silica to move in/out when grinding. This was overcome through the introduction of a custom component made from brass, which coupled the stainless-steel tubing to a system which took a standard 1/16" PEEK tubing fitting.

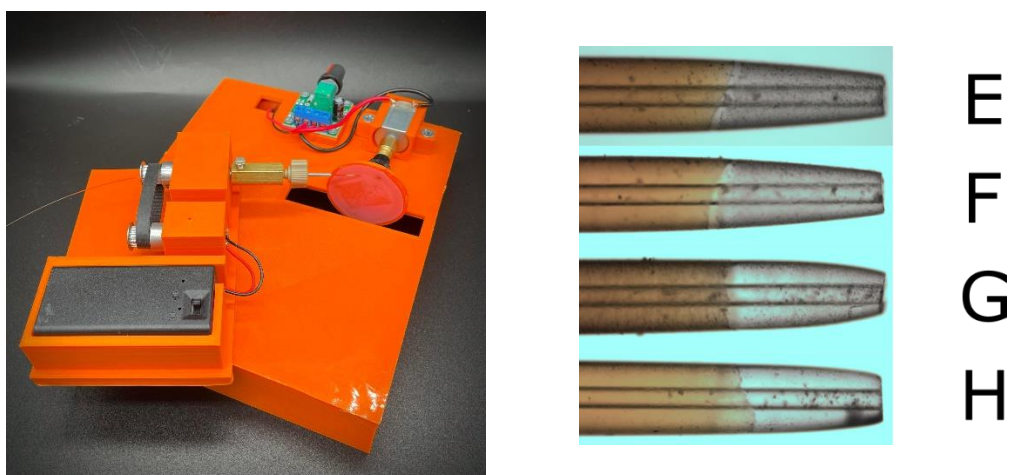


Figure 141 - Final Fused Silica Grinder (Left) and the Electro spray Tips generated (Right)

Although concerns were raised over the repeatability of the electrospray needles without the grinding angle being fixed, the reproducibility of the fused silica needles remained similar to those produced using Version 2. This can be seen

visually in the appearance of the needles produced, shown in Figure 141, as well as the reproducibility data, shown in Figure 142. A parts list with an approximate costing is given in the appendix.

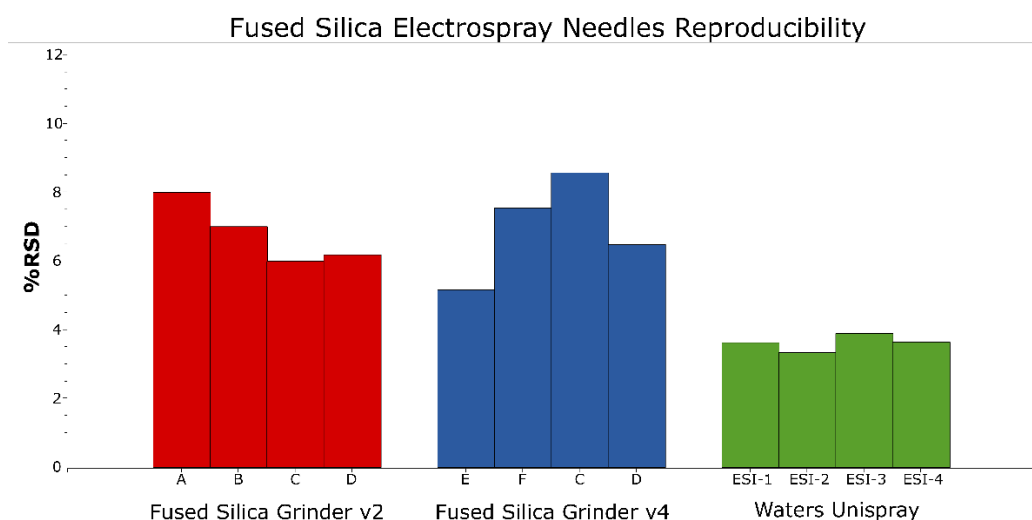


Figure 142 – Fused Silica Electrospray Needle Reproducibility

5.4.5 Further Development

Electrospray tips produced using Version 4 of the fused silica grinding device generated good quality data throughout the project. However, further improvements to the system could be made which would enhance the repeatability of the electrospray needles produced and make the system more user friendly. The first of these recommended improvements would be to use a motor with a higher RPM and a higher tolerance for torque. When grinding, a clear decrease in the rotational speed of the fused silica and the lapping film can be seen where the motors suffer from torque effects. Moreover, the system would be significantly improved by introducing an adjustable guide rail which would give the user fine control over the grinding angle of the fused silica on the lapping film.

5.5 Summary

This chapter has described tools created to assist the development of the ion source. The software developed during this project allowed for the control and manipulation of the hardware and many basic data processing functions. The fused silica grinding system shown was developed as a reproducible and low-cost method of generating electrospray tips.

Chapter 6: Future Suggested Work

Thus far, the development and subsequent applications of the PUPP system within mass spectrometry have been shown. However, there remain a number of potential applications which have been beyond the scope of this project that remain unexplored, in addition to some next stages of the ion source's development for applications discussed previously.

Herein, suggested future work has been outlined for the ionisation source. New applications, including Tandem MS encoded internal mass recalibration, on tip/plate enzymatic digestions and the potential coupling of the PUPP system to a DART system are presented as theoretical experiments.

6.0 Future Suggested Work

During the course of this project, there were a number of investigations which were discussed for the ionisation source, which could not be explored because of limitations on time or resources available. This chapter presents these areas as future suggested work, and gives a brief overview on some of the underlying principles which would guide the direction of the development.

6.1 Tandem MS Internal Encoded Calibration

As shown previously in Chapter 4, the ability to perform internal encoded recalibration was demonstrated on a variety of instruments and for different complex sample types. However, most applications require tandem mass spectrometry data to ensure confident peak assignment. External calibration methods are typically performed for tandem MS data collection. This method, as discussed in Chapter 1 and again in Chapter 4, has a series of limitations. In short, these include the user intensiveness of performing the calibration, instrument drift and for FTMS instruments the space charge effect.

Using instrumentation not available during the period of the PhD, the PUPP system can perform tandem MS calibration for instruments with ion cloud mixing capabilities. Instruments which have more than one ion trap are generally capable of performing ion cloud mixing, such as the Thermo Orbitrap Fusion or a Q-Exactive fitted with the Omnitrap system developed by FasmaTech.

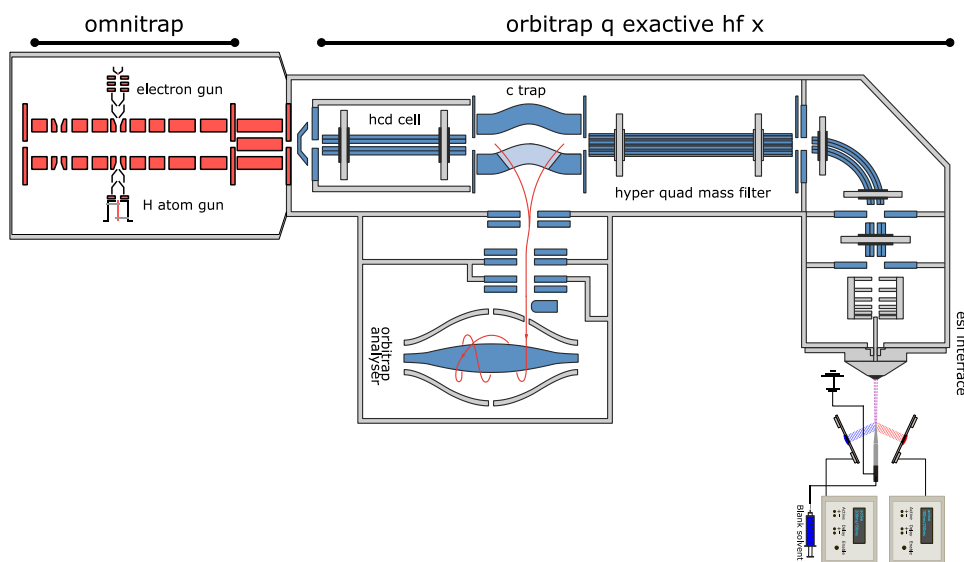


Figure 143 - Prototype Orbitrap Schematic with Omnitrap System and two PUPP systems²⁰⁵

To perform Tandem MS calibration, two PUPPs would be mounted to the system, which would spray onto a single needle held at a high voltage, as shown in Figure

143. One PUPP would spray the sample, whilst the other would be set to spray the chosen calibrant. The system would operate through the workflow shown in Figure 144.

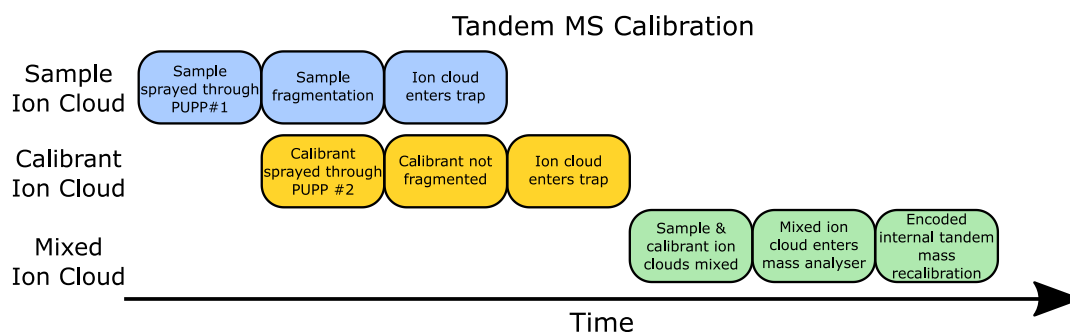


Figure 144 - Tandem MS Internal Encoded Calibration Workflow

When performing DDA experiment on unknown samples, the ability to have additional confidence in fragment assignment through improved mass accuracy will be highly beneficial, and following this workflow this would be achieved.

6.2 "In-source" Enzymatic Digestion

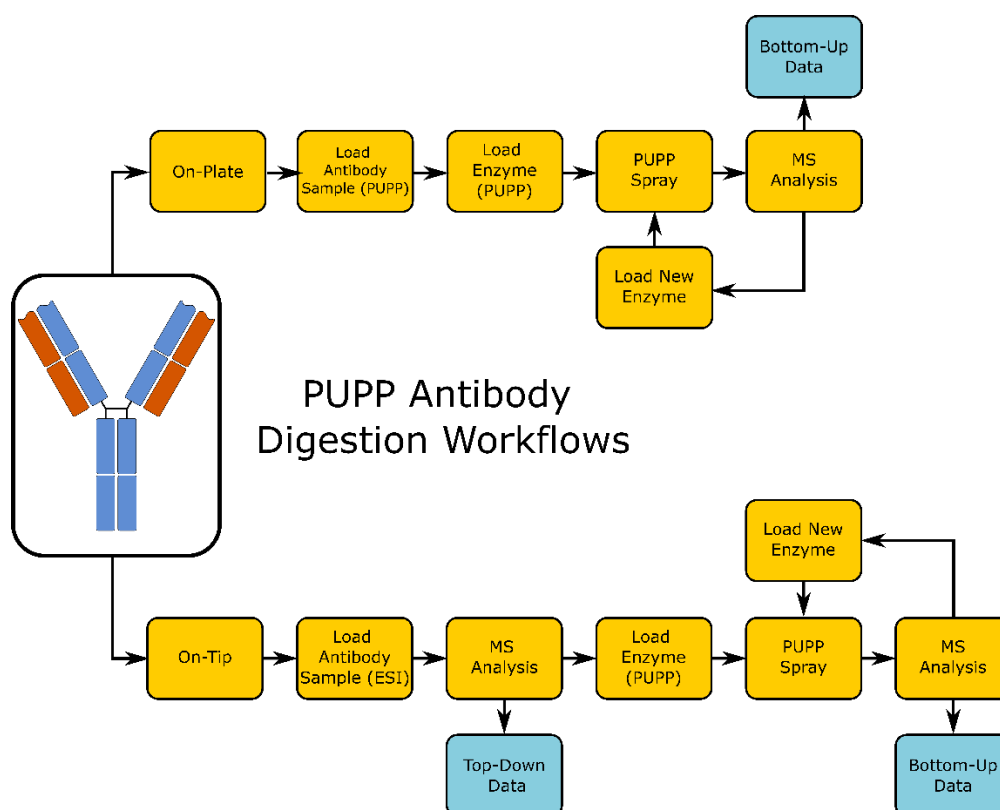


Figure 145 - Antibody Digestion Workflows using PUPP System

Microdroplet accelerated reactions have been successfully applied to a wide range of reaction types. More recently, focus has shifted towards their ability to perform reactions with biological molecules.^{206,207} Initially, ultrafast enzymatic digestions

of small-medium sized proteins were demonstrated within microdroplets. Since then, this has been extended to the digestion, reduction and deglycosylation of intact antibodies.²⁰⁸

The PUPP system is an effective way of rapidly generating microdroplet plumes, within which microdroplet accelerated reactions can be performed. Naturally therefore, the next step in this work is to apply this method to enable rapid structural characterization of intact antibodies using the PUPP system. There are different ways in which this can be performed, either by mixing the enzyme from the PUPP onto the ESI tip spraying the antibody (on-tip digestion) or by mixing the antibody and enzyme on the surface of the PUPP, and spraying the mixed solution (on-plate digestion). The workflows for both of these approaches have been summarized in Figure 145 and herein are discussed in further detail.

On-Tip Digestion:

Performing on-tip digestion requires the protein/antibody of interest to be continuously infused through an electrospray needle into the mass spectrometer. The PUPP is set to introduce short bursts of microdroplets containing the enzyme of choice onto the ESI tip. Here, the protein/antibody and enzyme solutions mix and co-electrospray, in which time the microdroplet accelerated enzymatic digestion takes place.

This method approach would enable users to rapidly switch between collecting top-down and bottom-up proteomics for protein/antibody analysis. Moreover, performing on-tip digestion allows the user to rapidly switch between digestion enzymes, giving more structural data for bottom-up analysis in a shorter space of time.

On Plate Digestion:

The alternative approach is to mix the protein/antibody and the digestion enzyme on the surface of the PUPP itself, before spraying for analysis. This approach does not allow for the rapid switching between top-down and bottom-up proteomics that on-tip digestion does. However, this approach would be more suitable for high throughput screening or optimization of reaction conditions (pH, protein/antibody to enzyme ratio, buffer concentration etc.) for protein digestions.

6.3 Rapid Analysis - Liquid Handling Robot Capability

As discussed in Chapter 4, the PUPP system is suitable for rapid analysis of samples, and throughout the duration of this project the system was only limited

by engineering requirements. Perhaps the most important of these is the capability to couple the system to a liquid handling robot, which would enable the analysis of hundreds of samples within a single run.

Liquid handling robots are routinely coupled to ambient ionisation sources. Work conducted using a liquid handling robot to prepare reaction screening samples in a 96-well plate and their subsequent transfer to a DESI plate is a good example of this.²⁰⁹ Similar coupling could be performed using the PUPP system, with the liquid handling robot being able to prepare the samples “on-plate” for subsequent analysis.

Moreover, correct use of a liquid handling robot would likely also overcome the carryover issued discussed in Chapter 4. Pre-programmed cleaning routines (akin to those used for cleaning the LC injection needle) could easily be installed, and use of more than one PUPP system would allow for the simultaneous cleaning of one PUPP whilst analysis continues using other PUPPs.

6.4 PUPP-DART-MS

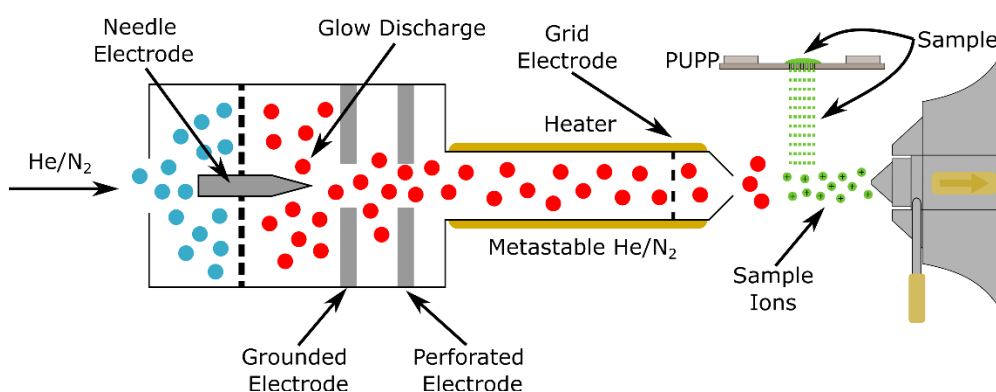


Figure 146 - PUPP-DART-MS Schematic

Direct Analysis in Real Time (DART) is an ionisation technique suitable for the rapid analysis of samples with little or no sample preparation required. The principles of DART are given in Chapter 1 of this thesis. In short, a carrier gas (typically He or N₂) is passed over a needle held at several kilovolts. The needle forms a glow discharge with the grounded electrode in front of it, which the carrier gas interacts with, forming a mixture of metastable ions which pass through a heated tube towards the inlet of the mass spectrometer, where they then ionize the sample.

During the development of the ionisation source for this project, methods of performing secondary charging of the microdroplet plume generated by the PUPP system were tested. Modifications to a DART ionisation source would be relatively

simple, as the sample region is open air allowing for the easy introduction of the PUPP microdroplets into the flow of plasma. Figure 146 shows an example schematic for how this set up would look.

Ultrasonic systems have been coupled to plasma-based ionisation sources before. Shimada et al. presented a system used for the analysis of ingredients in creams.²¹⁰ They used an ultrasonic transducer dispensed in water to pass ultrasonic waves into a sample bottle submerged in the same water, generating a mist of sample droplets. The sample droplets were then mixed with the metastable helium gas and directed into the MS inlet.

It is worth noting that Shimada et al. chose to mix the sample droplets and metastable gas immediately prior to the heated transfer tube. Sample ions were then generated by mixing of the sample mist with ionized water clusters formed by the DART metastable gas, as the mix passes through the heated transfer tube, the solvent evaporates, leaving charged sample ions. This process is akin to the charge residue model of ionisation. Moreover, the authors chose to run the DART ion source at low temperatures, enabling the analysis of heat unstable and non-volatile components often found in creams and lotions. An investigation into the optimum stage to introduce the PUPP mist into the metastable gas flow would need to be performed, and careful consideration for the temperature of the metastable gas should be maintained depending on the composition of the sample.

6.5 Summary

This chapter presents some recommended future work to be taken in this research which were beyond the scope of this project. These suggestions are broad projects, each of which would require significant development work, but the advantages of these systems/techniques are clear and have been outlined within this chapter.

Conclusion

This project presents a novel ionisation source for mass spectrometry which overcomes the limitations currently associated with performing internal recalibration for the analysis of complex samples. Initially, a commercially available piezoelectric droplet-on-demand device from Microdrop was tested with varying success. The system was coupled to a μ ESI system which generated the sample signal. Calibrant was able to be introduced to the analysis on demand. However, the system suffered from a series of limitations, including the droplet size, sample loading speed and system cost.

These limitations were overcome by switching to a Porous Ultrasonic Piezoelectric Plate (PUPP) system coupled to ESI. The PUPP-ESI was used for the analysis of a complex organic matter sample, Suwanee River Fulvic Acid, with high performance FT-ICR and Orbitrap Mass Spectrometry systems. The data was processed using Beacon software (Vibrat-Ion Ltd., UK) and using custom software constructed using LabVIEW. As expected, analysis using the encoded internal recalibration system did not change the peak assignments generated compared to conventional calibration techniques. However, the workflow necessary to process the data is entirely automated through the Beacon software, therefore significantly reducing the time to perform the same process on large batches of spectra.

Further to this, additional features of the software have been demonstrated which will be useful in a number of different applications. This includes the ability to identify and remove calibrant peaks from the spectra, and the software's ability to indicate why peaks selected for calibration were chosen, a tool that would be useful for retrospective audit purposes.

Further applications of the PUPP system have also been explored, and the system's capability to perform rapid analysis using low sample volumes (1-2 μ L) was shown through the analysis of beer, fruit juice, plasma and pharmaceutical samples. PUPP-PESI and conventional ESI data collected for 27 beer samples was subjected to PCA analysis to distinguish between pale, dark and malt beers, with the PUPP-PESI able to distinguish between the three as well as ESI.

Moreover, proof of concept data for component confirmation analysis for MS/MS experiments has been shown. Using the PUPP source to introduce a target component into the analysis at defined points, the system confirms the presence of a component in the sample, avoiding the use of expensive isotopically labelled standards for some applications. Alternatively, where the use of isotopically

labelled components is unavoidable, they can be introduced via the PUPP system, thereby reducing the quantity necessary as the standard can be introduced in selected spectra on demand.

In addition, data has been presented which shows the ability to perform on-the-fly solution adduct modification. When the PUPP system sprays solutions containing the target charge carrying species (e.g. Silver Nitrate to generate Silver Adducts), a rapid change in the adduct profile of the sample can be induced. It is well reported in the literature that the adduct of ions can impact the fragmentation pattern of the molecule, and can therefore be used to gain additional confidence in structural information.

The tools I have developed (both physical and software tools) throughout this project to assist with the development process have been presented. These include a 3D printed fused silica grinder, developed to enable to production of high quality electrospray needles at a fraction of the cost of commercially available electrospray needles. Moreover, the software tools used, including "Mezzo" - an mz5 file format reader, "THRASHer" - a peak detection algorithm, "Ion-Sync" - a tool to synchronize the ionisation source and the mass spectrometer, "Transcend" - for viewing and processing transient data files, and "MISSI" - an interface to control the Microdrop Ion Source have all been presented.

Finally, an in-depth discussion around future applications of the ionisation source, beyond the scope of this project, has been given. The system's potential ability to perform on-tip and on-plate protein/antibody digestion, tandem MS internal encoded recalibration and the introduction of a liquid handling robot to advance the capabilities of the system to perform rapid analysis are all discussed.

The PUPP ionisation source has been shown to be a highly sensitive system which can be used for a variety of applications with little or no modifications. Data has been presented which characterizes the ion source's performance in internal encoded recalibration, on-tip protein digestion, adduct modification, rapid analysis and component confirmation. Finally, further potential applications have been discussed in detail, which should be subsequently explored in future work.

Section B: Microdroplet Accelerated Reactions

This section of the thesis is dedicated to the work conducted into performing microdroplet accelerated reactions, specifically investigating whether performing synthesis on a gram scale using this technique was possible. The first chapter of this section provides the reader with a fundamental understanding of the mechanisms behind this effect, as well as the current literature. After this, a chapter is dedicated to the investigations performed into two reactions: the Hydrazone synthesis and the Pechmann condensation.

Chapter 7: Introduction, Aims & Experimental

This chapter provides an overview into the substantial increase in reaction rates observed within microdroplets, most commonly performed using mass spectrometry ionisation sources. The mechanisms behind this effect are explained, along with an overview of the current chemical and biochemical reactions found to undergo this effect and the methods of generating the desired microdroplet reaction vessels. Finally, the reactions and systems used for scale-up microdroplet synthesis experiments are discussed, which was the primary focus for this work.

7.0 Introduction

Within the last decade, there has been significant work conducted within the mass spectrometry community which focuses on the use of mass spectrometers as a tool for chemical synthesis. The work stems from the observed significant acceleration in chemical reaction rate when performed in charged microdroplets compared to their conventional synthesis counterparts. The magnitude of the acceleration varies, although in many cases the effect is significant, with acceleration factors of six orders of magnitude reported in some studies.²¹¹

Mass Spectrometry ionisation sources generate small, uniform and highly charged droplets (ideal environments for accelerated reactions) which subsequently desolvate, reducing in size until bare gaseous ions are left. The majority of the work conducted thus far uses electrospray ionisation or variations of this technique as the mechanism of generating microdroplets, although accelerated reactions have been demonstrated in a range of different ambient and non-ambient ionisation sources.

The effect is not limited to a specific class of reactions, with various reports of acceleration observed in small organic, inorganic and biochemical reactions. Whilst the literature covers a spectrum of different reaction classes, there is still much to be understood on the mechanism by which microdroplets drive reactions.

There are a number of different ways in which this rate acceleration can be adopted to advantage chemical synthesis. When coupled to higher throughput ionisation sources, such as DESI, microdroplet acceleration can be used to perform reaction screening, synthetic route planning, solvent selection and optimization of conditions.

Various excellent reviews which cover the literature in microdroplet synthesis have been published, which review the droplet generation techniques and reactions which were susceptible to acceleration.²¹²⁻²¹⁶

Herein, this chapter gives an overview of the progress made thus far in microdroplet chemistry. This begins by exploring the history of microdroplet acceleration, the principles which drive this effect, the reactions shown to proceed via microdroplet chemistry and the droplet generation mechanisms which have been successfully used thus far. Finally, the progress in performing scaled up microdroplet synthesis is discussed.

7.1 History

Despite the recent flourish of attention which microdroplet chemistry has seen, there are examples of mass spectrometry being used preparatively since the 1940s. Calutron mass spectrometers were used to purify Uranium samples by m/z selection to isolate the 42 kg of ^{235}U used in the first nuclear weapons for the Manhattan project.²¹⁷

There have been a series of reports of ion-ion chemistry being performed in the gas phase of mass spectrometers since the 1970s.²¹⁸ These showed a significant rate enhancement of several orders of magnitude, at the time suggested to be due to the enhanced attractive forces between ions due to their lack of solvation, that would otherwise have required energy to overcome when performed in solution phase.

In 2006, the Eberlin reaction, whereby cyclic acetals undergo transacetalization with acylium ions, was demonstrated to occur via microdroplet-ion interactions.²¹⁹ Microdroplets containing the acylium ion were generated through electrosonic spray ionisation (ESSI), which were passed through a vapour of cyclic acetal, generating product yields of over 60%. This is one of the earlier examples of the reaction acceleration being attributed towards the effects of the microdroplet surface region, and subsequently inspired much of the early work investigating microdroplet chemistry. Today, there is a vast array of different reaction types accelerated by microdroplets, an overview of which is given in Section 7.4.

7.2 Mechanism

Reaction acceleration is driven by a series of properties of microdroplets which provide a unique environment for reactions to occur in. Although each of these properties contributes to the acceleration observed, significant work is still needed to fully understand the mechanisms of acceleration, and to quantify the

contribution of each property towards the acceleration effect (which may not be consistent between reactions). Overall, the microdroplet properties can be summarized as; rapid desolvation, pH effects, enthalpy effects, entropy effects, and rapid diffusion/mixing of reactants. These effects are each subsequently discussed in detail.

7.2.1 Rapid Desolvation

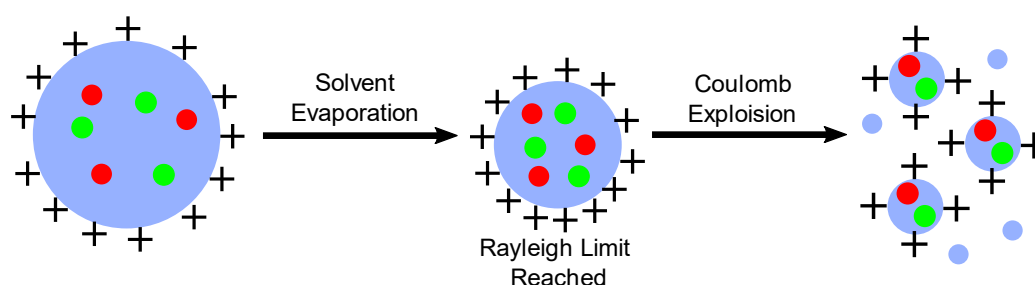


Figure 147 - Microdroplet Concentration Effect

Microdroplets exhibit a much faster rate of solvent evaporation compared to larger droplets or bulk solutions of the equivalent solvent. This is due to the high surface area to volume ratio seen at such low radius droplets, which gives a large surface area for the solvent to evaporate into the surrounding environment.

When the microdroplets in question are charged, such as those generated by most mass spectrometry ionisation sources, there is an additional factor which drives the droplet desolvation process. This process is identical to that described for electrospray ionisation in Chapter 1. In summary, the point charges of the droplet gather at the surface where alike charges will repel one another. As the droplet volume (and therefore surface area) decreases due to solvent evaporation, these surface charges are forced closer together. Eventually, the repulsive force experienced between surface charges overcomes the surface tension of the droplet itself, causing the droplet to break up into a number of smaller droplets (known as a Coulombic explosion). This process further increases the surface area to volume ratio of the remaining liquid, and hence accelerates the evaporation process.

These two processes mean that reagents compartmentalized inside a microdroplet, undergo a significant increase in their observed concentration, as the droplet volume rapidly reduces. This rapid increase in concentration could drive reactions at a much faster rate than a bulk solution at the starting concentration.

When performing microdroplet acceleration within a mass spectrometry ionisation source, there have been numerous pieces of research which focus on the effect of

increasing desolvation on the reactant/product distribution observed in the spectra. Increasing inlet temperature, decreasing spray emitter size, increasing droplet flight distance, and increasing surfactant concentration are all examples of methods used to increase desolvation rates.^{220,221} As expected therefore, these parameters can be adjusted to drive the extent of microdroplet acceleration, observed by changes in the product/reactant ratio.

7.2.2 pH Effects

Microdroplets also exhibit extremes in the pH level which drive reactions. Acidic microdroplets for example which decrease in volume will also see a decrease in the pH.²²²⁻²²⁴ This is in part due to the solvent evaporation causing an overall increase in the proton concentration of the droplet, but also due to the effect of the electric field the microdroplet experiences, inducing proton transfer from the solvent. This has been observed during DESI, whereby a bulk solution of pH 3.0 sprayed gives a primary droplet pH of 2.0 and a pH of just 0.5 at the point of impact on the surface. The principle is also true of basic droplets, for which during the DESI microdroplet Michael reaction, the bulk solution of pH 10.1 gave a primary microdroplet of pH 12.6 and pH 13.3 for the secondary microdroplet.²²⁵

7.2.3 Enthalpy

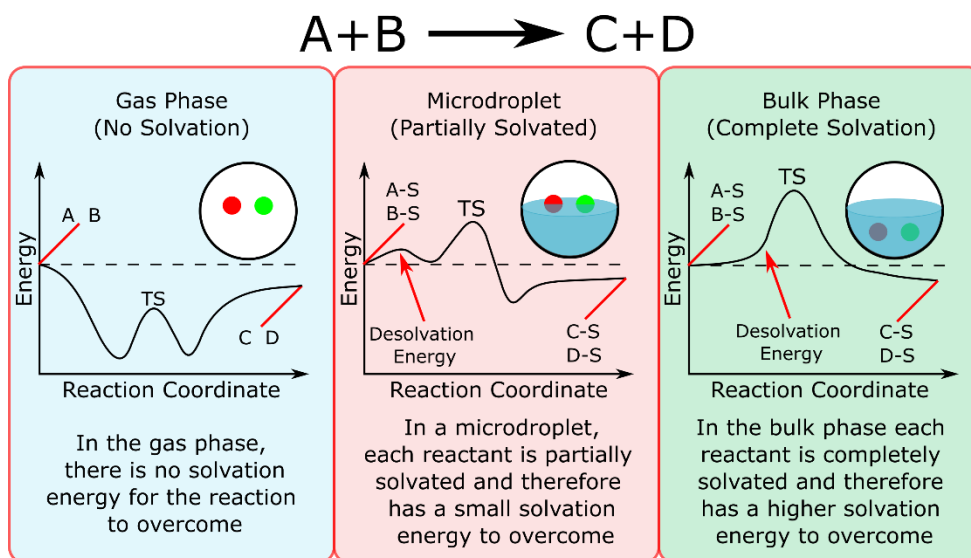


Figure 148 - Effect of different levels of solvation on activation energy

Note: this is an adaptation of a Figure by Wei et al.²²⁶

There is an enormous difference in the rate constants for common reaction steps performed in the gas phase compared to solution phase. This difference is because of the additional energy required for the desolvation of reactants in solution, which is not necessary for reactions performed in the gas phase. Polar reactants in microdroplets tend to aggregate towards the surface of the microdroplet, where

they are partially solvated. This partial solvation means the activation energy for microdroplet reactions lies between that of reactions performed in the gas phase and those performed in solution. Figure 148, shows the difference in activation energy for different levels of solvation with example reaction coordinate diagrams.

7.2.4 Entropy

As mentioned, polar molecules tend to aggregate at the droplet surface, leading to a concentration gradient within the droplet itself. This aggregation has been observed through Fluorescence Anisotropy, using Rhodamine R6G as a dye to perform visualization experiments.²²⁷ The results of this study not only showed the aggregation of molecules at the surface, but also the fixed orientation of said molecules. As surface molecules are more ordered they therefore have a reduced entropy, which reduces the free energy change necessary for the reaction to occur.

This entropy effect has already been documented in micro-diameter emulsion droplets, which gave a reduction in the overall free energy change for an imine synthesis, because of the ordered molecular orientation of reactants at the droplet interface.²²⁸

The phosphorylation of sugars provides an excellent example of a reaction which is thermodynamically unfavorable in bulk solution, with a ΔG value of +5.4 kcal/mol, which is able to proceed spontaneously in microdroplets. The reduction in entropy reduces the overall free energy necessary for the reaction to proceed, down to just -1.1 kcal/mol.²²⁹

7.2.5 Rapid Diffusion/Mixing of Reactants

The contribution of the droplet surface to accelerated microdroplet reactions is clear. However, the surface of the droplet remains a very small portion of the droplet itself, and therefore this does not completely justify how reactions are being driven if only a very small portion of the droplet undergoes these effects. However, this is explained by the very high rate of diffusion of reactants towards the droplet surface which is observed.

Microdroplets produced in an ambient environment experience a degree of turbulence, which in turn drives diffusion and mixing within the microdroplet. This irregular motion is the summed effect of droplet interaction with the surrounding gas as it moves through the air, solvent evaporation and Rayleigh jets produced by charged droplets.²³⁰⁻²³²

Moreover, the reactants and products experience rapid rates of diffusion within the microdroplet. Reactants in the surface region of the droplet are much more likely to react and form products, and thus a concentration gradient for both reactants and products forms very quickly between the droplet core and the droplet surface, inducing diffusion of both. This has been shown visually in Figure 149. Theoretical models have been presented which describe the formation of products at the droplet surface which subsequently rapidly diffuse into the inner volume of the droplet.²²⁸

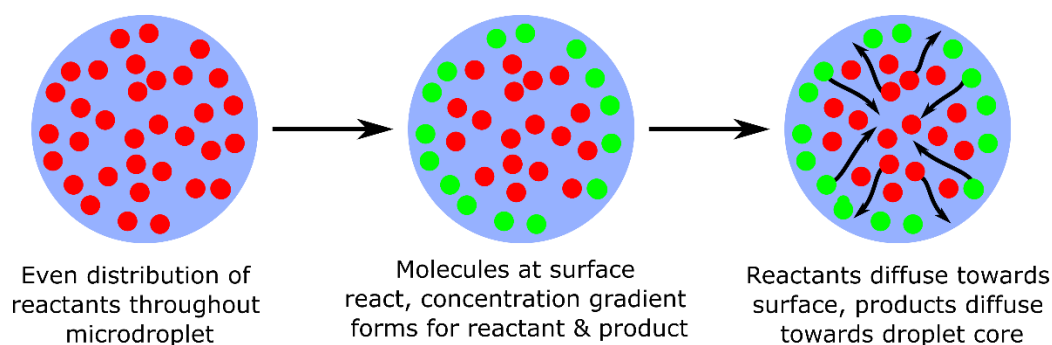


Figure 149 - Rapid Diffusion in Microdroplets

7.3 Microdroplet Generating Methods

Many mass spectrometry ionisation sources act as an efficient method of generating small highly charged microdroplets ideal for accelerated synthesis. Much of the work uses ESI, DESI and Paper Spray ionisation, the principles of which are all given in Chapter 1. Some other spray-based techniques that have been applied to microdroplet chemistry include Extractive Electrospray Ionisation (EESI), Electrosonic Spray Ionisation (ESSI) and Thermospray Ionization.^{208,230,233} Larger volumes of microdroplets can be generated through ultrasonic methods, which often do not suffer from the limitations associated with many other spray-based techniques of the maximum flow rate of the nozzle/spray tip.

The microdroplet effect is not limited to spray-based techniques, there are a number of reactions which have been shown to proceed within a Leidenfrost droplet. Leidenfrost droplets are formed when a solvent droplet is created above a surface at a temperature higher than the solvent boiling point, which is levitated by a vapour cushion that forms.^{234,235} Many of the underlying principles behind microdroplet reaction acceleration are also observed for reactions performed in thin films, whereby a thin layer of reaction mixture (and therefore large surface area) is deposited on a surface.²³⁶⁻²³⁹

7.4 Current Reactions

The majority of the work around microdroplet synthesis has focused on small organic molecule reactions. There are a variety of different reactions which have been performed, including, but not limited to; the Claisen-Schmidt Condensation, Fisher-Indole Synthesis, Hantzsch Synthesis, Isoquinoline Synthesis and Suzuki Couplings.^{211,221,235,240-243}

The unimolecular ring closure of imines to form the Isoquinoline products are a rare example of a unimolecular reaction accelerated by microdroplets.^{211,243} These reactions are not influenced by the reactant concentration effect seen through desolvation, suggesting that the surface and pH effects discussed previously are sufficient to drive these reactions.

Although the majority of the work has focused on small organic molecule synthesis, microdroplet reactions are by no means limited to this. Gold and Silver nanoparticle synthesis, forced degradation, hydrogen-peroxide generation, and Hydrogen-Deuterium exchange reactions have all been shown to proceed at significantly faster rates in microdroplets than in bulk solution.²⁴⁴⁻²⁵⁰

More recently, microdroplet acceleration has been applied to biochemical reactions. These include the reactions commonly associated with structural analysis of proteins and larger structures such as antibodies, including the reduction, digestion and deglycosylation of proteins.^{206-208,251} Although these reactions have not yet been performed simultaneously within the confinement of a microdroplet, this is the early stage of being able to perform a complete ultra-fast bottom-up proteomic analysis, which could have a potentially significant impact on proteomic workflow approaches. Alongside structural analysis, protein folding/unfolding and protein-ligand interaction studies, such as the complexation between cytochrome c and maltose, have also been studied through microdroplet chemistry.^{230,243,252}

7.5 Large Scale Microdroplet Synthesis

The acceleration factor observed for microdroplet synthesis makes it an appealing method of generating product away from the mass spectrometer, often referred to as "offline" synthesis. Early work in this area was limited in the volume of microdroplets generated per unit time, and the ability to recycle the solvent used. Although the former of these issues was improved by using multiple sprayers, this is neither a cost-effective approach nor a practical method of significant scale up.

As systems focused towards the use of ultrasonic or pneumatic based sprayers which could generate significant volumes of microdroplets per unit time, the rate of product generation increased, as shown in Table 9, which summarises the significant research published for offline synthesis.

Table 9 - Overview of Scale Up Microdroplet Synthesis			
Year	Reaction *	Method	Rate (mg/hr) [‡]
2012 ²⁵³	Claisen-Schmidt	Preparative Electrospray	≈ 35 mg/hr
2017 ²³⁷	Claisen-Schmidt	Preparative Electrospray	≈ 98 mg/hr
2017 ²⁵⁴	Alcohol Oxidation to Aldehyde/Ketone	Dual Phase Pneumatic Spray	≈ 72 mg/hr
2018 ²⁵⁵	Aldehyde Oxidation to Carboxylic Acid	Dual Phase Pneumatic Spray	≈ 630 mg/hr
2019 ²⁵⁶	Alcohol Oxidation to Carboxylic Acid	Preparative Paper Spray	≈ 19 mg/hr
2019 ²⁵⁷	Eschenmoser Coupling	Heated Ultrasonic Nebulisation	≈ 2400 mg/hr
2019 ²⁵⁸	Claisen-Schmidt	Pneumatic Spray & Solvent Recycling System	≈ 3180 mg/hr
<i>*Where more than one reaction is reported in the article, the reaction which generated the highest rate of product has been reported</i>			
<i>‡All reported rates have been converted to mg/hr for direct comparison between methods</i>			

The two most significant advances in systems reported at the time of writing are the Heated Ultrasonic Nebuliser by Liu et al. and the Pneumatic Sprayer with Solvent Recycling capabilities by Nie et al.^{257,258} These systems are both capable of generating grams of high purity product per hour for a series of different reactions. It is clear that the ultimate goal of this area of research is to provide a new approach for industrial synthesis. Over the coming years, continuing to increase the scale of microdroplet synthesis and the ability to perform multistep reactions will likely be the next hurdles to overcome before this approach is applied within industry.

7.6 Summary

The ability to perform reactions at such high rates within the confinement of a microdroplet has opened a new door to chemical and biochemical synthesis. This chapter has given an overview on the underlying mechanisms behind the acceleration effect. There is a vast array of different reaction types which have been shown to undergo rate acceleration in microdroplets, including small organic

molecule, non-covalent and biochemical reactions. This chapter has presented an overview of these reactions.

The majority of the work thus far has been performed online, whereby the microdroplets generated in an ionisation source are directed into a mass spectrometer for immediate analysis. More recently however, focus has shifted towards how microdroplet chemistry can be used to perform scaled up offline synthesis, whereby more significant amounts of product can be collected away from the mass spectrometer. For both of these approaches, an overview has been given for the methods of producing the desired microdroplets.

7.7 Aims

The aim of this project was to develop a system which could rapidly generate gram scale yields of product through the use of microdroplet accelerated reactions. However, as will be shown in this chapter, the focus of the project shifted during the testing of the system. Two reactions that were investigated as part of this development work both produced unexpected results which are reported within.

Henceforth, the aim of the project was altered to focus on development of a recommended series of screening tests which should be performed for microdroplet accelerated reactions, in order to ensure data transparency between publications.

7.8 Experimental

Herein, the equipment, reagents and methods used within this research are given.

7.8.1 Equipment/Instrumentation

- Chemyx Fusion 200 Dual Syringe Pump
- Waters Xevo G2-XS Q-TOF Mass Spectrometer
- Waters Acquity UPLC System
- Ultimaker S3 3D Printer
- JEOL ECZ 400 MHz NMR Spectrometer

7.8.2 Reagents

LC-MS grade Acetonitrile used for Mobile Phase was purchased through Fisher Scientific. All other organic solvents, formic acid and sulfuric acid were purchased through Fisher and, unless specified otherwise, were Analytical Reagent Grade. LC-MS Water obtained through a Thermo Barnstead Nanopure Analytical UV System. Ethyl Acetoacetate, Ethyl 2-benzyl-acetoacetate, Malonic Acid, Ethyl 2-ethyl-acetoacetate, Resorcinol, Phloroglucinol, 2-Methyl-Resorcinol, Isatin,

Phenylhydrazine were all purchased through Sigma-Aldrich and were reagent grade.

7.8.3 Instrument Methods

Throughout analysis the LC method shown in Table 10 was used. Analysis was performed on a Waters Acquity UPLC System coupled to a Acquity PDA Detector (190 to 500 nm) and a Waters Xevo G2-XS Q-TOF Mass Spectrometer. The column used was a Raptor C18 Column (2.7 μm , 100 x 2.1 mm). Direct Infusion was performed on the same Waters Xevo G2-XS Q-TOF Mass Spectrometer with a Chemyx Fusion 200 Dual Syringe Pump and using the same tune method for the UPLC analysis. NMR Spectra were collected using a JEOL ECZ 400 MHz NMR Spectrometer. The solvent used for all NMR analysis was DMSO- d_6 .

Table 10 - UPLC-UV/MS Method			
Mobile Phase A	H ₂ O:ACN:FA 90:10:0.1		
Mobile Phase B	ACN:FA 100:0.1		
Time (mins)	%A	%B	Flow Rate (mL/min)
0.00	80.0	20.0	0.250
1.50	80.0	20.0	0.250
5.00	10.0	90.0	0.250
10.00	10.0	90.0	0.250
12.00	80.0	20.0	0.250
13.00	80.0	20.0	0.250

7.8.4 Hydrazone Reaction

Reference Material Synthesis:

5 mmol of Isatin and Phenylhydrazine added to 100mL round bottom flask containing 50 mL Ethanol. Mixture refluxed at 90°C for 2 Hours. Crude product recrystallized from Ethanol. Method adapted from Sridhar et al.²⁵⁹

Online Microdroplet Synthesis:

25 μL of Phenylhydrazine was added to 2.5 mL of 3 mmol Isatin prepared in MeOH. 25 μL of Formic Acid was added, and immediately loaded onto a 5 mL Hamilton Syringe. Direct Infusion was performed at 0.05 $\mu\text{L}/\text{min}$ and recorded on a Xevo G2-XS Q-TOF Mass Spectrometer. Method adapted from Bain et al.²⁶⁰

Offline Microdroplet Synthesis:

Equal volumes of 100 mmol dm⁻³ solutions of Isatin and Phenylhydrazine in Acetonitrile were mixed in a reaction vessel and sprayed using an ultrasonic humidifier for a user controlled period of time (usually between 10 and 60 minutes). Samples were filtered using a 0.45 µm syringe filter before analysis.

7.8.5 Pechmann Condensation

Bulk Synthesis:

0.010 mol of Resorcinol and 0.010 mol of Ethyl Acetoacetate were weighed into a 100 mL round bottom flask. 10 mL of conc. H₂SO₄ was added dropwise to the reaction mixture so it did not rise above 10°C. The reaction mixture was stirred for 15 hours at room temperature before rapidly cooling in an ice bath to form crude product. Crude product was vacuum filtered off before being recrystallized from Ethanol. Method adapted from Sahni et al.²⁶¹

Online Microdroplet Synthesis:

2.5 mmol dm⁻³ solution of Resorcinol and Ethyl Acetoacetate were prepared in 50:50 MeOH:H₂O. Sulfuric Acid was added to give a final acid concentration of 1.25 mmol dm⁻³. The solution was loaded onto a 5 mL Hamilton Gas Tight Syringe and infused at 0.05 mL/min into the ESI Source.

Chapter 8: Microdroplet Accelerated Synthesis

This chapter describes the microdroplet accelerated reaction work performed during this PhD. The initial aim of this chapter was to develop a system which would be capable of generating useful quantities of product in a short space of time (up to grams per minute) by using the accelerated rate of reactions observed within microdroplets discussed in Chapter 7.

Initially, the Hydrazone reaction was used to perform development work on the system. However, a previously unreported and interesting difference in the product formed was observed, leading to an investigation into the identity of this unexpected product. The Pechmann condensation reaction was subsequently used for development work, but this reaction was later found to be unsuitable. These results are presented and discussed within this chapter.

The two hurdles encountered when using these reactions for scale-up system development led to the creation of a set of recommended screening methods which are presented in this chapter. These experiments, which are in some cases either not performed or not reported within the literature, aim to reduce the likelihood of reactions which are unlikely to be successful as candidates for scaled up microdroplet synthesis.

8.0 Microdroplet Accelerated Synthesis

This chapter presents some of the work performed investigating microdroplet accelerated reactions, with the specific aim of performing them away from the mass spectrometer on a gram-scale synthesis level. This work initially focuses on the Hydrazone synthesis, previously reported in the literature online only, and then subsequently focuses on a previously unreported microdroplet accelerated reaction: the Pechmann condensation.

8.1 Hydrazone Synthesis

Initially, a microdroplet accelerated reaction which had been previously published by the Cooks group was selected for method development purposes; the Hydrazone reaction. This reaction was chosen to ensure that development of an offline synthesis system was being tested on a reaction which is known to proceed via microdroplet chemistry. This reaction was selected to ensure that the focus on the project remained on the development of the microdroplet synthesis system, rather than presenting a previously unreported reaction susceptible to microdroplet acceleration. The mechanism for the reaction between Isatin and Phenylhydrazine, used throughout development, can be seen below in Figure 150.

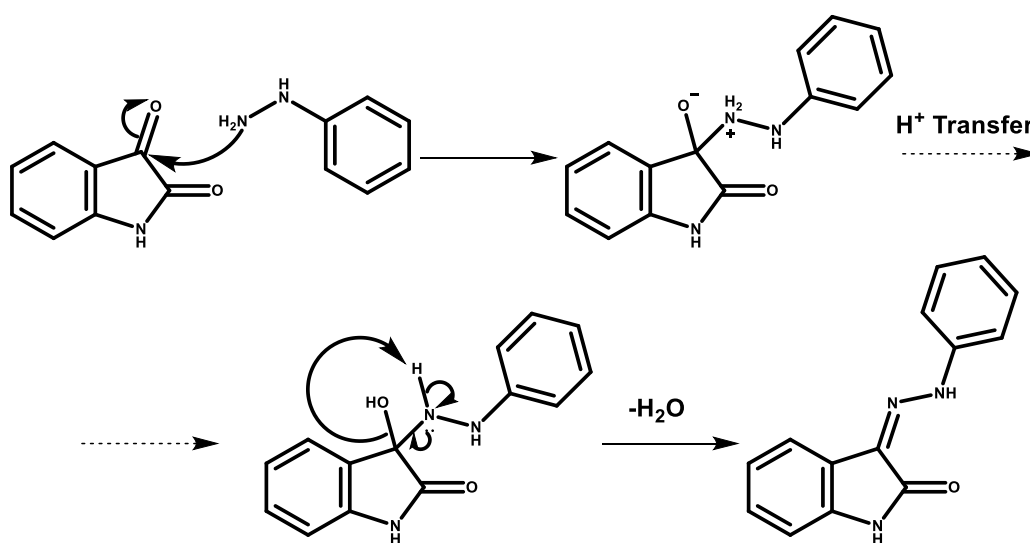


Figure 150 – The Hydrazone Reaction

The work published by Cooks et al. focused on performing the Hydrazone reaction "online", whereby charged microdroplets generated through ESSI are directed into the inlet of the mass spectrometer for immediate analysis. The online synthesis gave a rate acceleration factor of approximately 10^4 , relative to the bulk synthesis rate. Their work showed the effect of increasing the distance the microdroplets travelled on the reaction; as the distance between the ESSI needle and the inlet is increased, the intensity of the product peak relative to the reactants increases.

Their work concluded that this would most likely be due to the additional desolvation the droplets were able to undergo before entering the inlet. Hydrazone synthesis has also been shown to proceed in Leidenfrost droplets.^{234,262} The work conducted on the Hydrazone synthesis showed an acceleration factor of 6 compared to the bulk reaction.

Finally, accelerated microdroplet Hydrazone synthesis has been shown using Field Desorption (FD) Ionisation.^{263,264} FD uses small microstructures to create very high electric field strengths despite only using modest potentials. The emitter used a 13 μm wide tungsten wire, onto which micro-graphite whiskers were electrolytically grown. An aliquot of the reaction mixture was transferred onto the emitter by dipping it into the reaction mixture itself. The work includes data which shows an increase in product observed by increasing the distance between emitter and inlet, supporting that of the ESSI study. It should be noted however, that for field desorption ionisation both the radical product cation ($[\text{M}]^+$) and the protonated molecule ($[\text{M}+\text{H}]^+$) are observed, and the ratio of the two changes as the emitter is moved further away from the inlet in favor of the protonated molecule. This is assumed to be because of the decrease in field strength as the emitter moves further away.

8.1.1 Online Synthesis:

Initially, online synthesis was performed through electrospray ionisation to confirm the presence of Hydrazone product to match the results obtained by the Cooks group. The spectrum obtained (Figure 151) confirms a clear product peak is present, and the fragmentation pattern matched that of the bulk synthesis reference material produced, indicating the reaction as proceeding via ESI. This was deemed to be sufficient evidence that the literature result could be repeated, and therefore focus shifted towards the development of offline synthesis systems.

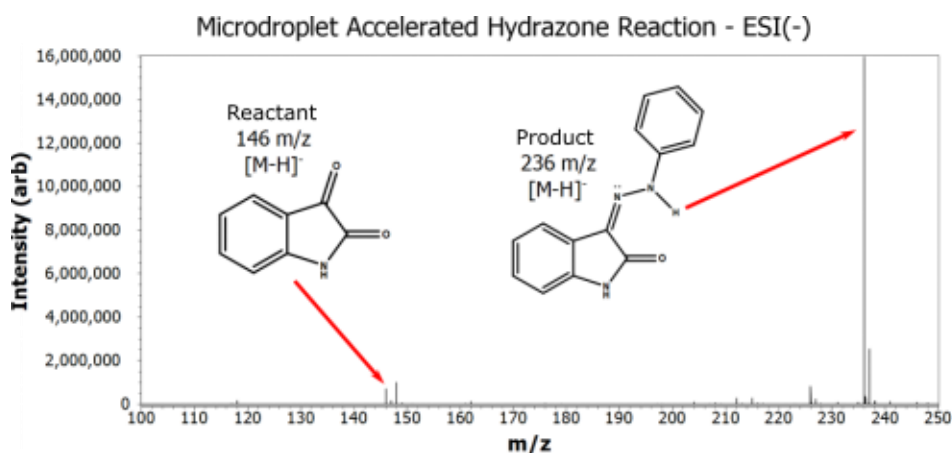


Figure 151 - Microdroplet Accelerated Hydrazone Reaction Spectra - ESI(-)

8.1.2 Offline Synthesis:

Performing offline microdroplet synthesis requires a system which is capable of generating a large number of small microdroplets, and should be easily adaptable for a range of solvents. Many of the systems used for online microdroplet acceleration have been used to generate small quantities of product away from the mass spectrometer. Electro spray is one of the most common examples of this, and increased throughput has achieved by running multiple electro sprays simultaneously. However, as discussed previously in Chapter 7, this is not a suitable technique for true large scale microdroplet synthesis, because of the modest increase in throughput achieved at high cost and complexity.

Greater success was achieved through the use of ultrasonic based systems by the Cooks and Zare groups, which has been thoroughly discussed in Chapter 7.^{257,258} These publications were released during the development of the large scale microdroplet synthesis method herein discussed during this thesis.

The PUPP system, previously presented as a method of generating microdroplets for the ionisation source(s) discussed during Section A, was highlighted as an ideal method of generating microdroplets which would be suitable for large scale synthesis. The PUPP system is capable of generating large plumes of small microdroplets for liquid of varying viscosities.

The PUPP system, enclosed in a plastic housing to protect the electronics, was placed inside a sealed container with the reaction mixture at the bottom (see Figure 152). The PUPP system could be set to continuously generate microdroplets of the reaction mixture, which would condense on the sides of the sealed container, where they would eventually pass back into the solution for respraying.

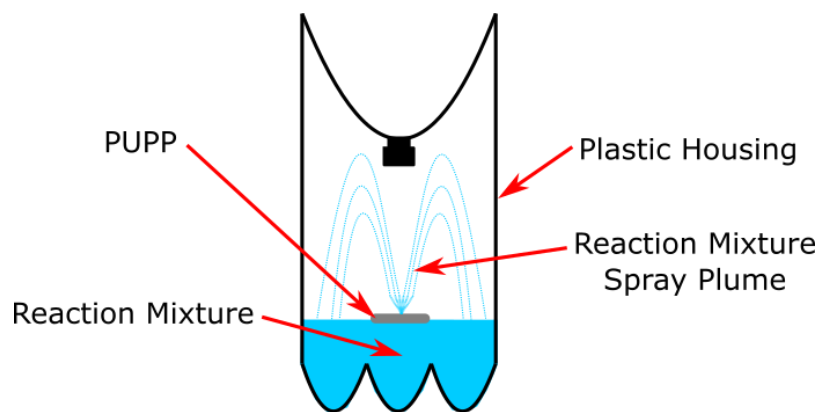


Figure 152 - Offline Microdroplet Synthesis Setup

A reaction mixture containing 0.25 mol dm^{-3} of Isatin and Phenylhydrazine was prepared in MeOH. 20 mL of reaction mixture was transferred to the microdroplet spray vessel and sprayed for 20 minutes. An aliquot of this mixture was then immediately diluted to prevent any product formation outside of the microdroplet environment, and analysed by LC-MS.

Unexpectedly, two LC-MS peaks were observed for the corresponding mass (m/z) of the product ($238.1 \pm 0.05 \text{ m/z}$), at retention times of 3.68 and 5.04 minutes, and these peaks were both present when analysis of the reference material is performed. However, there was a significant difference in the ratio of the peak areas between the sprayed sample and the reference material. The peak ratio shifted from an approximate ratio of 1:10 to 3:1.

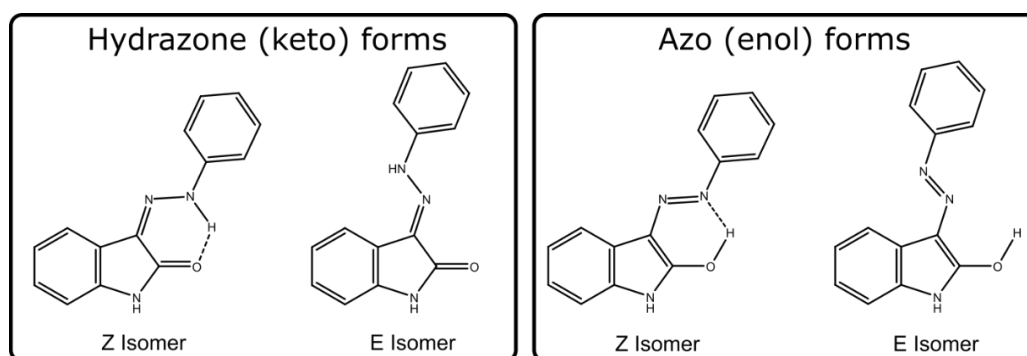


Figure 153 - Keto vs Enol Products

Two possible solutions for this were discussed. The first is that the microdroplet reaction preferentially forms the Azo (enol) product over the hydrazone (keto) product, both of which are shown in Figure 153. Alternatively, it was hypothesized that the microdroplet reaction forms the same structural isomer, but preferentially forms one stereoisomer (E or Z) over the stereoisomer conventionally seen in excess following a conventional bulk reaction.

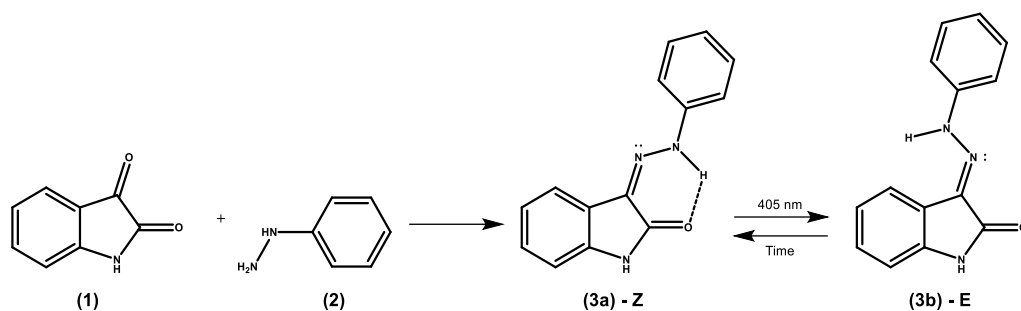


Figure 154 - Hydrazone Synthesis with E/Z Isomer Formation

Fragmentation patterns of the two LC peaks were shown to be identical, indicating that both the LC peaks contained identical structural isomers (Data shown in Table 23 in the appendix). Further evidence that the two LC peaks were stereoisomers was gathered by exploiting a photochromism property of these molecules; isatin phenylhydrazone undergoes photo-switching between E and Z isomers when exposed to 405 nm light for short periods of time.^{265,266} The reaction scheme for the photoswitching between E/Z isomers is given in Figure 154.

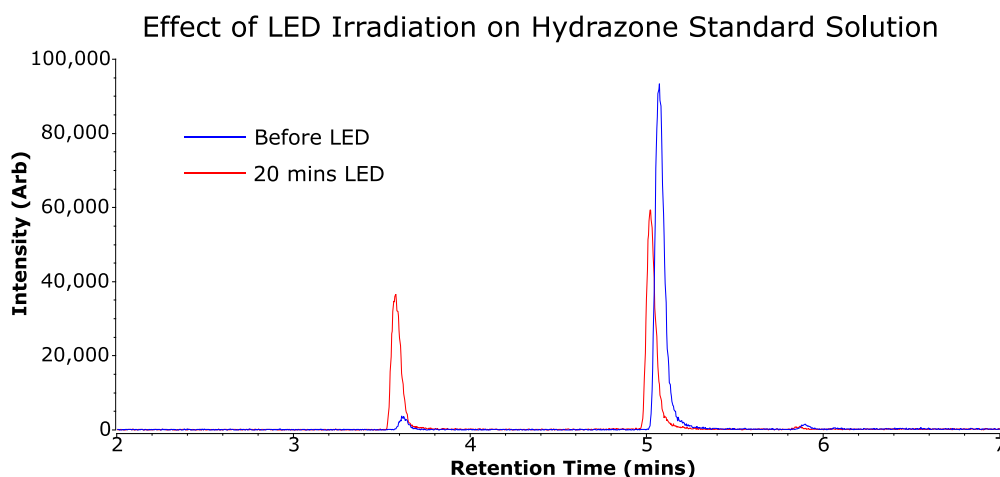


Figure 155 - Effect of LED Irradiation on Isatin Phenylhydrazone LC-MS

Solutions of the reference material were analysed by LC-MS/MS and ^1H NMR before and after irradiation using 405 nm LEDs. Significant shifts in the ratio between the two LC peaks were observed (Figure 155), with no other peaks changing, which suggested the two LC peaks were the E/Z stereoisomers. Similarly in the ^1H NMR the appearance of two singlets at 10.54 and 10.44 ppm and a doublet at 8.16 ppm (Figure 156) is observed identical to that described in the literature for these stereoisomers.²⁶⁵ Assignments for both ^1H NMR spectra can be found in the appendix, along with a discussion around the changes observed.

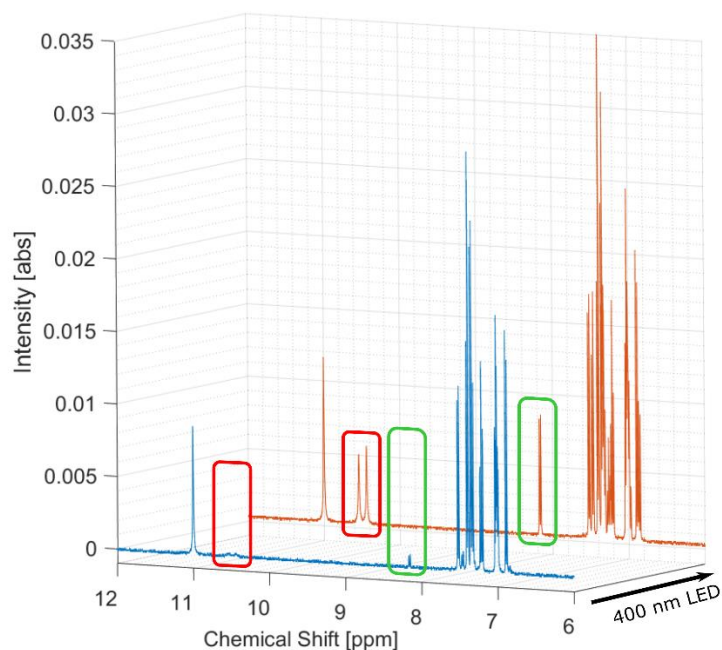


Figure 156 – Effect of LED Irradiation on ¹H NMR Spectrum of Isatin Phenylhydrazone

The literature discussing the photochromic behavior also presents data to show how the E isomer undergoes photorelaxation over time to reform the more stable Z isomer. This can also be seen in a time course of multiple runs of LC-MS taken at specific times after synthesis for the microdroplet accelerated product; the ratio of the two LC-MS peaks changes as the Z isomer re-forms. Isatin Phenylhydrazone synthesized by microdroplets was injected regularly over an 18-hour time period. Figure 157 shows a waterfall plot for the analysis of this sample over time, clearly showing the change in the E/Z isomer ratio observed.

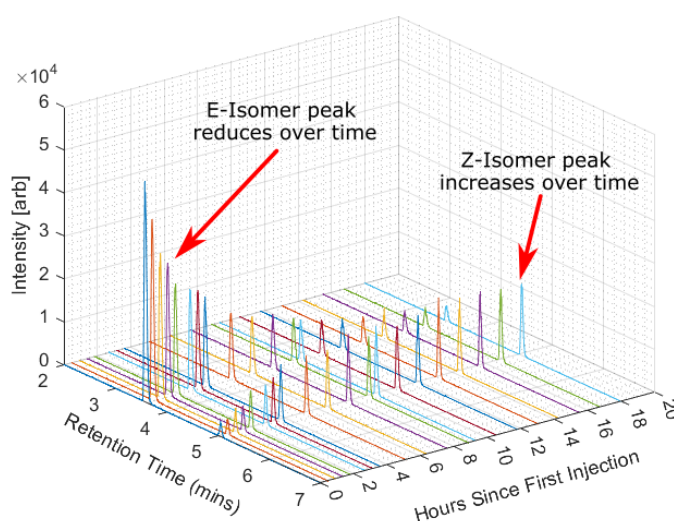


Figure 157 – Shift in E/Z Isomer Ratio Over Time observed for Microdroplet Accelerated Hydrazone Product

Data was collected to confirm that this is a true microdroplet spray effect, and not that the reaction is simply occurring when left as a bulk solution. Identical reaction mixtures were prepared and only one set of solutions were subsequently sprayed (in the same manner described previously). The two sets of solutions were then diluted (to prevent further reaction) and analysed by LC-MS. Typical LC-MS chromatograms obtained for these two solutions are shown in Figure 158, clearly showing a significantly higher yield of product for the sprayed solutions compared to the unsprayed solutions.

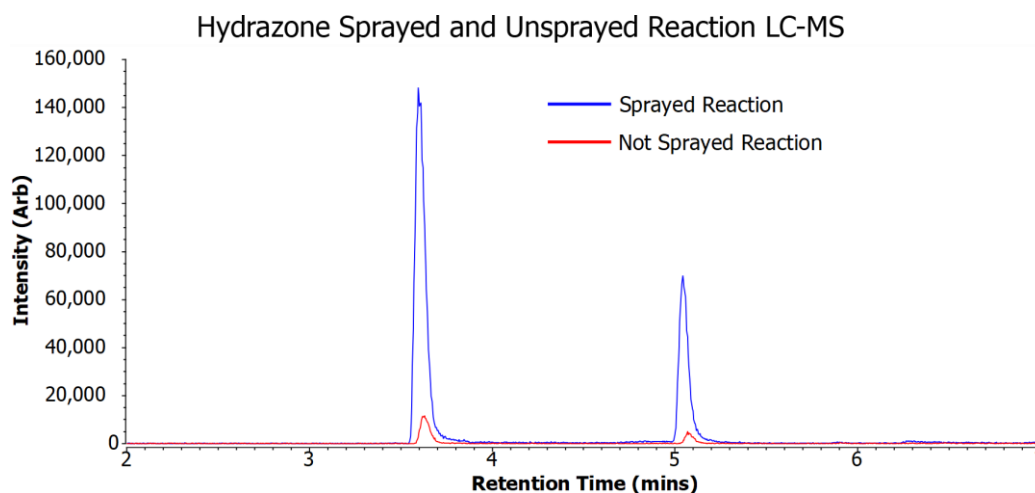


Figure 158 – LC-MS for Sprayed and Unsprayed Hydrazone Reaction Solution

This data shows the microdroplet synthesis forming a kinetically favored product (E-Isomer) over the thermodynamically more stable product (Z-Isomer).²⁶⁷ This is not the first example of a microdroplet synthesis product differing from the bulk synthesis product, however, it is believed to be the first example of a microdroplet preferentially forming a kinetically favoured but ultimately less stable stereoisomer. The Diels-Alder reaction, N-Alkylation of Indoles, and the Michael reaction with cinnamic acid, were shown to form different products in microdroplets compared to the conventional bulk synthesis products.^{214,225,268} A similar effect is observed for the synthesis of Pyridazine derivatives, which produces a mixture of two products when performed in bulk, but only one of these is produced through microdroplet synthesis.²⁶⁹

Online measurements of different stereoisomer formation could be completed with access to Ion Mobility Spectroscopy (IMS), which would separate ions of identical mass (in this case stereoisomers) based on their different collision cross section (CCS) values. Unfortunately, access to IMS was not possible during the course of this project, but this work is presented as an example of where this data would have been beneficial. Future work which focuses on the synthesis of products

which are known to form stereoisomers should consider collecting this data to show evidence of which stereoisomers are being formed.

Ion Mobility Spectroscopy of online synthesis was previously applied to the Biginelli reaction by Sahota et al., although this work focused on the different distribution of cis/trans isomers for reaction intermediates rather than the final product, which remained the same as the bulk synthesis counterpart.²⁷⁰

8.2 Pechmann Synthesis

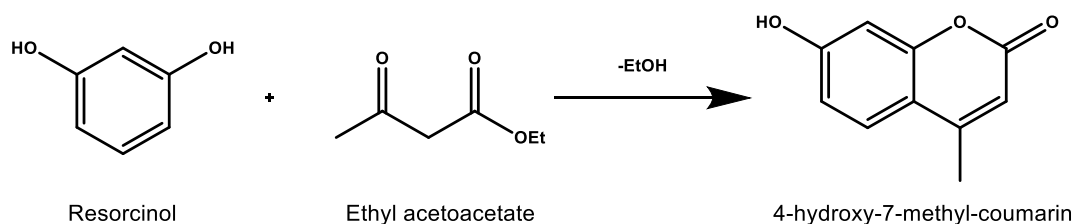


Figure 159 – The Pechmann Condensation

Coumarins are a common moiety for a number of different applications, including the synthesis of the anticoagulant Warfarin, rodenticides, laser dyes and in perfumes because of their naturally occurring odour akin to vanilla. Their general structure consists of a benzene ring fused with an α -pyrone ring. Various synthetic routes can be taken to generate them, including the Perkin reaction, Kostanecki reaction and the Pechmann condensation. The latter of these, the Pechmann condensation, generally requires both strong acids and high temperatures ($>100^{\circ}\text{C}$), or expensive catalysts to generate the coumarin product.

Experimentation ran in parallel to the Hydrazone reaction sought to find a new reaction which would exhibit microdroplet associated acceleration. After a screening process for a number of pharmaceutically relevant reaction types, the Pechmann condensation (specifically, the synthesis of 4-hydroxy-7-methylcoumarin, shown in Figure 159) suggested it was undergoing accelerated synthesis in microdroplets, and was therefore selected to perform scale up microdroplet synthesis development work.

8.2.1 Online Synthesis

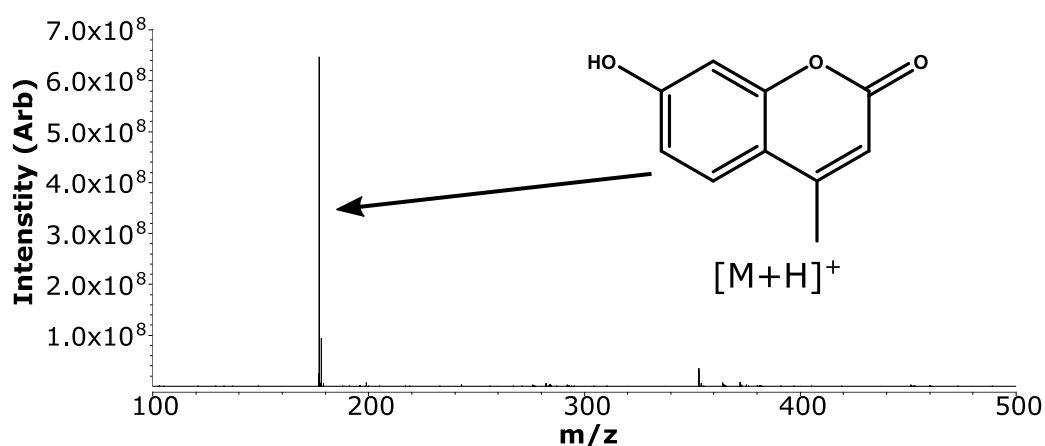


Figure 160 – Pechmann Reaction Mixture ESI Spectra Obtained

A 2.5 mmol dm⁻³ solution of Resorcinol and Ethyl acetoacetate were prepared in 50:50 MeOH:H₂O. Sulfuric Acid was added to give a final acid concentration of 1.25 mmol dm⁻³. The reaction mixture was loaded onto a 5 mL Hamilton Gas Tight Syringe and infused at 0.02 mL/min into the ESI Source. The ESI source settings are given below in Table 11. Figure 160 shows the spectra obtained for the reaction mixture, which clearly show a peak at 177 m/z corresponding to [M+H]⁺. The fragmentation data obtained matched that of the reference material. The solution which was not sprayed showed no LC-MS peak at the retention time observed for the reference material produced, indicating that the reaction was proceeding within the microdroplet and not within the solution.

Condition	Value
Syringe Flow Rate	0.02 mL/min
Capillary Voltage	3000 V
Desolvation Gas Flow:	800 L/hr
Cone Gas Flow:	50 L/hr
Inlet Temperature:	120°C

In addition to the synthesis of 4-hydroxy-7-methyl-coumarin, the synthesis of 11 other Pechmann condensation syntheses were screened. Figure 180 and Figure 181 in the Appendix show the results of this screening, which was performed as a bulk synthesis (to collect reference material), and as an online microdroplet acceleration reaction. The reference materials were characterised by NMR, the results of which are in the appendix. Of the 7 reactions which proceeded via the bulk synthesis, 5 of these showed evidence of online microdroplet accelerated

synthesis. The fragmentation patterns of the peaks obtained by microdroplet synthesis were compared to the fragmentation patterns of the bulk material, which matched in all 7 cases.

8.2.2 Offline Synthesis

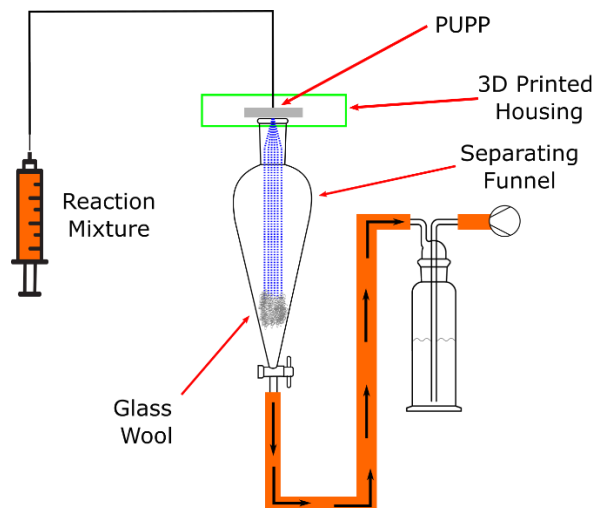


Figure 161 – Offline Synthesis Schematic

Development of an offline synthesis method was performed using the setup shown in Figure 152 and Figure 161. The fundamental difference between the two systems is that whilst the system illustrated in Figure 161 sprays and then traps the reaction mixture (in glass wool), the other system (Figure 152) allows the spray plume to precipitate and remix with the reaction mixture bulk, from where it can then be resprayed, forming a continuous spraying loop whilst the system is active. As discussed in Chapter 7, the literature gives examples of scaled up microdroplet systems which fall under each category. Herein for clarity, these will be referred to as a linear and continuous systems respectively, and have been summarised below in Table 12.

Table 12 – Linear vs Looped Microdroplet Synthesis Systems		
System Type	Example	Explanation
Linear	Figure 161	Reaction Mixture is sprayed and microdroplet plume is deposited/trapped onto surface
Continuous	Figure 152	Reaction Mixture is sprayed and subsequently returns to reaction mixture bulk for respraying

Throughout experimentation, and contrary to our hypothesis, using both systems, no product was detected. Variations in the reaction solution composition (changes to pH, solvent, concentration) were tested. The temperature and droplet distance was varied for the linear system (Figure 161) but no difference in the quantity was observed.

8.2.3 Online Investigation

Investigation into why no product could be obtained during offline synthesis, despite its presence being detected in the online synthesis, was performed by revisiting the online synthesis data. The conversion ratio is commonly used during microdroplet synthesis studies as a method of measuring the effect of changing parameters (temperature, pH, distance etc.) on the microdroplet acceleration effect. The effect of increasing the desolvation gas temperature on the online synthesis conversion ratio was investigated to determine whether the temperature of the offline synthesis systems was too low. Conversion ratio is calculated as shown in Eq. 25 below:

$$\text{Conversion Ratio (\%)} = \frac{I_{177}}{I_{177} + I_{111} + I_{233}} \times 100 \quad \text{Eq. 25}$$

I_{177} = Intensity of product peak (177 m/z)

I_{111} = Intensity of reactant peak (111 m/z)

I_{233} = Intensity of intermediate peak (233 m/z)

Figure 162 shows a clear increase in the conversion ratio with increasing desolvation gas temperature. But, even at the lowest desolvation gas temperature (200 °C), product is still observed at over 10% conversion rate.

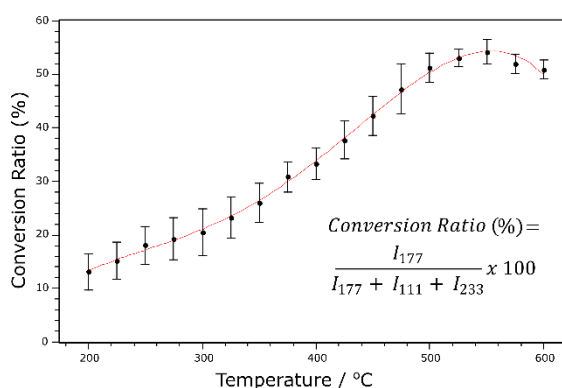


Figure 162 – Pechmann Reaction Conversion Ratio vs Desolvation Gas Temperature

However, data was then collected to correct for the inherent ionisation efficiencies of the reactants and the products as I hypothesized that this could have a significant effect on the actual conversion ratio being detected. Figure 163 shows the same conversion ratio data in Figure 162, but in this case the data has been corrected to include the ionisation efficiency coefficients. In addition, because the intermediate product cannot easily be isolated (and therefore its ionisation coefficient determined) the intensity of the intermediate has been removed from the calculation. The equation for this is given below in Eq. 26.

$$\text{Conversion Ratio (\%)} = \frac{I_{177}\alpha_{177}}{I_{177}\alpha_{177} + I_{111}\alpha_{111}} \times 100 \quad \text{Eq. 26}$$

Although there is a slight difference in the shape of the curve observed, the most significant difference is that there is a substantial decrease in the conversion ratio obtained. This data gives an indication as to why no product could be obtained using the offline synthesis method. Even at the highest temperatures, no more than 0.05% conversion ratio is obtained. This difference is because of the significantly higher ionisation efficiency of the products relative to the reactants, therefore giving a substantial peak in the spectra when the true concentration of product is actually significantly lower than that of the reactants.

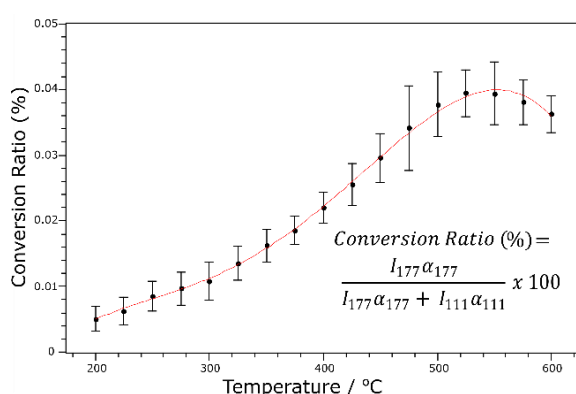


Figure 163 – Pechmann Reaction Conversion Ratio vs Desolvation Gas Temperature with Correction Factor Applied

This data highlights the importance of considering the ionisation efficiencies of reactants and products when performing microdroplet accelerated reactions online, which much of the literature either fails to report or negates to consider this key parameter all together – which may have some important ramifications when interpreting the existing literature. So, although the Pechmann condensation has been shown to proceed by some degree through microdroplet synthesis, the amount of product generated is actually minimal.

8.3 Recommended Screening Methods

As the field of microdroplet accelerated synthesis continues to advance, ensuring that the foundation data is consistent and transparent across the field becomes increasingly important. In light of the issues encountered previously for the Hydrazone synthesis and the Pechmann condensation, I developed a series of recommended screening methods which could ensure the avoidance (or at least a significant reduction) of reporting false positives. These methods are a suggested

approach which would have flagged many of the issues encountered during this research at an earlier stage.

8.3.1 Test 1: Identification of Products

The first test (Figure 164) is used to identify the products being obtained through online microdroplet synthesis by comparing the ions and subsequent fragmentation patterns of the microdroplet product and the bulk synthesis product (or reference material). If the fragmentation products do not match, then an investigation should be performed to determine whether the microdroplet accelerated synthesis is forming an alternative structural isomer or stereoisomer to the bulk synthesis product. The Fisher Indole synthesis for example, shown to form the N-Alkylated product in microdroplets rather than the C-Alkylated product formed in bulk solution by Gnanamani et al., would have been a good example of a reaction which would have benefitted from this workflow.²⁶⁸ If the reaction had been performed online (their work collected the product on a surface offline), then the difference in product would only have been observed by comparison of the fragmentation patterns to that of the literature or of bulk solution product. Where stereoisomers are formed as products which produce identical fragmentation patterns, where possible, confirmation of the stereoisomer produced should be achieved using Ion Mobility Spectrometry (IMS).

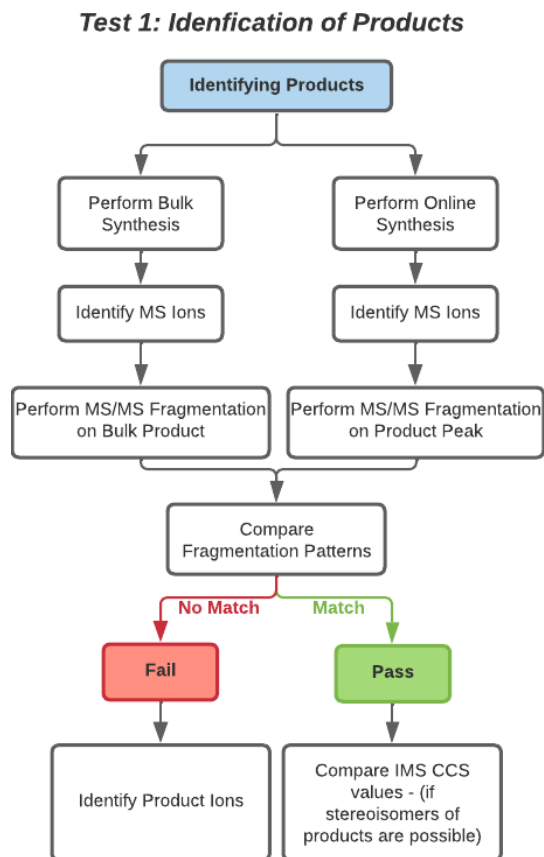


Figure 164 – Test #1 – Identification of Products

8.3.2 Test 2: Confirmation of True Microdroplet Effect

After the identity of the microdroplet product has been established online, work should be conducted to confirm that this is a true microdroplet effect, and not just the observed product which forms slowly in solution without spraying. This can be done by creating a reaction mixture which should be left to react as a bulk solution (and not sprayed). Aliquots of the unsprayed solution should be taken at different time points, in order to build up a time series of data, which should be immediately diluted to quench the reaction, or analysed immediately. Product formation, by both methods should then be quantified by LC-MS. If there is significant product formation, then this is evidence that the reaction may not be being accelerated in the microdroplets, and instead is simply proceeding in the bulk solution. The workflow for Test 2 is shown below in Figure 165.

Test 2: Confirmation of True Microdroplet Effect

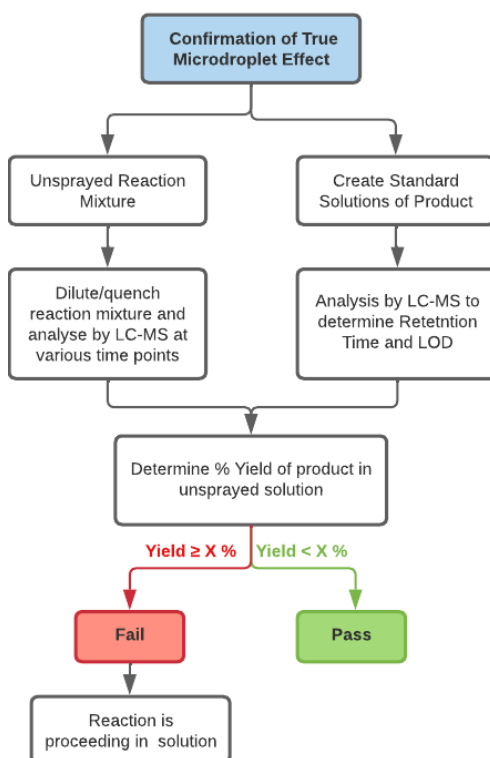


Figure 165 – Test #2 – Confirmation of True Microdroplet Effect

8.3.3 Test 3: Determine the Yield for Online Microdroplet Synthesis

After a true microdroplet effect has been identified, it is necessary to determine the % yield (or conversion ratio) for the reaction when performed online. As highlighted during the Pechmann condensation work, this is a critical step which may avoid offline microdroplet synthesis research work being performed on reactions which are unlikely to yield a significant portion of product. And, for this purpose you cannot simply rely on the peak intensities from the LC-MS data because, as was demonstrated earlier in this thesis, this can be confounded by differences between the ionisation efficiencies of the reactants and products.

Reactions which produce a high yield via microdroplet synthesis online, but which show very little or no product formation in solution according to the results of Test 2 are very likely to be of interest to offline microdroplet synthesis.

Therefore, it is important to determine the relative ionisation efficiencies of the reactants, products, and (if they can be isolated) any intermediates observed. There are different ways in which this could be performed, the simplest of which is to spike a solution of pure product with an equimolar concentration of reactant and observing the relative signal intensities when directly infused into the mass

spectrometer. Care should be taken to ensure that the instrument conditions and solvent composition is identical to that of the microdroplet accelerated reaction experiment, as variations in this will change the relative ionisation efficiencies. A similar approach was adopted by the Nie et al., who spiked a quenched reaction mixture with reactant and observed the relevant intensities, more details of which can be found in their publication and in the supplementary material.²⁵⁸ The corrected conversion ratio is then calculated as per Eq. 27 below, with the relative ionisation coefficients accounted for:

$$A + B \rightarrow C$$
$$\text{Conversion Ratio (\%)} = \frac{I_C \alpha_C}{I_A \alpha_A \text{ or } I_B \alpha_B} \times 100 \quad \text{Eq. 27}$$

Reactions which generate a low yield are not necessarily immediately ruled out as candidates for offline microdroplet synthesis. Instead, this may be a function of the microdroplet reaction conditions. Optimisation of the method should therefore be performed by investigating the effect of pH, temperature, initial droplet size, distance etc. Adjustment of these conditions may drive the microdroplet reaction further to completion, increasing the % yield. However, it should be noted that any change in the properties of the reaction mixture (pH, solvent, concentration etc.) would require confirmation that the reaction is not proceeding in solution by reperforming Test 2. The workflow for Test 3 is summarised in Figure 166 below.

Test 3: Determine the Yield for Online Microdroplet Synthesis

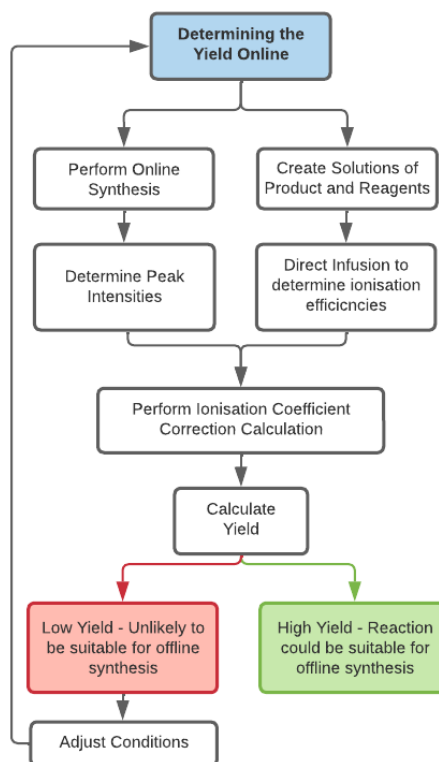


Figure 166 – Test #3 – Determine the Yield for Online Microdroplet Synthesis

8.3.4 Test 4: Determine the Yield for Offline Microdroplet Synthesis

The final test is only recommended if performing the same microdroplet accelerated reaction away from the mass spectrometer is relevant to the research. Test 4 (shown in Figure 167) aims to determine the yield of product obtained when microdroplet synthesis is performed offline. If offline microdroplet synthesis is being performed using a novel system, then this test should at all stages consider optimisation of both the reaction mixture and the system design itself. Thus far, all of the research which has published offline microdroplet synthesis methods has done this, as the work published focuses on pushing the horizon of product yield obtained per unit time.

The yield of the offline microdroplet synthesis product yield is usually determined by LC-MS quantitation of the sprayed solution. Alternatively, for linear offline systems which generate a solid product material, yield can be assessed by weight, however the purity of the resulting product should be determined. Regardless of the method used, if yield is low, then optimisation should be performed through adjustments to the reaction mixture properties (pH, concentration, solvent etc.),

the spray conditions (microdroplet size, distance travelled, temperature) or the system itself (set up dependent).

Test 4: Determine the Yield for Offline Microdroplet Synthesis

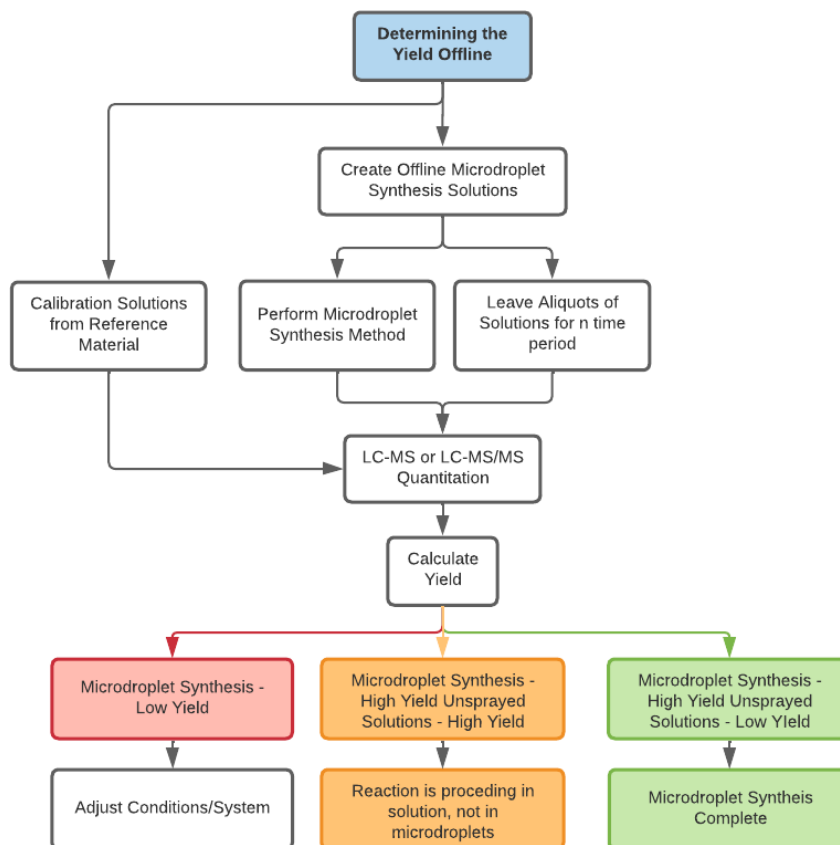


Figure 167 – Test #4 – Determine the Yield for Offline Microdroplet Synthesis

8.4 Summary

The field of microdroplet accelerated reactions is rapidly advancing, with an ever-increasing understanding of the mechanisms behind the phenomenon and growing pool of chemical and biological reactions which have been shown to undergo this effect. This work highlights the need for thorough and in-depth data analysis when reporting microdroplet accelerated reactions, in particular when considering the scale up of these reactions to generate useful quantities of products in a short space of time.

The Hydrazone synthesis, previously reported as a reaction which undergoes microdroplet acceleration in the literature, has been shown to form the kinetically favoured isomer when synthesised in microdroplets. This is the first reported example of a microdroplet accelerated product forming a thermodynamically less favourable stereoisomer.

Another investigation initially suggested the Pechmann condensation undergoes significant rate acceleration when performed via microdroplet synthesis. However, this effect could only be observed when performed online, and little or no product was ever observed when performed using offline techniques. Further investigation into the online microdroplet synthesis revealed that the true extent to which the reactants undergo synthesis was masked because of the significant difference in ionisation efficiencies between the reactants and products.

This project has presented a series of suggested screening methods which should be followed for all microdroplet acceleration reactions proposed as candidates for offline microdroplet synthesis. These tests reduce the possibility of time spent on false positives or reactions which have a low conversion rate are brought forward for offline method development where they are less likely to succeed.

Conclusion:

Chemical and biochemical reactions which experience rate acceleration when performed in confined volumes are already an exciting development within the scientific community. Our understanding of the mechanisms driving this effect continues to grow, together with the library of reactions which proceed via microdroplet synthesis. Most previously published work in this area reports "online synthesis", whereby synthesis is performed within an ionisation source and immediately analysed by mass spectrometry. More recently however, focus has shifted towards how this effect can be used to perform rapid large scale microdroplet synthesis for industrial use, or "offline synthesis".

The initial aim of this project was to develop a system which could perform microdroplet accelerated synthesis away from the mass spectrometer, which would be capable of generating grams of a desired product in a short space of time. Ultrasonic nebulizers were highlighted as being the most effective method of performing this, owing to their ability to generate large plumes of microdroplets on demand. The PUPP system, previously described within Section A, was selected as an effective method of generating microdroplets suitable for offline synthesis.

The synthesis of the phenylhydrazone of isatin was selected as a suitable reaction for system development, as this reaction had previously been shown in the literature to proceed via online microdroplet synthesis. The PUPP system was successfully used to perform offline microdroplet synthesis. However, it was found that microdroplets preferentially create the thermodynamically less stable E-stereoisomer over the favored Z-stereoisomer. Conventional bulk synthesis also produces both isomers, but at a ratio of 1:10, whereas the microdroplet shows a clear shift in the preferred isomer, giving a ratio of 3:1. After initial synthesis, the E-stereoisomer relaxes to form the same ratio of products as the conventional bulk synthesis over an approximately 18-hour time period. This is the first known example of a microdroplet synthesis preferentially forming a different stereoisomer compared to the conventional synthesis product distribution.

The Pechmann condensation was found to proceed via online microdroplet synthesis, previously unreported in the literature. After the Hydrazone E/Z isomerism effect was found, this was therefore selected as a reaction to proceed with further offline microdroplet synthesis system development. However, after a significant development period with little success, a retrospective investigation into the online synthesis data was performed.

Additional experimentation showed that the ionisation efficiencies were masking the true nature of the microdroplet effect. The ionisation efficiency of the product, which is significantly higher than that of the two reactants, meant that despite the spectra being dominated by a product peak there was actually a very low conversion ratio of reactants to product. Therefore, the reaction is unlikely to be a suitable candidate for scale up investigations, because the amount of product being produced even in the small, highly charged and rapidly desolvating environment of an electrospray microdroplet, very little product is produced.

After this finding, the decision was taken to establish a robust screening method which could be recommended for future publications reporting microdroplet accelerated reactions. This would ensure that microdroplet reactions unlikely to be suitable for scale up were highlighted, and a higher level of data consistency between publications in the field. Four screening steps were presented:

1. **Identification of Products:** Confirms that products generated through microdroplet synthesis match that of the conventional bulk synthesis
2. **Confirmation of Microdroplet Effect:** Determines % yield of reaction when products are mixed without spraying as microdroplets over time
3. **Determine Yield (Online):** Uses ionisation efficiency to determine conversion rate
4. **Determine Yield (Offline):** Perform Microdroplet Synthesis offline, and compare % yield to that of an identical but unsprayed solutions

This project has presented the novel microdroplet synthesis of thermodynamically unfavored stereoisomers for the Hydrazone reaction. In addition, the Pechmann condensation has been shown to be an example of a reaction which proceeds via microdroplet synthesis, but one which is unlikely to be suitable for offline synthesis because of the low product yield obtained online when the ionisation efficiencies of reactants and products are accounted for. This work highlights the need for consistent and thorough data analysis when performing online microdroplet synthesis. In order to do this, a set of four experiments have been recommended, which aim to screen reactions which are most likely to be suitable for large scale offline microdroplet synthesis.

References

- (1) Loos, M.; Gerber, C.; Corona, F.; Hollender, J.; Singer, H. Accelerated Isotope Fine Structure Calculation Using Pruned Transition Trees. *Anal Chem* **2015**, *87* (11), 5738–5744. <https://doi.org/10.1021/acs.analchem.5b00941>.
- (2) Brenton, A. G.; Godfrey, A. R. Accurate Mass Measurement: Terminology and Treatment of Data. *J Am Soc Mass Spectrom* **2010**, *21* (11), 1821–1835. <https://doi.org/10.1016/j.jasms.2010.06.006>.
- (3) Wenger, C. D.; McAlister, G. C.; Xia, Q.; Coon, J. J. Sub-Part-per-Million Precursor and Product Mass Accuracy for High-Throughput Proteomics on an Electron Transfer Dissociation-Enabled Orbitrap Mass Spectrometer. *Molecular and Cellular Proteomics* **2010**, *9* (5), 754–763. <https://doi.org/10.1074/mcp.M900541-MCP200>.
- (4) Li, Y.; Zhang, N.; Zhou, Y.; Wang, J.; Zhang, Y.; Wang, J.; Xiong, C.; Chen, S.; Nie, Z. Induced Dual-Nanospray: A Novel Internal Calibration Method for Convenient and Accurate Mass Measurement. *J Am Soc Mass Spectrom* **2013**, *24* (9), 1446–1449. <https://doi.org/10.1007/s13361-013-0670-5>.
- (5) Zhang, L. K.; Rempel, D.; Pramanik, B. N.; Gross, M. L. Accurate Mass Measurements by Fourier Transform Mass Spectrometry. *Mass Spectrom Rev* **2005**, *24* (2), 286–309. <https://doi.org/10.1002/mas.20013>.
- (6) Muddiman, D. C.; Oberg, A. L. Statistical Evaluation of Internal and External Mass Calibration Laws Utilized in Fourier Transform Ion Cyclotron Resonance Mass Spectrometry. *Anal Chem* **2005**, *77* (8), 2406–2414. <https://doi.org/10.1021/ac048258l>.
- (7) Hop, C. Generation of High Molecular Weight Cluster Ions by Electrospray Ionization: Implications for Mass Spectrometry. *Journal of Mass Spectrometry* **1996**, *31*, 1314–1316.
- (8) Stout, S. J.; daCunha, A. R. Tuning and Calibration in Thermospray Liquid Chromatography/Mass Spectrometry Using Trifluoroacetic Acid Cluster Ions. *Anal Chem* **1989**, *61* (18), 2126–2128. <https://doi.org/10.1021/ac00193a027>.
- (9) Anacleto, J. F.; Pleasance, S.; Boyd, R. K. Calibration of Ion Spray Mass Spectra Using Cluster Ions. *Organic Mass Spectrometry* **1992**, *27* (6), 660–666. <https://doi.org/10.1002/oms.1210270603>.
- (10) Lou, X.; van Dongen, J. L. J.; Meijer, E. W. Generation of Csi Cluster Ions for Mass Calibration in Matrix-Assisted Laser Desorption/Ionization Mass Spectrometry. *J Am Soc Mass Spectrom* **2010**, *21* (7), 1223–1226. <https://doi.org/10.1016/j.jasms.2010.02.029>.
- (11) Larsen, B. S.; McEwen, C. N. An Electrospray Ion Source for Magnetic Sector Mass Spectrometers. *J Am Soc Mass Spectrom* **1991**, *2* (3), 205–211. [https://doi.org/10.1016/1044-0305\(91\)80045-9](https://doi.org/10.1016/1044-0305(91)80045-9).
- (12) Cody, R. B.; Tamura, J.; Musselman, B. D. Electrospray Ionization/Magnetic Sector Mass Spectrometry: Calibration, Resolution,

- and Accurate Mass Measurements. *Anal Chem* **1992**, 64 (14), 1561–1570. <https://doi.org/10.1021/ac00038a012>.
- (13) Grayson, S. M.; Myers, B. K.; Bengtsson, J.; Malkoch, M. Advantages of Monodisperse and Chemically Robust “Spherical” Polyester Dendrimers as a “Universal” MS Calibrant. *J Am Soc Mass Spectrom* **2014**, 25 (3), 303–309. <https://doi.org/10.1007/s13361-013-0777-8>.
- (14) Hu, P.; Cole, D. P. Routine Absorption Mode FTMS Data Display with an Ethoxylated Anionic Detergent as a Dual-Role (Mass and Phase) Calibrant. *Journal American Society for Mass Spectrometry* **2019**, 30, 468–475. <https://doi.org/10.1007/s13361-018-2099-3>.
- (15) Giles, K.; Pringle, S. D.; Worthington, K. R.; Little, D.; Wildgoose, J. L.; Bateman, R. H. Applications of a Travelling Wave-Based Radio-Frequency-Only Stacked Ring Ion Guide. *Rapid Communications in Mass Spectrometry* **2004**, 18 (20), 2401–2414. <https://doi.org/10.1002/rcm.1641>.
- (16) Waters. StepWave: Enhancing MS Sensitivity and Robustness. Waters Corporation 2012.
- (17) de Hoffman, E.; Stroobant, V. *Mass Spectrometry: Principles and Applications*, Third.; Wiley, 2007.
- (18) Marsh, R. E. An Introduction to Quadrupole Ion Trap Mass Spectrometry. *Journal of Mass Spectrometry* **1997**, 32, 351–369. [https://doi.org/https://doi.org/10.1002/\(SICI\)1096-9888\(199704\)32:4<351::AID-JMS512>3.0.CO;2-Y](https://doi.org/https://doi.org/10.1002/(SICI)1096-9888(199704)32:4<351::AID-JMS512>3.0.CO;2-Y).
- (19) Shukla, A. K.; Futrell, J. H. Tandem Mass Spectrometry: Dissociation of Ions by Collisional Activation. *Journal of Mass Spectrometry* **2000**, 35 (9), 1069–1090. [https://doi.org/10.1002/1096-9888\(200009\)35:9<1069::AID-JMS54>3.0.CO;2-C](https://doi.org/10.1002/1096-9888(200009)35:9<1069::AID-JMS54>3.0.CO;2-C).
- (20) McLuckey, S. A. Principles of Collisional Activation in Analytical Mass Spectrometry. *J Am Soc Mass Spectrom* **1992**, 3 (6), 599–614. [https://doi.org/10.1016/1044-0305\(92\)85001-Z](https://doi.org/10.1016/1044-0305(92)85001-Z).
- (21) Mamyryn, B.; Karataev, V.; Shmikk, D.; Zagulin, V. The Mass-Reflectron, a New Nonmagnetic Time-of-Flight Mass Spectrometer with High Resolution. *Soviet Journal of Experimental and Theoretical Physics* **1973**, 37 (1), 45.
- (22) Doroshenko, V.; Cotter, R. A Quadrupole Ion Trap/Time-of-Flight Mass Spectrometer with a Parabolic Reflectron. *Journal of Mass Spectrometry* **1998**, 33, 305–318.
- (23) Zhurov, K. O.; Kozhinov, A. N.; Tsybin, Y. O. Evaluation of High-Field Orbitrap Fourier Transform Mass Spectrometer for Petroleomics. *Energy and Fuels* **2013**, 27 (6), 2974–2983. <https://doi.org/10.1021/ef400203g>.
- (24) Gorshkov, M. V.; Good, D. M.; Lyutvinskiy, Y.; Yang, H.; Zubarev, R. A. Calibration Function for the Orbitrap FTMS Accounting for the Space Charge Effect. *Journal American Society for Mass Spectrometry* **2010**, 21, 1846–1851. <https://doi.org/10.1016/j.jasms.2010.06.021>.
- (25) Boja, E. S.; Phillips, D.; French, S. A.; Harris, R. A.; Balaban, R. S. Quantitative Mitochondrial Phosphoproteomics Using ITRAQ on an LTQ-

- Orbitrap with High Energy Collision Dissociation. *J Proteome Res* **2009**, *8* (10), 4665–4675. <https://doi.org/10.1021/pr900387b>.
- (26) McAlister, G. C.; Phanstiel, D.; Wenger, C. D.; Violet Lee, M.; Coon, J. J. Analysis of Tandem Mass Spectra by FTMS for Improved Large-Scale Proteomics with Superior Protein Quantification. *Anal Chem* **2010**, *82* (1), 316–322. <https://doi.org/10.1021/ac902005s>.
- (27) Jedrychowski, M. P.; Huttlin, E. L.; Haas, W.; Sowa, M. E.; Rad, R.; Gygi, S. P. Evaluation of HCD- and CID-Type Fragmentation within Their Respective Detection Platforms for Murine Phosphoproteomics. *Molecular and Cellular Proteomics* **2011**, *10* (12). <https://doi.org/10.1074/mcp.M111.009910>.
- (28) Pichler, P.; Köcher, T.; Holzmann, J.; Möhring, T.; Ammerer, G.; Mechtler, K. Improved Precision of ITRAQ and TMT Quantification by an Axial Extraction Field in an Orbitrap HCD Cell. *Anal Chem* **2011**, *83* (4), 1469–1474. <https://doi.org/10.1021/ac102265w>.
- (29) Dayon, L.; Pasquarello, C.; Hoogland, C.; Sanchez, J. C.; Scherl, A. Combining Low- and High-Energy Tandem Mass Spectra for Optimized Peptide Quantification with Isobaric Tags. *J Proteomics* **2010**, *73* (4), 769–777. <https://doi.org/10.1016/j.jprot.2009.10.015>.
- (30) Olsen, J. V.; de Godoy, L. M. F.; Li, G.; Macek, B.; Mortensen, P.; Pesch, R.; Makarov, A.; Lange, O.; Horning, S.; Mann, M. Parts per Million Mass Accuracy on an Orbitrap Mass Spectrometer via Lock Mass Injection into a C-Trap. *Molecular and Cellular Proteomics* **2005**, *4* (12), 2010–2021. <https://doi.org/10.1074/mcp.T500030-MCP200>.
- (31) Hu, Q.; Noll, R. J.; Li, H.; Makarov, A.; Hardman, M.; Cooks, R. G. The Orbitrap: A New Mass Spectrometer. *Journal of Mass Spectrometry* **2005**, *40* (4), 430–443. <https://doi.org/10.1002/jms.856>.
- (32) Hecht, E. S.; Scigelova, M.; Eliuk, S.; Makarov, A. *Fundamentals and Advances of Orbitrap Mass Spectrometry*; 2019. <https://doi.org/10.1002/9780470027318.a9309.pub2>.
- (33) Zubarev, R. A.; Makarov, A. Orbitrap Mass Spectrometry. *Anal Chem* **2013**, *85* (11), 5288–5296. <https://doi.org/10.1021/ac4001223>.
- (34) Makarov, A. Electrostatic Axially Harmonic Orbital Trapping: A High-Performance Technique of Mass Analysis. *Anal Chem* **2000**, *72* (6), 1156–1162. <https://doi.org/10.1021/ac991131p>.
- (35) Shaw, J. B.; Lin, T. Y.; Leach, F. E.; Tolmachev, A. V.; Tolić, N.; Robinson, E. W.; Koppelaar, D. W.; Paša-Tolić, L. 21 Tesla Fourier Transform Ion Cyclotron Resonance Mass Spectrometer Greatly Expands Mass Spectrometry Toolbox. *J Am Soc Mass Spectrom* **2016**, *27* (12), 1929–1936. <https://doi.org/10.1007/s13361-016-1507-9>.
- (36) Smith, D. F.; Kilgour, D. P. A.; Konijnenburg, M.; O'Connor, P. B.; Heeren, R. M. A. Absorption Mode FTICR Mass Spectrometry Imaging. *Anal Chem* **2013**, *85* (23), 11180–11184. <https://doi.org/10.1021/ac403039t>.
- (37) Kooijman, P. C.; Nagornov, K. O.; Kozhinov, A. N.; Kilgour, D. P. A.; Tsybin, Y. O.; Heeren, R. M. A.; Ellis, S. R. Increased Throughput and

Ultra-High Mass Resolution in DESI FT-ICR MS Imaging through New-Generation External Data Acquisition System and Advanced Data Processing Approaches. *Sci Rep* **2019**, 9 (1), 1–11. <https://doi.org/10.1038/s41598-018-36957-1>.

- (38) Bowman, A. P.; Blakney, G. T.; Hendrickson, C. L.; Ellis, S. R.; Heeren, R. M. A.; Smith, D. F. Ultra-High Mass Resolving Power, Mass Accuracy, and Dynamic Range MALDI Mass Spectrometry Imaging by 21-T FT-ICR MS. *Anal Chem* **2020**, 92 (4), 3133–3142. <https://doi.org/10.1021/acs.analchem.9b04768>.
- (39) N. Nikolaev, E.; N. Vladimirov, G.; Jertz, R.; Baykut, G. From Supercomputer Modeling to Highest Mass Resolution in FT-ICR. *Mass Spectrometry* **2013**, 2 (Special_Issue), S0010–S0010. <https://doi.org/10.5702/massspectrometry.s0010>.
- (40) Cho, Y.; Ahmed, A.; Islam, A.; Kim, S. Developments in FT-ICR Ms Instrumentation, Ionization Techniques, and Data Interpretation Methods for Petroleomics. *Mass Spectrom Rev* **2015**, 34 (2), 248–263. <https://doi.org/10.1002/mas.21438>.
- (41) Marshall, A. G.; Hendrickson, C. L.; Jackson, G. S. Fourier Transform Ion Cyclotron Resonance Mass Spectrometry: A Primer. *Mass Spectrom Rev* **1998**, 17 (1), 1–35. [https://doi.org/10.1002/\(SICI\)1098-2787\(1998\)17:1<1::AID-MAS1>3.0.CO;2-K](https://doi.org/10.1002/(SICI)1098-2787(1998)17:1<1::AID-MAS1>3.0.CO;2-K).
- (42) Nikolaev, E.; Lioznov, A. Evaluation of Major Historical ICR Cell Designs Using Electric Field Simulations. *Mass Spectrometry Reviews*. John Wiley and Sons Inc March 1, 2022, pp 262–283. <https://doi.org/10.1002/mas.21671>.
- (43) Nikolaev, E. N.; Boldin, I. A.; Jertz, R.; Baykut, G. Initial Experimental Characterization of a New Ultra-High Resolution FTICR Cell with Dynamic Harmonization. *J Am Soc Mass Spectrom* **2011**, 22 (7), 1125–1133. <https://doi.org/10.1007/s13361-011-0125-9>.
- (44) Francl, T. J.; Sherman, M. G.; Hunter, R. L.; Locke, M. J.; Bowers, W. D.; Mctver, R. T. Experimental Determination of the Effects of Space Charge on Ion Cyclotron Resonance Frequencies. *International Journal of Mass Spectrometry and Ion Processes* **1983**, 54, 189.
- (45) Ledford, E. B.; Rempel, D. L.; Gross, M. L. *Space Charge Effects in Fourier Transform Mass Spectrometry*. *Mass Calibration*; 1984; Vol. 56. <https://pubs.acs.org/sharingguidelines>.
- (46) D-H Shi, S.; Drader, J. J.; Freitas, M. A.; Hendrickson, C. L.; Marshall, A. G. Comparison and Interconversion of the Two Most Common Frequency-to-Mass Calibration Functions for Fourier Transform Ion Cyclotron Resonance Mass Spectrometry. *Int J Mass Spectrom* **2000**, 195–196, 591–598. [https://doi.org/10.1016/S1387-3806\(99\)00226-2](https://doi.org/10.1016/S1387-3806(99)00226-2).
- (47) Qi, Y.; O'Connor, P. B. Data Processing in Fourier Transform Ion Cyclotron Resonance Mass Spectrometry. *Mass Spectrom Rev* **2014**, 33 (5), 333–352. <https://doi.org/10.1002/mas.21414>.
- (48) Hofstadler, S. A.; Laude, D. A. Trapping and Detection of Ions Generated in a High Magnetic Field Electrospray Ionization Fourier Transform Ion

- Cyclotron Resonance Mass Spectrometer. *J Am Soc Mass Spectrom* **1992**, 3 (6), 615–623. [https://doi.org/10.1016/1044-0305\(92\)85002-2](https://doi.org/10.1016/1044-0305(92)85002-2).
- (49) van Agthoven, M. A.; Lam, Y. P. Y.; O'Connor, P. B.; Rolando, C.; Delsuc, M. A. Two-Dimensional Mass Spectrometry: New Perspectives for Tandem Mass Spectrometry. *European Biophysics Journal* **2019**, 48 (3), 213–229. <https://doi.org/10.1007/s00249-019-01348-5>.
- (50) Monge, M. E.; Fernández, F. M. An Introduction to Ambient Ionization Mass Spectrometry. In *New Developments in Mass Spectrometry*; Marek, D., Cody, R., Eds.; Royal Society of Chemistry, 2015; pp 1–22.
- (51) Rohner, T. C.; Lion, N.; Girault, H. H. Electrochemical and Theoretical Aspects of Electrospray Ionisation. *Physical Chemistry Chemical Physics*. June 21, 2004, pp 3056–3068. <https://doi.org/10.1039/b316836k>.
- (52) Kebarle, P. A Brief Overview of the Present Status of the Mechanisms Involved in Electrospray Mass Spectrometry. *Journal of Mass Spectrometry* **2000**, 35, 804–817.
- (53) Grimm, R. L.; Beauchamp, J. L. Evaporation and Discharge Dynamics of Highly Charged Multicomponent Droplets Generated by Electrospray Ionization. *Journal of Physical Chemistry A* **2010**, 114 (3), 1411–1419. <https://doi.org/10.1021/jp907162w>.
- (54) Strutt, J. On the Equilibrium of Liquid Conducting Masses Charged with Electricity. *The London, Edinburgh, and Dublin Philosophical Magazine and Journal of Science* **1882**, 14, 184–186. <https://doi.org/10.1017/cbo9780511703973.013>.
- (55) Konermann, L.; Ahadi, E.; Rodriguez, A. D.; Vahidi, S. Unraveling the Mechanism of Electrospray Ionization. *Anal Chem* **2013**, 85, 2–9. <https://doi.org/dx.doi.org/10.1021/ac302789c>.
- (56) Konermann, L.; Metwally, H.; Duez, Q.; Peters, I. Charging and Supercharging of Proteins for Mass Spectrometry: Recent Insights into the Mechanisms of Electrospray Ionization. *Analyst* **2019**, 144 (21), 6157–6171. <https://doi.org/10.1039/c9an01201j>.
- (57) Cody, R. B.; Laramée, J. A. Atmospheric Pressure Ion Source. 6949741, 2005.
- (58) Cody, R. B.; Laramée, J. A.; Durst, H. D. Versatile New Ion Source for the Analysis of Materials in Open Air under Ambient Conditions. *Anal Chem* **2005**, 77 (8), 2297–2302. <https://doi.org/10.1021/ac050162j>.
- (59) Harding, L. P.; Parkes, G. M. B.; Townend, J. D. Parameters Affecting Ion Intensities in Transmission-Mode Direct Analysis in Real-Time Mass Spectrometry. *Analyst* **2014**, 139 (17), 4176–4180. <https://doi.org/10.1039/c4an00859f>.
- (60) Guo, T.; Yong, W.; Jin, Y.; Zhang, L.; Liu, J.; Wang, S.; Chen, Q.; Dong, Y.; Su, H.; Tan, T. Applications of DART-MS for Food Quality and Safety Assurance in Food Supply Chain. *Mass Spectrom Rev* **2017**, 36 (2), 161–187. <https://doi.org/10.1002/mas.21466>.

- (61) Penning, F. M. Über Ionisation Durch Metastabile Atome. *Naturwissenschaften* **1927**, *15* (40), 818. <https://doi.org/10.1007/BF01505431>.
- (62) Harris, G. A.; Hostetler, D. M.; Hampton, C. Y.; Fernandez, F. M. Comparison of the Internal Energy Deposition of Direct Analysis in Real Time and Electrospray Ionization Time-of-Flight Mass Spectrometry. *J Am Soc Mass Spectrom* **2010**, *21* (5), 855–863. <https://doi.org/10.1016/j.jasms.2010.01.019>.
- (63) Cody, R. B.; Laramée, J. A.; Nilles, J. M.; Durst, H. D. Direct Analysis in Real Time (DART) Mass Spectrometry. *JEOL News* **2005**, *40* (1), 8–12.
- (64) Song, L.; Chuah, W. C.; Lu, X.; Remsen, E.; Bartmess, J. E. Ionization Mechanism of Positive-Ion Nitrogen Direct Analysis in Real Time. *J Am Soc Mass Spectrom* **2018**, *29* (4), 640–650. <https://doi.org/10.1007/s13361-017-1885-7>.
- (65) Hajslova, J.; Cajka, T.; Vaclavik, L. Challenging Applications Offered by Direct Analysis in Real Time (DART) in Food-Quality and Safety Analysis. *TrAC - Trends in Analytical Chemistry* **2011**, *30* (2), 204–218. <https://doi.org/10.1016/j.trac.2010.11.001>.
- (66) Chernetsova, E. S.; Bochkov, P. O.; Ovcharov, M. V.; Zhokhov, S. S.; Abramovich, R. A. DART Mass Spectrometry: A Fast Screening of Solid Pharmaceuticals for the Presence of an Active Ingredient, as an Alternative for IR Spectroscopy. *Drug Test Anal* **2010**, *2* (6), 292–294. <https://doi.org/10.1002/dta.136>.
- (67) Haefliger, O. P.; Jeckelmann, N. Direct Mass Spectrometric Analysis of Flavors and Fragrances in Real Applications Using DART. *Rapid Communications in Mass Spectrometry* **2007**, *21* (8), 1361–1366. <https://doi.org/10.1002/rcm.2969>.
- (68) Song, L.; Dykstra, A. B.; Yao, H.; Bartmess, J. E. Ionization Mechanism of Negative Ion-Direct Analysis in Real Time: A Comparative Study with Negative Ion-Atmospheric Pressure Photoionization. *J Am Soc Mass Spectrom* **2009**, *20* (1), 42–50. <https://doi.org/10.1016/j.jasms.2008.09.016>.
- (69) Takáts, Z.; Wiseman, J. M.; Gologan, B.; Cooks, R. G. Mass Spectrometry Sampling under Ambient Conditions with Desorption Electrospray Ionization. *Science (1979)* **2004**, *306* (5695), 471–473. <https://doi.org/10.1126/science.1104404>.
- (70) Chen, H.; Pan, Z.; Talaty, N.; Raftery, D.; Graham Cooks, R. Combining Desorption Electrospray Ionization Mass Spectrometry and Nuclear Magnetic Resonance for Differential Metabolomics without Sample Preparation. *Rapid Communications in Mass Spectrometry* **2006**, *20* (10), 1577–1584. <https://doi.org/10.1002/rcm.2474>.
- (71) Takáts, Z.; Wiseman, J. M.; Cooks, R. G. Ambient Mass Spectrometry Using Desorption Electrospray Ionization (DESI): Instrumentation, Mechanisms and Applications in Forensics, Chemistry, and Biology. *Journal of Mass Spectrometry* **2005**, *40* (10), 1261–1275. <https://doi.org/10.1002/jms.922>.

- (72) Talaty, N.; Mulligan, C. C.; Justes, D. R.; Jackson, A. U.; Noll, R. J.; Cooks, R. G. Fabric Analysis by Ambient Mass Spectrometry for Explosives and Drugs. *Analyst* **2008**, *133* (11), 1532–1540. <https://doi.org/10.1039/b807934j>.
- (73) Fernández, F. M.; Cody, R. B.; Green, M. D.; Hampton, C. Y.; McGready, R.; Sengaloundeth, S.; White, N. J.; Newton, P. N. Characterization of Solid Counterfeit Drug Samples by Desorption Electrospray Ionization and Direct-Analysis-in-Real-Time Coupled to Time-of-Flight Mass Spectrometry. *ChemMedChem* **2006**, *1* (7), 702–705. <https://doi.org/10.1002/cmdc.200600041>.
- (74) Bachman, M.; Sinclair, I.; Ivanov, D.; Wingfield, J. Information-Rich High-Throughput Cellular Assays Using Acoustic Mist Ionisation Mass Spectrometry. *Analyst* **2021**, *146* (1), 315–321. <https://doi.org/10.1039/d0an01519a>.
- (75) Liu, C.; Van Berkel, G. J.; Cox, D. M.; Covey, T. R. Operational Modes and Speed Considerations of an Acoustic Droplet Dispenser for Mass Spectrometry. *Anal Chem* **2020**, *92* (24), 15818–15826. <https://doi.org/10.1021/acs.analchem.0c02999>.
- (76) Sinclair, I.; Stearns, R.; Pringle, S.; Wingfield, J.; Datwani, S.; Hall, E.; Ghislain, L.; Majlof, L.; Bachman, M. Novel Acoustic Loading of a Mass Spectrometer: Toward Next-Generation High-Throughput MS Screening. *J Lab Autom* **2016**, *21* (1), 19–26. <https://doi.org/10.1177/2211068215619124>.
- (77) Hadimioglu, B.; Stearns, R.; Ellson, R. Moving Liquids with Sound: The Physics of Acoustic Droplet Ejection for Robust Laboratory Automation in Life Sciences. *J Lab Autom* **2016**, *21* (1), 4–18. <https://doi.org/10.1177/2211068215615096>.
- (78) Sinclair, I.; Bachman, M.; Addison, D.; Rohman, M.; Murray, D. C.; Davies, G.; Mouchet, E.; Tonge, M. E.; Stearns, R. G.; Ghislain, L.; Datwani, S. S.; Majlof, L.; Hall, E.; Jones, G. R.; Hoyes, E.; Olechno, J.; Ellson, R. N.; Barran, P. E.; Pringle, S. D.; Morris, M. R.; Wingfield, J. Acoustic Mist Ionization Platform for Direct and Contactless Ultrahigh-Throughput Mass Spectrometry Analysis of Liquid Samples. *Anal Chem* **2019**, *91* (6), 3790–3794. <https://doi.org/10.1021/acs.analchem.9b00142>.
- (79) Dirico, K. J.; Hua, W.; Liu, C.; Tucker, J. W.; Ratnayake, A. S.; Flanagan, M. E.; Troutman, M. D.; Noe, M. C.; Zhang, H. Ultra-High-Throughput Acoustic Droplet Ejection-Open Port Interface-Mass Spectrometry for Parallel Medicinal Chemistry. *ACS Med Chem Lett* **2020**, *11* (6), 1101–1110. <https://doi.org/10.1021/acsmchemlett.0c00066>.
- (80) Wagner, A.; Zhang, J.; Liu, C.; Covey, T. R.; Olah, T. V.; Weller, H. N.; Shou, W. Z. Ultrahigh-Throughput and Chromatography-Free Bioanalysis of Polar Analytes with Acoustic Ejection Mass Spectrometry. *Anal Chem* **2020**, *92* (19), 13525–13531. <https://doi.org/10.1021/acs.analchem.0c03006>.
- (81) Zhang, J.; Zhang, Y.; Liu, C.; Covey, T.; Nielsen, J.; Li, S.; Weller, H.; Shou, W. Acoustic Ejection/Full-Scan Mass Spectrometry Analysis for

- High-Throughput Compound Quality Control. *SLAS Technol* **2021**, 26 (2), 178–188. <https://doi.org/10.1177/2472630320967625>.
- (82) Wen, X.; Liu, C.; Ghislain, L.; Tovar, K.; Shah, V.; Stout, S. J.; Cifelli, S.; Satapati, S.; O'Donnell, G.; Sheth, P. R.; Wildey, M. J.; Datwani, S. S.; Covey, T. R.; Bateman, K. P.; McLaren, D. G. Direct Analysis from Phase-Separated Liquid Samples Using ADE-OPI-MS: Applicability to High-Throughput Screening for Inhibitors of Diacylglycerol Acyltransferase 2. *Anal Chem* **2021**. <https://doi.org/10.1021/acs.analchem.0c04312>.
- (83) Häbe, T. T.; Liu, C.; Covey, T. R.; Simon, R. P.; Reindl, W.; Büttner, F. H.; Winter, M.; Bischoff, D.; Luippold, A. H.; Runge, F. Ultrahigh-Throughput ESI-MS: Sampling Pushed to Six Samples per Second by Acoustic Ejection Mass Spectrometry. *Anal Chem* **2020**, 92 (18), 12242–12249. <https://doi.org/10.1021/acs.analchem.0c01632>.
- (84) Shaffer, S. A.; Goodlett, D. R.; Heron, S. R.; Cooper, J. M.; Wilson, R. Surface Acoustic Wave Nebulization of Peptides As a Microfluidic Interface for Mass Spectrometry. *Anal Chem* **2010**, 82 (10), 3985–3989. <https://doi.org/10.1021/ac100372c>.
- (85) Astefanei, A.; van Bommel, M.; Corthals, G. L. Surface Acoustic Wave Nebulisation Mass Spectrometry for the Fast and Highly Sensitive Characterisation of Synthetic Dyes in Textile Samples. *J Am Soc Mass Spectrom* **2017**, 28 (10), 2108–2116. <https://doi.org/10.1007/s13361-017-1716-x>.
- (86) Dodd, E. E. The Statistics of Liquid Spray and Dust Electrification by the Hopper and Laby Method. *J Appl Phys* **1953**, 24 (1), 73–80. <https://doi.org/10.1063/1.1721137>.
- (87) Song, L.; You, Y.; Evans-Nguyen, T. Surface Acoustic Wave Nebulization with Atmospheric-Pressure Chemical Ionization for Enhanced Ion Signal. *Anal Chem* **2019**, 91 (1), 912–918. <https://doi.org/10.1021/acs.analchem.8b03927>.
- (88) Hirabayashi, A.; Sakairi, M.; Koizumi, H. Sonic Spray Mass Spectrometry. *Anal Chem* **1995**, 67 (17), 2878–2882. <https://doi.org/10.1021/ac00113a023>.
- (89) Huang, Y. Surface Acoustic Wave Nebulization as a Mass Spectrometry Ionization Source, Characterization and Application. PhD Thesis, University of Washington, 2013.
- (90) Qi, A.; Yeo, L.; Friend, J.; Ho, J. The Extraction of Liquid, Protein Molecules and Yeast Cells from Paper through Surface Acoustic Wave Atomization. *Lab Chip* **2010**, 10 (4), 470–476. <https://doi.org/10.1039/b915833b>.
- (91) Astefanei, A.; van den Berg, K. J.; Burnstock, A.; Corthals, G. Surface Acoustic Wave Nebulization-Mass Spectrometry as a New Tool to Investigate the Water Sensitivity Behavior of 20th Century Oil Paints. *Journal of the American Society for Mass Spectrometry*. American Chemical Society February 3, 2021, pp 444–454. <https://doi.org/10.1021/jasms.0c00272>.

- (92) Huang, Y.; Yoon, S. H.; Heron, S. R.; Masselon, C. D.; Edgar, J. S.; Turecek, F.; Goodlett, D. R. Surface Acoustic Wave Nebulization Produces Ions with Lower Internal Energy than Electrospray Ionization. *J Am Soc Mass Spectrom* **2012**, *23* (6), 1062–1070. <https://doi.org/10.1007/s13361-012-0352-8>.
- (93) Hampton, C. Y.; Forbes, T. P.; Varady, M. J.; Meacham, J. M.; Fedorov, A. G.; Degertekin, F. L.; Fernández, F. M. Analytical Performance of a Venturi-Assisted Array of Micromachined Ultrasonic Electrospays Coupled to Ion Trap Mass Spectrometry for the Analysis of Peptides and Proteins. *Anal Chem* **2007**, *79* (21), 8154–8161. <https://doi.org/10.1021/ac071297n>.
- (94) Hampton, C. Y.; Silvestri, C. J.; Forbes, T. P.; Varady, M. J.; Meacham, J. M.; Fedorov, A. G.; Degertekin, F. L.; Fernández, F. M. Comparison of the Internal Energy Deposition of Venturi-Assisted Electrospray Ionization and a Venturi-Assisted Array of Micromachined UltraSonic Electrospays (AMUSE). *J Am Soc Mass Spectrom* **2008**, *19* (9), 1320–1329. <https://doi.org/10.1016/j.jasms.2008.06.012>.
- (95) Meacham, J. M.; Varady, M. J.; Degertekin, F. L.; Fedorov, A. G. Droplet Formation and Ejection from a Micromachined Ultrasonic Droplet Generator: Visualization and Scaling. *Physics of Fluids* **2005**, *17* (10). <https://doi.org/10.1063/1.1921249>.
- (96) Hampton, C. Y. Applications and Fundamental Characterization of Open Air Acoustic-Driven Ionization Methods for Mass Spectrometry. PhD Thesis, Georgia Institute of Technology, 2009.
- (97) Chen, T.-Y.; Lin, J.-Y.; Chen, J.-Y.; Chen, Y.-C. Ultrasonication-Assisted Spray Ionization Mass Spectrometry for the Analysis of Biomolecules in Solution. *J Am Soc Mass Spectrom* **2010**, *21* (9), 1547–1553. <https://doi.org/10.1016/j.jasms.2010.04.021>.
- (98) Chen, T. Y.; Chao, C. S.; Mong, K. K. T.; Chen, Y. C. Ultrasonication-Assisted Spray Ionization Mass Spectrometry for on-Line Monitoring of Organic Reactions. *Chemical Communications* **2010**, *46* (44), 8347–8349. <https://doi.org/10.1039/c0cc02629h>.
- (99) Lin, S. H.; Lo, T. J.; Kuo, F. Y.; Chen, Y. C. Real Time Monitoring of Accelerated Chemical Reactions by Ultrasonication-Assisted Spray Ionization Mass Spectrometry. *Journal of Mass Spectrometry* **2014**, *49* (1), 50–56. <https://doi.org/10.1002/jms.3319>.
- (100) Gordon, E. F.; Mansoori, B. A.; Carroll, C. F.; Muddiman, D. C. Hydrophobic Influences on the Quantification of Equine Heart Cytochrome c Using Relative Ion Abundance Measurements by Electrospray Ionization Fourier Transform Ion Cyclotron Resonance Mass Spectrometry. *Journal of Mass Spectrometry* **1999**, *34* (10), 1055–1062. [https://doi.org/10.1002/\(SICI\)1096-9888\(199910\)34:10<1055::AID-JMS864>3.0.CO;2-E](https://doi.org/10.1002/(SICI)1096-9888(199910)34:10<1055::AID-JMS864>3.0.CO;2-E).
- (101) Fenn, J. B. Ion Formation from Charged Droplets: Roles of Geometry, Energy, and Time. *J Am Soc Mass Spectrom* **1993**, *4* (7), 524–535. [https://doi.org/10.1016/1044-0305\(93\)85014-O](https://doi.org/10.1016/1044-0305(93)85014-O).

- (102) Kebarle, P.; Verkcerk, U. H. Electrospray: From Ions in Solution to Ions in the Gas Phase, What We Know Now. *Mass Spectrom Rev* **2009**, *28* (6), 898–917. <https://doi.org/10.1002/mas.20247>.
- (103) Nepomuceno, A. I.; Muddiman, D. C.; Bergen, H. R.; Craighead, J. R.; Burke, M. J.; Caskey, P. E.; Allan, J. A. Dual Electrospray Ionization Source for Confident Generation of Accurate Mass Tags Using Liquid Chromatography Fourier Transform Ion Cyclotron Resonance Mass Spectrometry. *Anal Chem* **2003**, *75* (14), 3411–3418. <https://doi.org/10.1021/ac0342471>.
- (104) Satomi, Y.; Kudo, Y.; Sasaki, K.; Hase, T.; Takao, T. Accurate Mass Measurement in Nano-Electrospray Ionization Mass Spectrometry by Alternate Switching of High Voltage between Sample and Reference Sprayers. *Rapid Communications in Mass Spectrometry* **2005**, *19* (4), 540–546. <https://doi.org/10.1002/rcm.1813>.
- (105) Wolff, J. C.; Eckers, C.; Sage, A. B.; Giles, K.; Bateman, R. Accurate Mass Liquid Chromatography/Mass Spectrometry on Quadrupole Orthogonal Acceleration Time-of-Flight Mass Analyzers Using Switching between Separate Sample and Reference Sprays. 2. Applications Using the Dual-Electrospray Ion Source. *Anal Chem* **2001**, *73* (11), 2605–2612. <https://doi.org/10.1021/ac001419a>.
- (106) Bowers, J. J.; Zimmerman, J. R.; Oglesbee, R. A.; McLuckey, S. A. Adjacent Pulsed Nanoelectrospray Ionization Emitters for the Alternating Generation of Ions of Opposite Polarity. *Anal Chem* **2010**, *82*, 1147–1150. <https://doi.org/10.1021/ac902485e>.
- (107) Bowers, J. J. Gas Phase Analysis of Biomolecular Ions in a Quadrupole Ion Trap: Protein Analysis and Instrumentation, University of Purdue, 2010.
- (108) Xia, Y.; Liang, X.; McLuckey, S. A. Pulsed Dual Electrospray Ionization for Ion/Ion Reactions. *J Am Soc Mass Spectrom* **2005**, *16* (11), 1750–1756. <https://doi.org/10.1016/j.jasms.2005.07.013>.
- (109) Liang, X.; Han, H.; Xia, Y.; McLuckey, S. A. A Pulsed Triple Ionization Source for Sequential Ion/Ion Reactions in an Electrodynamic Ion Trap. *J Am Soc Mass Spectrom* **2007**, *18* (3), 369–376. <https://doi.org/10.1016/j.jasms.2006.10.004>.
- (110) Liang, X.; Han, H.; Xia, Y.; McLuckey, S. A. Pulsed Dual Electrospray Ionization for Ion/Ion Reactions. *J Am Soc Mass Spectrom* **2005**, *16*, 1750–1756. <https://doi.org/10.1016/j.jasms.2005.07.013>.
- (111) Williams, D. K.; McAlister, G. C.; Good, D. M.; Coon, J. J.; Muddiman, D. C. Dual Electrospray Ion Source for Electron-Transfer Dissociation on a Hybrid Linear Ion Trap-Orbitrap Mass Spectrometer. *Anal Chem* **2007**, *79* (20), 7916–7919. <https://doi.org/10.1021/ac071444h>.
- (112) Flora, J. W.; Hannis, J. C.; Muddiman, D. C. High-Mass Accuracy of Product Ions Produced by SORI-CID Using a Dual Electrospray Ionization Source Coupled with FTICR Mass Spectrometry. *Anal Chem* **2001**, *73* (6), 1247–1251. <https://doi.org/10.1021/ac0011282>.
- (113) Flora, J. W.; Null, A. P.; Muddiman, D. C. Dual-Micro-ESI Source for Precise Mass Determination on a Quadrupole Time-of-Flight Mass

- Spectrometer for Genomic and Proteomic Applications. *Anal Bioanal Chem* **2002**, 373 (7), 538–546. <https://doi.org/10.1007/s00216-002-1357-0>.
- (114) Nepomuceno, A. I.; Mason, C. J.; Muddiman, D. C.; Bergen, H. R.; Zeldenrust, Steven. R. Detection of Genetic Variants of Transthyretin by Liquid Chromatography-Dual Electrospray Ionization Fourier-Transform Ion-Cyclotron-Resonance Mass Spectrometry. *Clin Chem* **2004**, 50 (9), 1535–1543. <https://doi.org/10.1373/clinchem.2004.033274>.
- (115) Johnson, K. L.; Mason, C. J.; Muddiman, D. C.; Eckel, J. E. Analysis of the Low Molecular Weight Fraction of Serum by LC-Dual ESI-FT-ICR Mass Spectrometry: Precision of Retention Time, Mass, and Ion Abundance. *Anal Chem* **2004**, 76 (17), 5097–5103. <https://doi.org/10.1021/ac0497003>.
- (116) Hannis, J. C.; Muddiman, D. C. A Dual Electrospray Ionization Source Combined with Hexapole Accumulation to Achieve High Mass Accuracy of Biopolymers in Fourier Transform Ion Cyclotron Resonance Mass Spectrometry. *J Am Soc Mass Spectrom* **2000**, 11 (10), 876–883. [https://doi.org/10.1016/S1044-0305\(00\)00160-4](https://doi.org/10.1016/S1044-0305(00)00160-4).
- (117) Cody, R. B.; Dane, A. J. Alternative Mass Reference Standards for Direct Analysis in Real Time Mass Spectrometry. *Rapid Communications in Mass Spectrometry* **2016**, 30 (10), 1206–1212. <https://doi.org/10.1002/rcm.7554>.
- (118) Wilhelm, M.; Kirchner, M.; Steen, J. A. J.; Steen, H. Mz5: Space- and Time-Efficient Storage of Mass Spectrometry Data Sets. *Molecular and Cellular Proteomics* **2012**, 11 (1). <https://doi.org/10.1074/mcp.O111.011379>.
- (119) Chambers, M. et. al. A Cross-Platform Toolkit for Mass Spectrometry and Proteomics. *Nat Biotechnol* **2012**, 30 (10), 918–920. <https://doi.org/10.1038/nbt.2377>.
- (120) Li, H.; Liu, J.; Li, K.; Liu, Y. Piezoelectric Micro-Jet Devices: A Review. *Sens Actuators A Phys* **2019**, 297, 111552. <https://doi.org/10.1016/j.sna.2019.111552>.
- (121) Carina Minardi, M. Fundamental Investigation and Novel Applications of Electrospray and Gas-Phase Ionizations, Georgetown University, 2015.
- (122) Kilgour, D. P. A.; Mackay, L.; Hardman, M. E.; Makarov, A. A.; Patrick, ;; Langridge-Smith, R. R. Poster: A Piezoelectric Droplet-on-Demand Interface for the Orbitrap Mass Spectrometer. In *50th American Society for Mass Spectrometry Annual Conference*; 2002.
- (123) Mackay, C. L. Towards Chemical Profiling at the Cellular Level, University of Edinburgh, 2003.
- (124) Shin, P.; Lee, S.; Sung, J.; Kim, J. H. Operability Diagram of Drop Formation and Its Response to Temperature Variation in a Piezoelectric Inkjet Nozzle. *Microelectronics Reliability* **2011**, 51 (2), 437–444. <https://doi.org/10.1016/j.microrel.2010.08.015>.
- (125) Fraters, A.; Jeurissen, R.; Van Den Berg, M.; Reinten, H.; Wijshoff, H.; Lohse, D.; Versluis, M.; Segers, T. Secondary Tail Formation and Breakup

- in Piezoacoustic Inkjet Printing: Femtoliter Droplets Captured in Flight. *Phys Rev Appl* **2020**. <https://doi.org/10.1103/PhysRevApplied.13.024075>.
- (126) Duft, D.; Achtzehn, T.; Müller, R.; A. Huber, B.; Leisner, T. Rayleigh Jets from Levitated Microdroplets. *Nature* **2003**, *421*, 128–128.
- (127) Achtzehn, T.; Müller, R.; Duft, D.; Leisner, T. The Coulomb Instability of Charged Microdroplets: Dynamics and Scaling. In *European Physical Journal D*; 2005; Vol. 34, pp 311–313. <https://doi.org/10.1140/epjd/e2005-00102-1>.
- (128) Grimm, R. L.; Beauchamp, J. L. Dynamics of Field-Induced Droplet Ionization: Time-Resolved Studies of Distortion, Jetting, and Progeny Formation from Charged and Neutral Methanol Droplets Exposed to Strong Electric Fields. *Journal of Physical Chemistry B* **2005**, *109* (16), 8244–8250. <https://doi.org/10.1021/jp0450540>.
- (129) Schneider, B. B.; Covey, T. R. Calibrant Delivery for Mass Spectrometry. *J Am Soc Mass Spectrom* **2007**, *18* (6), 991–996. <https://doi.org/10.1016/j.jasms.2007.02.007>.
- (130) Young, N. L.; Sisto, M. C.; Young, M. N.; Grant, P. G.; Killilea, D. W.; LaMotte, L.; Wu, K. J. J.; Lebrilla, C. B. Steady-State Asymmetric Nanospray Dual Ion Source for Accurate Mass Determination within a Chromatographic Separation. *Anal Chem* **2007**, *79* (15), 5711–5718. <https://doi.org/10.1021/ac070446z>.
- (131) Tang, K.; Tolmachev, A. v.; Nikolaev, E.; Zhang, R.; Belov, M. E.; Udseth, H. R.; Smith, R. D. Independent Control of Ion Transmission in a Jet Disrupter Dual-Channel Ion Funnel Electrospray Ionization MS Interface. *Anal Chem* **2002**, *74* (20), 5431–5437. <https://doi.org/10.1021/ac0202583>.
- (132) Zhu, L.; Gamez, G.; Chen, H.; Chingin, K.; Zenobi, R. Rapid Detection of Melamine in Untreated Milk and Wheat Gluten by Ultrasound-Assisted Extractive Electrospray Ionization Mass Spectrometry (EESI-MS). *Chemical Communications* **2009**, No. 5, 559–561. <https://doi.org/10.1039/b818541g>.
- (133) Forbes, T. P. Rapid Detection and Isotopic Measurement of Discrete Inorganic Samples Using Acoustically Actuated Droplet Ejection and Extractive Electrospray Ionization Mass Spectrometry. *Rapid Communications in Mass Spectrometry* **2014**, *29* (1), 19–28. <https://doi.org/10.1002/rcm.7074>.
- (134) Yu, Z.; Chen, L. C.; Ninomiya, S.; Mandal, M. K.; Hiraoka, K.; Nonami, H. Piezoelectric Inkjet Assisted Rapid Electrospray Ionization Mass Spectrometric Analysis of Metabolites in Plant Single Cells via a Direct Sampling Probe. *Analyst* **2014**, *139* (22), 5734–5739. <https://doi.org/10.1039/c4an01068j>.
- (135) Microdrop Technologies. *Microdrop Dispenser Heads*. Microdrop Dispenser Heads Datsheet. <https://www.microdrop.de/microdrop-dispenser-heads.html> (accessed 2021-09-19).

- (136) Shen, S. C. A New Cymbal-Shaped High Power Microactuator for Nebulizer Application. *Microelectron Eng* **2010**, *87* (2), 89–97. <https://doi.org/10.1016/j.mee.2009.05.036>.
- (137) Shen, S. C.; Wang, Y. J.; Chen, Y. Y. Design and Fabrication of Medical Micro-Nebulizer. *Sens Actuators A Phys* **2008**, *144* (1), 135–143. <https://doi.org/10.1016/j.sna.2007.12.004>.
- (138) Guerra-Bravo, E.; Lee, H. J.; Baltazar, A.; Loh, K. J. Vibration Analysis of a Piezoelectric Ultrasonic Atomizer to Control Atomization Rate. *Applied Sciences (Switzerland)* **2021**, *11* (18). <https://doi.org/10.3390/app11188350>.
- (139) Maehara, N.; Ueha, S.; Mori, E. Optimum Design Procedure for Multi-Pinhole-Plate Ultrasonic Atomizer. *Jpn J Appl Phys* **1987**, *26* (S1), 215–217. <https://doi.org/10.7567/JJAPS.26S1.215>.
- (140) Forbes, T. P.; Staymates, M. Enhanced Aerodynamic Reach of Vapor and Aerosol Sampling for Real-Time Mass Spectrometric Detection Using Venturi-Assisted Entrainment and Ionization. *Anal Chim Acta* **2017**, *957*, 20–28. <https://doi.org/10.1016/j.aca.2016.12.037>.
- (141) Wu, M. X.; Wang, H. Y.; Zhang, J. T.; Guo, Y. L. Multifunctional Carbon Fiber Ionization Mass Spectrometry. *Anal Chem* **2016**, *88* (19), 9547–9553. <https://doi.org/10.1021/acs.analchem.6b02166>.
- (142) Bruker Daltonik GmbH. *Pulse Programming In*; 2010. www.bdal.de.
- (143) Averett, R. C.; Leenheer, J. A.; Mcknight, D. M.; Thorn, K. A. *Humic Substances in the Suwannee River, Georgia: Interactions, Properties, and Proposed Structures*; 1994. <https://doi.org/10.3133/wsp2373>.
- (144) Green, N. W.; McInnis, D.; Hertkorn, N.; Maurice, P. A.; Perdue, E. M. Suwannee River Natural Organic Matter: Isolation of the 2R101N Reference Sample by Reverse Osmosis. *Environ Eng Sci* **2015**, *32* (1), 38–44. <https://doi.org/10.1089/ees.2014.0284>.
- (145) Leenheer, J. A.; Rostad, C. E.; Gates, P. M.; Furlong, E. T.; Ferrer, I. Molecular Resolution and Fragmentation of Fulvic Acid by Electrospray Ionization/Multistage Tandem Mass Spectrometry. *Anal Chem* **2001**, *73* (7), 1461–1471. <https://doi.org/10.1021/ac0012593>.
- (146) Kujawinski, E. B.; Hatcher, P. G.; Freitas, M. A. High-Resolution Fourier Transform Ion Cyclotron Resonance Mass Spectrometry of Humic and Fulvic Acids: Improvements and Comparisons. *Anal Chem* **2002**, *74* (2), 413–419. <https://doi.org/10.1021/ac0108313>.
- (147) Witt, M.; Fuchser, J.; Koch, B. P. Fragmentation Studies of Fulvic Acids Using Collision Induced Dissociation Fourier Transform Ion Cyclotron Resonance Mass Spectrometry. *Anal Chem* **2009**, *81* (7), 2688–2694. <https://doi.org/10.1021/ac802624s>.
- (148) Stenson, A. C.; Marshall, A. G.; Cooper, W. T. Exact Masses and Chemical Formulas of Individual Suwannee River Fulvic Acids from Ultrahigh Resolution Electrospray Ionization Fourier Transform Ion Cyclotron Resonance Mass Spectra. *Anal Chem* **2003**, *75* (6), 1275–1284. <https://doi.org/10.1021/ac026106p>.

- (149) Rostad, C. E.; Leenheer, J. A. Factors That Affect Molecular Weight Distribution of Suwannee River Fulvic Acid as Determined by Electrospray Ionization/Mass Spectrometry. *Anal Chim Acta* **2004**, *523* (2), 269–278. <https://doi.org/10.1016/j.aca.2004.06.065>.
- (150) Fievre, A.; Solouki, T.; Marshall, A. G.; Cooper, W. T. High-Resolution Fourier Transform Ion Cyclotron Resonance Mass Spectrometry of Humic and Fulvic Acids by Laser Desorption/Ionization and Electrospray Ionization. *Energy & Fuels* **1997**, *11*, 554–560.
- (151) Leenheer, J. A.; Rostad, C. E.; Gates, P. M.; Furlong, E. T.; Ferrer, I. Molecular Resolution and Fragmentation of Fulvic Acid by Electrospray Ionization/Multistage Tandem Mass Spectrometry. *Anal Chem* **2001**, *73* (7), 1461–1471. <https://doi.org/10.1021/ac0012593>.
- (152) Kilgour, D. P. A.; Hughes, S.; Kilgour, S. L.; Mackay, C. L.; Palmblad, M.; Tran, B. Q.; Goo, Y. A.; Ernst, R. K.; Clarke, D. J.; Goodlett, D. R. Autopiquer - a Robust and Reliable Peak Detection Algorithm for Mass Spectrometry. *J Am Soc Mass Spectrom* **2017**, *28* (2), 253–262. <https://doi.org/10.1007/s13361-016-1549-z>.
- (153) Cortacero-Ramírez, S.; Hernáinz-Bermúdez, De Castro, M.; Segura-Carretero, A.; Cruces-Blanco, C.; Fernández-Gutiérrez, A. Analysis of Beer Components by Capillary Electrophoretic Methods. *TrAC - Trends in Analytical Chemistry* **2003**, *22* (7), 440–455. [https://doi.org/10.1016/S0165-9936\(03\)00704-0](https://doi.org/10.1016/S0165-9936(03)00704-0).
- (154) Araújo, A. S.; da Rocha, L. L.; Tomazela, D. M.; Sawaya, A. C. H. F.; Almeida, R. R.; Catharino, R. R.; Eberlin, M. N. Electrospray Ionization Mass Spectrometry Fingerprinting of Beer. *Analyst* **2005**, *130* (6), 884–889. <https://doi.org/10.1039/b415252b>.
- (155) Cajka, T.; Riddellova, K.; Tomaniova, M.; Hajslova, J. Ambient Mass Spectrometry Employing a DART Ion Source for Metabolomic Fingerprinting/Profiling: A Powerful Tool for Beer Origin Recognition. *Metabolomics* **2011**, *7* (4), 500–508. <https://doi.org/10.1007/s11306-010-0266-z>.
- (156) Cajka, T.; Riddellova, K.; Tomaniova, M.; Hajslova, J. Recognition of Beer Brand Based on Multivariate Analysis of Volatile Fingerprint. *J Chromatogr A* **2010**, *1217* (25), 4195–4203. <https://doi.org/10.1016/j.chroma.2009.12.049>.
- (157) Mattarucchi, E.; Stocchero, M.; Moreno-Rojas, J. M.; Giordano, G.; Reniero, F.; Guillou, C. Authentication of Trappist Beers by LC-MS Fingerprints and Multivariate Data Analysis. *J Agric Food Chem* **2010**, *58* (23), 12089–12095. <https://doi.org/10.1021/jf102632g>.
- (158) Pérez-Ràfols, C.; Saurina, J. Liquid Chromatographic Fingerprints and Profiles of Polyphenolic Compounds Applied to the Chemometric Characterization and Classification of Beers. *Analytical Methods* **2015**, *7* (20), 8733–8739. <https://doi.org/10.1039/c5ay02113h>.
- (159) Klein, O.; Roth, A.; Dornuf, F.; Schöller, O.; Mäntele, W. The Good Vibrations of Beer. The Use of Infrared and UV/Vis Spectroscopy and Chemometry for the Quantitative Analysis of Beverages. *Zeitschrift für*

Naturforschung - Section B Journal of Chemical Sciences **2012**, 67 (10), 1005–1015. <https://doi.org/10.5560/ZNB.2012-0166>.

- (160) Polshin, E.; Aernouts, B.; Saeys, W.; Delvaux, F.; Delvaux, F. R.; Saison, D.; Hertog, M.; Nicolaï, B. M.; Lammertyn, J. Beer Quality Screening by FT-IR Spectrometry: Impact of Measurement Strategies, Data Pre-Processings and Variable Selection Algorithms. *J Food Eng* **2011**, 106 (3), 188–198. <https://doi.org/10.1016/j.jfoodeng.2011.05.003>.
- (161) Alves, V.; Gonçalves, J.; Figueira, J. A.; Ornelas, L. P.; Branco, R. N.; Câmara, J. S.; Pereira, J. A. M. Beer Volatile Fingerprinting at Different Brewing Steps. *Food Chem* **2020**, 326 (November 2019), 126856. <https://doi.org/10.1016/j.foodchem.2020.126856>.
- (162) Rossi, S.; Sileoni, V.; Perretti, G.; Marconi, O. Characterization of the Volatile Profiles of Beer Using Headspace Solid-Phase Microextraction and Gas Chromatography-Mass Spectrometry. *J Sci Food Agric* **2014**, 94 (5), 919–928. <https://doi.org/10.1002/jsfa.6336>.
- (163) Yang, Q.; Tu, J.; Chen, M.; Gong, X. Discrimination of Fruit Beer Based on Fingerprints by Static Headspace-Gas Chromatography-Ion Mobility Spectrometry. *Journal of the American Society of Brewing Chemists* **2021**, 0 (0), 1–7. <https://doi.org/10.1080/03610470.2021.1946654>.
- (164) Fu, Y.; Zhao, C.; Lu, X.; Xu, G. Nontargeted Screening of Chemical Contaminants and Illegal Additives in Food Based on Liquid Chromatography–High Resolution Mass Spectrometry. *TrAC - Trends in Analytical Chemistry*. Elsevier B.V. November 1, 2017, pp 89–98. <https://doi.org/10.1016/j.trac.2017.07.014>.
- (165) Cortés-Aguado, S.; Sánchez-Morito, N.; Arrebola, F. J.; Frenich, A. G.; Vidal, J. L. M. Fast Screening of Pesticide Residues in Fruit Juice by Solid-Phase Microextraction and Gas Chromatography-Mass Spectrometry. *Food Chem* **2008**, 107 (3), 1314–1325. <https://doi.org/10.1016/j.foodchem.2007.09.033>.
- (166) Feng, F.; Zhao, Y.; Yong, W.; Sun, L.; Jiang, G.; Chu, X. Highly Sensitive and Accurate Screening of 40 Dyes in Soft Drinks by Liquid Chromatography-Electrospray Tandem Mass Spectrometry. *J Chromatogr B Analyt Technol Biomed Life Sci* **2011**, 879 (20), 1813–1818. <https://doi.org/10.1016/j.jchromb.2011.04.014>.
- (167) Zambonin, C. G.; Quinto, M.; de Vietro, N.; Palmisano, F. Solid-Phase Microextraction - Gas Chromatography Mass Spectrometry: A Fast and Simple Screening Method for the Assessment of Organophosphorus Pesticides Residues in Wine and Fruit Juices. *Food Chem* **2004**, 86 (2), 269–274. <https://doi.org/10.1016/j.foodchem.2003.09.025>.
- (168) Swiner, D. J.; Jackson, S.; Burris, B. J.; Badu-Tawiah, A. K. Applications of Mass Spectrometry for Clinical Diagnostics: The Influence of Turnaround Time. *Analytical Chemistry*. American Chemical Society January 7, 2020, pp 183–202. <https://doi.org/10.1021/acs.analchem.9b04901>.
- (169) Alexander, J.; Gildea, L.; Balog, J.; Speller, A.; McKenzie, J.; Muirhead, L.; Scott, A.; Kontovounisios, C.; Rasheed, S.; Teare, J.; Hoare, J.; Veselkov, K.; Goldin, R.; Tekkis, P.; Darzi, A.; Nicholson, J.; Kinross, J.;

- Takats, Z. A Novel Methodology for in Vivo Endoscopic Phenotyping of Colorectal Cancer Based on Real-Time Analysis of the Mucosal Lipidome: A Prospective Observational Study of the IKnife. *Surg Endosc* **2017**, *31* (3), 1361–1370. <https://doi.org/10.1007/s00464-016-5121-5>.
- (170) Phelps, D. L.; Balog, J.; Gildea, L. F.; Bodai, Z.; Savage, A.; El-Bahrawy, M. A.; Speller, A. V.; Rosini, F.; Kudo, H.; McKenzie, J. S.; Brown, R.; Takáts, Z.; Ghaem-Maghani, S. The Surgical Intelligent Knife Distinguishes Normal, Borderline and Malignant Gynaecological Tissues Using Rapid Evaporative Ionisation Mass Spectrometry (REIMS). *Br J Cancer* **2018**, *118* (10), 1349–1358. <https://doi.org/10.1038/s41416-018-0048-3>.
- (171) Schäfer, K. C.; Dénes, J.; Albrecht, K.; Szaniszló, T.; Balogh, J.; Skoumal, R.; Katona, M.; Tóth, M.; Balogh, L.; Takáts, Z. In Vivo, in Situ Tissue Analysis Using Rapid Evaporative Ionization Mass Spectrometry. *Angewandte Chemie - International Edition* **2009**, *48* (44), 8240–8242. <https://doi.org/10.1002/anie.200902546>.
- (172) Wiseman, J. M.; Puolitaival, S. M.; Takáts, Z.; Cooks, R. G.; Caprioli, R. M. Mass Spectrometric Profiling of Intact Biological Tissue by Using Desorption Electrospray Ionization. *Angewandte Chemie - International Edition* **2005**, *44* (43), 7094–7097. <https://doi.org/10.1002/anie.200502362>.
- (173) Serna, J.; García-Seisdedos, D.; Alcázar, A.; Lasunción, M. Á.; Busto, R.; Pastor, Ó. Quantitative Lipidomic Analysis of Plasma and Plasma Lipoproteins Using MALDI-TOF Mass Spectrometry. *Chem Phys Lipids* **2015**, *189*, 7–18. <https://doi.org/10.1016/j.chemphyslip.2015.05.005>.
- (174) Engel, K. M.; Prabutzki, P.; Leopold, J.; Nimptsch, A.; Lemmnitzer, K.; Vos, D. R. N.; Hopf, C.; Schiller, J. A New Update of MALDI-TOF Mass Spectrometry in Lipid Research. *Progress in Lipid Research*. Elsevier Ltd April 1, 2022. <https://doi.org/10.1016/j.plipres.2021.101145>.
- (175) Cameron, S. J. S.; Alexander, J. L.; Bolt, F.; Burke, A.; Ashrafiyan, H.; Teare, J.; Marchesi, J. R.; Kinross, J.; Li, J. v.; Takáts, Z. Evaluation of Direct from Sample Metabolomics of Human Feces Using Rapid Evaporative Ionization Mass Spectrometry. *Anal Chem* **2019**, *91* (21), 13448–13457. <https://doi.org/10.1021/acs.analchem.9b02358>.
- (176) Iwano, T.; Yoshimura, K.; Inoue, S.; Odate, T.; Ogata, K.; Funatsu, S.; Tanihata, H.; Kondo, T.; Ichikawa, D.; Takeda, S. Breast Cancer Diagnosis Based on Lipid Profiling by Probe Electrospray Ionization Mass Spectrometry. *British Journal of Surgery* **2020**, *107* (6), 632–635. <https://doi.org/10.1002/bjs.11613>.
- (177) Lu, H.; Zhang, H.; Xu, S.; Li, L. Review of Recent Advances in Lipid Analysis of Biological Samples via Ambient Ionization Mass Spectrometry. *Metabolites*. MDPI November 1, 2021. <https://doi.org/10.3390/metabo11110781>.
- (178) Mandal, M. K.; Chen, L. C.; Hiraoka, K. Sequential and Exhaustive Ionization of Analytes with Different Surface Activity by Probe Electrospray Ionization. *J Am Soc Mass Spectrom* **2011**, *22* (9), 1493–1500. <https://doi.org/10.1007/s13361-011-0162-4>.

- (179) Schlosser, A.; Volkmer-Engert, R. Volatile Polydimethylcyclosiloxanes in the Ambient Laboratory Air Identified as Source of Extreme Background Signals in Nano electrospray Mass Spectrometry. *Journal of Mass Spectrometry* **2003**, *38* (5), 523–525. <https://doi.org/10.1002/jms.465>.
- (180) McCullough, B.; Hopley, C. *BMSS Ambient Ionisation Special Interest Group Interlaboratory Study II Report*; 2018.
- (181) McCullough, B. J.; Hopley, C. J. Results of the First and Second British Mass Spectrometry Society Interlaboratory Studies on Ambient Mass Spectrometry. *Rapid Communications in Mass Spectrometry* **2021**, *35* (S2). <https://doi.org/10.1002/rcm.8534>.
- (182) Qi, Y.; Volmer, D. A. Electron-Based Fragmentation Methods in Mass Spectrometry: An Overview. *Mass Spectrometry Reviews*. 2017, pp 4–15. <https://doi.org/10.1002/mas.21482>.
- (183) Bayat, P.; Lesage, D.; Cole, R. B. Tutorial: Ion Activation in Tandem Mass Spectrometry Using Ultra-High Resolution Instrumentation. *Mass Spectrom Rev* **2020**, *39* (5–6), 680–702. <https://doi.org/10.1002/mas.21623>.
- (184) Syka, J. E. P.; Coon, J. J.; Schroeder, M. J.; Shabanowitz, J.; Hunt, D. F. Peptide and Protein Sequence Analysis by Electron Transfer Dissociation Mass Spectrometry. *Proc Natl Acad Sci U S A* **2004**, *101* (26), 9528–9533. <https://doi.org/10.1073/pnas.0402700101>.
- (185) Little, D. P.; Speir, J. P.; Senko, M. W.; O'Connor, P. B.; McLafferty, F. W. Infrared Multiphoton Dissociation of Large Multiply Charged Ions for Biomolecule Sequencing. *Anal Chem* **1994**, *66* (18), 2809–2815. <https://doi.org/10.1021/ac00090a004>.
- (186) Bricker, D. L.; Adams, T. A.; Russell, D. H. Collision-Induced Dissociation with Fourier Transform Mass Spectrometry. *Anal Chem* **1983**, *55* (14), 2417–2418. <https://doi.org/10.1021/ac00264a048>.
- (187) Mosely, J. A.; Smith, M. J. P.; Prakash, A. S.; Sims, M.; Bristow, A. W. T. Electron-Induced Dissociation of Singly Charged Organic Cations as a Tool for Structural Characterization of Pharmaceutical Type Molecules. *Anal Chem* **2011**, *83* (11), 4068–4075. <https://doi.org/10.1021/ac200045n>.
- (188) Feketeová, L.; Wong, M. W.; O'Hair, R. A. J. The Role of Metal Cation in Electron-Induced Dissociation of Tryptophan. *European Physical Journal D* **2010**, *60* (1), 11–20. <https://doi.org/10.1140/epjd/e2010-00019-6>.
- (189) Wei, J.; Bristow, A. W. T.; O'Connor, P. B. The Competitive Influence of Li⁺, Na⁺, K⁺, Ag⁺, and H⁺ on the Fragmentation of a Pegylated Polymeric Excipient. *J Am Soc Mass Spectrom* **2014**, *26* (1), 166–173. <https://doi.org/10.1007/s13361-014-1009-6>.
- (190) Girod, M.; Carissan, Y.; Humbel, S.; Charles, L. Tandem Mass Spectrometry of Doubly Charged Poly(Ethylene Oxide) Oligomers Produced by Electrospray Ionization. *Int J Mass Spectrom* **2008**, *272* (1), 1–11. <https://doi.org/10.1016/j.ijms.2007.12.010>.

- (191) Wei, J. *Advanced Applications of High Performance Fourier Transform Ion Cyclotron Resonance Mass Spectrometry*, University of Warwick, 2014. <http://go.warwick.ac.uk/wrap><http://go.warwick.ac.uk/wrap/66290>.
- (192) Scionti, V.; Wesdemiotis, C. Electron Transfer Dissociation versus Collisionally Activated Dissociation of Cationized Biodegradable Polyesters. *Journal of Mass Spectrometry* **2012**, *47* (11), 1442–1449. <https://doi.org/10.1002/jms.3097>.
- (193) Kaczorowska, M. A.; Cooper, H. J. Characterization of Polyphosphoesters by Fourier Transform Ion Cyclotron Resonance Mass Spectrometry. *J Am Soc Mass Spectrom* **2009**, *20* (12), 2238–2247. <https://doi.org/10.1016/j.jasms.2009.08.012>.
- (194) Cerda, B. A.; Horn, D. M.; Breuker, K.; McLafferty, F. W. Sequencing of Specific Copolymer Oligomers by Electron-Capture-Dissociation Mass Spectrometry. *J Am Chem Soc* **2002**, *124* (31), 9287–9291. <https://doi.org/10.1021/ja0123756>.
- (195) Iavarone, A. T.; Paech, K.; Williams, E. R. Effects of Charge State and Cationizing Agent on the Electron Capture Dissociation of a Peptide. *Anal Chem* **2004**, *76* (8), 2231–2238. <https://doi.org/10.1021/ac035431p>.
- (196) Horn, D. M.; Zubarev, R. A.; McLafferty, F. W. Automated Reduction and Interpretation of High Resolution Electrospray Mass Spectra of Large Molecules. *J Am Soc Mass Spectrom* **2000**, *11* (4), 320–332. [https://doi.org/10.1016/S1044-0305\(99\)00157-9](https://doi.org/10.1016/S1044-0305(99)00157-9).
- (197) Kelly, R. T.; Page, J. S.; Luo, Q.; Moore, R. J.; Orton, D. J.; Tang, K.; Smith, R. D. Chemically Etched Open Tubular and Monolithic Emitters for Nanoelectrospray Ionization Mass Spectrometry. *Anal Chem* **2006**, *78* (22), 7796–7801.
- (198) P-1000 Flaming/Brown™ Micropipette Puller System Operation Manual. *Operation Manual*. 2020. https://www.sutter.com/manuals/P-1000_OpMan.pdf (accessed 2022-05-24).
- (199) Alexander, J. T.; Nastuk, W. L. An Instrument for the Production of Microelectrodes Used in Electrophysiological Studies. *Review of Scientific Instruments* **1953**, *24* (7), 528–531. <https://doi.org/10.1063/1.1770777>.
- (200) Tycova, A.; Prikryl, J.; Frantisek, F. Reproducible Preparation of Nanospray Tips for Capillary Electrophoresis Coupled to Mass Spectrometry Using 3D Printed Grinding Device. *Electrophoresis* **2016**, *37*, 924–930. <https://doi.org/10.1002/elps.20150046>.
- (201) Cheng, Y. Q.; Su, Y.; Fang, X. X.; Pan, J. Z.; Fang, Q. A Simple Fabrication Method for Tapered Capillary Tip and Its Applications in High-Speed CE and ESI-MS. *Electrophoresis* **2014**, *35* (10), 1484–1488. <https://doi.org/10.1002/elps.201300631>.
- (202) Kriger, M. S.; Cook, K. D.; Ramsey, R. S. *Durable Gold-Coated Fused Silica Capillaries for Use in Electrospray Mass Spectrometry*; 1995; Vol. 67. <https://pubs.acs.org/sharingguidelines>.

- (203) Tycova, A.; Foret, F. Capillary Electrophoresis in an Extended Nanospray Tip-Electrospray as an Electrophoretic Column. *J Chromatogr A* **2015**, *1388*, 274–279. <https://doi.org/10.1016/j.chroma.2015.02.042>.
- (204) Kusý, P.; Klepárník, K.; Aturki, Z.; Fanali, S.; Foret, F. Optimization of a Pressurized Liquid Junction Nanoelectrospray Interface between CE and MS for Reliable Proteomic Analysis. *Electrophoresis* **2007**, *28* (12), 1964–1969. <https://doi.org/10.1002/elps.200600640>.
- (205) TopSpec. *Periodic Reporting for Period 1 - Next Generation Precision Antibody Profiling - from Science Fiction to Reality*; 2019.
- (206) Zhong, X.; Chen, H.; Zare, R. N. Ultrafast Enzymatic Digestion of Deoxyribonucleic Acid in Aqueous Microdroplets for Sequence Discrimination and Identification. *QRB Discov* **2021**, *2*, 0–7. <https://doi.org/10.1017/qrd.2021.2>.
- (207) Zhong, X.; Chen, H.; Zare, R. N. Ultrafast Enzymatic Digestion of Proteins by Microdroplet Mass Spectrometry. *Nat Commun* **2020**, *11* (1), 1–9. <https://doi.org/10.1038/s41467-020-14877-x>.
- (208) Gunawardena, H. P.; Zare, R. N.; Chen, H.; Zhao, P.; Zhong, X. Microdroplet Ultrafast Reactions Speed Antibody Characterization. *Anal Chem* **2021**, *93* (8), 3997–4005. <https://doi.org/10.1021/acs.analchem.0c04974>.
- (209) Wleklinski, M.; Loren, B. P.; Ferreira, C. R.; Jaman, Z.; Avramova, L.; Sobreira, T. J. P.; Thompson, D. H.; Cooks, R. G. High Throughput Reaction Screening Using Desorption Electrospray Ionization Mass Spectrometry. *Chem Sci* **2018**, *9* (6), 1647–1653. <https://doi.org/10.1039/c7sc04606e>.
- (210) Shimada, H.; Maeno, K.; Kinoshita, K.; Shida, Y. Rapid Analysis of Ingredients in Cream Using Ultrasonic Mist–Direct Analysis in Real-Time Time-of-Flight Mass Spectrometry. *J Am Soc Mass Spectrom* **2017**, *28* (11), 2393–2400. <https://doi.org/10.1007/s13361-017-1746-4>.
- (211) Banerjee, S.; Zare, R. N. Syntheses of Isoquinoline and Substituted Quinolines in Charged Microdroplets. *Angewandte Chemie - International Edition* **2015**, *54* (49), 14795–14799. <https://doi.org/10.1002/anie.201507805>.
- (212) Yan, X. Emerging Microdroplet Chemistry for Synthesis and Analysis. *Int J Mass Spectrom* **2021**, *468*, 116639. <https://doi.org/10.1016/j.ijms.2021.116639>.
- (213) Yan, X.; Bain, R. M.; Cooks, R. G. Organic Reactions in Microdroplets: Reaction Acceleration Revealed by Mass Spectrometry. *Angewandte Chemie - International Edition* **2016**, *55* (42), 12960–12972. <https://doi.org/10.1002/anie.201602270>.
- (214) Banerjee, S.; Gnanamani, E.; Yan, X.; Zare, R. N. Can All Bulk-Phase Reactions Be Accelerated in Microdroplets? *Analyst* **2017**, *142* (9), 1399–1402. <https://doi.org/10.1039/c6an02225a>.
- (215) Ruiz-lopez, M. F.; Francisco, J. S. Molecular Reactions at Aqueous Interfaces. *Nat Rev Chem*. <https://doi.org/10.1038/s41570-020-0203-2>.

- (216) Ingram, A. J.; Boeser, C. L.; Zare, R. N. Going beyond Electrospray: Mass Spectrometric Studies of Chemical Reactions in and on Liquids. *Chem Sci* **2015**, *7* (1), 39–55. <https://doi.org/10.1039/c5sc02740c>.
- (217) Yergey, A. L.; Yergey, A. K. Preparative Scale Mass Spectrometry: A Brief History of the Calutron. *Journal of Mass Spectrometry* **1997**, *8*, 943–953. <https://doi.org/10.1002/jms.4509>.
- (218) Gronert, S. Mass Spectrometric Studies of Organic Ion/Molecule Reactions. *Chem Rev* **2001**, *101* (2), 329–360. <https://doi.org/10.1021/cr9900836>.
- (219) Augusti, R.; Chen, H.; Eberlin, L. S.; Nefliu, M.; Cooks, R. G. Atmospheric Pressure Eberlin Transacetalization Reactions in the Heterogeneous Liquid/Gas Phase. *Int J Mass Spectrom* **2006**, *253* (3), 281–287. <https://doi.org/10.1016/j.ijms.2006.05.005>.
- (220) Marsh, B. M.; Iyer, K.; Cooks, R. G. Reaction Acceleration in Electrospray Droplets: Size, Distance, and Surfactant Effects. *J Am Soc Mass Spectrom* **2019**, *30* (10), 2022–2030. <https://doi.org/10.1007/s13361-019-02264-w>.
- (221) Bain, R. M.; Pulliam, C. J.; Cooks, R. G. Accelerated Hantzsch Electrospray Synthesis with Temporal Control of Reaction Intermediates. *Chem Sci* **2015**, *6* (1), 397–401. <https://doi.org/10.1039/c4sc02436b>.
- (222) Kebarle, P.; Tang, L. From Ions in Solution to Ions in the Gas Phase: The Mechanism of Electrospray Mass Spectrometry. *Anal Chem* **1993**, *65* (22), 972–986.
- (223) Ashton, D. S.; Beddell, C. R.; Cooper B N Green, D. J.; A Oliver, R. W. Mechanism of Production of Ions in Electrospray Mass Spectrometry. *Organic Mass Spectrometry* **1993**, *28*, 721–728.
- (224) Kelly, M. A.; Vestling, M. M.; Fenselau, C. C.; Smith, P. B. Electrospray Analysis of Proteins: A Comparison of Positive-Ion and Negative-Ion Mass Spectra at High and Low PH. *Organic Mass Spectrometry* **1992**, *27*, 1143–1147.
- (225) Girod, M.; Moyano, E.; Campbell, D. I.; Cooks, R. G. Accelerated Bimolecular Reactions in Microdroplets Studied by Desorption Electrospray Ionization Mass Spectrometry. *Chem Sci* **2011**, *2* (3), 501–510. <https://doi.org/10.1039/c0sc00416b>.
- (226) Wei, Z.; Li, Y.; Cooks, R. G.; Yan, X. Accelerated Reaction Kinetics in Microdroplets: Overview and Recent Developments. *Annu Rev Phys Chem* **2020**, *71*, 31–51. <https://doi.org/10.1146/annurev-physchem-121319-110654>.
- (227) Zhou, Z.; Yan, X.; Lai, Y. H.; Zare, R. N. Fluorescence Polarization Anisotropy in Microdroplets. *Journal of Physical Chemistry Letters* **2018**, *9* (11), 2928–2932. <https://doi.org/10.1021/acs.jpcllett.8b01129>.
- (228) Fallah-Araghi, A.; Meguellati, K.; Baret, J. C.; el Harrak, A.; Mangeat, T.; Karplus, M.; Ladame, S.; Marques, C. M.; Griffiths, A. D. Enhanced Chemical Synthesis at Soft Interfaces: A Universal Reaction-Adsorption

- Mechanism in Microcompartments. *Phys Rev Lett* **2014**, *112* (2), 1–5. <https://doi.org/10.1103/PhysRevLett.112.028301>.
- (229) Nam, I.; Lee, J. K.; Nam, H. G.; Zare, R. N. Abiotic Production of Sugar Phosphates and Uridine Ribonucleoside in Aqueous Microdroplets. *Proc Natl Acad Sci U S A* **2017**, *114* (47), 12396–12400. <https://doi.org/10.1073/pnas.1714896114>.
- (230) Lee, J. K.; Kim, S.; Nam, H. G.; Zare, R. N. Microdroplet Fusion Mass Spectrometry for Fast Reaction Kinetics. *Proceedings of the National Academy of Sciences* **2015**, *112* (13), 3898–3903. <https://doi.org/10.1073/pnas.1503689112>.
- (231) Hu, L.; She, L.; Fang, Y.; Su, R.; Fu, X. Deformation Characteristics of Droplet Generated by Rayleigh Jet Breakup. *AIP Adv* **2021**, *11* (4). <https://doi.org/10.1063/5.0045196>.
- (232) Mortensen, D. N.; Williams, E. R. Theta-Glass Capillaries in Electrospray Ionization: Rapid Mixing and Short Droplet Lifetimes. *Anal Chem* **2014**, *86* (18), 9315–9321. <https://doi.org/10.1021/ac502545r>.
- (233) Liu, X. P.; Wang, H. Y.; Guo, Y. L. Online Investigation of Reaction Acceleration and Reaction Mechanism by Thermospray Ionization Mass Spectrometry. *Int J Mass Spectrom* **2019**, *435*, 1–6. <https://doi.org/10.1016/j.ijms.2018.09.032>.
- (234) Bain, R. M.; Pulliam, C. J.; Thery, F.; Cooks, R. G. Accelerated Chemical Reactions and Organic Synthesis in Leidenfrost Droplets. *Angewandte Chemie - International Edition* **2016**, *55* (35), 10478–10482. <https://doi.org/10.1002/anie.201605899>.
- (235) Fedick, P. W.; Iyer, K.; Wei, Z.; Avramova, L.; Capek, G. O.; Cooks, R. G. Screening of the Suzuki Cross-Coupling Reaction Using Desorption Electrospray Ionization in High-Throughput and in Leidenfrost Droplet Experiments. *J Am Soc Mass Spectrom* **2019**, *30* (10), 2144–2151. <https://doi.org/10.1007/s13361-019-02287-3>.
- (236) Salvitti, C.; de Petris, G.; Troiani, A.; Managò, M.; Villani, C.; Ciogli, A.; Sorato, A.; Ricci, A.; Pepi, F. Accelerated D-Fructose Acid-Catalyzed Reactions in Thin Films Formed by Charged Microdroplets Deposition. *J Am Soc Mass Spectrom* **2022**, *33* (3), 565–572. <https://doi.org/10.1021/jasms.1c00363>.
- (237) Wei, Z.; Wlekinski, M.; Ferreira, C.; Cooks, R. G. Reaction Acceleration in Thin Films with Continuous Product Deposition for Organic Synthesis. *Angewandte Chemie* **2017**, *129* (32), 9514–9518. <https://doi.org/10.1002/ange.201704520>.
- (238) Badu-Tawiah, A. K.; Campbell, D. I.; Cooks, R. G. Accelerated C-N Bond Formation in Dropcast Thin Films on Ambient Surfaces. *J Am Soc Mass Spectrom* **2012**, *23* (9), 1461–1468. <https://doi.org/10.1007/s13361-012-0394-y>.
- (239) Iyer, K.; Yi, J.; Bogdan, A.; Talaty, N.; Djuric, S. W.; Cooks, R. G. Accelerated Multi-Reagent Copper Catalysed Coupling Reactions in Micro Droplets and Thin Films. *React Chem Eng* **2018**, *3* (2), 206–209. <https://doi.org/10.1039/c8re00002f>.

- (240) Bain, R. M.; Pulliam, C. J.; Yan, X.; Moore, K. F.; Müller, T.; Cooks, R. G. Mass Spectrometry in Organic Synthesis: Claisen-Schmidt Base-Catalyzed Condensation and Hammett Correlation of Substituent Effects. *J Chem Educ* **2014**, *91* (11), 1985–1989. <https://doi.org/10.1021/ed500288m>.
- (241) Yan, X.; Augusti, R.; Li, X.; Cooks, R. G. Chemical Reactivity Assessment Using Reactive Paper Spray Ionization Mass Spectrometry: The Katritzky Reaction. *Chempluschem* **2013**, *78* (9), 1142–1148. <https://doi.org/10.1002/cplu.201300172>.
- (242) Bain, R. M.; Ayrton, S. T.; Cooks, R. G. Fischer Indole Synthesis in the Gas Phase, the Solution Phase, and at the Electrospray Droplet Interface. *J Am Soc Mass Spectrom* **2017**, *28* (7), 1359–1364. <https://doi.org/10.1007/s13361-017-1597-z>.
- (243) Lee, J. K.; Banerjee, S.; Nam, H. G.; Zare, R. N. Acceleration of Reaction in Charged Microdroplets. *Q Rev Biophys* **2015**, *48* (4), 437–444. <https://doi.org/10.1017/S0033583515000086>.
- (244) Hong, T.; Lu, A.; Liu, W.; Chen, C. Microdroplet Synthesis of Silver Nanoparticles with Controlled Sizes. *Micromachines (Basel)* **2019**, *10* (4). <https://doi.org/10.3390/mi10040274>.
- (245) Lee, J. K.; Samanta, D.; Nam, H. G.; Zare, R. N. Spontaneous Formation of Gold Nanostructures in Aqueous Microdroplets. *Nat Commun* **2018**, *9* (1562), 1–9. <https://doi.org/10.1038/s41467-018-04023-z>.
- (246) Jansson, E. T.; Lai, Y. H.; Santiago, J. G.; Zare, R. N. Rapid Hydrogen-Deuterium Exchange in Liquid Droplets. *J Am Chem Soc* **2017**, *139* (20), 6851–6854. <https://doi.org/10.1021/jacs.7b03541>.
- (247) Lee, J. K.; Walker, K. L.; Han, H. S.; Kang, J.; Prinz, F. B.; Waymouth, R. M.; Nam, H. G.; Zare, R. N. Spontaneous Generation of Hydrogen Peroxide from Aqueous Microdroplets. *Proc Natl Acad Sci U S A* **2019**, *116* (39), 19294–19298. <https://doi.org/10.1073/pnas.1911883116>.
- (248) Li, Y.; Liu, Y.; Gao, H.; Helmy, R.; Wuelfing, W. P.; Welch, C. J.; Cooks, R. G. Accelerated Forced Degradation of Pharmaceuticals in Levitated Microdroplet Reactors. *Chemistry - A European Journal* **2018**, *24* (29), 7349–7353. <https://doi.org/10.1002/chem.201801176>.
- (249) Li, Y.; Hu, Y.; Logsdon, D. L.; Liu, Y.; Zhao, Y.; Cooks, R. G. Accelerated Forced Degradation of Therapeutic Peptides in Levitated Microdroplets. *Pharm Res* **2020**, *37* (7). <https://doi.org/10.1007/s11095-020-02868-y>.
- (250) Crawford, E. A.; Esen, C.; Volmer, D. A. Real Time Monitoring of Containerless Microreactions in Acoustically Levitated Droplets via Ambient Ionization Mass Spectrometry. *Anal Chem* **2016**, *88* (17), 8396–8403. <https://doi.org/10.1021/acs.analchem.6b01519>.
- (251) Rainer, T.; Eidelpes, R.; Tollinger, M.; Müller, T. Microdroplet Mass Spectrometry Enables Extremely Accelerated Pepsin Digestion of Proteins. *J Am Soc Mass Spectrom* **2021**. <https://doi.org/10.1021/jasms.1c00126>.
- (252) Mortensen, D. N.; Williams, E. R. Ultrafast (1 Ms) Mixing and Fast Protein Folding in Nanodrops Monitored by Mass Spectrometry. *J Am Chem Soc* **2016**, *138* (10), 3453–3460. <https://doi.org/10.1021/jacs.5b13081>.

- (253) Müller, T.; Badu-Tawiah, A.; Cooks, R. G. Accelerated Carbon-Carbon Bond-Forming Reactions in Preparative Electrospray. *Angewandte Chemie - International Edition* **2012**, *51* (47), 11832–11835. <https://doi.org/10.1002/anie.201206632>.
- (254) Yan, X.; Cheng, H.; Zare, R. N. Two-Phase Reactions in Microdroplets without the Use of Phase-Transfer Catalysts. *Angewandte Chemie - International Edition* **2017**, *56* (13), 3562–3565. <https://doi.org/10.1002/anie.201612308>.
- (255) Yan, X.; Lai, Y. H.; Zare, R. N. Preparative Microdroplet Synthesis of Carboxylic Acids from Aerobic Oxidation of Aldehydes. *Chem Sci* **2018**, *9* (23), 5207–5211. <https://doi.org/10.1039/c8sc01580e>.
- (256) Zhu, X.; Zhang, W.; Lin, Q.; Ye, M.; Xue, L.; Liu, J.; Wang, Y.; Cheng, H. Direct Microdroplet Synthesis of Carboxylic Acids from Alcohols by Preparative Paper Spray Ionization without Phase Transfer Catalysts. *ACS Sustain Chem Eng* **2019**, *7* (7), 6486–6491. <https://doi.org/10.1021/acssuschemeng.9b00427>.
- (257) Liu, C.; Li, J.; Chen, H.; Zare, R. N. Scale-up of Microdroplet Reactions by Heated Ultrasonic Nebulization. *Chem Sci* **2019**, *10* (40), 9367–9373. <https://doi.org/10.1039/c9sc03701b>.
- (258) Nie, H.; Wei, Z.; Qiu, L.; Chen, X.; Holden, D. T.; Cooks, R. G. High-Yield Gram-Scale Organic Synthesis Using Accelerated Microdroplet/Thin Film Reactions with Solvent Recycling. *Chem Sci* **2020**. <https://doi.org/10.1039/c9sc06265c>.
- (259) Sridhar, S. K.; Saravanan, M.; Ramesh, A. Synthesis and Antibacterial Screening of Hydrazones, Schiff and Mannich Bases of Isatin Derivatives. *European Journal of Medicinal Chemistry* **2001**, *36*, 615–625. [https://doi.org/https://doi.org/10.1016/S0223-5234\(01\)01255-7](https://doi.org/https://doi.org/10.1016/S0223-5234(01)01255-7).
- (260) Bain, R. M.; Pulliam, C. J.; Ayrton, S. T.; Bain, K.; Cooks, R. G. Accelerated Hydrazone Formation in Charged Microdroplets. *Rapid Communications in Mass Spectrometry* **2016**, 1875–1878. <https://doi.org/10.1002/rcm.7664>.
- (261) Sahni, T.; Sharma, S.; Arora, G.; Verma, D. Synthesis, Characterization and Antifungal Activity of a Substituted Coumarin and Its Derivatives. *Pesticide Research Journal* **2020**, *32* (1), 39–48. <https://doi.org/10.5958/2249-524X.2020.00007.2>.
- (262) Bain, R. M. Monitoring of Organic Reactions With and Without Accelerated Rates Using Electrospray and Ambient Ionization Mass Spectrometry. **2017**, No. May.
- (263) Chen, X.; Cooks, R. G. Accelerated Reactions in Field Desorption Mass Spectrometry. *Journal of Mass Spectrometry* **2018**, *53* (10), 942–946. <https://doi.org/10.1002/jms.4254>.
- (264) Chen, X. Mass Spectrometry for Reaction Monitoring and Reaction Acceleration, Purdue University, West Lafayette, 2021.

- (265) Cigáň, M.; Jakusová, K.; Gáplovský, M.; Filo, J.; Donovalová, J.; Gáplovský, A. Isatin Phenylhydrazones: Anion Enhanced Photochromic Behaviour. *Photochemical and Photobiological Sciences* **2015**, *14* (11), 2064–2073. <https://doi.org/10.1039/c5pp00275c>.
- (266) Tisovský, P.; Csicsai, K.; Donovalová, J.; Šandrik, R.; Sokolík, R.; Gáplovský, A. Effect of a =X-NH-Fragment, (X = C, N), on Z/E Isomerization and ON/OFF Functionality of Isatin Arylhydrazones, ((Arylamino)Methylene)Indolin-2-Ones and Their Anions. *Molecules* **2020**, *25* (13). <https://doi.org/10.3390/molecules25133082>.
- (267) Filo, J.; Tisovský, P.; Csicsai, K.; Donovalová, J.; Gáplovský, M.; Gáplovský, A.; Cigáň, M. Tautomeric Photoswitches: Anion-Assisted Azo/Azine-to-Hydrazone Photochromism. *RSC Adv* **2019**, *9* (28), 15910–15916. <https://doi.org/10.1039/c9ra02906k>.
- (268) Gnanamani, E.; Yan, X.; Zare, R. N. Chemoselective N-Alkylation of Indoles in Aqueous Microdroplets. *Angewandte Chemie - International Edition* **2020**, *59* (8), 3069–3072. <https://doi.org/10.1002/anie.201913069>.
- (269) Zare, R. N.; Gao, D.; Jin, F.; Yan, X. Selective Synthesis in Microdroplets of 2-Phenyl-2,3-Dihydrophthalazine-1,4-Dione from Phenyl Hydrazine with Phthalic Anhydride or Phthalic Acid. *Chemistry - A European Journal* **2018**. <https://doi.org/10.1002/chem.201805585>.
- (270) Sahota, N.; Abusalim, D. I.; Wang, M. L.; Brown, C. J.; Zhang, Z.; El-Baba, T. J.; Cook, S. P.; Clemmer, D. E. A Microdroplet-Accelerated Biginelli Reaction: Mechanisms and Separation of Isomers Using IMS-MS. *Chem Sci* **2019**, *10* (18), 4822–4827. <https://doi.org/10.1039/c9sc00704k>.

Courses and Oral/Poster Presentations:

As part of my professional development, I have attended the conferences and completed the courses show below:

Courses:

- 13th Mass Spectrometry in Biotechnology & Medicine Summer School - July 2019
- HarvardX edX Principles of Biochemistry (MCB63X) - July 2020
- LabView Core 1 - April 2020
- LabView Core 2 - April 2020
- Nottingham Trent University DoctoratePlus Program Stage 1, 2 & 3

Conferences & Seminars:

- **Attendee** - Nottingham Trent University SST Research Seminars - October 2018 to March 2022
- **Attendee** - RSC Analytical Research Forum - June 2019
- **Poster Presentation** - Mass Spectrometry in Biotechnology & Medicine Summer School - July 2019
- **Oral Presentation** - Exploratory Measurement Scientific Group Ardgour Conference - September 2019
- **Poster Presentation** - Middle England Regional Chemistry Interactive Alliance (MERCIA) 5th Annual Conference - December 2019
- **Attendee** - BMSS Ambient Ionisation Meeting - January 2020
- **Oral Presentation** - M4I Division of Imaging Mass Spectrometry Faculty - March 2022
- **Poster Presentation** - The International Mass Spectrometry Conference, Maastricht - September 2022

Appendix

Chapter 1

Triton QS-15

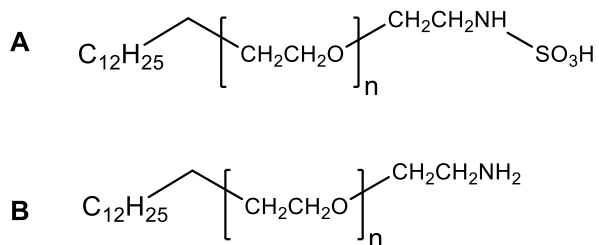


Figure 168 - Triton QS-15 Structures

Jeffamine M600

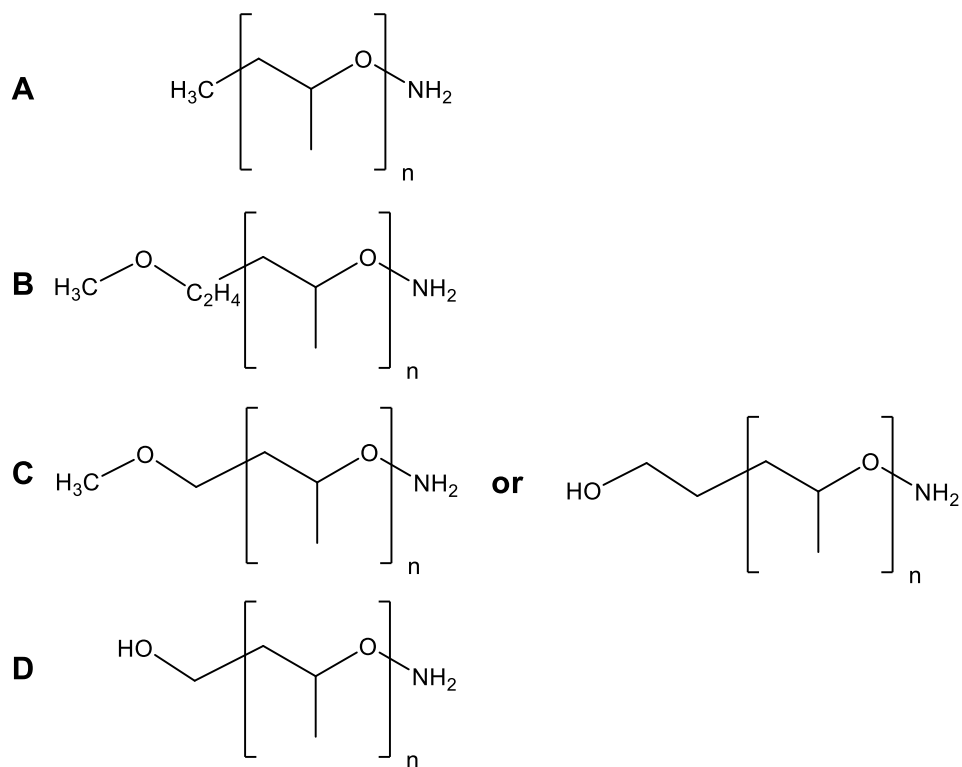
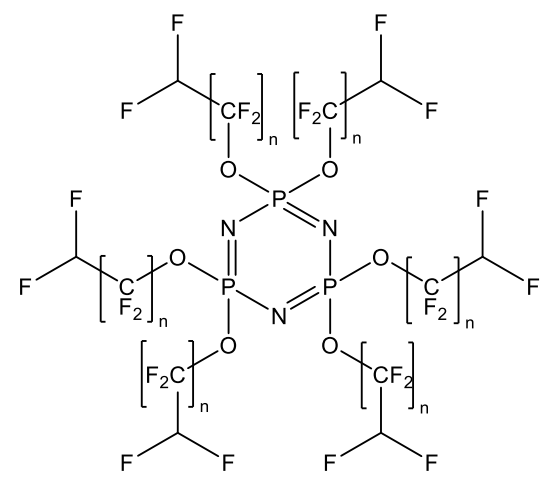
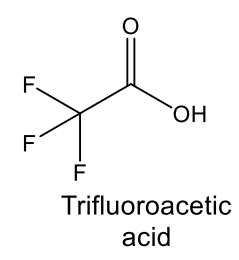
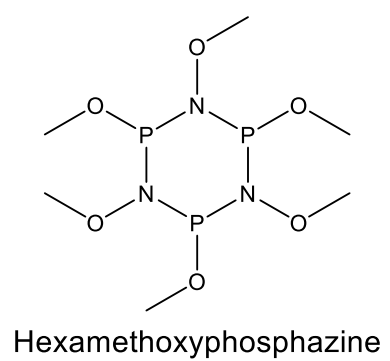
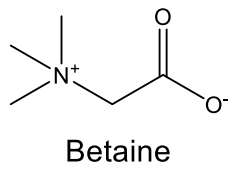


Figure 169 - Jeffamine M600 Structures



Structure for Hexakis phosphazine series (n = 0-7)

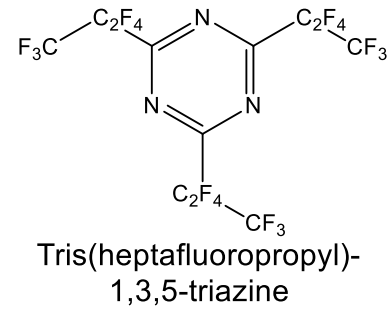
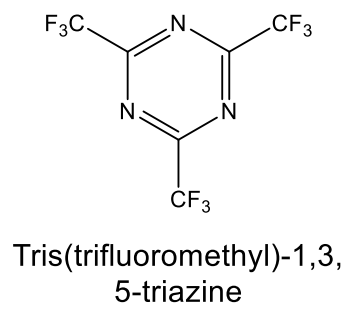
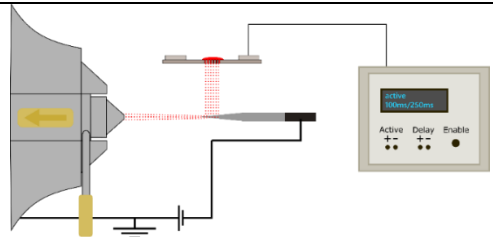
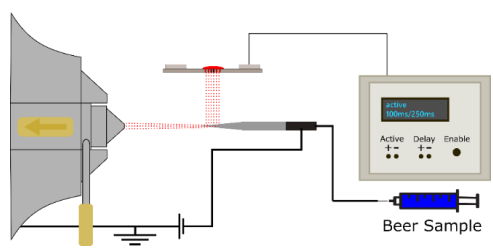


Figure 170 - ESI Cal Tuning Mix Component Structures

Chapter 3

Table 13 - Overview of Ionisation Sources				
Number	ID	Overview	General Schematic	Coupled to
Ion Source 1.0	MDD	Single Microdrop into MS Inlet		Waters Xevo G2-XS Q-TOF
Ion Source 2.0	MDD ²	Double Microdrop into MS Inlet		Waters Xevo G2-XS Q-TOF
Ion Source 3.0	MDD-ESI	Single Microdrop into ESI Stream		Waters Xevo G2-XS Q-TOF
Ion Source 4.0	MDD-PESI	Single Microdrop onto Needle		Waters Xevo G2-XS Q-TOF
Ion Source 5.0	MDD ² -PESI	Double Microdrop onto Needle		Waters Xevo G2-XS Q-TOF
Ion Source 6.0	PUPP	Single PUPP into MS Inlet		Waters Xevo G2-XS Q-TOF Thermo Fisher Orbitrap

Ion Source 7.0	PUPP-PESI	Single PUPP onto Needle		Waters Xevo G2-XS Q-TOF
Ion Source 8.0	PUPP-ESI	Single PUPP into ESI Spray		Waters Xevo G2-XS Q-TOF
Ion Source 8.1				Sciex TripleTOF 6600
Ion Source 8.2				Bruker solarix 12T FT-ICR
				Thermo Orbitrap QE-HF

Chapter 4:

Human Plasma Analysis

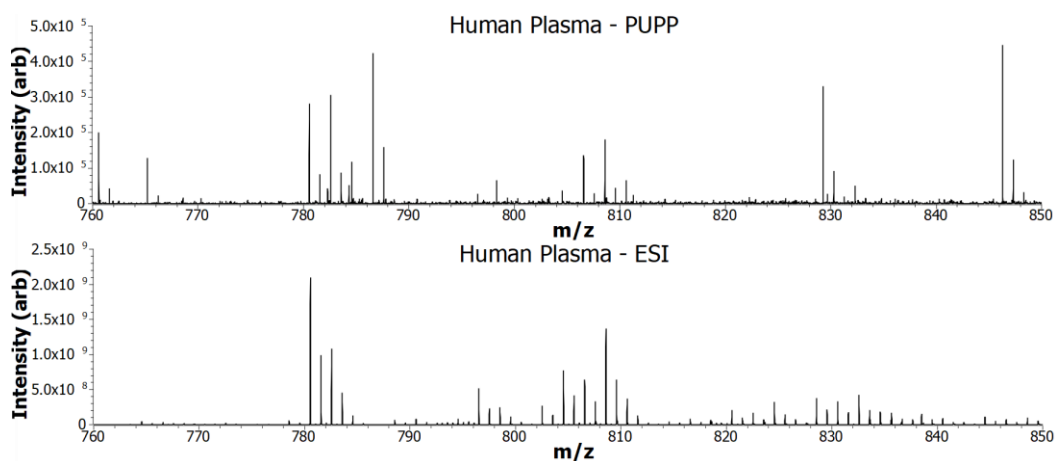


Figure 171 - Human Plasma Spectra obtained via PUPP and ESI

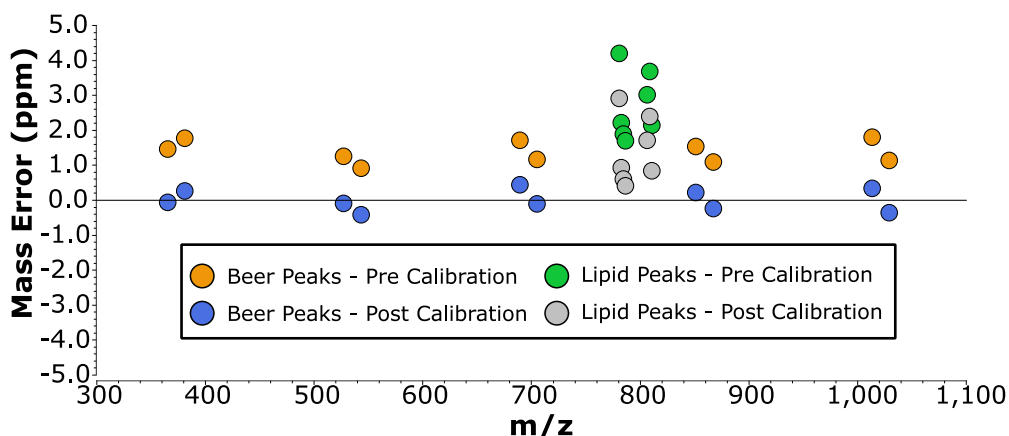


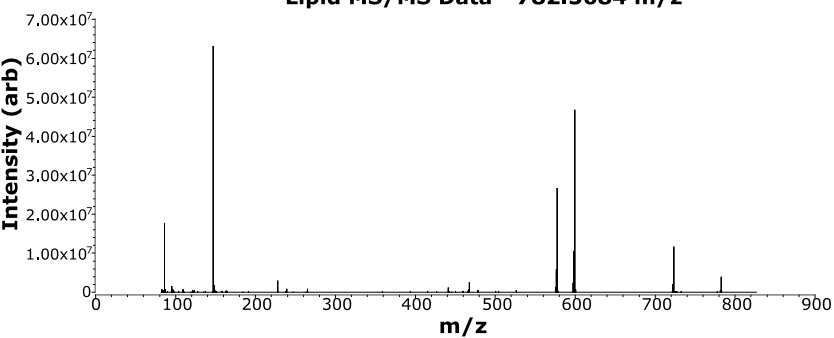
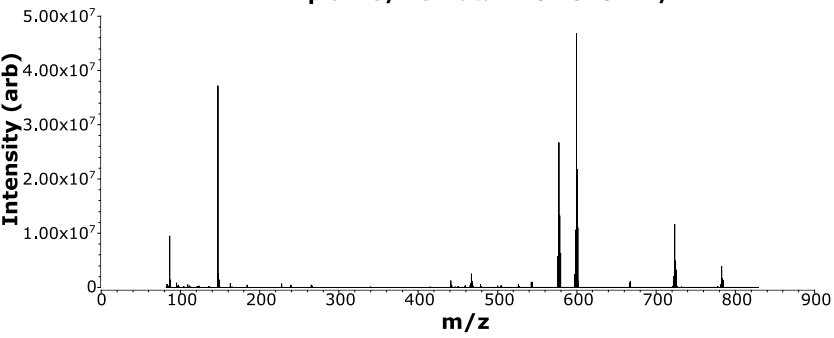
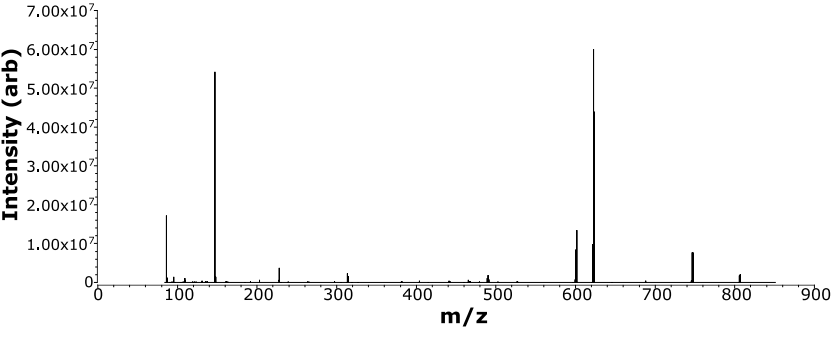
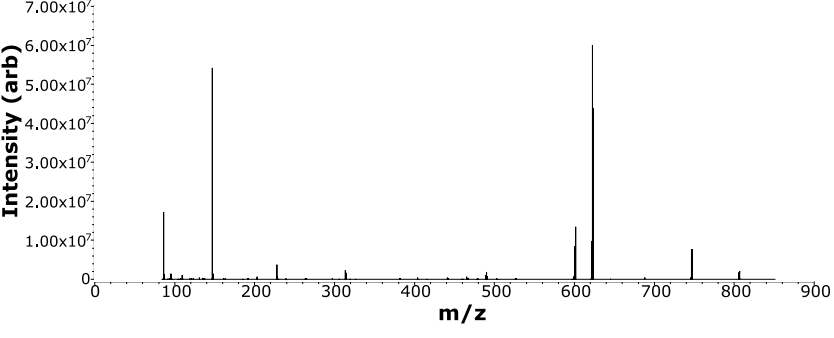
Figure 172 - Human Plasma Internal Calibration

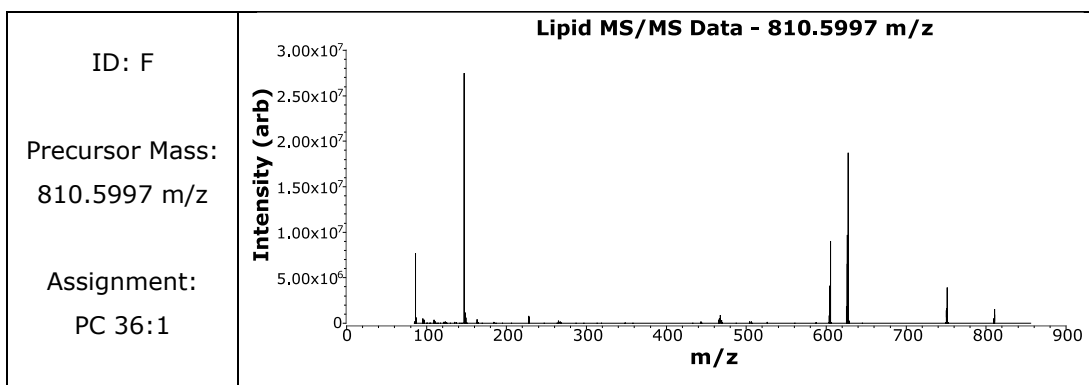
Lipid Extraction Method (ESI Data Only)

Table 14 - Human Plasma Analysis Instrument Settings	
Setting	Value
Mass Spectrometer	Orbitrap Exploris 480
Ion Source	ESI
Polarity	Positive
ESI Voltage	4350 V
Ion Transfer Tube Temperature	330°C
Full Scan Resolution	120000
Full Scan Mass Range	200-1450 m/z
HCD Collision Energy (%)	30
MS/MS Resolution	30000

Extraction performed by Andrej Grgić at Maastricht MultiModal Molecular Imaging Institute (M4i), Maastricht University. 100 µL of plasma + 900 µL of methanol (100%) were mixed in an Eppendorf tube. Sample was vortexed for 10 seconds and then left to incubate for 30 minutes on ice. Sample was centrifuged at 14,000 g for 16 minutes. The supernatant was transferred into a fresh Eppendorf tube, and the sample then analysed via direct infusion MS/MS.

Table 15 - Human Plasma Lipid ESI-MS/MS Data	
Ions	Spectrum
ID: A Precursor Mass: 780.5504 m/z Assignment: PC 34:2	<p style="text-align: center;">Lipid MS/MS Data - 780.5504 m/z</p>

<p>ID: B</p> <p>Precursor Mass: 782.5684 m/z</p> <p>Assignment: PC 34:1</p>	<p>Lipid MS/MS Data - 782.5684 m/z</p> 
<p>ID: C</p> <p>Precursor Mass: 784.5481 m/z</p> <p>Assignment: PC 34:0</p>	<p>Lipid MS/MS Data - 784.5481 m/z</p> 
<p>ID: D</p> <p>Precursor Mass: 806.5684 m/z</p> <p>Assignment: PC 36:3</p>	<p>Lipid MS/MS Data - 806.5684 m/z</p> 
<p>ID: E</p> <p>Precursor Mass: 808.5816 m/z</p> <p>Assignment: PC 36:2</p>	<p>Lipid MS/MS Data - 808.5816 m/z</p> 



Beer

Table 16 - Beer Peaks and Assignments

m/z	Component	Adduct
365.0999	Maltose/Sucrose	[M+Na] ⁺
381.0756	Maltose/Sucrose	[M+K] ⁺
527.1652	Maltotriose	[M+Na] ⁺
543.1371	Maltotriose	[M+K] ⁺
689.2261	Maltotetraose	[M+Na] ⁺
705.7984	Maltotetraose	[M+K] ⁺
851.2745	Maltopentaose	[M+Na] ⁺
867.2548	Maltopentaose	[M+K] ⁺
1013.3446	Maltohexaose	[M+Na] ⁺
1029.3285	Maltohexaose	[M+K] ⁺
1175.4280	Maltoheptaose	[M+Na] ⁺
1191.3945	Maltoheptaose	[M+K] ⁺

Table 17 - Origins of Beer Analysed

Code	Country of Origin	Code	Country of Origin
P1	UK	M1	Denmark
P2	UK	M2	Jamaica
P3	UK	M3	Germany
P4	UK	M4	Germany
P5	UK	M5	Germany
P6	UK	D1	UK
P7	UK	D2	Ireland
P8	UK	D3	UK
P9	UK	D4	UK
P10	UK	D5	UK
P11	UK	D6	UK

P12	UK	D7	Ireland
P13	UK	D8	Jamaica
P14	UK	D9	UK
P15	UK		

P = Pale, M = Malt, D = Dark

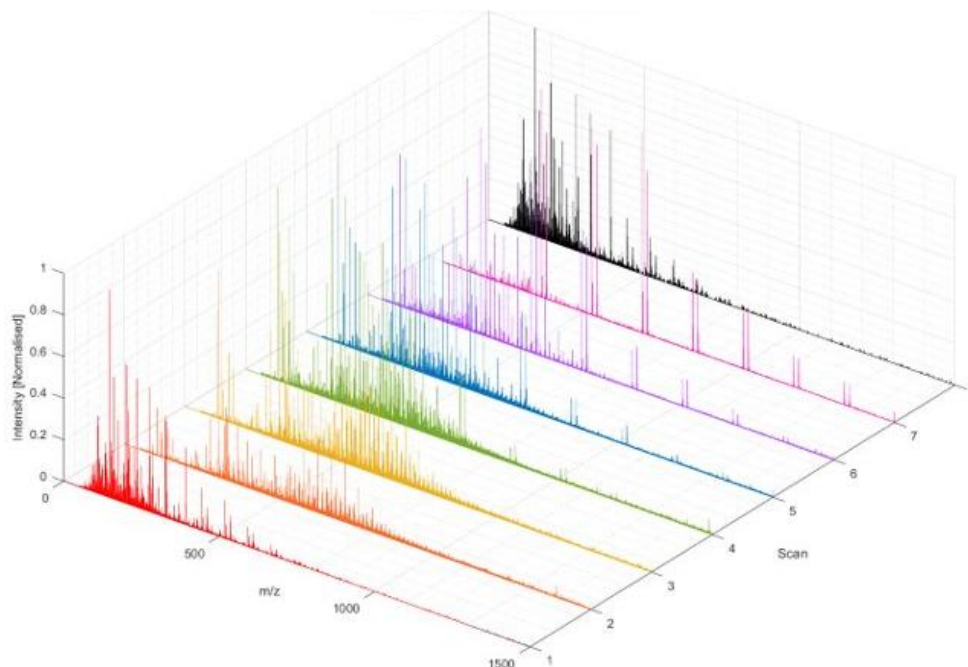


Figure 173 - Sequential Ionisation Effect (Waterfall Plot)

BMSS Ambient Ionisation Study

Table 18 - BMSS Study Sample Components		
Analyte	Formula	Monoisotopic Mass (Da)
Paracetamol	C ₈ H ₉ NO ₂	151.063
Paracetamol-d ₄	C ₈ H ₅ D ₄ NO ₂	155.088
Ibuprofen	C ₁₃ H ₁₈ O ₂	206.131
Diclofenac	C ₁₄ H ₁₁ Cl ₂ NO ₂	295.017
Colchicine	C ₂₂ H ₂₅ NO ₆	399.168
Terfenadine	C ₃₂ H ₄₁ NO ₂	471.314
Reserpine	C ₃₃ H ₄₀ N ₂ O ₉	608.273
Erythromycin	C ₃₇ H ₆₇ NO ₁₃	733.461

Table 19 - BMSS Mixture (Acetonitrile) Data for PUPP-Orbitrap			
Analyte	Ion	m/z	Mass Error (ppm)
Paracetamol	[M+H] ⁺	152.0704	-1.351
Paracetamol-d ₄	[M+H] ⁺	156.0956	-0.727
Diclofenac	[M+H] ⁺	296.0238	-0.545
Colchicine	[M+H] ⁺	400.1756	+0.336
Terfenadine	[M+H] ⁺	472.3212	+0.412
Reserpine	[M+H] ⁺	609.2808	+0.231
Erythromycin	[M-H ₂ O+H] ⁺	716.4568	-1.613

Ibuprofen	[M-H] ⁻	205.1231	-1.473
-----------	--------------------	----------	--------

Analyte	Ion	m/z	Mass Error (ppm)
Paracetamol	[M+Na] ⁺	174.0526	0.285
Paracetamol-d ₄	[M+Na] ⁺	178.0777	0.214
Diclofenac	[M+K] ⁺	333.9801	0.765
Colchicine	[M+H] ⁺	400.1756	0.336
Colchicine	[M+Na] ⁺	422.1575	0.212
Colchicine	[M+K] ⁺	438.1317	0.802
Terfenadine	[M+H] ⁺	472.3210	-0.011
Terfenadine	[M+Na] ⁺	494.3029	-0.102
Reserpine	[M+H] ⁺	609.2804	-0.426
Reserpine	[M+Na] ⁺	631.2613	-2.066
Erythromycin	[M-H ₂ O+H] ⁺	716.4583	0.469

Participant ID	Instrument	Ionisation Source	Metric
ASI03	Triple Quadrupole	ASAP	Area
ASI04	Orbitrap	DART	Area
ASI05	Single Quadrupole	ASAP	Area
ASI06	Triple Quadrupole	TD-CDI	Area
ASI08	Orbitrap	DART	Area
ASI09	Triple Quadrupole	Paperspray	Intensity
AIS11 A	Q-TOF	ASAP	Area
AIS11 B	Orbitrap	ASAP	Area
AIS12	Orbitrap	LESA	Intensity
AIS13	TOF	ASAP	Area
AIS14 A	TOF	ASAP	Area
AIS14 B	TOF	ASAP	Area
AIS14 C	Single Quadrupole	SESI	Area
AIS14 D	Single Quadrupole	ASAP	Area
AIS14 E	Single Quadrupole	ASAP	Area
AIS16	Single Quadrupole	ASAP	Area
AIS19	Q-TOF	DESI	Intensity
AIS20 A	Orbitrap	DART	Area
AIS20 B	Orbitrap	DART	Area
AIS23	Orbitrap	DART	Area
AIS24	Q-TOF	AP-MALDI	Intensity

Note: This data is taken from the British Mass Spectrometry Society (BMSS) Ambient Ionisation Special Interest Group Interlaboratory Study II. It has been included within this thesis for the reader's benefit to give some context for the data presented. For further details on the study, the author recommends reading the report in its full.

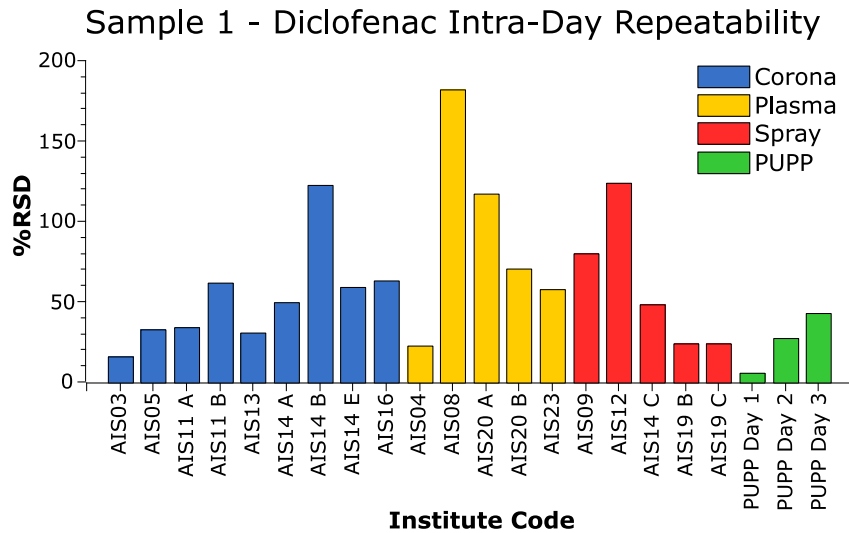


Figure 174 - Diclofenac in Acetonitrile - Intra-Day repeatability

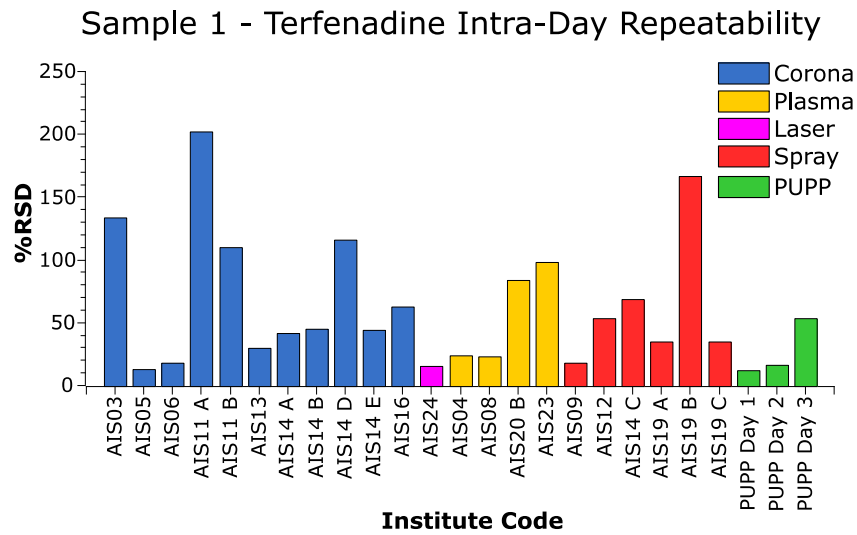


Figure 175 - Terfenadine in Acetonitrile - Intra-Day repeatability

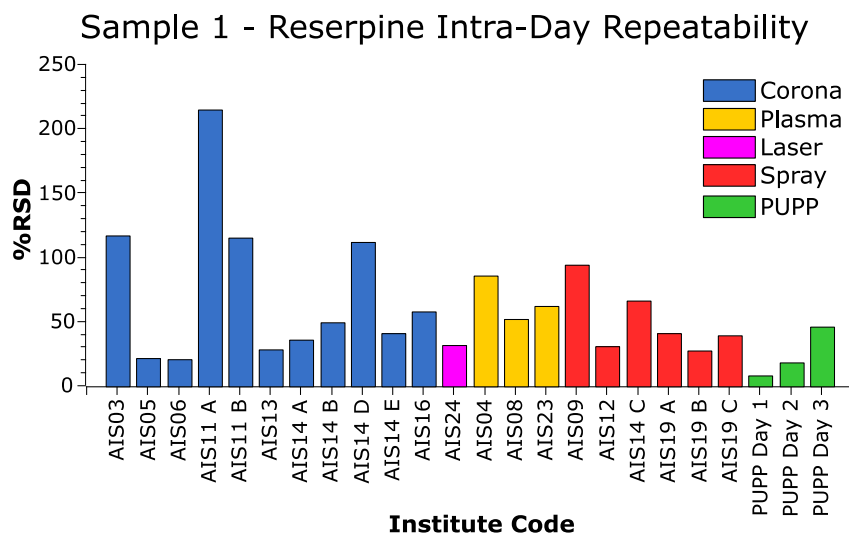


Figure 176 - Reserpine in Acetonitrile - Intra-Day repeatability

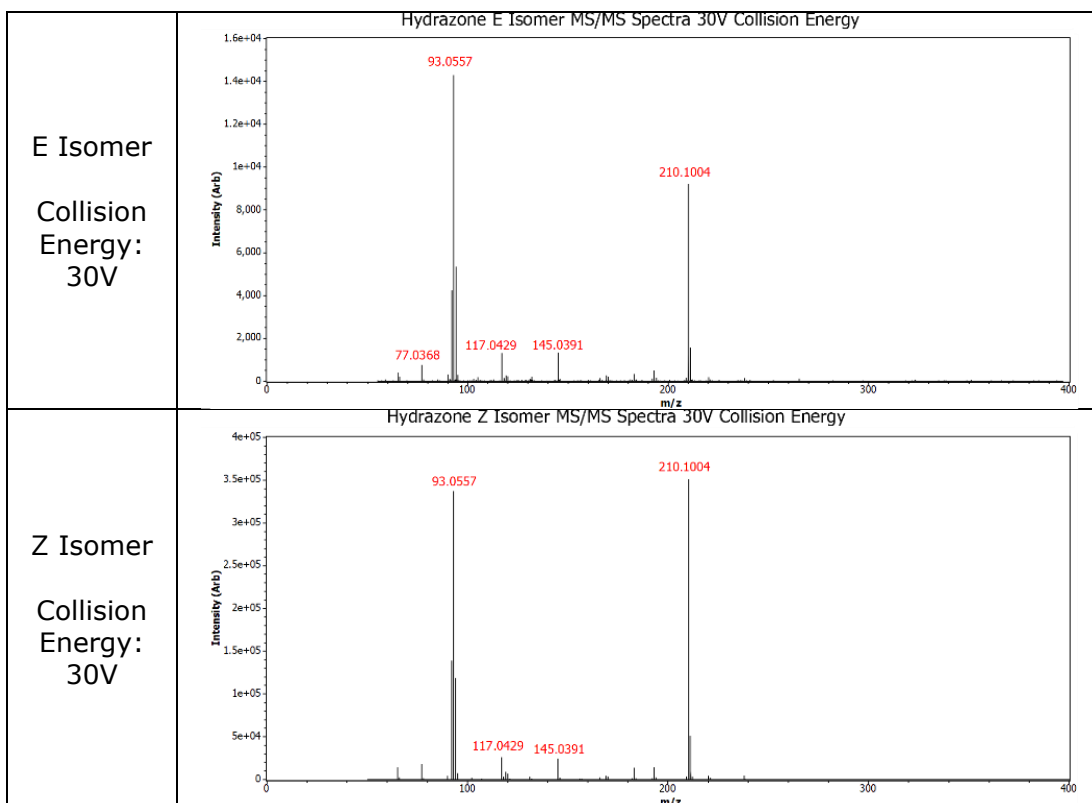
Chapter 5

Table 22 - Fused Silica Grinder Version 4 Parts List			
Part	Quantity	Notes:	Approx. Cost (£)
3D Printed Components	5	N/A	N/A
3V Motor	1	10,000 RPM, 2mm Shaft Ø	0.79
9V Battery	1	N/A	3.00
9V Battery Case	1	N/A	1.50
Speed Controller	1	N/A	1.39
12V Motor	1	2000 RPM	10.40
AA Batteries	2	N/A	0.85
AA Battery Holder	1	N/A	0.79
V Belt Pulleys	2	3mm bore	2.60
Closed Loop Timing Belt	1	110-2GT, 6 mm diameter	1.96
Bearings	2	3mm bore	1.58
Stainless Steel Tubing	1	3mm OD, 2mm ID.	0.98
Mini Drill Chuck	1	2mm bore	2.16
ZDV Union	1	N/A	15.80
Custom Brass Component	1	N/A	N/A
Assorted Nuts & Bolts	Various	N/A	N/A
<i>System Total Cost:</i>			£43.80

Chapter 8

Hydrazone

Table 23 - Isatin Phenylhydrazine LC-MS/MS Fragmentation Data	
Isomer	Collision Energy
E Isomer Collision Energy: 10V	<p>Hydrazone E Isomer MS/MS Spectra 10V Collision Energy</p> <p>Intensity (Ab)</p> <p>m/z</p>
Z Isomer Collision Energy: 10V	<p>Hydrazone Z Isomer MS/MS Spectra 10V Collision Energy</p> <p>Intensity (Ab)</p> <p>m/z</p>
E Isomer Collision Energy: 20V	<p>Hydrazone E Isomer MS/MS Spectra 20V Collision Energy</p> <p>Intensity (Ab)</p> <p>m/z</p>
Z Isomer Collision Energy: 20V	<p>Hydrazone Z Isomer MS/MS Spectra 20V Collision Energy</p> <p>Intensity (Ab)</p> <p>m/z</p>



Isomer	Collision Energy		
	10 V	20 V	30 V
E Isomer	238.10, 210.09, 94.06	238.10, 210.09, 145.04, 94.06	210.09, 145.04, 117.04, 93.06, 77.04
Z Isomer	238.10, 210.09, 94.06	238.10, 210.09, 145.04, 94.06	210.09, 145.04, 117.04, 93.06, 77.04

E/Z Isatin Phenylhydrazone ¹H NMR assignment and discussion:

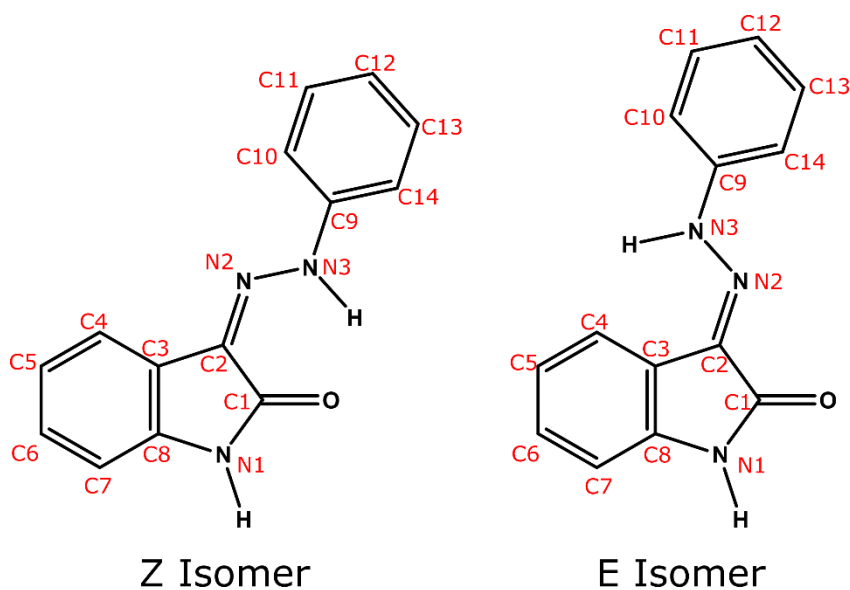


Figure 177 - Isatin Phenylhydrazone Carbon and Nitrogen Numbered

Isatin Phenylhydrazone Z-Isomer:

^1H NMR (400 MHz, DMSO- d_6): 11.00 (s, 1H, N(1)-H), 7.52 (d, 1H, J = 7.6 Hz, C(4)-H), 7.40 (d, 2H, J = 8.0 Hz, C(10,14)-H), 7.34 (t, 2H, J = 6.8 Hz, C(11,13)-H), 7.21 (t, 1H, J = 6.8 Hz, C(12)-H), 7.04-6.99 (m, 2H, C(5,6)-H), 6.89 (d, 1H, J = 7.6 Hz, C(7)-H).

Isatin Phenylhydrazone E-Isomer:

^1H NMR (400 MHz, DMSO- d_6): 10.54 (s, 1H, N(3)-H), 10.44 (s, 1H, N(1)-H), 8.16 (d, 1H, J = 7.6 Hz C(4)-H), 7.47 (d, 1H, J = J = 8.4 Hz, C(10,14)-H), 7.32 (t, 2H, J = 7.6 Hz, C(11,13)-H), 7.26 (t, 1H, J = 7.6 Hz, C(12)-H), 7.02-6.97 (m, 2H, C(5,6)-H), 6.85 (d, 1H, J = 7.6 Hz, C(7)-H)

Note: N(3)-H for the Z-Isomer is found outside of measured ppm range at \approx 12.75 ppm

Discussion:

As the LED irradiated ^1H NMR spectra has a mixture of the E and Z Isatin Phenylhydrazone isomers, there are peaks for both compounds present within this spectrum. As expected, there are no peaks for the E isomer observed within the sample which had not been subjected to LED light. This is shown in Figure 177, which shows a region of the NMR spectra for the sample with and without LED irradiation.

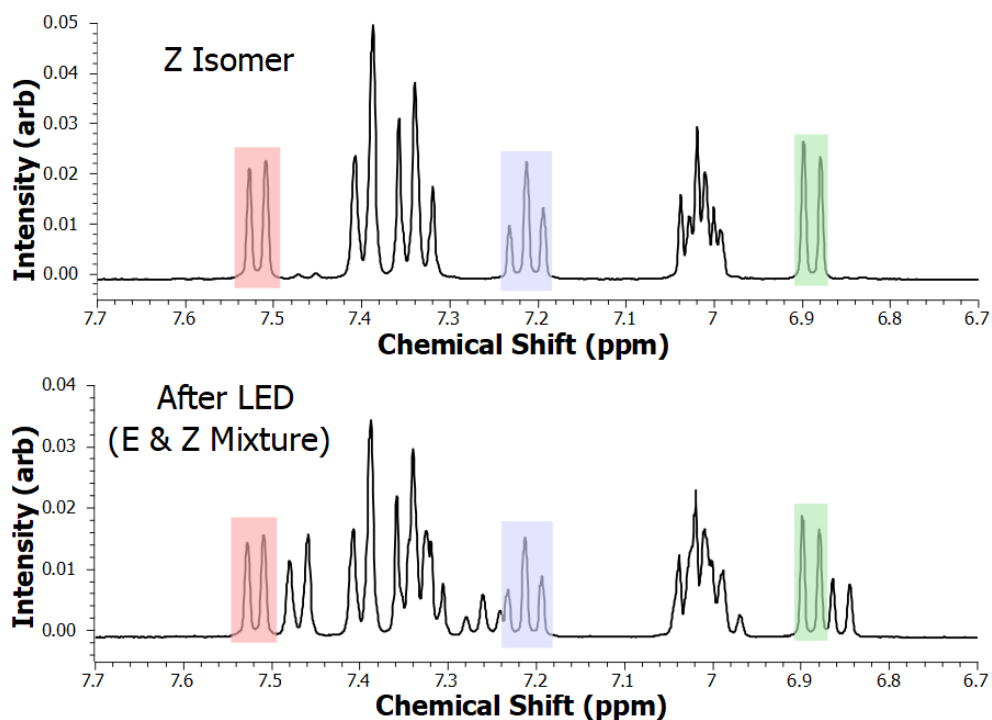


Figure 178 - ¹H NMR Spectra for E and Z Isatin Phenylhydrazine

Note: Peaks which appear in both spectra (Z-Isomer peaks) are coloured for clarity

Table 24 shows the change in ppm observed for some of the peaks between the Z and E isomers. The majority of these shifts are small, and this is reflected in the spectra.

Table 24 - Changes in Chemical Shift observed from Z to E Isatin Phenylhydrazine		
Z Isomer ppm	E Isomer ppm	Change in ppm
≈12.75 (s, 1H, N(3)-H)	10.54 (s, 1H, N(3)-H)	- 2.21 ppm
11.00 (s, 1H, N(1)-H)	10.44 (s, 1H, N(1)-H)	- 0.56 ppm
7.52 (d, 1H, J = 7.6 Hz, Ar-H)	8.16 (d, 1H, J = 7.6 Hz, Ar-H)	+ 0.64 ppm
7.40 (d, 2H, J = 8.0 Hz, Ar-H)	7.47 (d, 2H, J = 8.4 Hz, Ar-H)	+ 0.07 ppm
7.34 (t, 2H, J = 6.8 Hz, Ar-H)	7.32 (t, 2H, J = 7.6 Hz, Ar-H)	- 0.02 ppm
7.21 (t, 1H, J = 6.8 Hz, Ar-H)	7.26 (t, 1H, J = 7.6 Hz, Ar-H)	+ 0.05 ppm
7.04-6.99 (m, 2H, Ar-H)	7.02-6.97 (m, 2H, Ar-H)	- 0.02 ppm
6.89 (d, 1H, J = 7.6 Hz, Ar-H)	6.85 (d, 1H, J = 7.6 Hz, Ar-H)	- 0.04 ppm

The most significant differences between the two spectra were mentioned earlier in the chapter. This is the emergence of two singlets at 10.54 and 10.44 ppm, and the doublet at 8.16 ppm. These peaks correspond to the protons which undergo the most significant changes in electron density when switching from the Z to the E isomer. The C(4)-H proton shifts from a 7.52 ppm to 8.16 ppm, likely due to the effect of the phenyl ring. N(1)-H also experiences a small shift (11.00 ppm to 10.44 ppm), whilst the N(3)-H, which is no longer hydrogen bonded to the carbonyl, undergoes the most significant shift, from ≈ 12.75 ppm to 10.54 ppm.

Pechmann Condensation

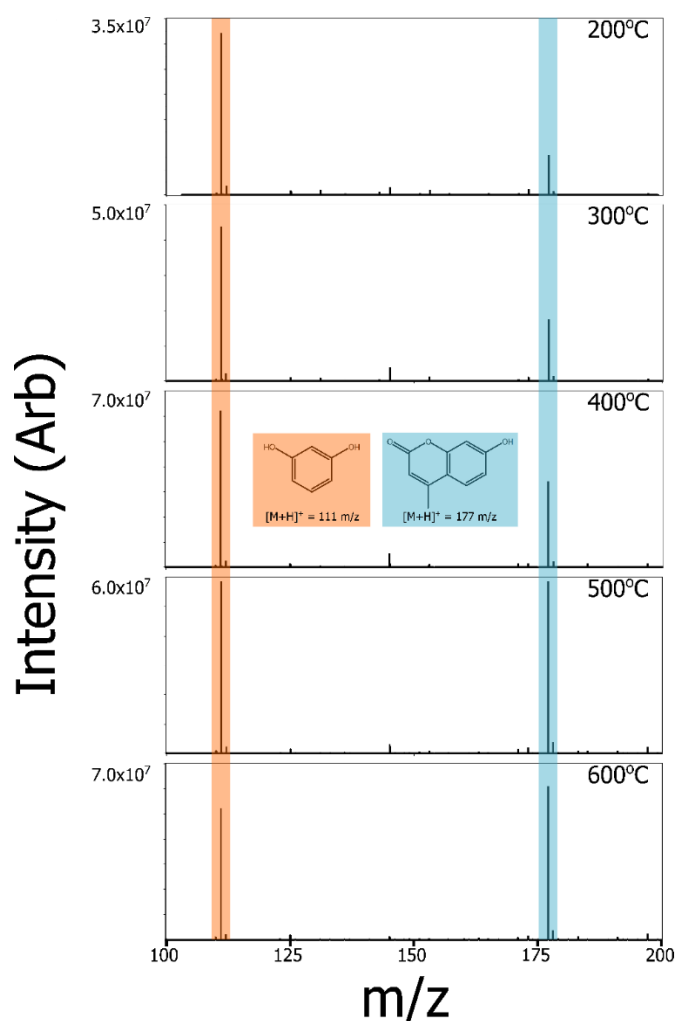


Figure 179 - Intensity of Reactant and Product Peaks vs Desolvation Gas Temperature

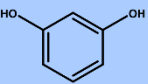
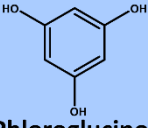
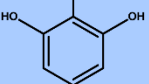
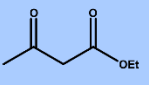
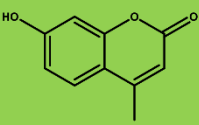
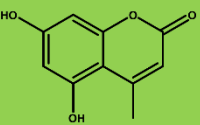
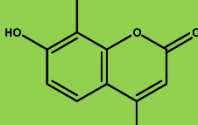
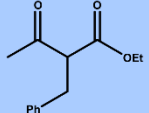
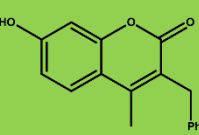
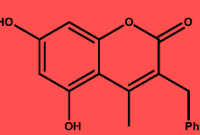
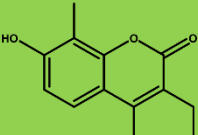
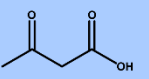
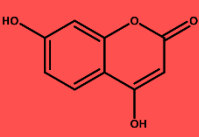
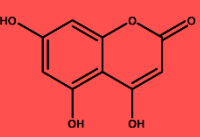
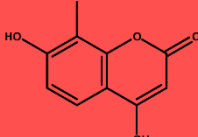
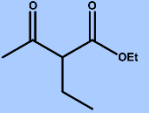
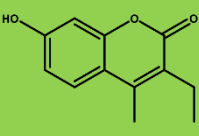
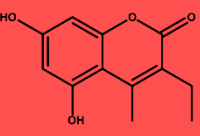
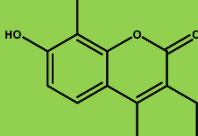
Pechmann Condensation Bulk Screening	 Resorcinol	 Phloroglucinol	 2-Methyl-Resorcinol
 Ethyl Acetoacetate			
 Ethyl-2-benzylacetoacetate			
 Malonic Acid			
 Ethyl-2-ethylacetoacetate			

Figure 180 - Pechmann Bulk Synthesis Screening

Note: Blue – Reactant, Green –Successful, Red – No Product Obtained

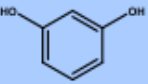
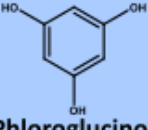
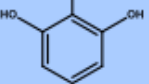
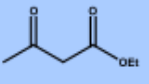
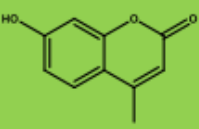
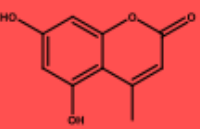
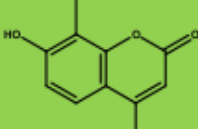
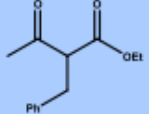
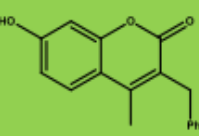
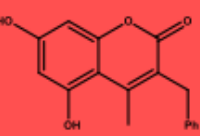
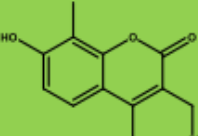
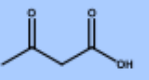
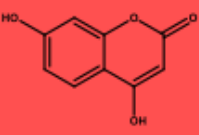
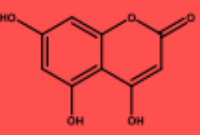
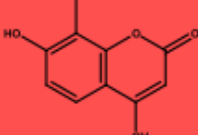
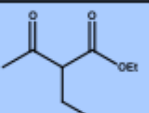
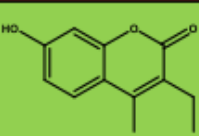
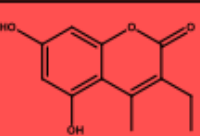
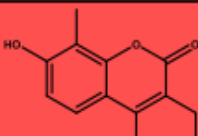
Pechmann Condensation Microdroplet Screening	 Resorcinol	 Phloroglucinol	 2-Methyl-Resorcinol
 Ethyl Acetoacetate			
 Ethyl-2-benzylacetoacetate			
 Malonic Acid			
 Ethyl-2-ethylacetoacetate			

Figure 181 - Pechmann Microdroplet Synthesis Screening

Note: Blue – Reactant, Green –Successful, Red – No Product Obtained

Pechmann Analogues Reference Material Synthesis:

Note: Reactions 3, 6, 7, 8 and 11 were unsuccessful for the bulk synthesis and therefore no data is reported for these.

Reaction 1: Synthesis of 7-Hydroxy-4-methylcoumarin

0.010 mol of Resorcinol and 0.010 mol of Ethyl Acetoacetate were weighed into a 100 mL round bottom flask. 10 mL of conc. H₂SO₄ was added dropwise to the reaction mixture so it did not rise above 10°C. The reaction mixture was stirred for 15 hours at room temperature before rapidly cooling in an ice bath to form crude product. Crude product was vacuum filtered off before being recrystallized from Ethanol.

Yield = 32%. ¹H NMR (400 MHz, DMSO-d₆): 2.33 (s, 3H, -CH₃), 6.10 (s, 1H, Ar-H), 6.67 (d, 1H, J = 2.4 Hz, Ar-H), 6.78 (d, J = 2.8 Hz, 1H, Ar-H), 6.75 (d, J = 2.8 Hz, 1H, Ar-H) 7.56 (d, J = 8.4 Hz, Ar-H), 10.51 (s, 1H, -OH).

Reaction 2: Synthesis of 3-Benzyl-7-hydroxy-4-methylcoumarin

0.010 mol of Resorcinol and 0.010 mol of Ethyl-2-Benzylacetoacetate were weighed into a 100 mL round bottom flask. 10 mL of conc. H₂SO₄ was added dropwise to the reaction mixture so it did not rise above 10°C. The reaction mixture was stirred for 15 hours at room temperature before rapidly cooling in an ice bath to form crude product. Crude product was vacuum filtered off before being recrystallized from Ethanol.

Yield = 26% ¹H NMR (400 MHz, DMSO-d₆): 2.36 (s, 3H, -CH₃), 3.55 (s, 2H, -CH₂), 6.66 (d, J = 2.4 Hz, Ar-H), 6.78 (d, J = 2.4 Hz, Ar-H), 6.75 (d, J = 2.4 Hz, Ar-H) 7.18 (m, Ar-H), 7.33 (m, Ar-H), 7.61 (d, J = 8.8 Hz, Ar-H) 10.43, (s, 1H, -OH).

Reaction 4: Synthesis of 3-Ethyl-7-hydroxy-4-methylcoumarin

0.011 mol of Resorcinol and 0.010 mol of Ethyl-2-Ethylacetoacetate were weighed into a 100 mL round bottom flask. 10 mL of conc. H₂SO₄ was added dropwise to the reaction mixture so it did not rise above 10°C. The reaction mixture was stirred for 15 hours at room temperature before rapidly cooling in an ice bath to form crude product. Crude product was vacuum filtered off before being recrystallized from Ethanol.

Yield = 20% ¹H NMR (400 MHz, DMSO-d₆): 0.99 (s, -CH₃), 2.31 (s, -CH₃), 2.47 (s, -CH₂), 6.64 (s, Ar-H), 6.74 (s, 1H, Ar-H), 6.64 (s, 1H, Ar-H) 7.57 (d, J = 7.6 Hz, Ar-H), 10.35 (s, -OH).

Reaction 5: Synthesis of 5,7-Dihydroxy-4-methylcoumarin

0.011 mol of Phloroglucinol and 0.010 mol of Ethyl Acetoacetate were weighed into a 100 mL round bottom flask. 10 mL of conc. H₂SO₄ was added dropwise to the reaction mixture so it did not rise above 10°C. The reaction mixture was stirred for 15 hours at room temperature before rapidly cooling in an ice bath to form crude product. Crude product was vacuum filtered off before being recrystallized from Ethanol.

Yield = 51% ¹H NMR (400 MHz, DMSO-d₆): 3.35 (s, -CH₃), 5.81 (s, Ar-H), 6.21 (s, 1H, Ar-H), 6.12 (s, 1H, Ar-H) 10.28 (s, -OH), 10.51 (s, -OH).

Reaction 9: Synthesis of 7-Hydroxy-4,8-dimethylcoumarin

0.010 mol of 2-Methyl-Resorcinol and 0.010 mol of Ethyl Acetoacetate were weighed into a 100 mL round bottom flask. 10 mL of conc. H₂SO₄ was added dropwise to the reaction mixture so it did not rise above 10°C. The reaction mixture was stirred for 15 hours at room temperature before rapidly cooling in an ice bath to form crude product. Crude product was vacuum filtered off before being recrystallized from Ethanol.

Yield = 35% ¹H NMR (400 MHz, DMSO-d₆): 2.04 (s, -CH₃), 2.11 (s, -CH₃), 6.08 (s, Ar-H), 6.82 (d, J = 8.8 Hz, Ar-H), 7.41 (d, J = 8.8 Hz, Ar-H), 10.38 (s, -OH).

Reaction 10: Synthesis of 3-Benzyl-7-hydroxy-4,8-dimethylcoumarin

0.010 mol of 2-Methyl-Resorcinol and 0.010 mol of Ethyl-2-Benzylacetoacetate were weighed into a 100 mL round bottom flask. 10 mL of conc. H₂SO₄ was added dropwise to the reaction mixture so it did not rise above 10°C. The reaction mixture was stirred for 15 hours at room temperature before rapidly cooling in an ice bath to form crude product. Crude product was vacuum filtered off before being recrystallized from Ethanol.

Yield = 39% ¹H NMR (400 MHz, DMSO-d₆): 2.12 (s, -CH₃), 2.35 (s, -CH₃), 3.90 (s, -CH₂), 6.82 (d, J = 8.4 Hz, Ar-H), 7.18 (m, Ar-H), 7.45 (d, J = 8.4 Hz, Ar-H), 10.29 (s, -OH).

Reaction 12: Synthesis of 3-Ethyl-7-hydroxy-4,8-dimethylcoumarin

0.010 mol of 2-Methyl-Resorcinol and 0.010 mol of Ethyl-2-Ethylacetoacetate were weighed into a 100 mL round bottom flask. 10 mL of conc. H₂SO₄ was added dropwise to the reaction mixture so it did not rise above 10°C. The reaction mixture was stirred for 15 hours at room temperature before rapidly cooling in an ice bath to form crude product. Crude product was vacuum filtered off before being recrystallized from Ethanol.

Yield = 36% ^1H NMR (400 MHz, DMSO- d_6): 0.98 (t, -CH $_3$), 2.10 (s, -CH $_3$), 2.30 (s, -CH $_3$), 2.50 (q, -CH $_2$), 6.81 (d, Ar-H), 7.41 (d, Ar-H), 10.23 (s, -OH).